USING TROPICAL WARM POOL-INTERNATIONAL CLOUD EXPERIMENT OBSERVATIONS TO EVALUATE AND IMPROVE HIGH RESOLUTION SIMULATIONS OF TROPICAL CONVECTIVE PRECIPITATION SYSTEMS

by

Adam Christopher Varble

A dissertation submitted to the faculty of
The University of Utah
in partial fulfillment of the requirements for the degree of

Doctor of Philosophy

Department of Atmospheric Sciences

The University of Utah

August 2013

The University of Utah Graduate School

STATEMENT OF DISSERTATION APPROVAL

The dissertation of **Adam Christopher Varble**

has been approved by the following supervisory committee members:

Edward Zipser	, Chair	**5/1/2013** Date Approved
Gerald Mace	, Member	**5/1/2013** Date Approved
Steven Krueger	, Member	**5/1/2013** Date Approved
Zhaoxia Pu	, Member	**5/1/2013** Date Approved
Ann Fridlind	, Member	**5/1/2013** Date Approved

and by **Kevin Perry** , Chair of the Department of **Atmospheric Sciences**

and by Donna M. White, Interim Dean of The Graduate School.

ABSTRACT

Ten separate idealized cloud-resolving model (CRM) and four separate nested limited area model (LAM) three-dimensional simulations having horizontal grid spacing of ~1 km and ~75–100 vertical levels are compared to observations during the active monsoon period of the Tropical Warm Pool – International Cloud Experiment, based in Darwin, Australia, with specific focus on a large mesoscale convective system observed on January 23–24, 2006. All simulations produce high biased convective radar reflectivity and low biased stratiform rainfall with these biases heavily modulated by bulk microphysics scheme assumptions.

High biased convective radar reflectivity aloft always involves a graupel/hail component, but also includes a snow component for some two-moment schemes. Making snow particle mass proportional to ~D^2 rather than D^3 may lower snow reflectivity. This high bias is also related to freezing of very large simulated rain water contents in deep convective updrafts. Peak vertical velocities are greater than dual-Doppler retrieved values, especially in the upper troposphere likely due to greater latent heating from freezing and deposition in simulations. A subdomain LES simulation also produces overly intense simulated updrafts. Therefore, they may be a product of interactions between convective dynamics and parameterized microphysics that promote a different convective mode and strength than observed, while inadequately simulated instability and vertical shear variability may also be involved.

Two-moment schemes do not outperform one-moment schemes in stratiform rainfall prediction. Excessive size sorting produces more large stratiform raindrops at low levels than observed in two-moment schemes. One-moment schemes produce too many small stratiform raindrops relative to observed because constant size intercepts are too high. Increasing the rain gamma shape parameter from 0 to 2.5 improves agreement with observations. Due to differences in raindrop size that create different mass sedimentation rates, low-level stratiform liquid water contents are close to observed in one-moment schemes, but lower than observed in two-moment schemes. Low biased stratiform rainfall is primarily due to an under-prediction of melting ice consistent with the lack of a large well-developed stratiform region in simulations. This may be caused by overly intense simulated convection, limited domain size in the CRM simulations, and large-scale forcing biases in the LAM simulations.

CONTENTS

ABSTRACT iii

ACKNOWLEDGMENTS vii

Chapter

1 INTRODUCTION 1

1.1 Motivation 1
1.2 Background 5
1.3 Objectives 17

2 DATA AND METHODS 20

2.1 Cloud-Resolving Model Simulations 20
2.2 Limited Area Model Simulations 25
2.3 Bulk Microphysics Scheme Properties 28
2.4 Calculation of Variables from Model Output 30
2.5 Observations 33
2.6 Convective-Stratiform Separation 39

3 CONVECTIVE AND STRATIFORM STRUCTURE 55

3.1 Overview 55
3.2 Area and Rain Rate 55
3.3 Convective Radar Reflectivity 61
3.4 Stratiform Radar Reflectivity 64
3.5 Relation to Model Microphysics Assumptions 66
3.6 Discussion 71

4 CONVECTIVE DRAFT PROPERTIES 98

4.1 Overview 98
4.2 Updraft Definition 98
4.3 Deep Updraft Radar Reflectivity, Vertical Velocity, and Size 100
4.4 Deep Updraft Hydrometeor Properties 105
4.5 Downdrafts and Cold Pools 112

4.6 Production Mechanisms for Strong Updrafts 114
4.7 Discussion 127

5 RAIN MICROPHYSICS 153

5.1 Overview 153
5.2 Sampling 154
5.3 Stratiform Radar Reflectivity and Rain Rate 156
5.4 Stratiform Doppler Velocity 158
5.5 Stratiform Liquid Water Content 159
5.6 Stratiform Raindrop Size 162
5.7 Convective Raindrop Size 166
5.8 Correlating Radar Reflectivity, Rain Rate, and Raindrop Size 169
5.9 Connection to Ice Water Content Aloft 171
5.10 Discussion 176

6 CONCLUSIONS 210

6.1 Summary 210
6.2 Caveats 215
6.3 Implications 216
6.4 Future Work 217

REFERENCES 224

ACKNOWLEDGMENTS

I would like to thank my committee members Zhaoxia Pu, Gerald Mace, Steve Krueger, Ann Fridlind, and my advisor Ed Zipser for their insight and guidance. To Ed especially, I greatly appreciate all you have done to advance my career, all you have taught me about the politics of our field, and your unyielding support of both my research and personal interests. You truly put students first, and I cannot think of a better quality in an advisor. To Ann whom I consider a second advisor, I could not have accomplished this research without your extraordinary time and effort spent helping me through seemingly endless e-mail exchanges. Your intellectual curiosity is infectious, and I aspire to work half as hard as you do. I would also like to acknowledge the Department of Energy Atmospheric System Research program that funded my graduate career and allowed me to connect with other scientists in our field, many of whom have kindly aided me in my research. Last but definitely not least, I would also like to thank my family and friends, especially my girlfriend Annie, without whom my anxiety level would almost certainly have boiled over on more than one occasion during this process.

CHAPTER 1

INTRODUCTION

1.1 Motivation

Deep convective systems are an integral part of large-scale tropical circulations, such as the Hadley and Walker circulations (e.g., Riehl and Malkus 1958; Hartmann et al. 1984; Schumacher et al. 2004; Fierro et al. 2009), because they largely determine the distribution of tropical free tropospheric heating. Unfortunately, achieving realistic modeling of deep convection remains a prominent problem, even at cloud-resolving scales. Despite this problem, cloud-resolving models (CRMs) are increasingly used in satellite algorithms (e.g., Kummerow et al. 2001; Kingsmill et al. 2004; Shige et al. 2009) to retrieve rainfall and latent heating distributions around the world and hence, will be a big part of Global Precipitation Measurement (GPM) satellite retrievals. CRMs are also increasingly used to guide global climate model (GCM) cloud and convective parameterization improvement (e.g., Tiedtke 1993; Lohmann and Roeckner 1996; Fowler et al. 1996; Ghan et al. 1997; Rotstayn 1997; Wilson and Ballard 1999) as these parameterizations remain among the largest sources of uncertainty in GCMs (Randall et al. 2003), while some have begun embedding two-dimensional CRMs in GCM grid boxes, a process known as superparameterization (Grabowski 2001; Khairoutdinov and Randall 2001; Randall et al. 2003).

Accurately representing and predicting the latent heating and radiative effects of deep convective systems in the context of large-scale environmental properties is required to confidently predict future weather and climate. Yet, the atmospheric science community continues to struggle with realistically representing these effects and their relationship with predicted large-scale environmental variables in global climate models (Del Genio and Kovari 2002; Neale and Slingo 2003; Stephens 2005; Randall et al. 2007). Recently, attention has turned toward representation of mesoscale convective organization in GCMs (e.g., Mapes and Neale 2011; Del Genio et al. 2012) since only one GCM to date attempts to represent mesoscale updrafts and downdrafts (Donner 1993, Donner et al. 2001), even though approximately 80 percent of tropical rainfall comes from mesoscale systems (Del Genio and Kovari 2002) with about 40 percent coming from stratiform rain (Schumacher and Houze 2003). Del Genio et al. (2012) discuss the importance of representing cold pool processes, which is difficult given 100 km or greater horizontal grid spacing in GCMs. With quickly increasing computing capabilities, it has been suggested by some in GCM model development that GCMs will be running with 10-km horizontal grid spacing in 10 years time. If this is the case, then mesoscale processes associated with deep convective systems will begin to be resolved and conventional convective parameterizations based on scale separation break down. This could provide a major step forward in mesoscale parameterization difficulties, but such systems will still depend on simulating the deep convective properties correctly, something that has proven difficult in CRMs.

Upscale effects on the large-scale circulation by the thermodynamic and radiative effects of mesoscale precipitation systems are sensitive to the proportion of convective to

stratiform precipitation (Houze 1982, 1989, 1997, 2004; Hartmann et al. 1984; Johnson 1984) because of their distinctly different vertical heating profiles with convective regions heating the entire troposphere and stratiform regions heating only the upper troposphere while cooling the lower troposphere. This effect is not only important in the mean, but the different timing in the peaks of convective and stratiform precipitation is key to convectively coupled waves (Mapes et al. 2006), which are not well represented in most GCMs (Lin et al. 2006), a good example being the Madden-Julian Oscillation (Kim et al. 2009). This proportioning depends on the convective morphology or mode, which is dependent on large-scale environmental parameters such as vertical wind shear, but vertical wind shear is mostly ignored in GCM convective parameterizations (Moncrieff et al. 2012). Even if it were represented, transitions between different convective modes are still not well understood (Stevens 2005), making the problem of proportioning convective and stratiform precipitation even more difficult to address. Del Genio et al. (2012) point out that the lack of mesoscale organization in GCMs combined with the erroneous peak in convective rainfall at noon over land can lead to a high bias in the shortwave effect from convection and a low bias in soil moisture.

Primary sources for error in model simulations are parameterizations of subgrid scale processes, which are often poorly constrained by theory and observations (Tao and Moncrieff 2009), often because few trustworthy observations exist. For this reason and because more complexity in model physics schemes requires more computing power, such parameterizations can often be quite crude. Over the past couple of decades, however, significant advances in computing power have allowed for increasingly more complex simulations of large convective cloud systems. This has led to three-

dimensional high-resolution mesoscale simulations down to the cloud-resolving scale of less than 4 km, a scale at which convective processes are explicitly simulated over horizontal domain dimensions of hundreds of kilometers. Despite this newfound ability to explicitly resolve convective clouds, subgrid scale processes still need to be approximated through parameterizations, which lead to introduction of error into simulations. Increasingly complex parameterization developments have accompanied the evolution of convective cloud simulations to finer scales, and with such developments come field experiments needed to both test and constrain parameterizations with high quality observations. This is a tall task for a few reasons. First, the most common and highest quality observations are often not the first variables that modelers would choose for evaluating, improving, and developing parameterizations. Second, the temporal and spatial scales of observations are often quite different from those of model output. And third, it is difficult to provide an accurate large-scale forcing for models. Still, comparing model output to observations is one of the best avenues for testing and improving parameterizations, especially when many complementary and co-located observations are available. Of the subgrid scale parameterizations that need much more constraint and guidance from observations, microphysics parameterizations are near the top of the list because of their direct linkages to latent and radiative heating and cooling, but they may be the most complex because of the high number of poorly constrained nonlinear interactions occurring within them.

1.2 Background

The detailed and comprehensive tropical observational datasets necessary for validating model simulations come primarily from intensive observational periods (IOPs) during field experiments. One such field experiment was the Tropical Warm Pool – International Cloud Experiment (TWP-ICE), which serves as the basis for the research presented in this dissertation.

1.2.1 TWP-ICE and Intercomparison Studies

TWP-ICE (May et al. 2008) was conducted out of Darwin, Australia in January and February of 2006. Darwin is an excellent location for studying deep convective systems because several field experiments have been performed there in the past (e.g., EMEX (Webster and Houze 1991); DUNDEE (Rutledge et al. 1992); MCTEX (Keenan et al. 2000); DAWEX (Hamilton et al. 2004)), there is a permanent Atmospheric Radiation Measurement (ARM) site with extensive observations there, and it experiences deep convective systems characteristic of tropical oceanic regions during active monsoon periods and continental regions during monsoon break periods (Keenan and Carbone 1992). From this experiment, a high quality model forcing data set was created using a variational analysis (Xie et al. 2010) that made use of a pentagonal array of three-hourly atmospheric soundings, rainfall estimation using the scanning C-band radar (CPOL) (Keenan et al. 1998), and surface flux sites. The first six days of the experiment, January 19–25, were characterized by active monsoon conditions in which the environment was oceanic in nature, although convective intensity was a bit more intense than that over some parts of the oceanic tropics because some lightning was observed. This period

covered an intense and large mesoscale convective system (MCS) that initiated over the area on January 23 and exited to the southwest on January 24. A prolonged period of suppressed monsoon conditions followed the active phase due to strong westerly advection of dry continental air at midlevels associated with "Landphoon John" to the south, the remnant of the January 23–24 MCS. This period primarily consisted of isolated congestus and little rainfall. February 6th through the end of the experiment consisted of break conditions, in which intense continental convection was observed, commonly forming on sea breeze convergence lines and propagating to the west in the characteristic easterly break period flow.

The active and suppressed periods served as the primary focus for the TWP-ICE CRM Intercomparison Study (Fridlind et al. 2010, 2012), a joint project through the ARM program, the Global Energy and Water Exchanges project (GEWEX) Cloud Systems Study (GCSS), and the Stratospheric Processes And their Role in Climate (SPARC) program. Intercomparison studies were also performed for limited area model (LAM) simulations of a 3.5 day period from 12Z on January 22 to 0Z on January 26 focusing on the intense MCS on January 23–24 (Zhu et al. 2012), single column model (SCM) simulations, and global atmospheric model (GAM) simulations covering the monsoon and break periods (Lin et al. 2012). These studies welcomed participants from modeling centers around the world to run their models using a common setup specification for the purpose of comparing models against each other and against observations. Intercomparisons have been used extensively for SCMs (e.g., Bechtold et al. 2000; Ghan et al. 2000; Wu and Moncrieff 2001; Xie et al. 2002) and CRMs (e.g., Wu et al. 1998; Redelsperger et al. 2000; Xu et al. 2002; Bryan et al. 2006; Grabowski et al.

2006), but the TWP-ICE limited area model (LAM) Intercomparison Study is the first of its kind. A general objective of intercomparison projects is to determine combinations of model setup and parameterizations that lead to the best agreement with observations and combinations that lead to the largest discrepancies with observations for the purpose of identifying model components that can be improved. For any given intercomparison study, specific scientific objectives also exist. For the TWP-ICE CRM Intercomparison Study, goals beyond analyzing model performance and methodology included quantifying convective transport to the tropopause and studying processes that controlled anvil cirrus longevity (Fridlind et al. 2010). For the TWP-ICE LAM Intercomparison Study, goals included finding out whether LAMs could reproduce observed dynamical processes from the convective scale to the monsoon trough scale for a large MCS event and whether they produced similar cloud structures as those in the CRMs (Zhu et al. 2012).

1.2.2 Model Setups

LAM setups have become increasingly popular as computing power has increased, and using them with CRM setups is beneficial because they have different sources for bias. LAMs are forced through updating lateral boundary conditions (typically through a large-scale analysis) whereas CRMs are idealized and use periodic or open boundary conditions, while being forced in a variety of ways. The advective forcing method uses large-scale vertical velocity and advective tendencies of temperature and moisture that are calculated from observationally derived constrained variational analyses (e.g., Xie et al. 2010) to allow convection to freely form, which differs from

some other popular methods that use idealized "warm bubbles" and cold pools to force the initial convective updrafts. The advective forcing method is used for the TWP-ICE CRM Intercomparison Study. The advantage of the CRM approach over the LAM approach is that it does not have inherent bias associated with a large-scale analysis. By being idealized, errors can be more easily attributed to specific sources because some sources of error are removed. The disadvantage is that it generally uses periodic lateral boundary conditions that require uniformity in surface and atmospheric conditions at the boundaries. This is problematic over land or in scenarios with substantial vertical vorticity on the scale of the domain. Furthermore, the variational analysis calculates a mean thermodynamic profile and large-scale vertical velocity, but this assumes that convection is responding to the mean environmental state on the scale of the CRM domain, which is not necessarily true. LAMs avoid this issue by nesting down the large-scale analyses that are forcing them, but if the large-scale analysis does not adequately represent reality, then those errors will be manifested in the LAM simulation. LAMs also involve more complexity because of heterogeneous surfaces and use of more parameterizations in nonconvection resolving domains. Lastly, LAMs often use large outer domains. With two-way nesting, inner domain processes can feedback upscale to the larger domains making a wide range of simulations possible because the inner domains are not strictly regulated. Therefore, without assimilation of observations or nudging of the atmospheric mean state, one has to be careful in attributing differences between simulations purely to alteration of model physics schemes.

1.2.3 Bulk Microphysics Schemes

Most large three-dimensional domain runs or ones run over long periods of time use bulk microphysics schemes. Bulk microphysics schemes are so-called because they define continuous hydrometeor size distributions using predicted bulk properties of the hydrometeor size distributions. Microphysical processes are then calculated from properties of the continuous size distributions rather than for discrete particle sizes. Warm cloud bulk microphysics started with Kessler (1969), which is the basis for many warm cloud bulk schemes, although representation of collection in a subset of bulk schemes has since evolved into bin emulating schemes (e.g., Feingold et al. 1998). Representation of ice microphysics is much more complicated because of the many forms of ice, the many ways in which ice can grow, and incomplete knowledge of mixed-phase and ice microphysical processes. Most schemes assume a finite number of hydrometeor categories, typically four to six, although up to 12 have been used (Straka and Mansell 2005). In recent years, novel approaches have been formulated to try and move away from ice categories that require arbitrary conversions between the categories by predicting ice riming fraction and/or varying mass-dimension and projected area-dimension relationships with ice size or temperature (e.g., Morrison and Grabowski 2008; Lin and Colle 2011).

Although there are many different schemes, many basic components of the schemes are quite similar, at least partially owing to a lack of large samples of quality observations. Many processes and hydrometeor characteristics in bulk microphysics schemes are based on observations obtained in mid-latitude field experiments (e.g., United States, Japan, and Europe) (e.g., Lin et al. 1983; Rutledge and Hobbs 1984;

Cotton et al. 1986; Dudhia 1989; Ikawa and Saito 1991; Ferrier 1994; Reisner et al. 1998). While processes should be physically universal, hydrometeor properties can differ substantially between different large-scale environments and dominant physical processes may differ in different meteorological regimes. Most schemes parameterize specific hydrometeor properties and processes from single field experiments, so parts of schemes are already somewhat tuned to specific cases without knowing the representativeness of those observations used.

Most bulk schemes that are commonly used are one-moment or two-moment schemes. One-moment bulk schemes predict one moment of hydrometeor size distributions, typically the mass mixing ratio, which is directly related to the 3rd moment of the size distribution for spherical, constant density hydrometeors. Two-moment schemes are more computationally expensive than one-moment schemes because they predict two moments of hydrometeor size distributions, typically number concentration, the 0th moment, in addition to mass mixing ratio. Even three-moment schemes exist (e.g., Milbrandt and Yau 2005), but these have not been extensively used in research to date. Because of these simplifications relative to the real world, substantial amounts of computing time are saved over potentially more realistic but costly bin (spectral) microphysics schemes.

Hydrometeor size distributions are typically assumed to be gamma distributions of the form $n(D) = N_0 D^{\mu} e^{-\lambda D}$ in most bulk schemes, where N_0 is the size intercept, μ is the shape parameter, and λ is the slope. For a given water content, a higher N_0 means a greater number of small sized particles. The higher μ is, the narrower the size distribution becomes, while the higher λ is, the faster the number of hydrometeors per

unit volume goes to 0 with increasing particle size. Figure 1.1 shows the ways by which N_0 and μ affect rain size distributions for a 1 g m^{-3} rain water content.

When $\mu = 0$, this gamma distribution reduces to a simpler exponential distribution. For one-moment schemes with $\mu = 0$, N_0 is generally assumed to be constant, but it can be diagnostically determined based on variables such as temperature as well. The classic Marshall-Palmer distribution assumes $\mu = 0$ and $N_0 = 8 \times 10^3$ m^{-3} mm^{-1} (Marshall and Palmer 1948). For a typical one-moment scheme, λ is dependent on the prognostic hydrometeor mass mixing ratio, N_0, air density, μ, and the hydrometeor mass-diameter relationship, which incorporates hydrometeor bulk density. For a typical two-moment scheme, λ is dependent on the prognostic hydrometeor number concentration and air density. N_0 in these two-moment schemes is equal to $\frac{N\lambda^{\mu+1}}{\Gamma(\mu+1)}$, where N is the hydrometeor number concentration. By predicting N, hydrometeor growth processes are better represented, and the size distribution is allowed to shift the proportioning of large to small hydrometeor sizes within the constraints of the assumed gamma distribution.

Each hydrometeor species has a mass-diameter ($m = aD^b$) relationship. For this relationship, raindrops are assumed to be spherical and thus have a simple relationship where $a = \frac{\pi}{6}\rho_x$ and $b = 3$, where ρ_x is the hydrometeor density. Many schemes also assume that snow, graupel, and hail are spherical for this relationship. When hydrometeors are assumed to be nonspherical ($b \neq 3$) with a set constant, hydrometeor density varies as a function of D because mass is no longer directly proportional to volume. Each prognostic variable has a terminal fall speed relationship ($v_f = cD^d e^{-fD}$)

with coefficients c, d, and f that are set constant and vary between schemes. These relationships are often based on field observations and thus do not assume hydrometeor shapes. Both one-moment and two-moment schemes incorporate mass mixing ratio fall speeds with two-moment schemes also incorporating number concentration fall speeds. For one-moment schemes, the entire hydrometeor size distribution sediments at the same rate. For two-moment schemes, the mass fall speed is often greater than the number fall speed, which mimics the effect of larger sized hydrometeors falling faster than smaller sized hydrometeors, a process called size sorting. Although two-moment schemes are clearly more realistic than one-moment schemes, greater complexity leads to greater computing expense and greater difficulty in constraining the scheme with observations.

1.2.4 Model Deep Convective Biases

Not only have most bulk microphysics schemes been based on mid-latitude continental observations, they are often tested in mid-latitude continental squall, supercell, or winter storm scenarios, which is likely a result of much more extensive observational networks in mid-latitude continental environments. Cloud-resolving simulations have a history of providing process level understanding of observations. Such simulations beginning in the late 1970s and progressing into the 2000s have been instrumental in our understanding of moist convective life cycles for a variety of modes, notably supercells and squall lines (e.g., Weisman and Klemp 1984; Rotunno and Klemp 1985; Weisman and Rotunno 2004).

In the 1990s, some studies began to emerge that compared results from different simulation setups and schemes, but only recently with vastly increased computing

resources have extensive comparisons of different microphysics parameterizations, limited area model simulations, and LES simulations begun. While using observations to improve high-resolution model parameterizations is far from extensive (Stephens 2005), some biases have become well known and widely accepted in recent years. Mesoscale simulations run on cloud-resolving horizontal scales down to approximately 1 km often fail to reproduce observed convective and stratiform structures (e.g., Lang et al. 2003; McFarquhar et al. 2006; Zhou et al. 2007; Luo et al. 2010; Varble et al. 2011) that depend on the large-scale environmental properties (Houze 2004). CRM simulations still struggle to produce adequately large and well-developed stratiform regions associated with squall lines, for example (e.g., Morrison et al. 2009).

In convective regions, several studies focusing on bulk microphysics schemes have found that a high bias in Rayleigh radar reflectivity due to graupel is common in CRM simulations (Blossey et al. 2007; Lang et al. 2007; Li et al. 2008; Matsui et al. 2009). This has led many to point fingers at ice growth processes as a major problem in bulk microphysics schemes. Lang et al. (2011) adjusted graupel growth processes and collection efficiencies to lower the amount of graupel aloft in CRM simulations of tropical convection. While this improved the comparison of observed and simulated radar reflectivity, it did not completely solve the problem. One problem with this approach is that it is aimed at improving comparisons with Rayleigh radar reflectivity, which is related to the sixth moment of the equivalent melted hydrometeor size distribution, whereas parameterized bulk microphysical processes are dependent on lower moments of the size distribution, such as number concentration and mass mixing ratio. Therefore, one has to be careful when tuning schemes to radar reflectivity so that they do

not worsen comparisons between observed and simulated lesser moments of hydrometeor size distributions. Another problem with this approach is that it ignores other sources of error, such as those that may exist in the liquid region of convective updrafts that may be leading to excessive graupel aloft. Tuning microphysics processes with limited information can cover up the real causes of problems, but recent studies have elucidated some key processes that can have major impacts on convective properties and thus should be carefully considered when designing a microphysics scheme. One such example is raindrop breakup. Morrison et al. (2012) found large sensitivities to different raindrop breakup parameterizations in mid-latitude continental squall line simulations through modulation of evaporation and the strength of cold pools. McCumber et al. (1991) found that three ice categories, one for cloud ice, one for snow, and one for graupel best simulated a tropical convective case, but that the quality of bulk microphysics parameterizations in cloud models could be case specific and that more ice categories or prediction of more moments of the size distributions would likely be necessary to adequately simulate some convective systems. Studies since then indeed have found large sensitivities to how those ice categories are represented including whether graupel or hail is used (e.g., Morrison and Milbrandt 2011; Bryan and Morrison 2012; Milbrandt and Morrison 2013). Van Weverberg et al. (2013) further found large sensitivities in tropical MCS anvil properties based on different cloud ice formulations in various bulk microphysics schemes.

Despite many studies showing excessive amounts of large graupel aloft in simulations of tropical deep convection, few studies exist that thoroughly compare simulated deep convective vertical velocity to observational retrievals in tropical

environments. Lang et al. (2007) compared dual-Doppler vertical velocity retrievals to simulated vertical velocity in simulations of Amazonian convection and concluded that convective vertical velocities were comparable in magnitude to those retrieved, but their comparisons were limited and did not take into account possible differences in terms of the vertical momentum equation. Other studies suggest that a primary issue is indeed the scale required to resolve convective motions. While 1-km horizontal grid spacing is considered "cloud-resolving," studies show that this is not really true (Craig and Dörnbrack 2008), while Bryan et al. (2003) recommend a 100-m grid spacing for simulating deep convection. Bryan and Morrison (2012) showed that the properties of an idealized mid-latitude continental squall line changed when the horizontal grid spacing was decreased from 1 km to 250 m because the size of individual convective drafts decreased, effectively increasing cloud water evaporation and altering the convective updraft and downdraft strength. Del Genio and Wu (2010) did not find major differences between 600-m and 125-m grid spaced WRF simulations of TWP-ICE monsoon break period convection, although entrainment increased some in the 125-m simulation. Romps and Kuang (2010) also found entrainment increased as horizontal grid spacing decreased between 3.2 km and 100 m in idealized simulations of deep convection, but differences were not tremendously large. The representativeness of such studies is unclear, especially for moist tropical environments, but the question of adequate resolution is an important one. LES simulations with horizontal grid spacing of 100 m begin resolving large eddies and these simulations are often used as "truth" when evaluating coarser resolution simulations. Such simulations do appear to better represent the transition from shallow to deep convection (Kuang and Bretherton 2006;

Khairoutdinov and Randall 2006; Khairoutdinov et al. 2009) than coarser resolution setups (e.g., 1-km horizontal grid spacing) that sometimes fail (e.g., Petch et al. 2002), but evaluation of such runs against high quality observational datasets for deep convection is far from thorough. Ten-meter scale turbulence representation in congestus and deep convection may be important, but it is difficult to measure the effects of turbulent entrainment and detrainment in the real world, even though they can have major impacts on processes such as evaporation. While microphysical processes are the focus of this dissertation, this is but one of many examples of how they cannot be completely untangled from convective dynamics.

Outside of convective regions, attention in recent years has turned to low biases in stratiform precipitation associated with deep convection (e.g., Morrison et al. 2009; Luo et al. 2010). Morrison et al. (2009) attributed a low bias in rain rate for simulations using one-moment bulk microphysics schemes to excessive evaporation because of a constant rain size intercept assumption. A two-moment scheme predicting rain number concentration significantly reduced this low bias by allowing the size intercept to shift to lower values and the raindrops to size sort while falling. Li et al. (2009) point out that high subcloud relative humidity can mitigate the low bias due excessive evaporation. Luo et al. (2010) further suggest that part of the problem in low biased stratiform precipitation is tied to detrainment from convective regions occurring too high in the troposphere. Morrison et al. (2009) showed that stratiform regions were indeed sensitive to the detrainment of buoyancy and condensate in the upper troposphere and that a two-moment scheme outperformed a one-moment scheme for an idealized squall line simulation because the convective strength was weaker in the two-moment simulation.

Despite improved performance by two-moment rain schemes in mid-latitude continental environments, studies such as Wacker and Seifert (2001) and Morrison et al. (2009) mention excessive vertical redistribution of raindrops by size (excessive size sorting) as a problem in such schemes.

It is clear from the preceding discussion that cloud-resolving simulations of deep convective systems are not perfect in their representation of convective and stratiform precipitation structure, nor should they be expected to be perfect. These simulations, however, are used in satellite retrievals and large-scale model parameterization development, and therefore, it is prudent to evaluate and improve such simulations as much as possible. Many biases and sensitivities to subgrid scale parameterizations, especially microphysics, have been established, but more research is needed to identify key parts of subgrid scale parameterizations that can be improved because many previous studies use specific model setups, schemes, and case studies. Of particular importance are processes that affect convective and stratiform anvil structures because of their importance in affecting global weather and climate patterns.

1.3 Objectives

The ultimate goal of this research is to improve mesoscale simulations of deep convective systems, primarily through improving bulk microphysics schemes, without substantially increasing the computing time for the scheme. This is accomplished by comparing many different CRM and LAM simulations with TWP-ICE observations much more thoroughly than has been done in previously published research. An attempt is made to find dynamical and microphysical sources of bias common to all simulations

and sources of bias that differ between simulations. For bias that substantially differs, unique microphysics scheme components are identified that may be responsible for modulating the bias. For bias common to all simulations, hypotheses on the causes of such biases are developed. As these are lofty goals, simulation improvements are not guaranteed; rather, this research picks a few well-supported pathways to improvement out of a great number of possibilities of future research directions.

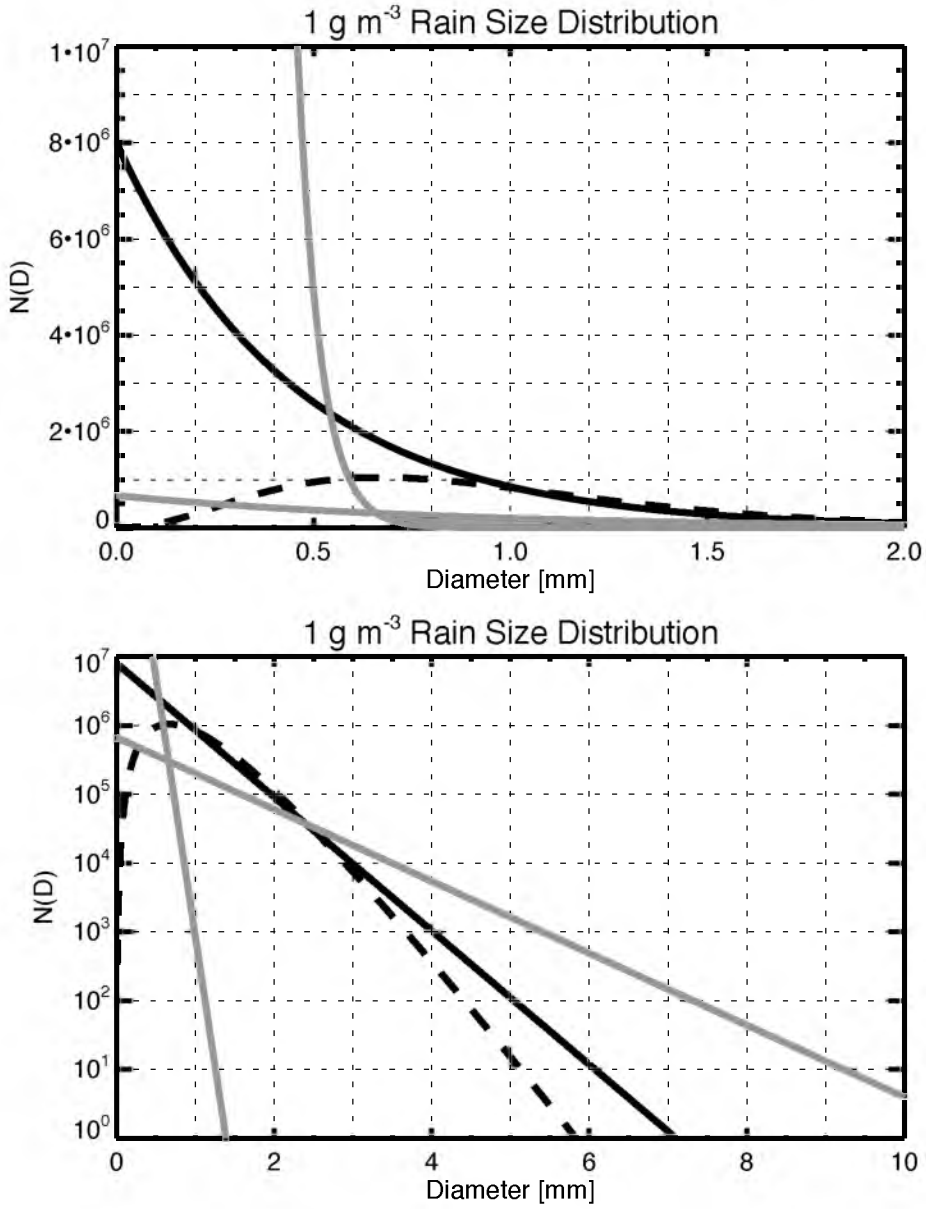

Figure 1.1. Raindrop size distributions for a rain water content of 1 g m^{-3} with the only difference in panels being the logarithmic y-axis in the bottom panel. The solid black line represents a one-moment constant N_0 and $\mu = 0$ distribution (Marshall-Palmer), the dashed black line represents a one-moment $\mu = 2.5$ distribution, and the solid gray lines represent a range of possible distributions in a $\mu = 0$ two-moment scheme.

CHAPTER 2

DATA AND METHODS

Numerous simulations and multiple observational datasets are utilized to achieve the objectives of this dissertation. These are described in this chapter.

2.1 Cloud-Resolving Model Simulations

Two different sets of three-dimensional CRM simulations are used. The first set covers the entire six-day active monsoon period from 12Z January 19 to 12Z January 25, 2006 during TWP-ICE. The second set covers the largest and most intense MCS event during the active monsoon period from 3Z January 23 to 12Z January 24, 2006.

2.1.1 Active Monsoon Period

Table 2.1 lists nine three-dimensional CRM simulations run as part of the TWP-ICE CRM Intercomparison Study (Fridlind et al. 2012). The simulations are spread across four different models: the Distributed Hydrodynamic-Aerosol-Radiation Model Application (DHARMA) (Ackerman et al. 2000; Stevens et al. 2002), the UK Met Office Large Eddy Model (UKMO) (Shutts and Gray 1994; Petch and Gray 2001), the Meso-NH Atmospheric Simulation System (MESONH) (Lafore et al. 1998), and the System for Atmospheric Modeling (SAM) (Khairoutdinov and Randall 2003). As shown in Table

2.1, all simulations have horizontal resolutions of 917–1000 m and vertical resolutions that vary from 100–225 m in the boundary layer to 250–500 m in the mid to upper troposphere. All simulations are idealized with horizontal domain boundaries that are periodic and a lower domain boundary that is assumed to be oceanic with a constant sea surface temperature of 29°C and albedo of 0.07. Large-scale forcing is supplied using three-hourly domain-mean profiles derived from a constrained variational objective analysis of available observations including three-hourly soundings and radar-derived rain rates, as described in Xie et al. (2010). Figure 2.1 shows a map of the region with sounding sites (triangles) enclosing the pentagonal forcing region. Model domains are approximately equal to the area covered by this pentagon. The location of the CPOL radar is also shown with the 150-km range ring dashed. In addition to the model forcing, domain-mean horizontal wind profiles are nudged on a two-hour time scale.

All of these simulations are run for 16 days starting on 0Z 18 January 2006 with 36 hours allowed for spin-up. The six days following spin-up are characterized by active monsoonal conditions with significant mesoscale rainfall events, while the rest of the time after the first six days is characterized by suppressed conditions with minimal rainfall. Because of the vastly different large-scale environment during these two periods and because the active monsoonal mesoscale convective systems are much more important to large-scale tropical circulations, only the active monsoon period is analyzed.

Table 2.2 shows the advection, turbulence, surface flux, and radiation schemes used for each model. All models solve the anelastic equations and use advection schemes shown in the 'Advection' column of Table 2.2. These schemes vary between models, but these differences do not appear to create much difference between simulation statistics, as

will be shown in Chapters 3–5. All radiation schemes use fast radiative transfer calculations by the methods shown in the 'Radiation' column of Table 2.2. Subgrid scale turbulence schemes use a Smagorinsky-Lilly model (Lilly 1967; Deardorff 1970) or a 1.5-order closure (Cuxart et al. 2000). Surface flux schemes for DHARMA and UKMO are based on Monin-Obukhov similarity theory (Monin and Obukhov 1954), whereas MESONH uses bulk iterative Exchange Coefficients from Unified Multi-Campaigns Estimates (ECUME) (Weill et al. 2003; Belamari 2005) and SAM uses the scheme in the National Center for Atmospheric Research Community Climate Model version 3.5 (Collins et al. 1997). Fridlind et al. (2012) shows that mean surface heat fluxes are not far off from those in the model forcing dataset for the active monsoon period, while sensitivity simulations are lower and match those measured at the Darwin harbor site. Fridlind et al. (2012) also shows moist static energy (MSE) drift in many simulations associated with net radiative flux divergence relative to net convergence in the forcing dataset. With reasonable fluxes despite the surface cooling from MSE drift, this could be an indication that simulated surface heat fluxes are too low. Of course, one of the complications is that the model forcing domain contains land, which exhibits a distinct diurnal cycle in surface sensible heat fluxes despite the humid maritime environment, while the CRM simulations assume an idealized oceanic surface, which should not experience a significant diurnal cycle because it is dominated by latent heat fluxes. This is supported by the surface flux data on the Southern Surveyor ship during this period, which is dominated by the latent heat flux with minimal diurnal variability.

All simulations use bulk microphysics schemes in which continuous hydrometeor size distributions are defined through prediction of either one (one-moment) or two (two-

moment) moments of each hydrometeor size distribution. All schemes predict the mass mixing ratio of every hydrometeor species used in the scheme, whereas some schemes include two-moment species for which number concentration is also predicted. If a simulation includes two-moment species, they are shown in the Microphysics column of Table 2.1 in parentheses. All simulations include cloud water and rain as species, but some differences exist in the ice species used. DHARMA-B and DHARMA-S include graupel and a combined cloud ice and snow category (Grabowski 1999). Cloud ice and snow are diagnostically separated into two separate size distributions that are defined in McFarquhar and Heymsfield (1997) so that proper comparisons involving snow can be made with the other simulations. SAM-B and SAM-S use an early version of the Morrison scheme (Morrison et al. 2009), which includes two-moment cloud ice, snow, and hail. These are the only simulations that use hail rather than graupel. All other simulations use cloud ice, snow, and graupel. UKMO-2M uses a slightly later version of the Morrison scheme than the SAM simulations use and includes two-moment cloud ice, snow, and graupel. The UKMO LEM scientific documentation version 2.3 (Gray et al. 2001) describes the schemes used in UKMO-1 and UKMO-2. UKMO-1 and UKMO-2 predict the number concentration of cloud ice. UKMO-2 differs from UKMO-1 in that it additionally predicts the number concentrations of snow and graupel. The MESONH model scientific documentation version 4.8 (Bougeault et al. 2009) describes the schemes used in MESONH-1 and MESONH-2. MESONH-2 differs from MESONH-1 in that cloud water and cloud ice number concentrations are predicted following Pinty (2002). Idealized aerosol profiles for three separate size modes generated from in situ aircraft observations during the Aerosol and Chemical Transport In tropical conVEction

(ACTIVE) field campaign (Vaughan et al. 2008), which preceded and partially overlapped the TWP-ICE field campaign in Darwin, are used as input to the simulations that include two-moment cloud water (SAM simulations and MESONH-2).

Two of the nine simulations are referred to as sensitivity simulations, DHARMA-S and SAM-S. In these simulations, the domain mean potential temperature and water vapor profiles are nudged on a six-hour time scale toward the observed domain mean profiles throughout the troposphere. These two simulations also include baseline (-B) counterparts in which this nudging only occurs in the far upper troposphere and lower stratosphere, so that these simulations are more freely allowed to alter the tropospheric thermodynamic profile. The sensitivity simulations give a sense of errors that may arise due to the idealized nature of the model forcing. More details on all simulations can be found in Varble et al. (2011) and Fridlind et al. (2012).

2.1.2 Mesoscale Convective System Event

To better understand statistical differences found between models and observations with the three-hour output over six days, two-day simulations covering 12Z 22 January 2006 to 12Z 24 January 2006 were run with 10-minute output produced for the 33-hour period between 3Z 23 January 2006 and 12Z 24 January 2006 during which a large MCS forms. Although a large MCS is not ideal for CRMs run with periodic lateral boundary conditions over a 176 km by 176 km domain, this period was chosen because of the unique observational retrievals and LAM simulations available for comparison. For this event, the UKMO simulations were altered from the original simulations to have higher vertical resolution, making them more comparable to the other simulations. All

else is the same as the original UKMO simulations. A tenth simulation was also added, DHARMA-2M, which uses the Morrison two-moment scheme in the DHARMA model with prognostic cloud water number concentration that uses idealized aerosols profiles in three size modes based on ACTIVE observations. This simulation is unique compared to others in that it accounts for aerosol transport and consumption. All other simulations (DHARMA-B, DHARMA-S, MESONH-1, MESONH-2, SAM-B, and SAM-S) are unchanged from the longer runs with three-hour output. Information on these MCS simulations is shown in Table 2.1.

2.2 Limited Area Model Simulations

Table 2.3 show the setups for four three-dimensional LAM simulations, all Advanced Research Weather Research and Forecasting (WRF-ARW) model (Skamarock et al. 2008) simulations, three of which were used as part of the TWP-ICE LAM Intercomparison Study (Zhu et al. 2012). The LAMs are set up in a very different manner than the CRMs although the horizontal and vertical resolution remains approximately the same. LAMs are forced through their horizontal boundaries. Rather than a constant sea surface temperature oceanic surface such as that used in the CRMs, the LAMs have an inhomogeneous surface with variable land and ocean properties. This setup is better equipped to simulate the large MCS event because of the nonperiodic lateral boundary conditions, which do not limit the size of the MCS and allow a mesoscale cyclonic wind field. The primary drawback is that the forcing is less constrained by observations and prone to errors from the large-scale analysis used to force the LAM. WRF-W, WRF-T, and WRF-M are run using WRF V3.1 and described

as WRF-1, WRF-2, and WRF-3, respectively, in the TWP-ICE LAM Intercomparison Study (Zhu et al. 2012). All three simulations share the same setup except for the use of different microphysics schemes as shown in Table 2.3. WRF-M uses the Morrison scheme (Morrison et al. 2009), WRF-W the WSM6 scheme (Hong and Lim 2006), and WRF-T the Thompson scheme (Thompson et al. 2008). The Morrison scheme used includes two-moment rain, graupel, snow, and cloud ice with one-moment cloud water. The Thompson scheme is a recent version that uses two-moment rain and cloud ice with one-moment graupel, snow, and cloud water. For one-moment graupel, the Thompson scheme varies the size intercept as a function of mass mixing ratio to mimic the transition from lightly rimed snow to hail (Thompson et al. 2008). For one-moment snow, the Thompson scheme uses a combination of two gamma size distributions with a dependence on temperature described in Field et al. (2005). Furthermore, the Thompson snow mass-diameter relationship assumes nonspherical particles based on the relationship in Cox (1988), whereas the Morrison and WSM6 schemes assume spherical particles. The WSM6 scheme is purely a one-moment scheme, although the snow size intercept varies diagnostically as a function of temperature using a relationship from Houze et al. (1979). Other model physics schemes used in all LAM simulations include the Rapid Radiative Transfer Model (RRTM) longwave radiation scheme (Mlawer et al. 1997), the Dudhia shortwave radiation scheme (Dudhia 1989), a five-layer thermal diffusion land surface scheme, and the Yonsei University planetary boundary layer scheme (Hong et al. 2006). Additional parameterizations used are comparable to those used in the CRM simulations, including a Smagorinsky-type first order turbulence closure, Monin-Obukhov similarity theory for surface fluxes, fifth order horizontal with third-order

vertical advection of momentum and scalars, and positive definite moisture advection. In D1 and D2 (27 and 9 km horizontal grid spaced domains), the Kain-Fritsch convective parameterization (Kain 2004) is used because the horizontal grid spacing is too coarse for explicitly resolved convection.

These simulations are all forced using ECMWF global analyses and nested down from an outer domain (D1) horizontal resolution of 27 km to an inner domain (D4) horizontal resolution of 1 km as shown in Figure 2.2. Two-way nesting is used in all four simulations, which allows inner domains to impact outer domains. The innermost domain covers 450 km by 330 km. A fourth WRF simulation was run using WRF V3.3.1 and the Morrison microphysics scheme. This simulation is referred to as WRF-M2. This simulation uses almost the same setup as the three other WRF runs, except that the cloud water number concentration is set to 100 cm^{-3} rather than 250 cm^{-3} and ECMWF analysis nudging is turned off in D3 and in the boundary layer of all domains. In WRF-W, WRF-T, and WRF-M, analysis nudging is used in D1, D2, and D3 throughout the entire troposphere on a six-hour time scale using a nudging coefficient of 0.0003 s^{-1}. While analysis nudging further imposes some of the large-scale analysis errors on the simulations, it keeps the large-scale conditions fairly similar in all simulations, which allows attribution of simulation differences to the different microphysics schemes used. For all comparisons to observations, only WRF output with 10-minute output frequency covering the same 33-hour period as the CRM simulations that is within the CPOL radar coverage area is included.

2.3 Bulk Microphysics Scheme Properties

Tables 2.4 through 2.6 show relevant properties of rain, graupel, and snow in every microphysics scheme used in the CRM and LAM setups, which are briefly discussed here for reference in Chapters 3 through 5. Most schemes assume gamma distributions with $\mu = 0$, which is equivalent to an exponential distribution. Snow is the most common precipitation hydrometeor that is not represented by such a distribution, as in the Grabowski (1999) and Thompson schemes, which assume lognormal and two combined gamma distributions, respectively. The complexity of determining N_0 can vary from setting it to a constant to computing it from predicted mass mixing ratio and number concentration. Some schemes avoid some of the pitfalls of having a constant N_0 and the additional computational expense of predicting number concentration by diagnostically varying N_0 with temperature in the case of snow (WSM6 and Thompson) or mass mixing ratio in the case of graupel (Thompson). Outside of the prediction of number concentration for rain, all schemes assume the same rain mass-diameter (*m-D*) relationship and similar fall speed relationships. The only scheme that does not assume spherical, bulk density graupel or hail is MESONH, which assumes an *m-D* relationship based on Locatelli and Hobbs (1974) that forces density to decrease with increasing size. This produces low density graupel of between 100 and 200 kg m^{-3} but N_0 values are generally close to 2×10^7, five times the constant value in the Grabowski (1999) and WSM6 schemes, which significantly limits the size of graupel. For the schemes that assume constant bulk graupel density, it is set to 400 or 500 kg m^{-3}, while hail in the Morrison scheme is set to 900 kg m^{-3}. Graupel terminal fall speed relationships are shown in Figure 2.3b. They produce similar values for particle diameters less than 2 mm,

so for most low to moderate graupel mass situations, the mass-weighted fall speed for simulations using graupel are similar. For larger sizes, however, fall speeds diverge with WSM6 and UKMO giving the highest fall speeds followed by Thompson, MESONH, and finally Morrison and Grabowski (1999). The Morrison hail scheme, not surprisingly, produces much higher fall speeds than any other scheme for a given particle size. Of course, the actual fall speeds in simulations are dependent on the size distributions. For large graupel mass mixing ratios (q_g), the Thompson scheme produces mass-weighted fall speeds on par with those in the Morrison hail scheme. It does this by lowering N_0 when q_g is large, as shown in Table 2.5. For graupel mass mixing ratios greater than 5 g kg^{-1}, the median mass-weighed mean diameter in WRF-T is nearly 13 mm! This has a major impact on the amount of graupel aloft, as will be discussed in Chapters 3 and 4. Snow terminal fall speed relationships, as opposed to graupel, are similar up to diameters of about 5 mm as shown in Figure 2.3a, despite their different coefficients.

For the majority of schemes, snow is assumed to be spherical with a constant bulk density of 100 kg m^{-3}. For the MESONH and Thompson schemes, snow mass is assumed to be proportional to $D^{1.9}$ and D^2, respectively, based on observations. This allows density to decrease with size, a more realistic assumption for a snow category that must represent all noncloud particle ice and nonheavily rimed particles, but one that can produce issues if placed in a scheme that is too simple, as will be discussed in Chapter 3. For small snow particle diameters of 100–200 μm, density in these schemes is near that of pure ice, but as size increases, the density quickly decreases. In MESONH, 500 μm diameter snow particles have a density of 163 kg m^{-3}, 1 mm snow particles a density of 76 kg m^{-3}, and 5 mm snow particles a density of 13 kg m^{-3}. In the Thompson scheme,

snow is higher density, decreasing from 264 kg m^{-3} for a 500 μm diameter particle to 132 kg m^{-3} for a 1mm particle and 26 kg m^{-3} for a 5 mm particle.

While fall speed relationships differ and create some differences between simulations, especially for graupel and hail, the effects of N_0 and the *m-D* relationship on the distribution of particle diameters significantly affects particle fall speeds as well. Van Weverberg et al. (2013) found that different MCS anvil coverage was strongly related to cloud ice fall speed, which was dominated by differences in number concentration (size) of particles rather than the fall speed formulation. As will be shown in Chapters 3 through 5, the largest differences in model output are indeed between one-moment and two-moment schemes because two-moment schemes can produce a range of fall speeds for a given mass mixing ratio through the prediction of number concentration.

2.4 Calculation of Variables From Model Output

To compare model output to observations requires calculation of many variables from model output. These variables include Rayleigh horizontal radar reflectivity (henceforth radar reflectivity) and Doppler velocity, rain rate, liquid water content for a limited range of raindrop sizes, mass-weighted mean diameter, median volume diameter, normalized size intercept parameter, and moist static energy. Calculation of all of these variables is consistent with the assumptions of each simulation's microphysics scheme.

Model Rayleigh radar reflectivity is computed by integrating from a diameter of 0 to a diameter of infinity over the sixth moment of the hydrometeor melted equivalent diameter size distributions for rain, graupel, snow, and cloud ice, and adding components

from each of these four hydrometeor species. For a given hydrometeor species, the Rayleigh reflectivity computation is

$$Z_e = 0.224 \times 10^{18} \int_0^{\infty} D_e^6 n\{D(D_e)\} \left| \frac{\partial D}{\partial D_e} \right| dD_e, \tag{2.1}$$

where D_e is the equivalent melted diameter, D is the original diameter, and $n(D)$ is the size distribution. A dielectric factor of 0.224 is assumed for ice species, following Smith (1984). This factor is related to the dielectric function divided by the ice density, which is constant for Rayleigh scattering when the dielectric function is approximated by the relationship in Debye (1929) and assuming a dielectric function of 1.0 for air. Actual measurements show that this factor does in fact vary as a function of ice density, but only slightly, as shown in Bohren and Battan (1980), and thus this assumption does not have any significant impact on computed reflectivity. A general solution to this integration for ice species represented by gamma distributions is shown in equation 2.2:

$$Z_e = 0.224 \times 10^{18} N \lambda^X \lambda^{-X-2b} \left(\frac{6a}{\pi \rho_w} \right)^2 \frac{\Gamma(2b+\mu+1)}{\Gamma(\mu+1)}, \tag{2.2}$$

where Z_e has units of $mm^6\ m^{-3}$, N is the number concentration with units of m^{-3}, a and b are coefficients in the mass-diameter relationship, ρ_w is the density of liquid water with units of $kg\ m^{-3}$, λ is the gamma slope parameter with units of m^{-1}, X is equal to $1+\mu$, where μ is the gamma shape parameter. The size intercept, N_0, is shown in equation 2.3:

$$N_0 = \frac{N\lambda^{1+\mu}}{\Gamma(1+\mu)}\ , \tag{2.3}$$

where N_0 has units of m^{-4}. Non-gamma distributions such as those for combined cloud ice and snow in DHARMA-B and DHARMA-S and snow in WRF-T have more complicated solutions. This approximation is valid for the observational radar's 5.5-cm wavelength for convective systems without significant hail as is expected during Darwin's active monsoon period (see Section 2.4.1 and Keenan et al. (1998) for more details on the observational radar (CPOL)). Additionally, observed radar reflectivity used for comparisons with simulated radar reflectivity is primarily within 100 km of the radar location and attenuation corrected. Because observed radar reflectivity resolution is 2.5 km horizontally for data covering the entire CPOL domain, the computed model radar reflectivities are degraded to 2.5-km horizontal resolution in a process that conserves radar reflectivity factor for most comparisons to observations. Simulated Rayleigh reflectivity-weighted Doppler velocity is computed in a similar manner to Rayleigh radar reflectivity by computing equation 2.4:

$$V_{doppler} = \frac{\int_0^\infty v(D)D^6 n(D)dD}{\int_0^\infty D^6 n(D)dD}, \tag{2.4}$$

where D is melted equivalent diameter, $v(D)$ is the hydrometeor fall speed relationship, and $n(D)$ is the size distribution assumed in the microphysics scheme.

2.5 Observations

2.5.1 C-Band Polarimetric Radar (CPOL)

A central source of observational data is the 5.5-cm wavelength C-band polarimetric scanning radar (CPOL) described in detail in Keenan et al. (1998) and located at Gunn Point about 30 km northeast of Darwin. CPOL provides three-dimensional radar reflectivity at 10-minute resolution. The radar reflectivity is interpolated onto a 2.5-km horizontal and 0.5-km vertical grid. Reflectivity uncertainty is estimated to be approximately 1 dBZ (Peter May, personal communication).

As described in Bringi et al. (2009), rain rates were calculated using a climatological radar reflectivity-rain rate (*Z-R)* relationship based on a wet season of disdrometer data at Darwin for low rain rates. For higher rain rates, the retrieval makes use of differential reflectivity (Z_{DR}) and specific differential phase (K_{DP}), which brings down the uncertainty at higher rain rates. Z_{DR} provides information on the median raindrop size, while K_{DP} is not affected by radar calibration, attenuation by precipitation, or partial beam blockage (Rhyzkov et al., 2005). Uncertainty ranges from about 100 percent (e.g. 1 mm h^{-1} represents a range of 0.5 to 2 mm h^{-1}) for the lowest rain rates to 25 percent for rain rates of 10 mm h^{-1} or more (Peter May, personal communication). The rain rates are calculated at a 2.5-km height due to radar beam height restrictions at far ranges, and these are the rain rates that went into the variational analysis used to force the CRM simulations. Because the sensitivity of the CPOL radar is approximately 0 dBZ at a 150-km range and clutter was found to be an issue around 0 dBZ, comparisons with simulations are limited to reflectivities of 5 dBZ or greater.

2.5.2 Scanning Radar Retrievals

In addition to deriving rain rates at 2.5 km, Bringi et al. (2009) developed an algorithm based on an entire wet season of disdrometer data at Darwin to derive the rain size distribution median volume diameter (D_0) and normalized size intercept (N_w) at 2.5 km. D_0 is the diameter in the rain size distribution at which half of the water content is contained in raindrops smaller than D_0 and half is contained in raindrops larger than D_0. For the gamma distributions used in simulations, D_0 is equal to $\frac{3.67+\mu}{\lambda}$. N_w is defined as the size intercept of an exponential size distribution that has the same mass-weighted mean diameter and liquid water content as the retrieved gamma size distribution. As discussed in Bringi et al. (2009), the disdrometer data were fitted to a normalized gamma drop size distribution (DSD) and T-matrix scattering calculations were performed to output observable polarimetric radar quantities such as horizontal reflectivity, differential reflectivity, and specific differential phase. The variability of raindrop shape and orientation were taken into account in scattering calculations based on fall bridge experiments in which raindrops were formed with a hose and released off of an 80-m bridge and measured at the ground with a two-dimensional video disdrometer. From the outputted radar variables produced in the scattering calculations, algorithms were developed relating rain rate, D_0, and N_w to the radar variables. Bringi et al. (2009) showed that this retrieval compared favorably with dual-profiler retrievals at an altitude of 2.5 km. May et al. (2011) state that the retrieval uncertainty (δ) is 0.11 mm in the D_0 retrievals and 0.24 in the N_w retrievals for most D_0 and N_w values.

Another scanning radar retrieval, a dual-Doppler retrieval, is described in Collis et al. (2013, accepted). It uses radial velocity vectors from the operational Berrima and

research CPOL radars where the horizontal component of these vectors is between 30° and 150°. This yields two lobes covering an area of 4165 km^2, approximately 7–8 times smaller than the CRM domain areas. The retrieval covers a five-hour period from 1310Z to 1750Z on January 23 during the peak of convective activity. Vertical velocity is assumed to be 0 at echo top, and convergence is assumed to be constant below the lowest radar beam down to the surface if a valid radar return is detected in that column by the lowest radar beam. These are two important sources of error because convergence may actually more commonly increase toward the surface, as is seen in simulations, and significant divergence may occur above the radar echo top, as discussed in Mapes and Houze (1995). Due to accumulating error as one integrates the continuity equation upward or downward, the continuity equation is integrated both upward from the surface and downward from cloud top with a weighting function used in combining the two. Assumed hydrometeor fall speeds are used with the vertical component of the radial velocity vectors as a weak constraint on the analysis. Due to smoothing, the true resolution of the analysis is likely 2-3 km despite output on 1-km grids, but the exact resolution is not known. Despite assumed lower horizontal resolution, Collis et al. (2013, accepted) shows that retrieved vertical velocities are comparable to vertical profiler vertical velocity retrievals, which are positioned between the two lobes, with a root mean square error (RMSE) of 1.9 m s^{-1} and a negative bias in the dual-Doppler retrieval of 2.2 m s^{-1}. Because of the stated uncertainties in this analysis, it is reserved for comparing the deepest and strongest convective updrafts to those in the models. This dual-Doppler dataset also has radar reflectivity interpolated onto a 1-km horizontal grid rather than the 2.5-km horizontal grid used for the entire CPOL domain since the dual-Doppler lobes are

closer to the radar than most of the CPOL domain. This higher resolution reflectivity dataset is used in Chapter 4 when examining dual-Doppler derived convective drafts.

2.5.3 Joss-Waldvogel Disdrometer

The Joss-Waldvogel disdrometer data were collected in 127 diameter bins with a 10-second dwell time, but were processed with a dead-time correction into 20 diameter bins with one-minute resolution. The minimum size measured is 0.308 mm and the maximum size 5.258 mm. Tokay et al. (2001) show that this type of disdrometer severely underreports raindrops less than 0.5 mm. Therefore, comparisons of disdrometer observed and simulated liquid water content are limited to the stratiform liquid water content of raindrops with diameters greater than 0.308 mm and less than 5.258 mm. The liquid water content is designated convective or stratiform based on the classification of the CPOL column over the disdrometer. The separation of convective and stratiform regions is described in Section 2.5. The convective sample size is too small for comparisons with model output. Because model output for the MCS event is generated every 10 minutes, disdrometer observations are sampled every 10 minutes for comparisons with model output. Comparing the distribution of all stratiform one-minute disdrometer samples to samples every 10 minutes yields very similar distributions. Given the one-minute temporal resolution and depending on the propagation speed of the precipitation system, the disdrometer observations are slightly higher to approximately the same resolution as the model output along the propagation direction, but the sampling volume is smaller because of the nearly one-dimensional nature of the disdrometer. There is not any great way to adjust for this, but stratiform rain by definition varies

slowly in space and time, so differences in sampling volume should be minimized as long as the sample size is large enough.

2.5.4 Vertically-Pointing Profilers

As with the disdrometer data, comparisons of vertical profiler datasets with model output are limited to stratiform regions due to sample size. The highest frequency vertical profiler used is S-band (2835-MHz), which provides Rayleigh radar reflectivity and Doppler velocity. The dual-profiler retrieval of rain DSDs follows Williams and Gage (2009), which uses a VHF (50-MHz) vertical profiler to measure the clear air Bragg scattering Doppler spectrum and a UHF (920-MHz) vertical profiler to measure the Rayleigh scattering Doppler spectrum of precipitation. With the use of both profilers, precipitation spectral broadening due to air motions is accounted for. In Williams and Gage (2009), 42 different retrieval models were used to estimate retrieval bias and uncertainty. For the retrievals used in this study, a gamma distribution is assumed (Section 2.1 in Williams and Gage (2009)), the convolution method is used as the numerical inverse model (Section 4.1 of Williams and Gage (2009)), and a spectral two-norm cost function (Section 5.1 of Williams and Gage (2009)) is applied. Even if it isn't the best possible fit to the real rain size distribution, assuming a gamma distribution is appealing because it is the general form of the rain size distributions used in the simulations. Relative to the 42-member ensemble mean, this methodology produced a 0.031 mm bias in the retrieved mass-weighted mean diameter (D_m). Williams and Gage (2009) also estimated rain rate and D_m retrieval uncertainty by calculating the 10^{th}, 50^{th}, and 90^{th} percentiles of the standard deviation of rain rate and D_m for small intervals of

mean rain rate and D_m. For the most common D_m values between 0.8 and 1.8 mm, the 50th and 90th percentiles were less than 0.11 and 0.15 mm, respectively. Uncertainties for rain rate increase as rain rate increases. While the 90th percentile is 0.6 mm hr^{-1} for a 2 mm hr^{-1} rain rate, the 50th percentile is only 0.15 mm hr^{-1}.

D_m, N_w, and μ are derived from the best fit to the observed spectra from which moments of the gamma size distribution such as liquid water content and reflectivity are calculated. D_m is the fourth moment of the rain size distribution divided by the third moment of the size distribution. For the gamma distributions assumed in the simulations, $D_m = \frac{4+\mu}{\lambda}$. DSD profiles are retrieved between 1.5 and 4 km every minute. The profiler retrievals have a dwell time of 45 seconds. The VHF profiler has a beam width of 3° and vertical resolution of 310 m, while the UHF profiler has a beam width of 9° and vertical resolution of 105 m. Assuming a reasonable horizontal wind speed such as 10 m s^{-1}, this dwell time with the beam width gives a horizontal resolution in the along wind direction of approximately 700 to 1100 m depending on height. Calculating from the UHF profiler beam width, the approximate resolution in the direction perpendicular to the wind decreases from approximately 240 m at 1.5 km to 630 m at 4 km. Therefore, the sampling area is similar to the model grid spacing of 917 m by 917 m or 1000 m by 1000 m. Because model output is saved every 10 minutes, profiler retrievals are used every 10 minutes as well. This is done to avoid greater autocorrelation in observational retrievals than in model output and to maintain similar sample sizes for comparison of simulated and dual-profiler retrieved temporal mean profiles in Chapter 5. Using all one-minute samples produces a similar distribution to samples every 10 minutes. Each retrieved DSD profile is designated as convective or stratiform based on the classification of the

CPOL column that encompasses the profilers' location with only stratiform regions being considered for comparison with simulated output owing to small sample size and large retrieval error in convective regions. The separation of convective and stratiform regions is described in the next section.

2.6 Convective-Stratiform Separation

Model output and observations are compared for convective and stratiform regions separately because of the fundamentally different radar reflectivity structure in each region owing to distinctly different dynamical and microphysical processes (Houze, 1997). As will be shown in Chapter 3, this separation is crucial to identifying model biases in variables such as rainfall that would be largely covered up if all precipitating regions were included in statistics. Separation of convective and stratiform regions can be done in many ways. The method used in this dissertation uses low-level horizontal radar reflectivity texture as the separating variable. This allows radar reflectivity to be used as a separator of the two regions. A simple texture-based separation algorithm based on Steiner et al. (1995) is applied to 2.5 km altitude radar reflectivity. This algorithm works especially well for Darwin because it is based on Darwin radar data. This is a three-step algorithm. First, all grid points with reflectivities of at least 40 dBZ are labeled as convective. Second, a "peakedness" definition is applied that labels a grid point as convective if it has a reflectivity sufficiently above the background reflectivity. This threshold varies based on the value of the background reflectivity, and the background reflectivity is determined within an 11-km radius surrounding the grid point being labeled. In Steiner et al. (1995), only grid points with reflectivities above the

detection limit of the radar are included, but in this analysis, all points are included and any points that are below the CPOL detection limit are set to the detection limit value of 0 dBZ. The last step involves setting a radius around convective identified grid points that grows as the radar reflectivity at the convective grid point is increased. All grid points enveloped by this radius are then set as convective. All remaining columns with 2.5 km altitude radar reflectivities greater than 5 dBZ are considered stratiform. Figures 2.4 and 2.5 show observed and CRM simulated horizontal cross-sections of radar reflectivity at 2.5-km and 7.5-km altitudes, respectively, for 3Z on January 20. Outlined in thick black are the convective regions and outlined in thin black are the stratiform. These figures show that the convective-stratiform separation method separates the regions as would be expected with high echoes and very "peaked" echoes in space identified as convective. Although not shown, the DHARMA-2M simulation looks very similar. Figures 2.6 and 2.7 show observed and LAM simulated horizontal cross-sections of radar reflectivity at 2.5 km and 7.5 km altitudes, respectively, for 18Z on January 23. The positions of the simulated and observed precipitation fields are not directly comparable because of timing and location errors in the ECMWF analysis forcing the LAM simulations, but the convective and stratiform structures within observations and simulations are fairly representative. WRF-T, WRF-M, and WRF-M2 produce large areas identified as convective through radar reflectivities that are greater than 40 dBZ even though substantial portions of those areas are free of convective drafts (not shown). This is related to large amounts of ice being produced with slow fall speeds near the center of the mesoscale circulation. Even though such large convective regions are not

realistic, that does not invalidate the separation technique because they are a result of model errors.

Table 2.1. Descriptions of all CRM simulations being used including the symbol representing them in figures, their domain size and resolution, the type of bulk microphysics used, and the frequency of model output. In the Microphysics column, letters in the parentheses indicate two-moment hydrometeor species: cloud ice (i), cloud water (w), rain (r), graupel (g), hail (h), and snow (s).

CRM Simulation Characteristics							
Simulation	Symbol	Domain	ΔX (m)	ΔZ (m)	Microphysics	3-hr Output	10-min Output
DHARMA-B	Solid diamond	$(176\ km)^2$	917	100–250	1-moment	X	X
DHARMA-S	Open diamond	$(176\ km)^2$	917	100–250	1-moment	X	X
DHARMA-2M	X	$(176\ km)^2$	917	100–250	2-moment (i,w,r,g,s)		X
UKMO-1	Right-pointing triangle	$(177\ km)^2$	917	225–500	2-moment (i)	X	
UKMO-2	Left-pointing triangle	$(177\ km)^2$	917	225–500	2-moment (i,g,s)	X	
UKMO-2M	Square	$(177\ km)^2$	917	225–500	2-moment (i,r,g,s)	X	
UKMO-1	Right-pointing triangle	$(177\ km)^2$	917	100–250	2-moment (i)		X
UKMO-2	Left-pointing triangle	$(177\ km)^2$	917	100–250	2-moment (i,g,s)		X
UKMO-2M	Square	$(177\ km)^2$	917	100–250	2-moment (i,r,g,s)		X
MESONH-1	Up-pointing triangle	$(192\ km)^2$	1000	100–250	1-moment	X	X
MESONH-2	Down-pointing triangle	$(192\ km)^2$	1000	100–250	2-moment (i,w)	X	X
SAM-B	Solid circle	$(192\ km)^2$	1000	100–400	2-moment (i,w,r,h,s)	X	X
SAM-S	Open circle	$(192\ km)^2$	1000	100–400	2-moment (i,w,r,h,s)	X	X

Table 2.2. The advection, turbulence, surface flux, and radiation schemes used in the four CRMs. All models solve the equations of motion using the anelastic approximation.

Other CRM Simulations Schemes				
Model	Advection	Turbulence	Surface Flux	Radiation
DHARMA	2nd order forward in time with 3rd order upwinding advection (Stevens and Bretherton 1996)	Smagorinsky -Lilly	Monin-Obukhov similarity theory	2-stream with equivalent spheres (Toon et al. 1989)
MESONH	4th order forward in time with piecewise parabolic method advection (Colella and Woodward 1984)	1.5 order closure (Cuxart et al. 2000)	Bulk iterative Exchange Coefficients from ECUME (Belamari 2005)	Rapid Radiative Transfer Model (Mlawer et al. 1997)
UKMO	Leapfrog scheme with a Robert-Asselin time filter; Piascek and Williams (1970) momentum advection; Monotonic scalar advection (Leonard et al. 1993)	Smagorinsky -Lilly	Monin-Obukhov similarity theory	Edwards-Slingo (Edwards and Slingo 1996)
SAM	3rd order Adams-Bashforth with variable time stepping, 2nd order momentum advection and monotonic positive-definite scalar advection (Smolarkiewicz and Grabowski 1990)	Smagorinsky -Lilly or 1.5-order closure	NCAR Community Climate Model version 3.5 (Collins et al. 1997)	NCAR Community Climate Model (CCM3) (Kiehl et al. 1998)

Table 2.3. Descriptions of all LAM simulations being used including the symbol representing them in figures, their domain size and resolution, and the type of bulk microphysics used. In the Microphysics column, letters in the parentheses indicate two-moment hydrometeor species: cloud ice (i), cloud water (w), rain (r), graupel (g), and snow (s).

LAM Simulations Characteristics					
Simulation	Symbol	Domain (D4)	ΔX (m)	ΔZ (m)	Microphysics
WRF-W	Triangle	450 km × 330 km	1000	~100–300	1-moment
WRF-T	Square	450 km × 330 km	1000	~100–300	2-moment (r)
WRF-M	Diamond	450 km × 330 km	1000	~100–300	2-moment (i,r,g,s)
WRF-M2	Dashed Line	450 km × 330 km	1000	~100–300	2-moment (i,r,g,s)

Table 2.4. Relevant rain characteristics for each microphysics scheme used in the CRM and LAM simulations. The first column shows the name of the scheme. The Grabowski (1999) scheme is used in DHARMA-B and DHARMA-S. The Morrison scheme is used in UKMO-2M, DHARMA-2M, SAM-B, SAM-S, WRF-M, and WRF-M2. The version with hail is used in SAM-B and SAM-S. The second column shows the size distribution (SD) shape. For gamma distributions, the gamma shape parameter (μ) is listed. The third column shows the size intercept and whether number concentration is prognostic or not. N is the number concentration and λ is the slope of the SD. The fourth and fifth columns show a_m and b_m coefficients in MKS units of the mass-diameter relationship $m = a_m D^{b_m}$, where ρ_r is the density of rain. The sixth and seventh columns show the a_v and b_v coefficients in MKS units of the terminal fall speed relationship $v_f = a_v D^{b_v} e^{-f_v D}$, where f_v equals 195 for the Thompson scheme[#] and 0 for all other schemes. The last column shows the rain density.

Rain Characteristics							
Scheme	SD	N_0 [m^{-4}]	a_m	b_m	a_v	b_v	ρ_r [kg m^{-3}]
Grabowski (1999)	Gamma ($\mu = 0$)	1×10^7	$\frac{\pi\rho_r}{6}$	3	130	0.5	1000
MESONH	Gamma ($\mu = 0$)	8×10^6	$\frac{\pi\rho_r}{6}$	3	842	0.8	1000
UKMO	Gamma ($\mu = 2.5$)	1.1×10^{15}	$\frac{\pi\rho_r}{6}$	3	362	0.65	1000
Morrison	Gamma ($\mu = 0$)	Prognostic: $N\lambda$	$\frac{\pi\rho_r}{6}$	3	841.9	0.8	1000
Thompson	Gamma ($\mu = 0$)	Prognostic: $N\lambda$	$\frac{\pi\rho_r}{6}$	3	4854.4[#]	1[#]	1000
WSM6	Gamma ($\mu = 0$)	8×10^6	$\frac{\pi\rho_r}{6}$	3	841.9	0.8	1000

Table 2.5. Relevant graupel characteristics for each microphysics scheme used in the CRM and LAM simulations. The first column shows the name of the scheme. The Grabowski (1999) scheme is used in DHARMA-B and DHARMA-S. The Morrison scheme is used in UKMO-2M, DHARMA-2M, WRF-M, and WRF-M2. The version with hail is used in SAM-B and SAM-S. The second column shows the size distribution (SD) shape. For gamma distributions, the gamma shape parameter (μ) is listed. The third column shows the size intercept and whether number concentration is prognostic or not. N is the number concentration, λ is the slope of the SD, and q_g is the graupel mass mixing ratio. The fourth and fifth columns show a_m and b_m coefficients in MKS units of the mass-diameter relationship $m = a_m D^{b_m}$, where ρ_g is the density of graupel. The sixth and seventh columns show the a_v and b_v coefficients in MKS units of the terminal fall speed relationship $v_f = a_v D^{b_v} e^{-f_v D}$, where f_v equals 0 for all graupel schemes. The last column shows the graupel density.

Graupel Characteristics							
Scheme	SD	N_0 [m^{-4}]	a_m	b_m	a_v	b_v	ρ_g [kg m^{-3}]
Grabowski (1999)	Gamma ($\mu = 0$)	4×10^6	$\frac{\pi\rho_g}{6}$	3	19.3	0.37	400
MESONH	Gamma ($\mu = 0$)	$5\times10^5\lambda^{0.5}$	19.6	2.8	124	0.66	$\frac{6a_m}{\pi}D^{b_m-3}$
UKMO	Gamma ($\mu = 2.5$)	$5\times10^{25}\lambda^{-4}$/ Prognostic: $\frac{N\lambda^{3.5}}{\Gamma(3.5)}$	$\frac{\pi\rho_g}{6}$	3	253	0.734	500
Morrison (hail)	Gamma ($\mu = 0$)	Prognostic: $N\lambda$	$\frac{\pi\rho_g}{6}$	3	114.5	0.5	900
Morrison	Gamma ($\mu = 0$)	Prognostic: $N\lambda$	$\frac{\pi\rho_g}{6}$	3	19.3	0.37	400
Thompson	Gamma ($\mu = 0$)	$\max[1\times10^4, \min(\frac{200}{q_g}, 5\times10^6)]$	$\frac{\pi\rho_g}{6}$	3	442	0.89	400
WSM6	Gamma ($\mu = 0$)	4×10^6	$\frac{\pi\rho_g}{6}$	3	330	0.8	500

Table 2.6. Relevant snow characteristics for each microphysics scheme used in the CRM and LAM simulations. The first column shows the name of the scheme. The Grabowski (1999) scheme is used in DHARMA-B and DHARMA-S. The Morrison scheme is used in UKMO-2M, DHARMA-2M, SAM-B, SAM-S, WRF-M, and WRF-M2. The second column shows the size distribution (SD) shape. For gamma distributions, the gamma shape parameter (μ) is listed. The third column shows the size intercept and whether number concentration is prognostic or not. N is the number concentration, λ is the slope of the SD, T is temperature, and $T_0 = 273.15$ K. The fourth and fifth columns show a_m and b_m coefficients in MKS units of the mass-diameter relationship $m = a_m D^{b_m}$, where ρ_s is the density of snow. The sixth and seventh columns show the a_v and b_v coefficients in MKS units of the terminal fall speed relationship $v_f = a_v D^{b_v} e^{-f_v D}$, where f_v equals 125 in the Thompson scheme[#] and 0 in all other schemes. The fall speed relation in Grabowski [1999][$] is $v_f = 0.9 + 100IWC$ where IWC is the snow water content with units of kg m^{-3}. The last column shows the snow density.

Snow Characteristics							
Scheme	SD	N_0 [m^{-4}]	a_m	b_m	a_v	b_v	ρ_s [kg m^{-3}]
Grabowski (1999)	Log-normal	-	$\frac{\pi\rho_s}{6}$	3	-[$]	-[$]	100
MESONH	Gamma ($\mu = 0$)	$5\lambda^2$	0.02	1.9	5.1	0.27	$\frac{6a_m}{\pi} D^{b_m-3}$
UKMO	Gamma ($\mu = 2.5$)	$2\times10^{27}\lambda^{-3.5}$/ Prognostic: $\frac{N\lambda^{3.5}}{\Gamma(3.5)}$	$\frac{\pi\rho_s}{6}$	3	4.84	0.25	100
Morrison	Gamma ($\mu = 0$)	Prognostic: $N\lambda$	$\frac{\pi\rho_s}{6}$	3	11.72	0.41	100
Thompson	Two Gammas	-	0.069	2	40[#]	0.55[#]	$\frac{6a_m}{\pi} D^{b_m-3}$
WSM6	Gamma ($\mu = 0$)	$\min(2\times10^8, 2\times10^6 e^{0.12(T-T_0)})$	$\frac{\pi\rho_s}{6}$	3	11.72	0.41	100

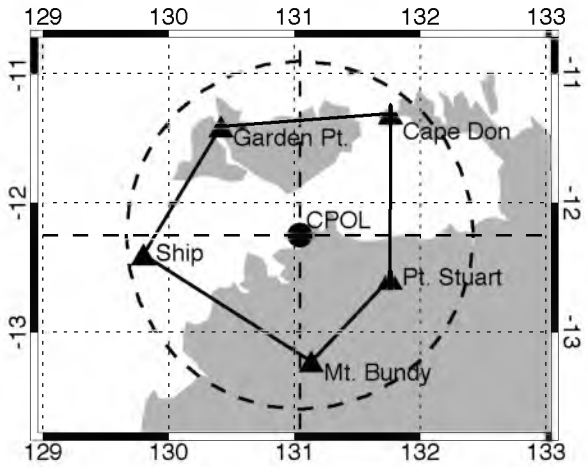

Figure 2.1. The five sites shown with triangles define the TWP-ICE pentagonal domain. Each site took three-hourly soundings. The variational analysis was performed for this region and used to force the CRM runs. The location of the CPOL radar used for observed radar reflectivity and derived rain rates is also shown on the map as a black circle with the 150-km CPOL range ring shown with a dashed line.

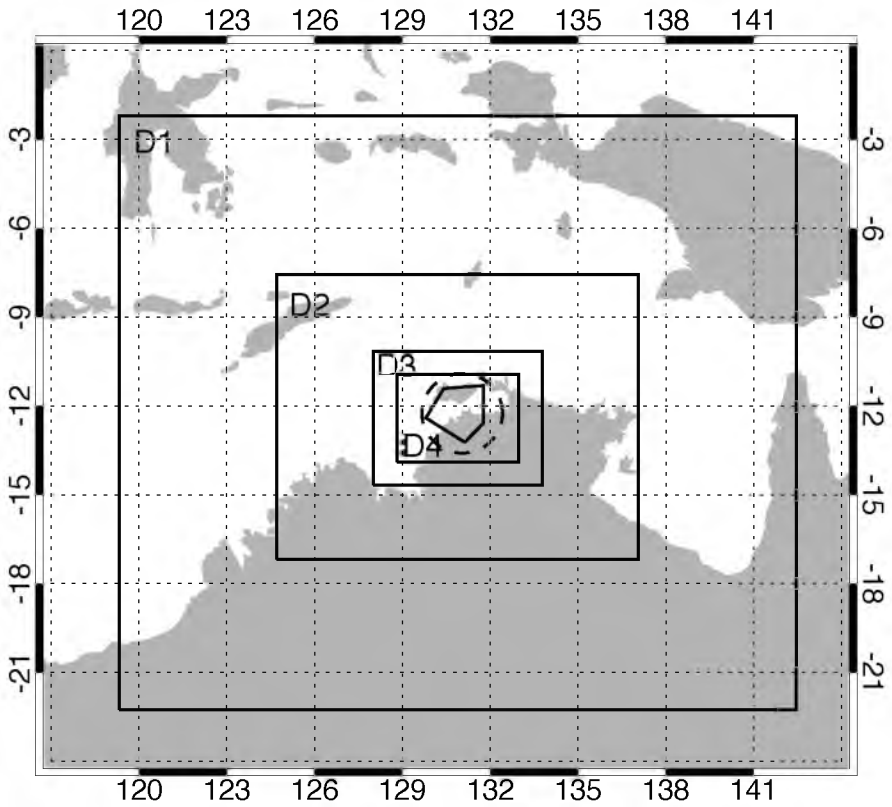

Figure 2.2. The WRF domains used for the TWP-ICE LAM Intercomparison Study. Domain 1 (D1) has a horizontal resolution of 27 km; domain 2 (D2), 9 km; domain 3 (D3), 3 km; and domain 4 (D4), 1 km. The CPOL range is shown with a dashed circle and the pentagonal forcing region for the CRM simulations is also plotted.

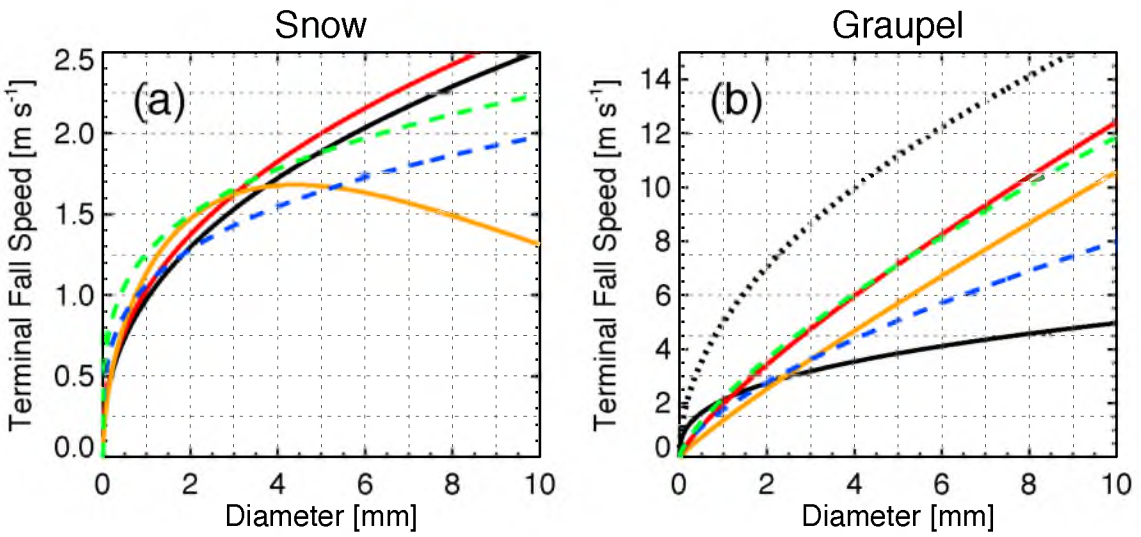

Figure 2.3. Mass terminal fall speed relationships for (a) snow and (b) graupel terminal as a function of particle diameter for the various bulk microphysics schemes used. An altitude of approximately 7 km (air density of ~0.57 kg m^{-3}) is used for calculations. The MESONH scheme is dashed in blue, the UKMO scheme dashed in green, the Thompson scheme in solid orange, the WSM6 scheme in solid red, the Morrison scheme in solid black, and the Morrison hail scheme in dotted black. The Grabowski (1999) scheme has the same graupel relationship of the Morrison scheme and a snow fall speed that depends on IWC as shown in the Table 2.6 caption, generally varying between 0.9 and 1.1 m s^{-1}.

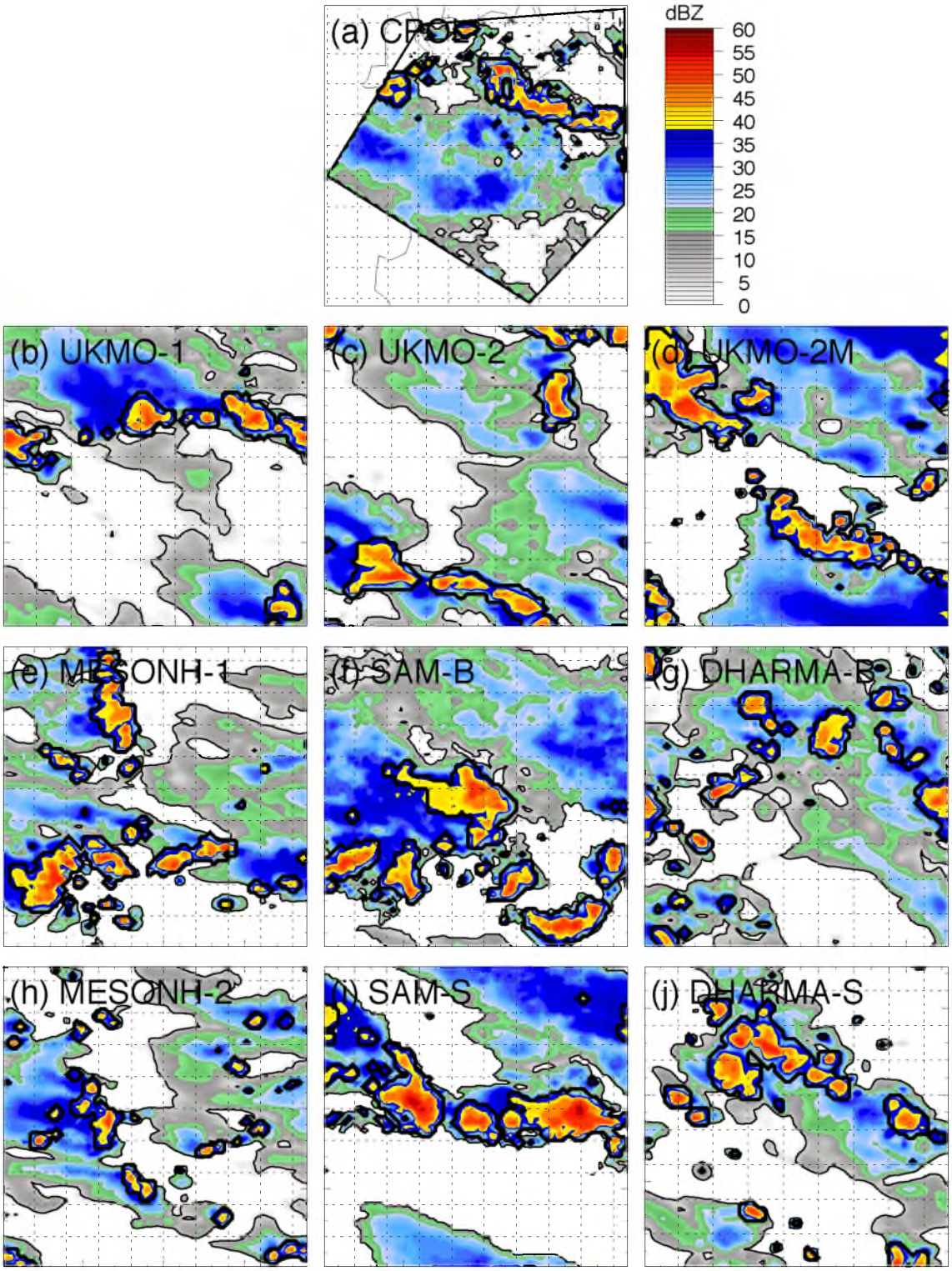

Figure 2.4. Representative 2.5-km altitude horizontal cross-sections of radar reflectivity at 3Z 20 January 2006: (a) CPOL, (b) UKMO-1, (c) UKMO-2, (d) UKMO-2M, (e) MESONH-1, (f) SAM-B, (g) DHARMA-B, (h) MESONH-2, (i) SAM-S, and (j) DHARMA-S. Convective regions are outlined in thick black and stratiform regions in thin black.

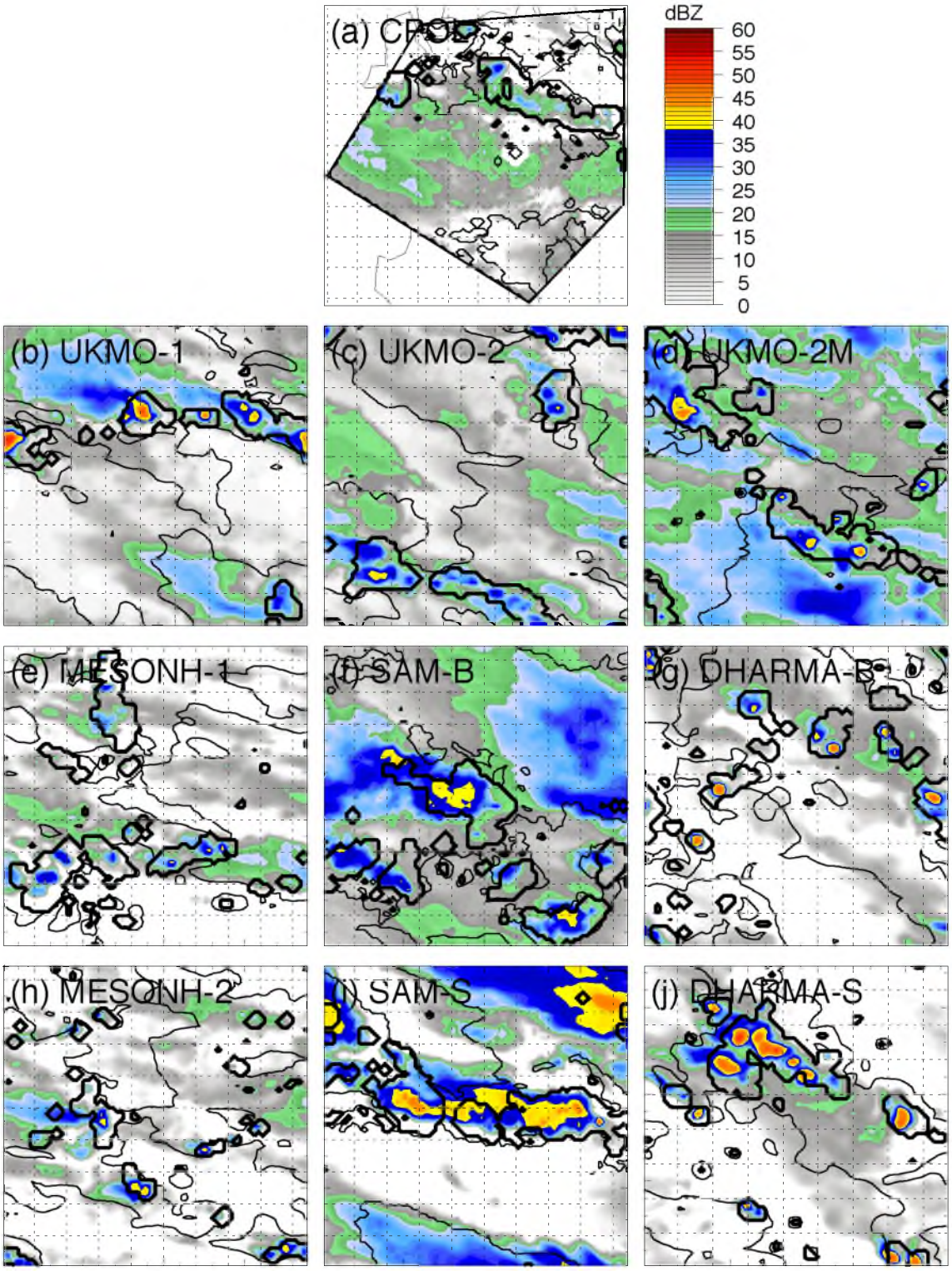

Figure 2.5. Representative 7.5-km altitude horizontal cross-sections of radar reflectivity at 3Z 20 January 2006: (a) CPOL, (b) UKMO-1, (c) UKMO-2, (d) UKMO-2M, (e) MESONH-1, (f) SAM-B, (g) DHARMA-B, (h) MESONH-2, (i) SAM-S, and (j) DHARMA-S. Convective regions are outlined in thick black and stratiform regions in thin black.

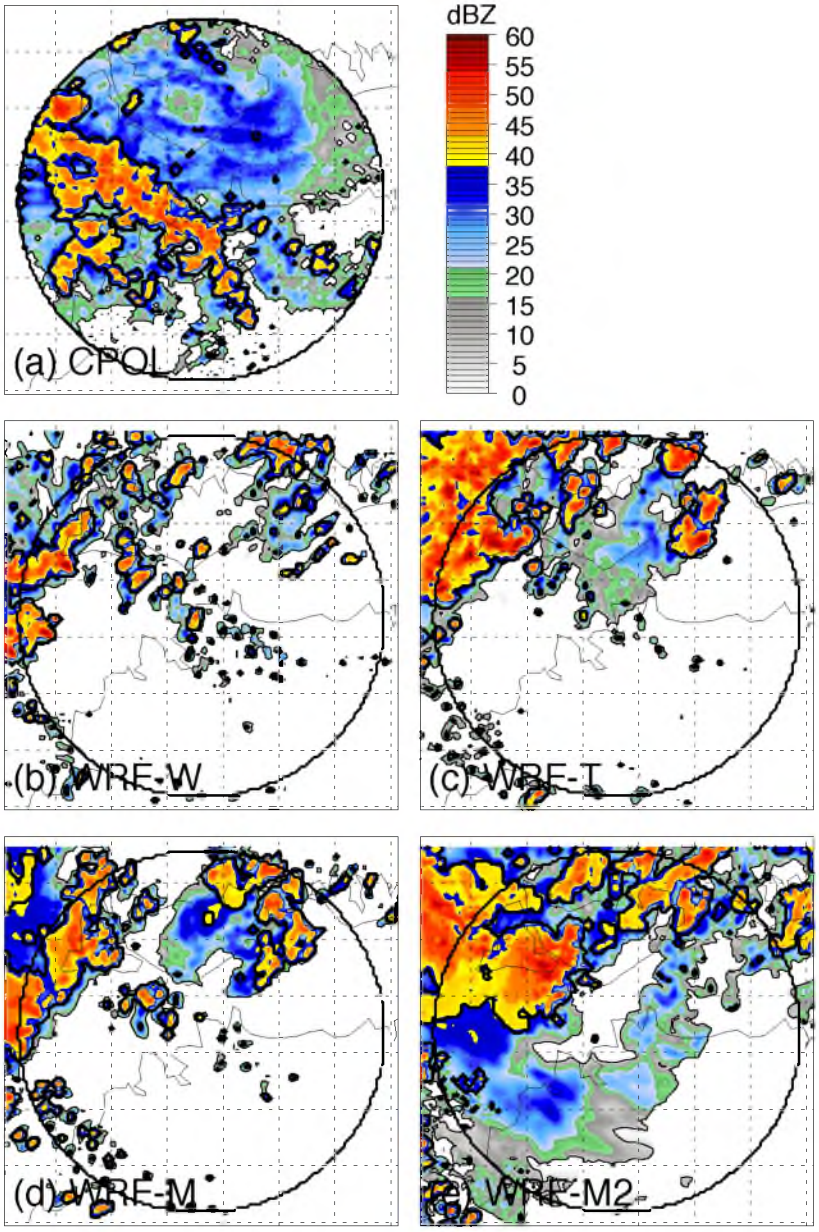

Figure 2.6. Representative 2.5-km altitude horizontal cross-sections of radar reflectivity at 18Z 23 January 2006: (a) CPOL, (b) WRF-W, (c) WRF-T, (d) WRF-M, and (e) WRF-M2. Convective regions are outlined in thick black and stratiform regions in thin black.

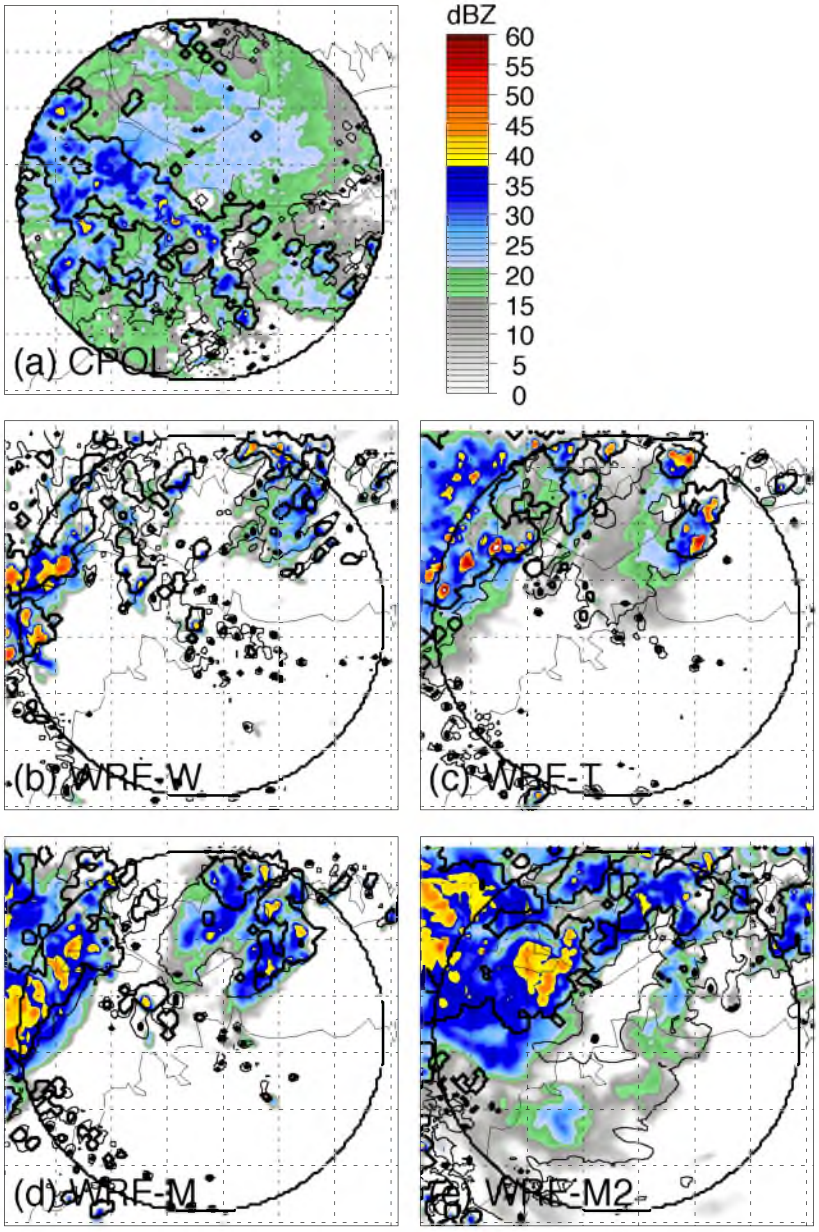

Figure 2.7. Representative 7.5-km altitude horizontal cross-sections of radar reflectivity at 18Z 23 January 2006: (a) CPOL, (b) WRF-W, (c) WRF-T, (d) WRF-M, and (e) WRF-M2. Convective regions are outlined in thick black and stratiform regions in thin black.

CHAPTER 3

CONVECTIVE AND STRATIFORM STRUCTURE

3.1 Overview

After separating convective and stratiform regions in observations and simulations, properties such as volumetric rainfall, area, rain rate, and radar reflectivity distribution are compared in this chapter. Differences in precipitation structure between simulations are then related to differences in microphysics assumptions between simulations. Because bulk microphysics schemes are used in the simulations, rain mass falls at the mass-weighted speed of the rain size distribution. Simulated rain rate is calculated by multiplying this speed by the rain water content. Radar reflectivity observations and simulated radar reflectivity calculations are described in Sections 2.3 and 2.4.1. The CRM results for the active monsoon period in this chapter are published in Varble et al. (2011).

3.2 Area and Rain Rate

3.2.1 CRM Simulations

Table 3.1 shows that the mean volumetric rainfall over the entire six-day active monsoon period is very similar in CRM simulations and observations. This is expected due to the advective forcing that incorporates CPOL-derived rain rates. The portioning of

rainfall into convective and stratiform components, however, shows far different results in simulations than in observations. Table 3.1 shows that most simulations over-predict convective rainfall and under-predict stratiform rainfall, although most values are within high levels of observational uncertainty. The highest simulated stratiform rainfalls are produced by UKMO-1, UKMO-2, and DHARMA-B, which all use one-moment rain schemes. Furthermore, Tables 3.2 and 3.3 show that when rainfall is broken down into area and rain rate components, both convective and stratiform areas are over-predicted while mean rain rates are under-predicted. Five of nine simulations over-predict convective area by 55 percent or more and seven of nine simulations over-predict stratiform area by 33 percent or more. Six of nine simulations underestimate mean convective rain rate by 20 percent or more, although only three are technically outside of observational uncertainty. UKMO-1 and UKMO-2 produce convective rain rates closest to observed, which is likely related to their unique size distributions, as discussed later in this section. All simulations underestimate mean stratiform rain rate by at least 33 percent with five simulations outside of observational uncertainty. The two sensitivity simulations are the only two simulations to accurately predict stratiform area, which implies that the idealized model forcing is at least partially responsible for the overly large stratiform areas, but rain rate is just as low in these simulations which combined with the lesser area produces even lower stratiform rainfall.

Figure 3.1 shows that both convective rainfall and area track observations in time very well because of strict regulation by the model forcing. Closer inspection, however, shows that most simulations over-predict the area during and after observed precipitation events. The over-prediction after precipitation peaks is likely a result of the periodic

lateral boundary conditions. The highest peak around 18Z on January 23 corresponds to the mesoscale convective system event described in Section 2.1.2. Convective rainfall, however, is not as over-predicted because most simulations have a larger proportion of convective rain rates at relatively low rain rates between 2 and 6 mm hr^{-1}, as shown in Figure 3.2a. Consistent with Table 3.3, UKMO-1 and UKMO-2 (right and left pointing triangles) closely follow the observed CDF of observed convective rain rates. These simulations are unique in that they assume a gamma shape parameter (μ) of 2.5 rather than 0 for rain. This may act to lower radar reflectivity for lesser convective rain rates by narrowing the rain size distribution, thus decreasing the number of lesser rain rates identified as convective. Figure 3.2b shows that very large rain rates greater than 50 mm hr^{-1} also contribute more to total convective rainfall in most simulations than in observations, and thus, simulations tend to have a larger range of convective rain rates that significantly contribute to convective rainfall.

Figure 3.3 shows that stratiform rainfall also closely follows the observed time series, but stratiform area is significantly over-predicted for most of the active monsoon period. Note the open symbols representing the sensitivity simulations do not over-predict stratiform area, but perform worse than baseline simulations in simulating stratiform rainfall. While the model forcing may be partially responsible for the high bias in stratiform area, it does not appear to affect the low bias in stratiform rain rate. Figure 3.4a shows that only DHARMA-B and DHARMA-S (diamonds) are able to match the median stratiform rain rate of 0.4 mm hr^{-1}, whereas all other simulations show median stratiform rain rates near the lower bound of observational uncertainty around 0.2 mm hr^{-1}. At higher rain rates near 2 mm hr^{-1}, all simulations fall along or outside of the lower

bound of observational uncertainty. Larger differences exist in contribution to stratiform rainfall. Rain rates less than 1 mm hr^{-1} contribute far more to simulated stratiform rainfall than observed rainfall and rain rates greater than 5 mm hr^{-1} contribute far more to observed stratiform rainfall than simulated rainfall. The only simulations within observational uncertainty for moderate to high rain rates are the UKMO-1 and UKMO-2 simulations (left and right pointing triangles) that use $\mu = 2.5$ rather than $\mu = 0$.

Chapters 4 and 5 will focus on the MCS event between 3Z on January 23 and 12Z on January 24 for which 10-minute simulation output is available for CRMs and LAMs. For reference in those chapters, the time series of CRM convective and stratiform area and rainfall for the MCS event are shown in Figure 3.5. Due to the use of periodic lateral boundary conditions, the issue of simulated convective regions not leaving the domain when they do in observations shows up in Figure 3.5, as does the issue of too little stratiform rainfall. The peak in observed stratiform area coincides with the peak in observed stratiform rainfall and rain rates. The peak in simulated stratiform rainfall, however, precedes the peak in simulated stratiform area. This too could be related to the issue of convection not leaving the domain, but also the inability to support a large stratiform region without convection feeding it, another issue in the idealized CRM setup. This issue is a possible reason for stratiform rainfall during this major event being more under-predicted than other events shown in Figure 3.3, even though stratiform rain rates are under-predicted in all events. Although not shown, differences between simulated and observed convective and stratiform rain rate CDFs for the MCS event look very similar to the entire active monsoon period shown in Figures 3.2 and 3.4.

3.2.2 LAM Simulations

The LAM (WRF) simulations show some similarities and some differences when compared with the CRM simulations. With volumetric rainfall less constrained than in the CRM simulations, all WRF simulations overestimate the volumetric rainfall for the mesoscale convective system event. As shown in Table 3.4, the over-prediction of convective rainfall and under-prediction of stratiform rainfall seen in CRM simulations is accentuated in the WRF simulations with all simulations overestimating convective rainfall by at least 80 percent and underestimating stratiform rainfall by at least 67 percent.

Tables 3.5 and 3.6 show that, as was the case for the CRM simulations, the overestimation of convective rainfall is due to overestimation of convective area rather than mean convective rain rate. Unlike the CRM simulations, the three WRF runs from the TWP-ICE LAM Intercomparison Study underestimate stratiform rainfall primarily through area rather than rain rate. WRF-M2 has vastly underestimated stratiform rain rates, but reasonable stratiform area, which is in better agreement with the CRM simulations. The vast under-prediction of stratiform area in WRF-W, WRF-T, and WRF-M is likely due to their tight coupling to the ECMWF analysis used to force them. Del Genio et al. (2012) point out a dry bias in the ECMWF analysis and high sensitivity of simulated stratiform regions to free tropospheric relative humidity. With WRF-M2 less constrained by the analysis, it may have more ability to humidify the free troposphere and develop more stratiform area. This is discussed more in later chapters.

Whereas observations show a clear convective precipitation peak around 18Z on January 23 (23.75) in Figure 3.7, WRF simulations have two less distinct peaks. WRF-

W, WRF-T, and WRF-M (symbols) closely track one another showing that the large-scale environment in those runs is strongly regulated through the analysis nudging. Thus, these errors in rainfall are very likely tied to the ECMWF analysis being used. WRF-M2 (dashed) shows even greater peaks in convective area and precipitation, although it much better approximates the observed stratiform area in Figure 3.7c. All simulations fail to simulate the strong peak in stratiform precipitation shown in Figure 3.7d between 21Z January 23 and 0Z January 24.

Figure 3.8 shows that LAMs have a greater occurrence of light to moderate convective rain rates with median convective rain rates from 5 to 8 mm hr^{-1} whereas observational retrievals yield a median convective rain rate greater than 10 mm hr^{-1}. This is in agreement with CRM simulations. Also in agreement with CRM simulations is the greater fraction of high convective rain rates than observational retrievals show. In fact, very high rain rates greater than 50 mm hr^{-1} contribute more to total convective rainfall than those in observational retrievals or CRM simulations. As was shown in Table 3.6, WRF-W, WRF-T, and WRF-M produce stratiform rain rates that are closer to those observed than those in most CRM simulations. However, WRF-M2 produces similar high fractions of low stratiform rain rates. Figure 3.8 also shows that observed high stratiform rain rates contribute much more to observed stratiform rainfall than simulated high stratiform rain rates do to simulated stratiform rainfall. For example, 40 percent of observationally retrieved stratiform rainfall is produced by rain rates greater than 5 mm hr^{-1}, but only 10–20 percent of simulated stratiform rainfall is produced by such rain rates. This too is in agreement with CRM simulation results and is likely related to the absence of a large stratiform region with a well-developed mesoscale updraft in

simulations. While CRM simulations and LAM simulations may have differences in convective and stratiform area, they show the same biases in convective radar reflectivity, which is discussed next.

3.3 Convective Radar Reflectivity

3.3.1 CRM Simulations

Figure 3.9 shows observed and CRM simulated histograms of 2.5-km altitude convective radar reflectivity for the active monsoon period. Statistics for the MCS event alone look very similar and are not shown. All simulations are able to produce the observed sharp peak in values between 35 and 40 dBZ. This is evidence that the convective-stratiform separation method performed well. It is also not all that surprising as radar reflectivity is not nearly as sensitive to rain water content at high rain water contents as it is at low rain water contents if one assumes a Marshall-Palmer size distribution, as might be expected in heavy convective rainfall on the spatial scale considered here.

The CRM simulations do not perform nearly as well at 7.5 km, where significant high biases in convective radar reflectivity show up. Figure 3.10 shows that the observed convective radar reflectivity distribution for the active monsoon period peaks sharply at 20 dBZ. This peaked distribution is evident at all height levels in observations and moves toward lower reflectivities as height increases (not shown). Simulated reflectivity distributions tend to be uniform from 5 dBZ through 30 to 40 dBZ. The Morrison 2-moment scheme (circles and square) produces more peaked distributions than most one-moment schemes and the UKMO-2 two-moment scheme because the Morrison scheme

has significant contributions to high radar reflectivities from snow, shown in Figure 3.10c, whereas most one-moment schemes and the UKMO-2 two-moment scheme have convective radar reflectivity that is more dominated by graupel in Figure 3.10b. Interestingly, the UKMO-1 simulation (right pointing triangle) is the only one-moment scheme that produces high snow radar reflectivity and it assumes $\mu = 2.5$. The two-moment UKMO-2 simulation (left pointing triangle) with $\mu = 2.5$ significantly decreases both the graupel and snow radar reflectivity from that in UKMO-1. The SAM simulations (circles), which are the only simulations that use hail, have the highest snow radar reflectivity and lowest dense precipitating ice reflectivity because hail has at least double the fall speed of graupel for the formulation in the Morrison scheme, meaning it falls out of the convective updraft much more efficiently than the graupel used by all other simulations. Convective radar reflectivity distributions aloft look similar for the MCS event, although the SAM simulations have slightly greater samples of high reflectivity, which is consistent with the stronger convective strength during the MCS event.

Just because simulated convective radar reflectivity aloft is biased high does not mean that simulated convective regions are deeper. Shown in Figure 3.11, a normalized CDF of 5-dBZ echo top heights in convective regions shows that observed 5 dBZ echo tops are higher than most CRM simulations' 5-dBZ echo tops. Observed 25-dBZ echo tops, on the other hand, are lower than in all simulations. This leads to a median difference in 25-dBZ and 5-dBZ convective echo tops of 6 km in observations but only 1–3 km in simulations. This means that convective regions are similar in depth between

simulations and observations but radar reflectivity decreases much more gradually in observations than in simulations.

3.3.2 LAM Simulations

As shown in Figure 3.12, WRF simulations show the same sharply peaked convective radar reflectivity distribution at 2.5 km that is seen in the CRM simulations and observations. This is not surprising considering the WRF rain microphysics schemes are very similar if not the same as several of those used in the CRM simulations. WRF-M and WRF-M2 (diamond and dashed line) produce a much larger peak associated with greater convective area. As in the CRM simulations, convective radar reflectivity aloft is biased high in Figure 3.13, although the WRF distributions are more peaked than the CRM distributions. The Morrison two-moment scheme (diamond and dashed line) is again plagued by high snow radar reflectivity, which leads to the worst high bias aloft of all of the simulations. Snow radar reflectivity appears more reasonable in the one-moment WSM6 (triangle) and Thompson (square) schemes, but graupel leads to high biases in those schemes, as it does in all schemes. The WSM6 and Thompson one-moment snow schemes produce higher radar reflectivities than the one-moment schemes used in DHARMA and MESONH because they vary the snow size distribution based on temperature, which mimics aggregation of snow that increases radar reflectivity.

3.4 Stratiform Radar Reflectivity

3.4.1 CRM Simulations

Whereas the primary issues in convective radar reflectivity were aloft, issues in stratiform radar reflectivity arise at all height levels. All CRM baseline simulations show substantial peaks in their 2.5-km altitude radar reflectivity distribution between 10 and 20 dBZ in Figure 3.14, whereas the observed distribution remains approximately constant between 5 and 30 dBZ before dropping off between 30 and 40 dBZ. The two sensitivity simulations eliminate the large peak at low radar reflectivities, again implying the idealized model forcing may be the primary driver of the over-prediction of stratiform area in the CRM baseline simulations. These two simulations do not, however, increase the number of samples between 25 and 35 dBZ, the range that contains most of the high stratiform rain rates. Differences in radar reflectivity between simulations are larger in stratiform regions than convective regions partly because radar reflectivity is more sensitive to changes in liquid water content at low liquid water contents than at high liquid water contents. The simulations using the Morrison two-moment scheme (circles and square) have more samples than observed at reflectivities between 35 and 40 dBZ. Results are similar for the MCS event alone.

A large model spread exists in radar reflectivity histograms at a 7.5-km altitude, shown in Figure 3.15. The simulations using various forms of the Morrison 2-moment scheme (circles and square) and the UKMO simulations (left and right pointing triangles) show substantial samples of radar reflectivity greater than 25 dBZ whereas observed samples decrease from a peak at 20 dBZ to almost no samples greater than 25 dBZ. The DHARMA (diamonds) and MESONH (up and down pointing triangles) simulations

using 1-moment schemes have much lower radar reflectivity than observed, peaking between 5 and 10 dBZ. No simulation is close to reproducing the observed distribution. Histograms for the MCS event produce similar conclusions, except that the observed histogram is much more strongly peaked at 20 dBZ due to the large uniform stratiform region produced during that event. The reasons for these large differences in simulated radar reflectivity aloft are explored in Section 3.5.

3.4.2 LAM Simulations

Shown in Figure 3.16, the WRF simulations do not have the large peaks at low radar reflectivities seen in CRM simulations. The simulations with the Morrison two-moment scheme (diamond and dashed line), especially WRF-M2, produce the closest agreement with observations at 2.5 km, while WRF-W (triangle) and WRF-T (square) under-predict 2.5-km radar reflectivity. All simulations struggle, as did the CRM simulations, to reproduce the distinct peak at 30 dBZ, perhaps owing to a lack of a large, continuous, well-developed stratiform region in simulations. WRF-M and WRF-M2, however, have too many samples of reflectivity over 30 dBZ at 7.5 km without the distinct peak at 20 dBZ. WRF-T (squares) is the only LAM simulation to not over-predict reflectivity and hint at this peak, although it is at 16 dBZ and not as pronounced. Still, this can be seen as a success and may be due to the relatively complicated bi-gamma snow size distribution (see Field et al., 2005) used in the Thompson scheme that varies as a function of temperature and assumes mass is proportional to D^2.

3.5 Relation to Model Microphysics Assumptions

There are substantial differences between simulated precipitation structures aloft. This section relates such differences to differences in assumed hydrometeor properties in the CRM simulations. Figure 3.17 shows 7.5-km altitude graupel and snow radar reflectivity histograms for the MCS event with specific simulations highlighted based on assumptions in the microphysics scheme they use. Highlighted in blue in (a) and (d) are the SAM simulations that use hail rather than graupel as the precipitating dense ice category. This assumption substantially reduces the amount of dense ice aloft, but any reduction in radar reflectivity is offset by very high snow radar reflectivity in this case. The two other simulations with many high snow radar reflectivity echoes (squares and x's) use the Morrison two-moment microphysics scheme. Part of the issue with that snow scheme is that it allows for aggregation of snow, but assumes snow has a constant bulk snow density of 100 kg m^{-3}, whereas aggregated dendritic snow typically has lower density than smaller snow particles, as shown by *m-D* relationships in Locatelli and Hobbs (1974) and Field et al. (2005), for example.

One solution to this problem could be to assume a nonspherical snow *m-D* relationship that allows snow density to decrease with increasing size, as is assumed in the MESONH simulations highlighted in (e) and described in Table 2.6. Unfortunately, with the one-moment treatment in MESONH, the *m-D* relationship used produces an under-prediction in snow radar reflectivity because small snow has such high density and aggregation is not well represented even though N_0 shifts to smaller sizes as λ decreases, as shown in Table 2.6. MESONH also assumes a nonspherical graupel *m-D* with coefficients shown in Table 2.5 that assumes low density graupel, but N_0 values are very

high based on their dependence on λ in Table 2.5, which limits the maximum graupel radar reflectivity in (b) from reaching the levels of DHARMA-B and DHARMA-S (diamonds).

The dispersion of the gamma size distribution is controlled by μ, which also has a significant impact on graupel and snow radar reflectivity as one might expect. As described in Tables 2.4 and 2.6, UKMO-1 and UKMO-2 assume $\mu = 2.5$ rather than 0 as all other simulations do. Revisit Figure 1.1 to see how this affects the size distribution. Simply put, increasing μ results in a narrower size distribution for a given number concentration and mass mixing ratio. This can lead to closer agreement with observed reflectivity through narrowing of the graupel and snow size distributions, but this only occurs when number concentration is predicted in the case of UKMO-1 and UKMO-2. The green line with higher reflectivity values in Figure 3.17 (c) and (d) is the one-moment UKMO-1 simulation and the one with the lower values is the two-moment UKMO-2 simulation. As all of these examples illustrate, the way in which hydrometeor size distributions are defined can create large differences in radar reflectivity.

Figure 3.18 shows normalized cumulative distributions of convective graupel radar reflectivity, water content (IWC), number concentration (N), and mass-weighted mean diameter (D_m). The DHARMA simulations (diamonds) produce the highest graupel radar reflectivity in Figure 3.18a, whereas the simulations employing two-moment schemes (circles, square, and left pointing triangle) and the MESONH simulations (up and down pointing triangles) group together at lower reflectivity values. These distributions of radar reflectivity are not highly correlated with the distributions of graupel IWC in Figure 3.18b because of very different assumptions in size distribution

characteristics between different microphysics schemes. The MESONH simulations (up and down pointing triangles) have the highest graupel IWC despite having the lowest reflectivities of the one-moment schemes because MESONH has the highest graupel N of any scheme in Figure 3.18c. This is the result of the N_0-λ relationship used in MESONH as discussed earlier. With the highest N, MESONH has the smallest D_m of all CRM simulations in Figure 3.18d. The other one-moment schemes have larger D_m, which is consistent with lower graupel N values in those simulations rather than higher IWC. UKMO-1 (right pointing triangle) is an outlier in both D_m and N because it uses $\mu = 2.5$. The only other simulation with a nonzero μ is UKMO-2, but N is predicted in that simulation.

As in the case of graupel, simulations with the highest snow radar reflectivities also tend to have the highest mass-weighted mean diameters. As shown in Figure 3.19, the snow D_m distributions for two-moment schemes (circles and square) cover a larger range of diameters than one-moment schemes due to their ability to predict N. This ability also allows a broader range of snow IWC and N than the one-moment schemes used in MESONH (up and down pointing triangles) and DHARMA (diamonds). Nonzero μ had implications for graupel and has implications for snow as well. UKMO-1 (right pointing triangle) is the only one-moment simulation that covers a large range of IWC and N due to its use of a nonzero μ. Relative to convective snow IWC (not shown), the stratiform snow IWC for all two-moment schemes and UKMO-1 is significantly lower, whereas it is only slightly lower for MESONH and DHARMA. In fact, DHARMA has the highest stratiform snow IWC but the lowest stratiform snow radar reflectivity because of its log-normal size distribution described in McFarquhar and

Heymsfield (1997) that forces extremely high N and limits the size of snow. UKMO-1 again has the lowest N due to a μ value of 2.5 rather than 0 and nonprognostic N, which allows for reflectivities closer to observations. Whereas the nonspherical m-D and N_0-λ relationships used in MESONH aided those simulations with respect to graupel radar reflectivity, they produce snow reflectivities that are too low. This is clearly shown in Figure 3.20, which shows radar reflectivity as a function of IWC for graupel and snow.

One-moment microphysics schemes produce single lines in Figure 3.20 because each water content has but one size distribution and hence one radar reflectivity in these treatments (unlike more complex one-moment schemes, with diagnostic intercepts, such as Thompson et al. (2004)). Two-moment schemes, however, allow for different size distributions for a given ice water content and hence, such schemes are depicted by frequency distributions in which the shading contours are logarithmically spaced. This figure reaffirms some of the previous conclusions drawn about differences in radar reflectivity relating to differences in size distribution assumptions. For graupel/hail in panels (a), (b), and (c), MESONH (up pointing triangle) has the lowest radar reflectivity for any given IWC, but the MESONH convective radar reflectivity agrees much better with observations than the other simulations. The Morrison hail scheme used in SAM-B shown in 3.20a tends to have a higher radar reflectivity for a given IWC than the Morrison graupel scheme in UKMO-2M (3.20b), but there are also fewer occurrences of large ice water contents. It can also be seen that radar reflectivities are generally brought down for a given IWC in UKMO-2 (3.20c) relative to UKMO-1 (right pointing triangles) showing the impact of predicting N in a scheme. For both graupel and snow, the range of reflectivity possibilities for a given IWC is very large as shown in the shadings. The

slope and values of the relation for UKMO-1 snow is closest to the two-moment schemes for low to moderate IWC while MESONH produces the best agreement at high IWC, but clearly aggregation leads to a spread to higher reflectivities in the two-moment schemes that the one-moment schemes cannot produce if they use a fixed N_0 and μ in the size distribution. In reality, snow aggregates as it approaches the melting level (Houze and Churchill 1987; Heymsfield et al. 2002; Stith et al. 2002) leading to a decrease in the number concentration and an increase in the size of snow particles. Microphysics schemes, such as two-moment schemes, that have the ability to predict a large spread of reflectivity values for a given IWC have the ability to better predict the observed radar reflectivity distribution. However, simulations with the two-moment Morrison scheme generally over-predict snow radar reflectivity. This is not to say that all two-moment schemes have this problem because the UKMO two-moment scheme that uses $\mu = 2.5$ (shaded in Figure 3.20c and 3.20f) has far fewer samples of high radar reflectivity at very low IWC for both graupel and snow.

LAM simulations include two versions of the Morrison two-moment scheme, which had multiple versions used in the CRM simulations, which although not shown, align very nicely with the statistics from those CRM simulations. The two other schemes used, WSM6 and Thompson, provide different schemes for comparison. Graupel and snow characteristics are outlined in Tables 2.5 and 2.6. The WSM6 scheme is a one-moment scheme but allows the snow size intercept to diagnostically shift based on temperature in an attempt to mimic aggregation. These diagnostic shifts in the size distribution are popular because they reduce computational expense, but produce more realistic shifts in snow sizes and number concentrations. For the Thompson scheme,

diagnostics based on temperature combined with a unique *m-D* relationship ($m = 0.069D^2$) and a complicated size distribution defined by two combined gamma distributions based on Field et al. (2005) leads to very realistic snow reflectivities. The Thompson scheme uses a diagnostic size intercept for graupel as well. For graupel, the scheme decreases the size intercept as the predicted mass mixing ratio increases to mimic the shift from lightly rimed snow to hail. This scheme produces much more snow than graupel aloft, which is somewhat due to the faster fallout of large graupel amounts with lower diagnosed size intercepts and hence larger sizes. Interestingly, despite the lower graupel water contents, graupel radar reflectivities are higher in the Thompson scheme where the graupel has not yet fallen out because of those much larger sizes and much lower size intercepts. This is but one example that supports the CRM results that show more dependence of radar reflectivity on size distribution assumptions than significant differences in water content.

Although it is obvious that radar reflectivity aloft depends on IWC for any one simulation, differences in radar reflectivity across the CRM and LAM simulations are more dependent on differences in assumed size distribution properties, such as N_0, μ, and λ. The difficulty in choosing the appropriate assumptions is that IWC may be incorrect, which is explored in the next chapter. Either way, it is important that any changes in microphysics assumptions are guided by observations and theory.

3.6 Discussion

Both CRM and LAM simulations do not correctly proportion convective and stratiform regions. Some of this difference between simulations and observations can be

attributed to model initialization and forcing, but some can likely be attributed to model parameterizations as well. Convective radar reflectivity aloft is biased high and stratiform rain rate is biased low, indicating dynamics and microphysics components to model biases. Differences in model ice microphysics parameterization assumptions play a larger role in radar reflectivity differences between simulations than do differences in graupel and snow water contents, but this does not mean that ice water contents are correct. The next two chapters explore dynamical and microphysical sources of model biases including those due to model forcing, convective draft properties, and microphysics.

Table 3.1. Six-day active monsoon mean rainfall for all precipitating regions, convective regions, and stratiform regions for observations and CRM simulations. Precipitation is calculated using rain rates at a 2.5-km altitude and only includes points with radar reflectivity of 5 dBZ or greater. Precipitation is defined as convective or stratiform following Steiner et al. (1995). The percentage difference between each simulation and observations is also shown. Observed mean rainfalls in parentheses show the lower and upper bounds with observational error taken into account. Rainfall has units of 10^3 mm h^{-1} km^2.

	CRM Active Monsoon Volumetric Rainfall					
	All		Convective		Stratiform	
	Mean	Difference	Mean	Difference	Mean	Difference
Observed	33.36 (23.66–48.51)	-	20.68 (16.19–26.59)	-	12.68 (7.48–21.92)	-
DHARMA-B	35.66	+7%	24.66	+19%	11.00	-13%
DHARMA-S	35.95	+8%	27.90	+35%	8.05	-37%
UKMO-1	35.26	+6%	23.30	+12%	12.06	-5%
UKMO-2	36.65	+10%	24.79	+20%	11.85	-7%
UKMO-2M	34.92	+5%	25.98	+26%	8.93	-30%
MESONH-1	33.11	-1%	23.79	+15%	9.33	-26%
MESONH-2	20.52	-38%	11.96	-42%	8.55	-33%
SAM-B	35.50	+6%	26.12	+26%	9.37	-26%
SAM-S	27.41	-18%	21.14	+2%	6.27	-51%

Table 3.2. Six-day active monsoon mean domain fractions covered by all precipitation, convective precipitation, and stratiform precipitation. Precipitation is defined as convective or stratiform following Steiner et al. (1995) with a lower bound of 5 dBZ. The percentage difference between each simulation and observations is also shown.

	CRM Active Monsoon Precipitating Area					
	All		Convective		Stratiform	
	Mean	Difference	Mean	Difference	Mean	Difference
Observed	0.363	-	0.044	-	0.319	-
DHARMA-B	0.491	+35%	0.068	+55%	0.423	+33%
DHARMA-S	0.379	+2%	0.071	+61%	0.308	-3%
UKMO-1	0.507	+40%	0.047	+7%	0.460	+44%
UKMO-2	0.496	+37%	0.053	+20%	0.443	+39%
UKMO-2M	0.517	+42%	0.073	+66%	0.444	+39%
MESONH-1	0.521	+44%	0.068	+55%	0.453	+42%
MESONH-2	0.521	+44%	0.042	-5%	0.479	+50%
SAM-B	0.598	+65%	0.072	+64%	0.526	+65%
SAM-S	0.360	-1%	0.057	+30%	0.303	-5%

Table 3.3. Six-day active monsoon 2.5-km altitude mean rain rates (mm h^{-1}) for all precipitating regions, convective regions, and stratiform regions. Only grid points with radar reflectivity of 5 dBZ or greater are included. Precipitation is defined as convective or stratiform following Steiner et al. (1995). The percentage difference between each simulation and observations is also shown. Mean rain rates in parentheses show lower and upper bounds with observational error taken into account.

	CRM Active Monsoon Rain Rate					
	All		Convective		Stratiform	
	Mean	Difference	Mean	Difference	Mean	Difference
Observed	2.95 (2.09–4.29)	-	15.14 (11.85–19.47)	-	1.27 (0.75–2.20)	-
DHARMA-B	2.37	-20%	11.86	-22%	0.85	-33%
DHARMA-S	3.10	+5%	12.84	-15%	0.85	-33%
UKMO-1	2.25	-24%	15.98	+6%	0.85	-33%
UKMO-2	2.39	-19%	15.17	0%	0.87	-31%
UKMO-2M	2.19	-26%	11.57	-24%	0.65	-49%
MESONH-1	2.10	-29%	11.58	-24%	0.68	-46%
MESONH-2	1.30	-56%	9.46	-38%	0.59	-54%
SAM-B	1.96	-34%	11.99	-21%	0.59	-54%
SAM-S	2.51	-15%	12.15	-20%	0.68	-46%

Table 3.4. Mesoscale convective system event rainfall for all precipitating regions, convective regions, and stratiform regions for the CPOL domain and the portion of D4 of the LAM simulations that is covered by the CPOL domain. Precipitation is defined as any radar reflectivity echoes greater than or equal to 5 dBZ at an altitude of 2.5 km. All precipitation is defined as either convective or stratiform following Steiner et al. (1995). The percentage difference between each model simulation and observations is also shown. Observed mean rainfalls in parentheses show the lower and upper bounds with observational error taken into account. Rainfall has units of 10^3 mm h^{-1} km^2.

	LAM MCS Volumetric Rainfall					
	All		Convective		Stratiform	
	Mean	Difference	Mean	Difference	Mean	Difference
Observed	118.6 (86.07–167.8)	-	75.19 (59.08–96.18)	-	43.37 (26.99–71.58)	-
WRF-W	148.9	+26%	135.5	+80%	13.38	-69%
WRF-T	166.1	+40%	152.0	+102%	14.07	-68%
WRF-M	158.5	+34%	146.4	+95%	12.13	-72%
WRF-M2	191.3	+61%	177.1	+136%	14.23	-67%

Table 3.5. Mesoscale convective system event domain mean fractions covered by all precipitation, convective precipitation, and stratiform precipitation. Precipitation is defined as convective or stratiform following Steiner et al. (1995) with a lower bound of 5 dBZ. The percentage difference between each simulation and observations is also shown.

	LAM MCS Precipitating Area					
	All		Convective		Stratiform	
	Mean	Difference	Mean	Difference	Mean	Difference
Observed	0.513	-	0.073	-	0.440	-
WRF-W	0.312	-39%	0.132	+81%	0.180	-59%
WRF-T	0.371	-28%	0.155	+112%	0.215	-51%
WRF-M	0.366	-29%	0.168	+130%	0.199	-55%
WRF-M2	0.568	+11%	0.196	+168%	0.371	-16%

Table 3.6. Mesoscale convective system event 2.5-km altitude mean rain rates (mm h^{-1}) for all precipitating regions, convective regions, and stratiform regions. Only grid points with radar reflectivity of 5 dBZ or greater are included. Precipitation is defined as convective or stratiform following Steiner et al. (1995). The percentage difference between each simulation and observations is also shown. Mean rain rates in parentheses show lower and upper bounds with observational error taken into account.

	LAM MCS Rain Rates					
	All		Convective		Stratiform	
	Mean	Difference	Mean	Difference	Mean	Difference
Observed	3.63 (2.64–5.14)	-	16.19 (12.72–20.71)	-	1.55 (0.96–2.56)	-
WRF-W	7.51	+107%	16.17	0%	1.17	-25%
WRF-T	7.04	+94%	15.38	-5%	1.03	-34%
WRF-M	6.80	+87%	13.72	-15%	0.96	-38%
WRF-M2	5.29	+46%	14.17	-12%	0.60	-61%

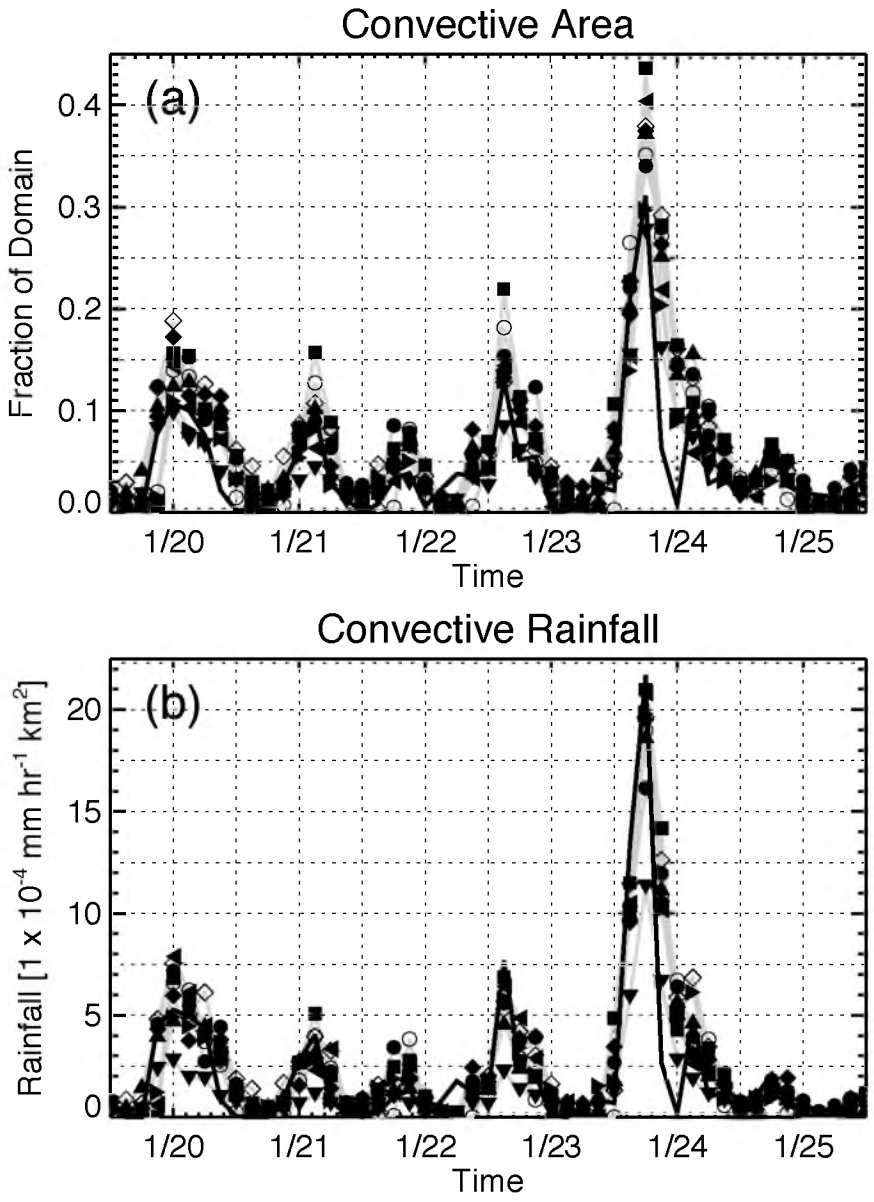

Figure 3.1. The six-day active monsoon time series of (a) convective area and (b) volumetric rainfall at a 2.5-km altitude. CRMs are represented by symbols (see Table 2.1). The thick black line represents observations derived from the CPOL radar. Volumetric rainfall has units of 1×10^{-4} mm h^{-1} km^2.

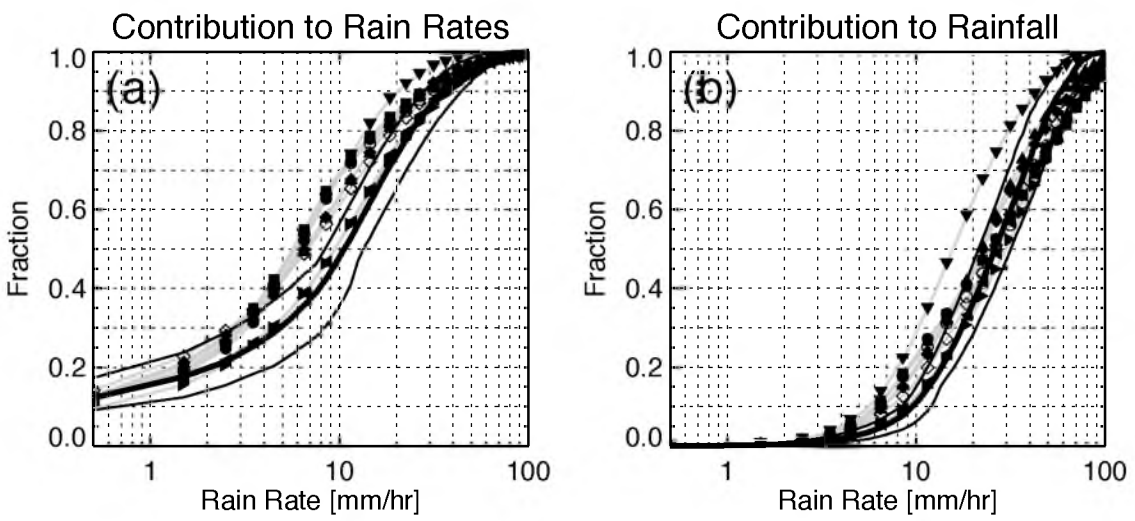

Figure 3.2. 2.5-km altitude CRM convective rain rate normalized cumulative distributions for the six-day active monsoon are shown in (a) with models represented by symbols (see Table 2.1) and observations by the thick black line. Thin black lines show the observational error bounds. The cumulative contribution of convective rain rates to total convective rainfall is shown in (b). Observations are derived from the CPOL radar.

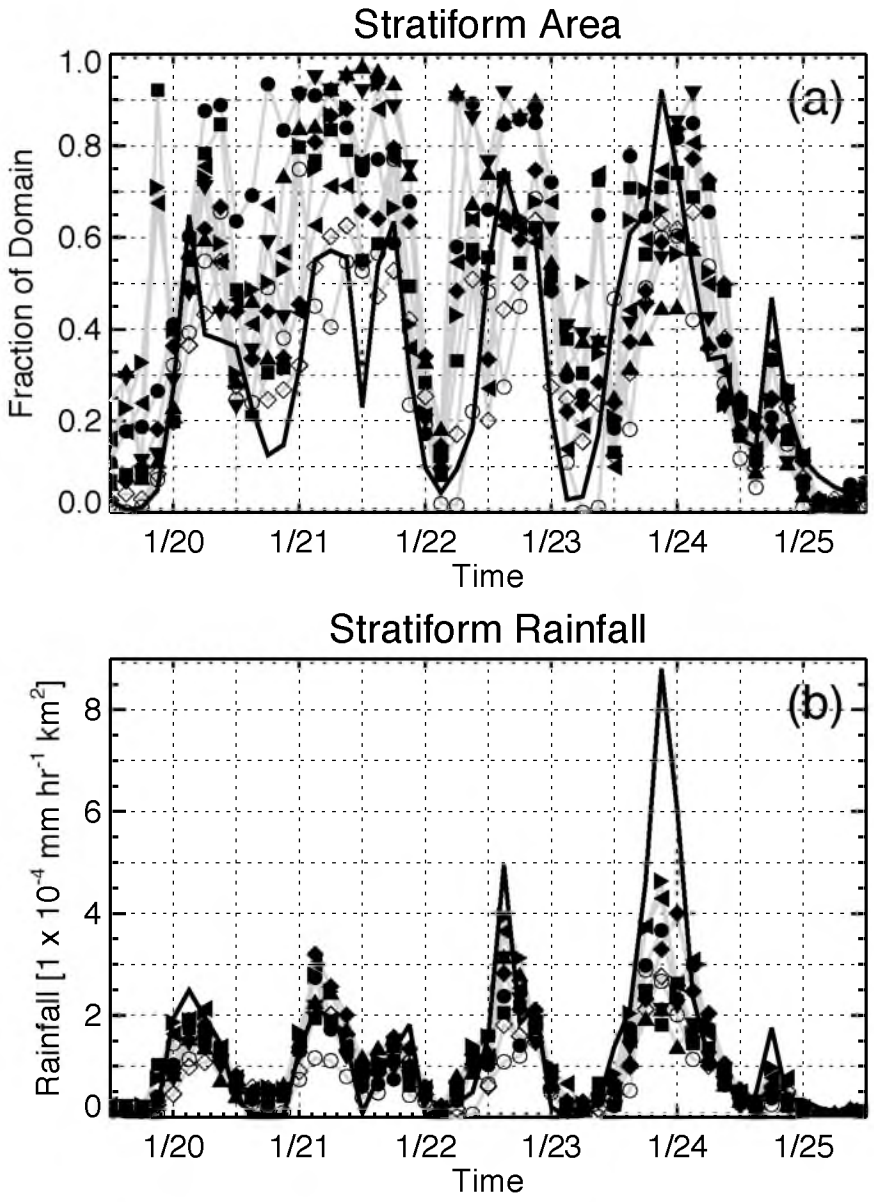

Figure 3.3. The six-day active monsoon time series of (a) stratiform area and (b) volumetric rainfall at a 2.5-km altitude. CRMs are represented by symbols (see Table 2.1). The thick black line represents observations derived from the CPOL radar. Volumetric rainfall has units of 1×10^{-4} mm h^{-1} km^2.

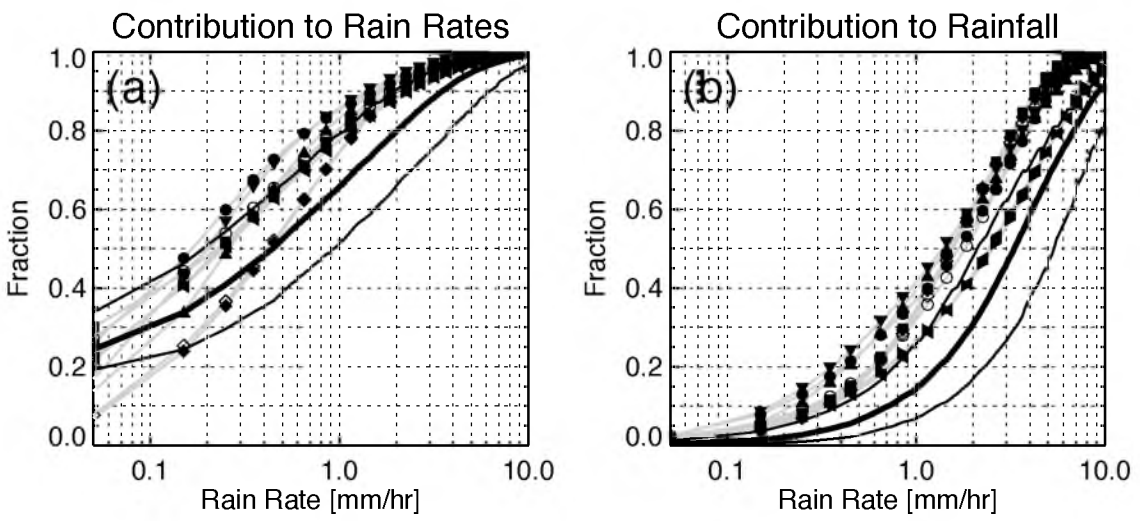

Figure 3.4. 2.5-km altitude CRM stratiform rain rate normalized cumulative distributions for the six-day active monsoon are shown in (a) with models represented by symbols (see Table 2.1) and observations by the thick black line. Thin black lines show the observational error bounds. The cumulative contribution of stratiform rain rates to total stratiform rainfall is shown in (b). Observations are derived from the CPOL radar.

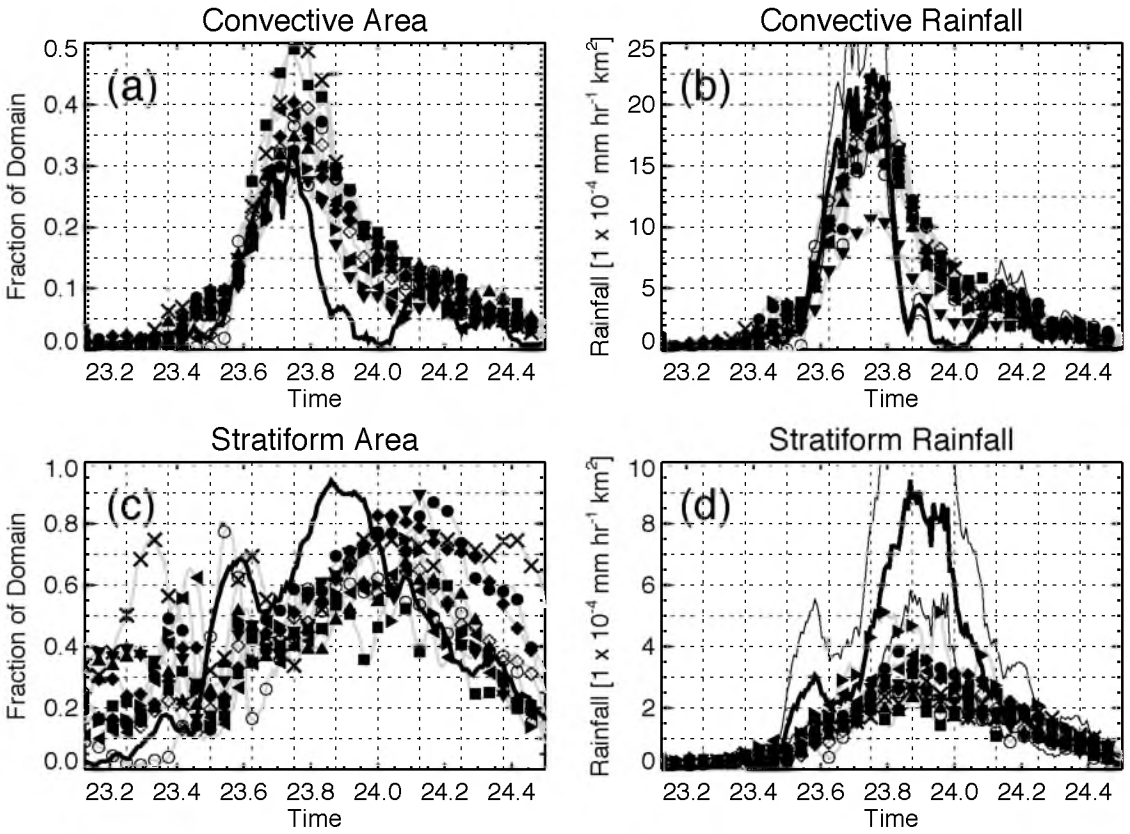

Figure 3.5. The time series of CRM (a) convective area, (b) convective volumetric rainfall at an altitude of 2.5 km, (c) stratiform area, and (d) stratiform volumetric rainfall at an altitude of 2.5 km for the MCS period between 3Z 1/23 and 12Z 1/24 using 10-minute output. Observations derived from the CPOL radar are represented by the black line and CRM simulations by the gray lines and symbols (see Table 2.1). The solid thin black lines represent volumetric rainfall retrieval uncertainty. Rainfall has units of 1×10^{-4} mm h^{-1} km^2.

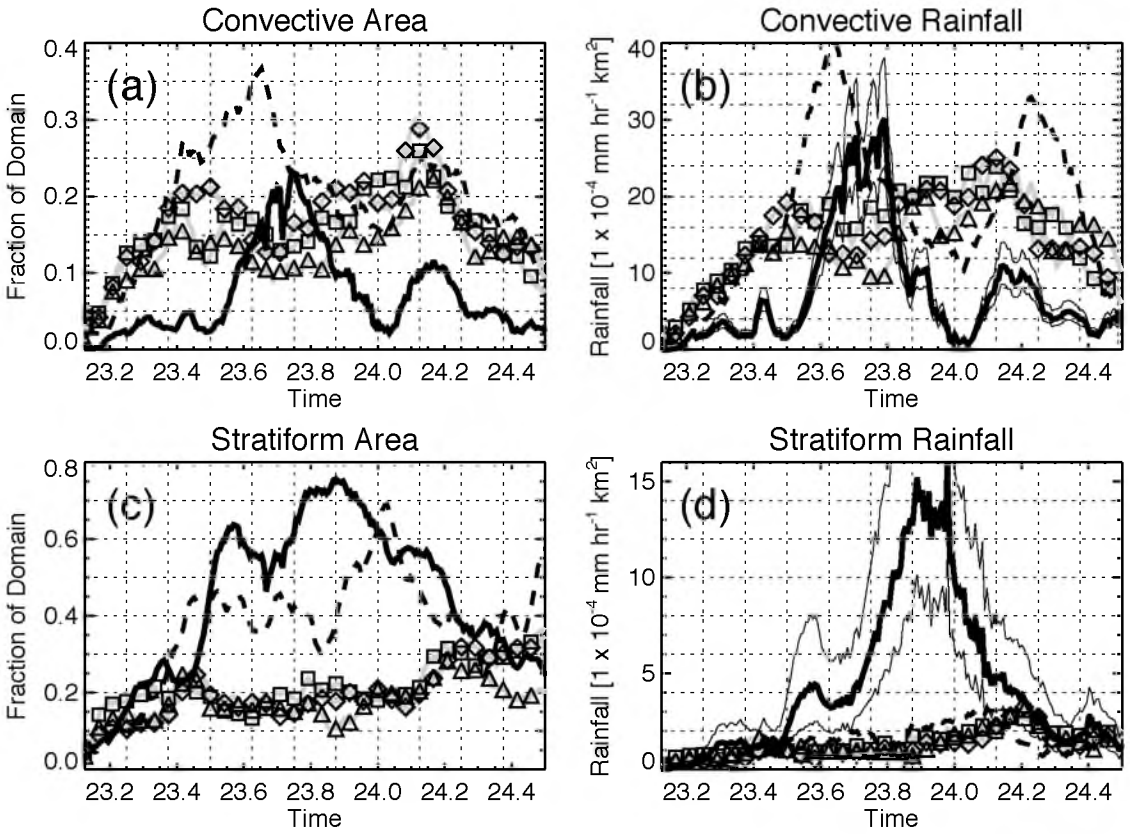

Figure 3.7. The time series of LAM convective (a) area and (b) volumetric rainfall at an altitude of 2.5 km is displayed next to a time series of stratiform (c) area and (d) volumetric rainfall at an altitude of 2.5 km for the mesoscale convective system event. The solid thick black line represents CPOL-derived observations with the solid thin black lines representing retrieval uncertainty. Symbols and the dashed line (see Table 2.3) represent LAM simulations. LAM statistics are limited to the CPOL domain. Rainfall has units of 1×10^{-4} mm h^{-1} km^2.

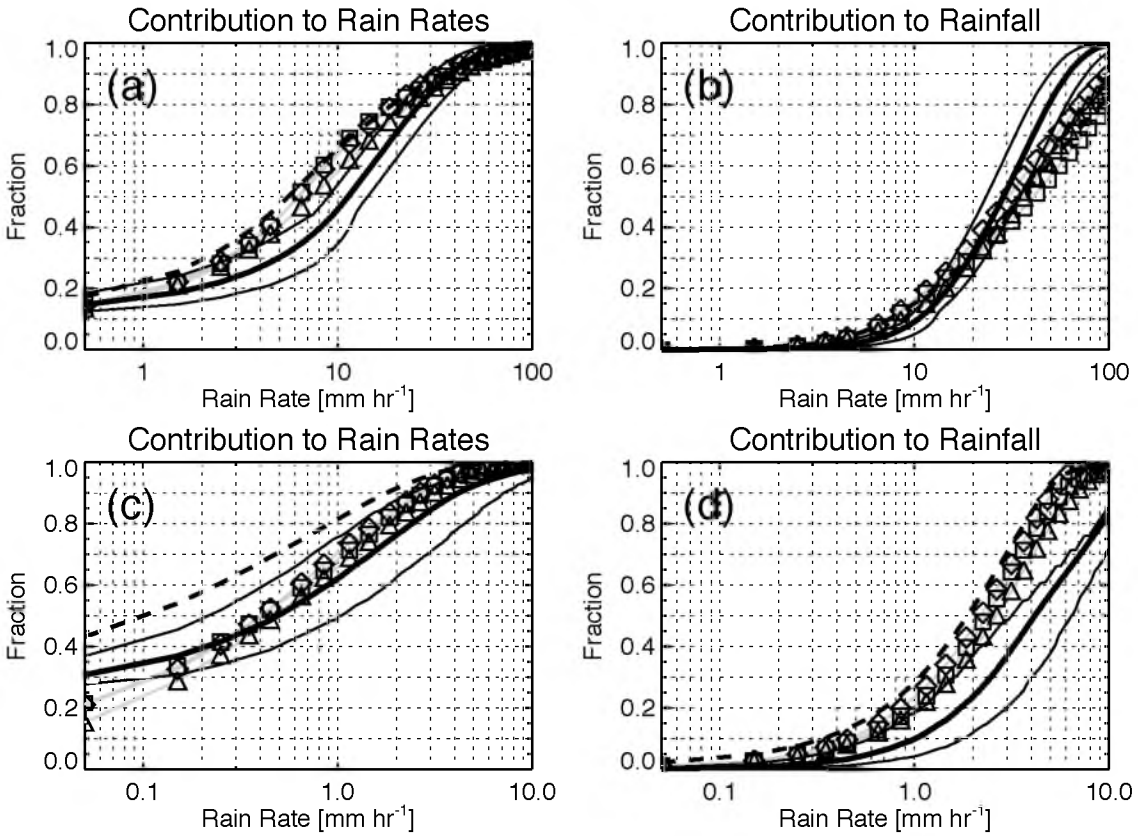

Figure 3.8. 2.5-km altitude LAM convective rain rate normalized cumulative distributions for the MCS event are shown in (a). Symbols and the dashed line represent simulations (see Table 2.3). The thick black line represents observations. Thin black lines show the observational error bounds. The cumulative contribution of convective rain rates to total convective rainfall is shown in (b). The same statistics for stratiform regions are shown in (c) and (d). Observations are derived from the CPOL radar.

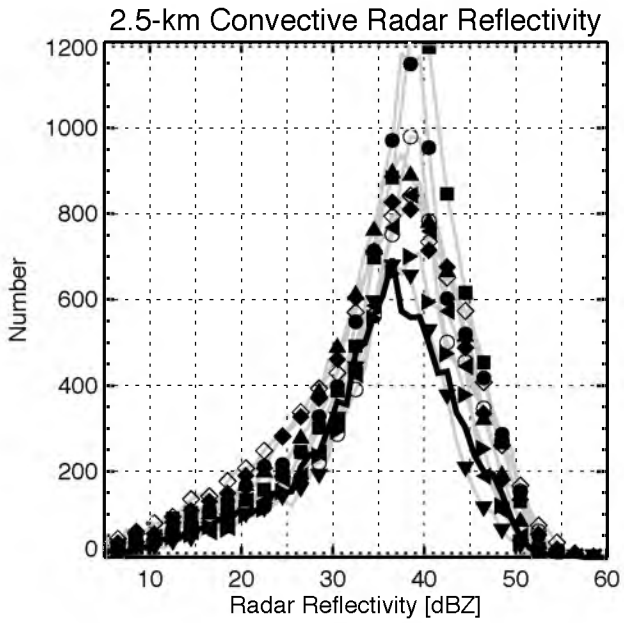

Figure 3.9. Histograms of observed and CRM simulated convective radar reflectivity at a 2.5-km altitude for the six-day active monsoon period. Models are represented by symbols (see Table 2.1), and the thick black line represents observations from the CPOL radar.

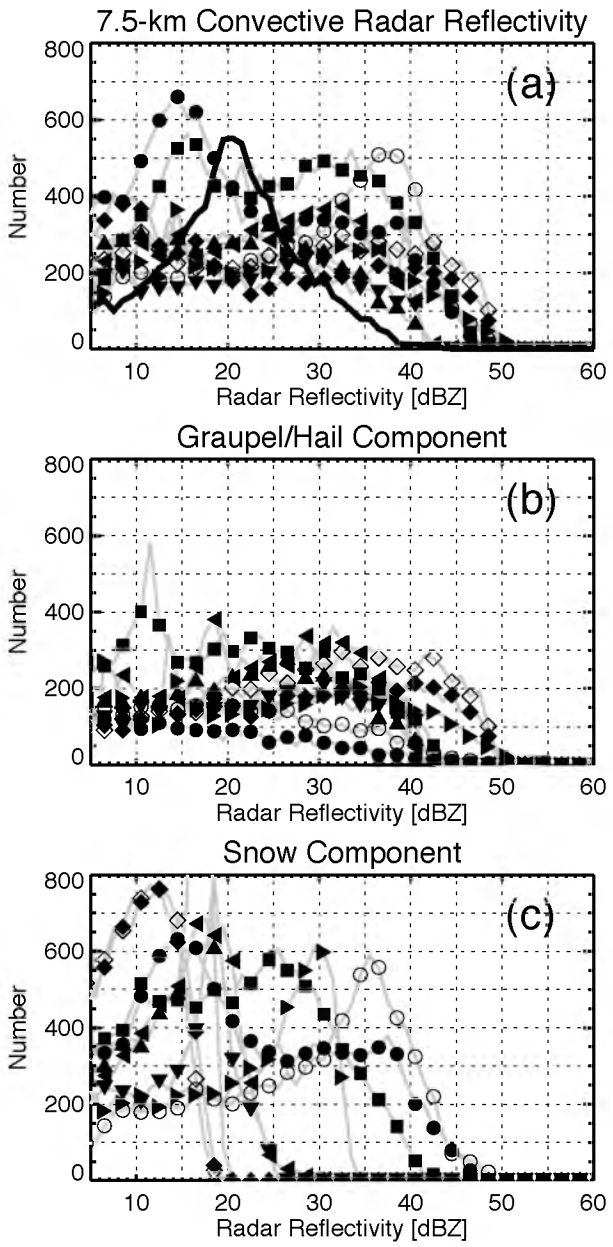

Figure 3.10. Histograms of (a) 7.5-km altitude observed and CRM simulated convective radar reflectivity, (b) 7.5-km simulated graupel (hail for SAM) radar reflectivity, and (c) 7.5-km simulated snow radar reflectivity for the six-day active monsoon period. Models are represented by symbols (see Table 2.1), and the thick black line represents observations from the CPOL radar.

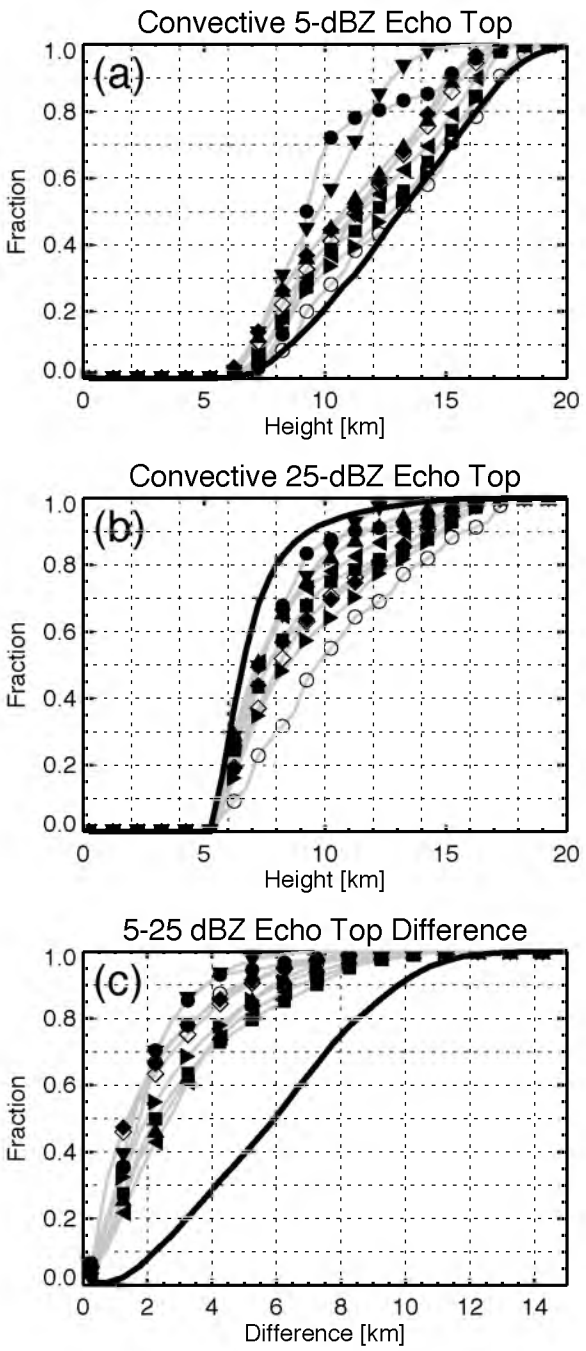

Figure 3.11. Observed and CRM simulated convective radar reflectivity echo top normalized cumulative distributions for (a) 5 dBZ and (b) 25 dBZ for the six-day active monsoon period. Shown in (c) are the cumulative distributions of the difference between 5-dBZ and 25-dBZ echo tops. With the focus on deeper convective regions, samples are limited to columns that have at least a 25-dBZ echo at 5.5 km or higher. Models are represented by symbols (see Table 2.1), and the thick black lines represent observations from the CPOL radar.

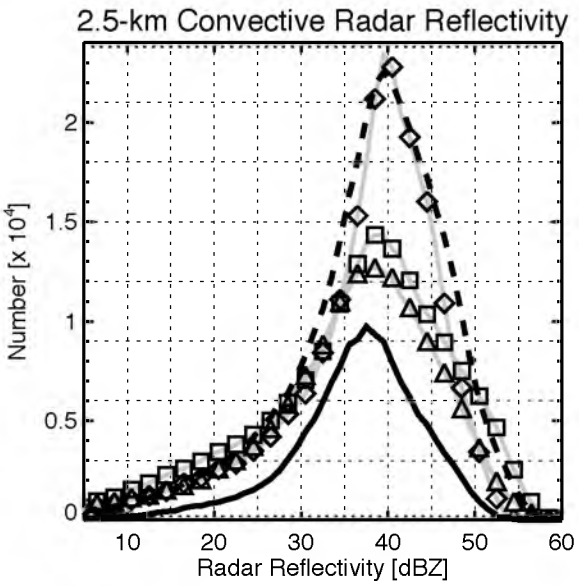

Figure 3.12. Histograms of 2.5-km altitude observed and LAM simulated convective radar reflectivity for the MCS event. Models are represented by symbols and the dashed line (see Table 2.3), while the thick black line represents CPOL observations. WRF output is limited to the CPOL domain.

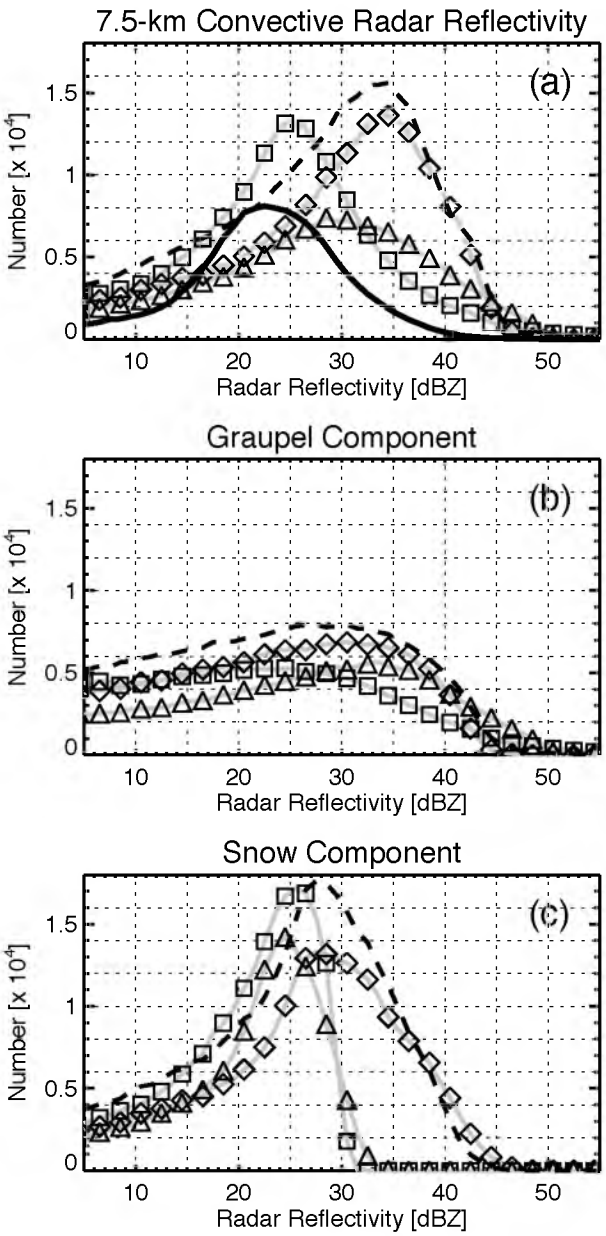

Figure 3.13. Histograms of (a) 7.5-km altitude observed and LAM simulated convective radar reflectivity, (b) 7.5-km simulated graupel radar reflectivity, and (c) 7.5-km simulated snow reflectivity for the MCS event. Models are represented by symbols and the dashed line (see Table 2.3), while the thick black line represents CPOL observations. WRF output is limited to the CPOL domain.

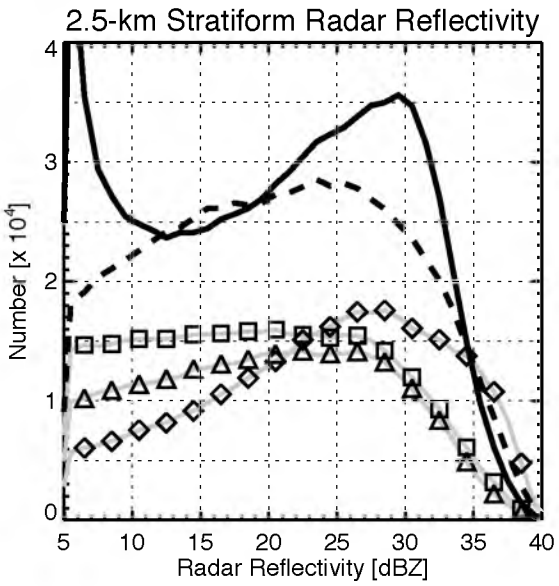

Figure 3.14. Histograms of observed and CRM simulated stratiform radar reflectivity at 2.5 km for the six-day active monsoon period. Models are represented by symbols (see Table 2.1), and the thick black line represents observations from the CPOL radar.

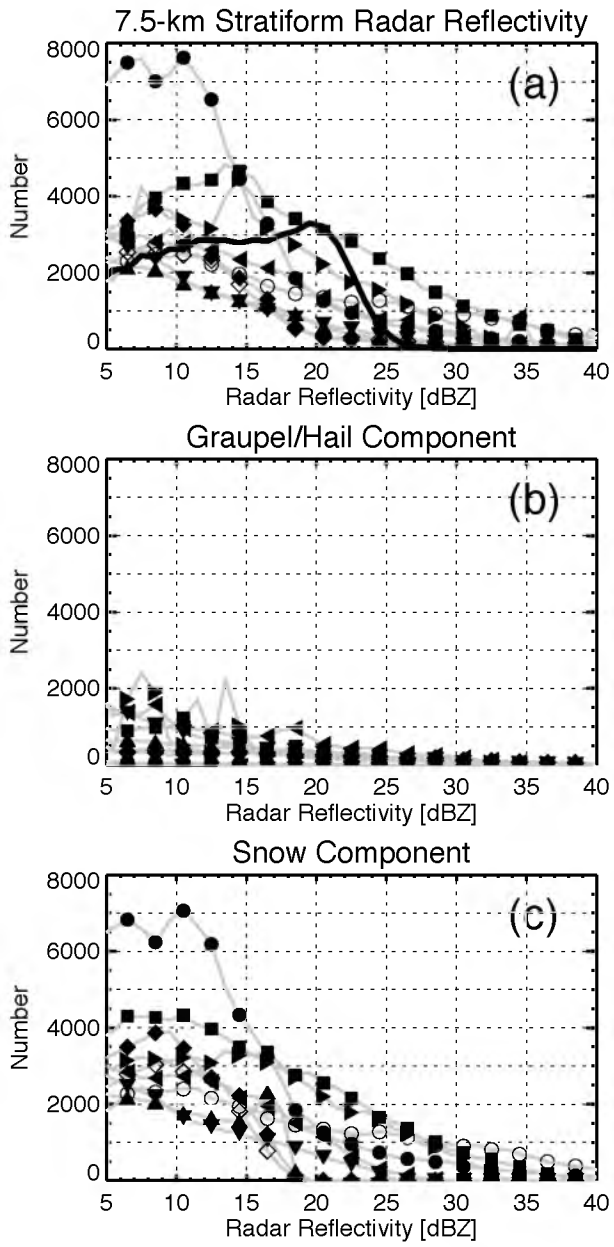

Figure 3.15. Histograms of (a) 7.5-km altitude observed and CRM simulated stratiform radar reflectivity, (b) 7.5-km simulated graupel radar reflectivity, and (c) 7.5-km simulated snow radar reflectivity for the six-day active monsoon period. Models are represented by symbols (see Table 2.1), and the thick black line represents observations from the CPOL radar.

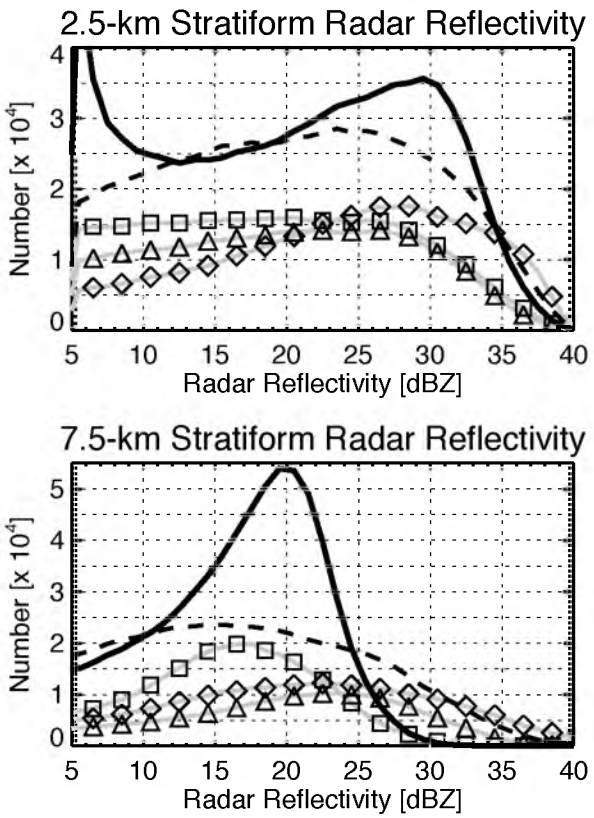

Figure 3.16. Histograms of (a) 2.5-km altitude observed and LAM simulated stratiform radar reflectivity and (b) 7.5-km altitude observed and LAM simulated stratiform radar reflectivity for the MCS event. Models are represented by symbols and the dashed line (see Table 2.3). CPOL observations are represented by the solid black lines.

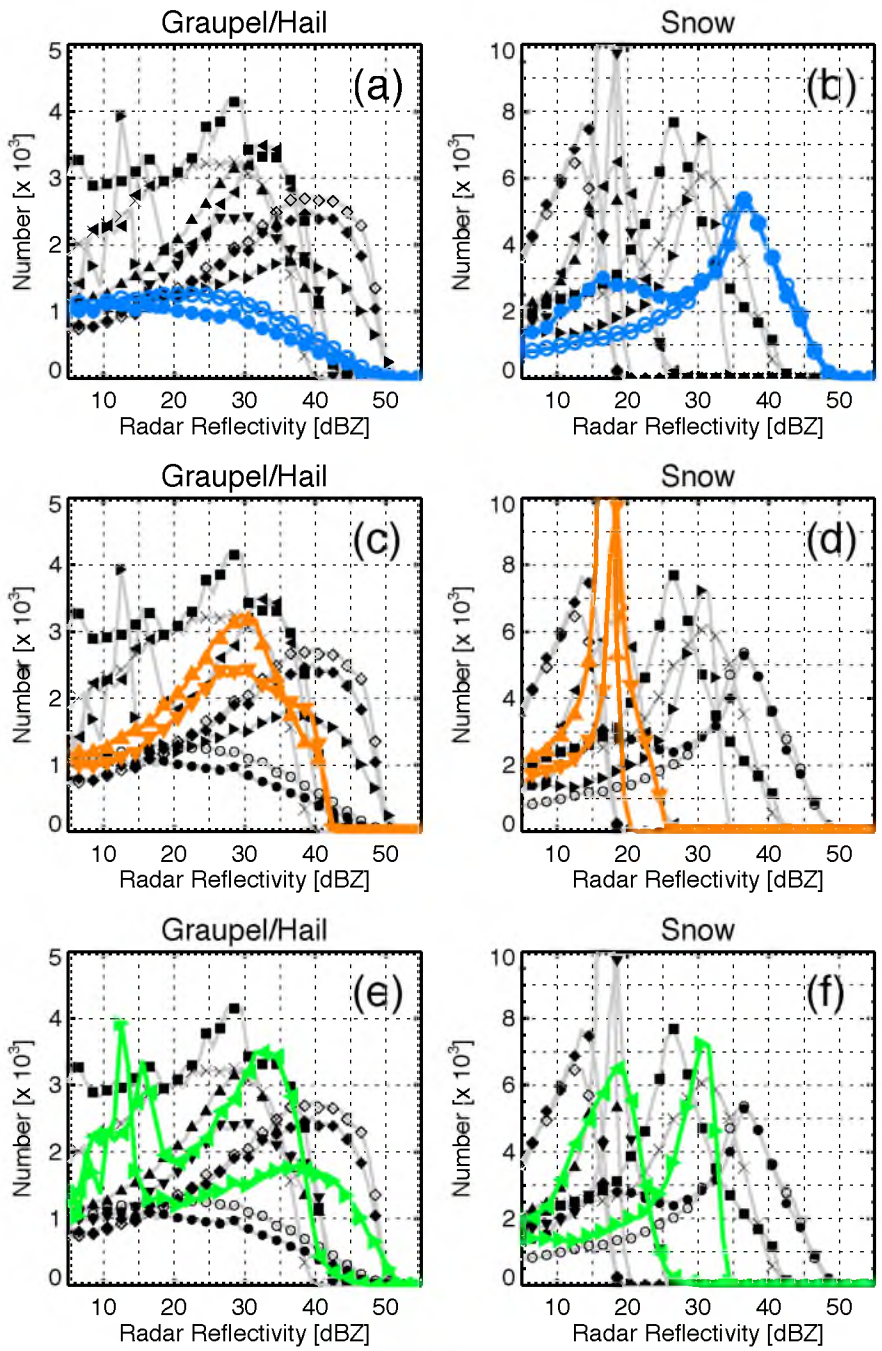

Figure 3.17. CRM simulated 7.5-km altitude histograms of graupel (a, c, e) and snow (b, d, f) radar reflectivity during the MCS event highlighting (a–b) SAM-B and SAM-S that use hail rather than graupel in blue, (c–d) MESONH-1 and MESONH-2 that assume non-spherical *m-D* relationships in orange, and (e–f) UKMO-1 and UKMO-2 that assume $\mu = 2.5$ rather than 0 in green.

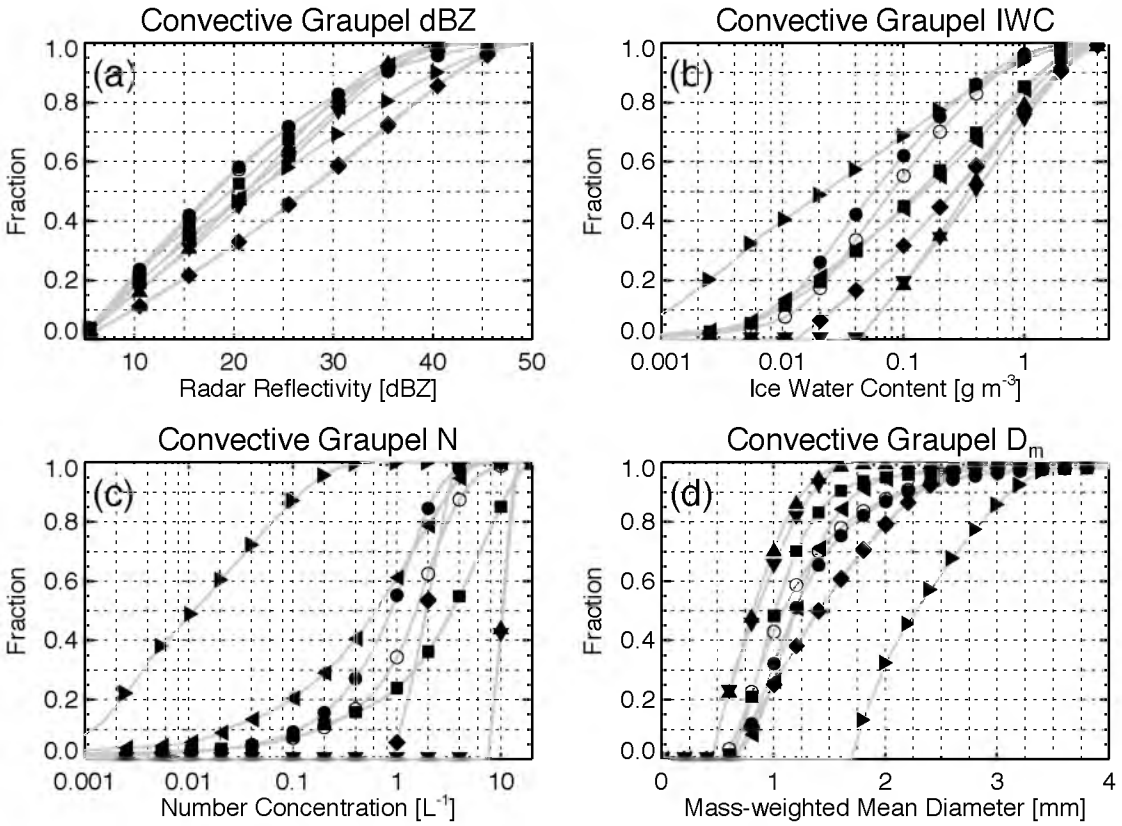

Figure 3.18. Normalized cumulative distributions of simulated convective graupel (hail for SAM) (a) radar reflectivity, (b) water content, (c) number concentration, and (d) mass-weighted mean diameter for the six-day active monsoon period. Results only include grid points at which the graupel/hail radar reflectivity is at least 5 dBZ and the temperature is less than 0°C. Symbols are defined in Table 2.1.

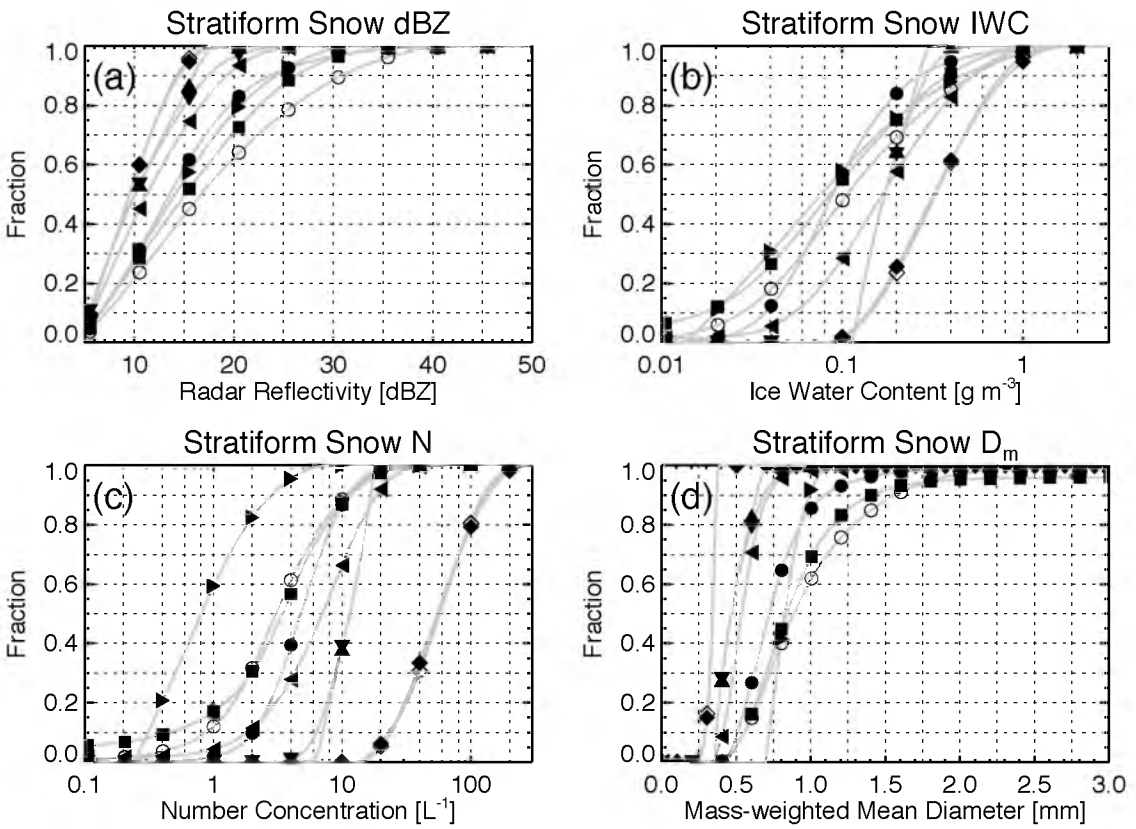

Figure 3.19. Normalized cumulative distributions of simulated stratiform snow (a) radar reflectivity, (b) water content, (c) number concentration, and (d) mass-weighted mean diameter for the six-day active monsoon period. Results only include grid points at which the snow radar reflectivity is at least 5 dBZ and the temperature is less than 0°C. Symbols are defined in Table 2.1.

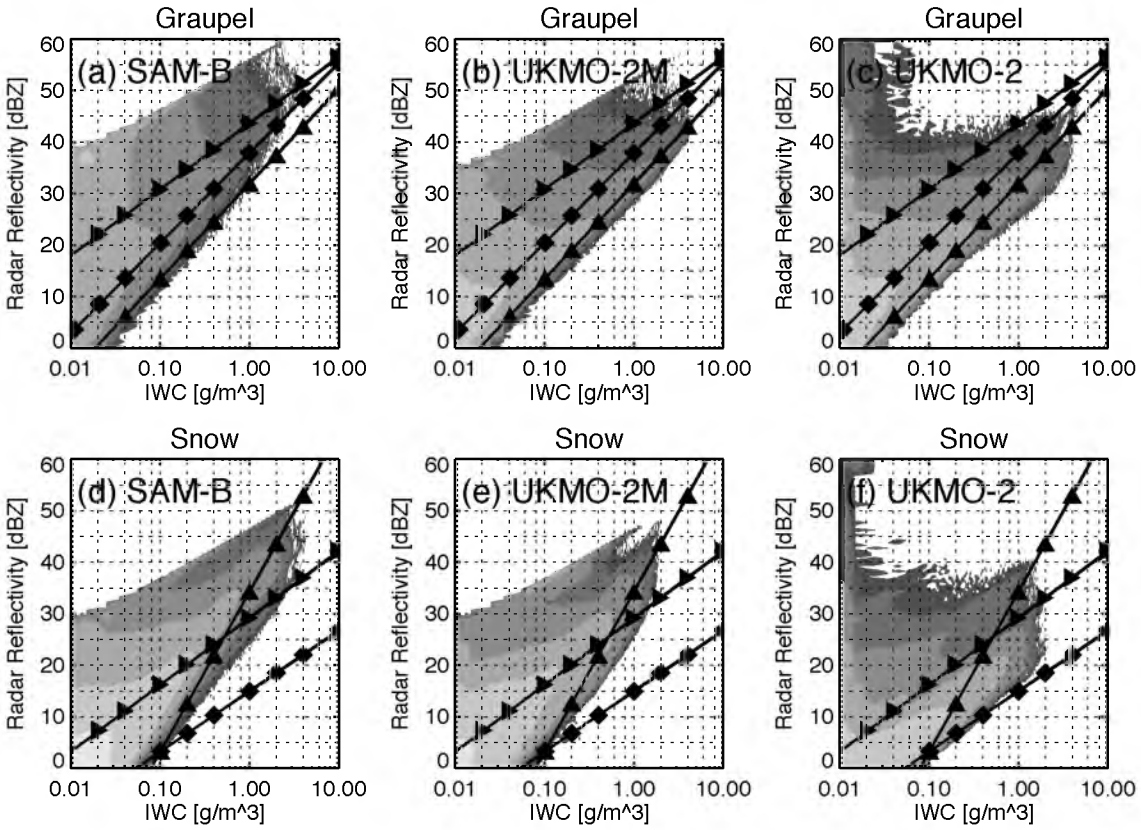

Figure 3.20. CRM simulated radar reflectivity as a function of water content: (a) for hail; (b) and (c) for graupel; and (d), (e), and (f) for snow. The diamond represents the microphysics scheme used in DHARMA-B and DHARMA-S; the right pointing triangle represents the scheme used in UKMO-1; and the up pointing triangle represents the scheme used in MESONH-1 and MESONH-2. The shading in (a) and (d) is from SAM-B results with each shading increasing by an order of magnitude starting with 1 to 10 samples per bin for the darkest shading increasing to 100,000 or more samples per bin for the brightest shading in (d) and (e); shading in (b) and (e) is from UKMO-2M results; and shading in (c) and (f) is from UKMO-2. Samples are taken from the six-day active monsoon period with three-hourly output.

CHAPTER 4

CONVECTIVE DRAFT PROPERTIES

4.1 Overview

Several recent studies attribute the high biases in convective radar reflectivity aloft discussed in Chapter 3 to poorly represented ice processes in bulk microphysics schemes. This has not been authoritatively linked to differences in observed and simulated convective strength in past studies because few comparisons exist with observationally retrieved vertical velocities. This chapter aims to go beyond the point at which many previous studies stopped to find the dynamical and microphysical reasons for the high bias in convective radar reflectivity aloft through extensive comparison of simulated and observationally retrieved convective updraft properties.

4.2 Updraft Definition

For simulation output and dual-Doppler retrieval output, which are both on three-dimensional spatial grids with ~1-km horizontal grid spacing, convective updrafts are defined three-dimensionally in space every 10 minutes between 1310Z and 1750Z on January 23 by connecting contiguous grid points at which vertical velocity at least 1 m s^{-1}. This vertical velocity threshold follows the one used for updraft cores in LeMone and Zipser (1980), although that study based on aircraft data during the GATE field program

over the tropical Atlantic west of Africa resolved smaller diameter (~500-m) updrafts along a one-dimensional aircraft trajectory than are possible given the ~1-km horizontal grid spacing in the TWP-ICE simulations. The 1310Z to 1750Z period on January 23 covers the available dual-Doppler retrieval data and the peak of the event near the CPOL radar. Using the vertical profile of convective radar reflectivity as a proxy for convective updraft vertical velocity magnitude as discussed in Zipser and Lutz (1994), Figure 4.1 shows that the vertical profile of convective radar reflectivity during this period in the dual-Doppler lobes is representative of both the dual-Doppler lobes for the entire event and the entire CPOL domain. The 50^{th}, 90^{th}, and 99^{th} percentiles of convective radar reflectivity nearly overlap for all periods and domains.

As discussed in Chapter 2, Lang et al. (2007) modeled Amazonian deep convection and compared simulated vertical velocities with dual-Doppler retrievals concluding that maximum upward vertical velocity values were similar in the simulations and retrievals. Often, a contoured frequency by altitude (CFAD) figure that incorporates all grid points is shown to justify this conclusion, but the use of such a figure is a misapplication of the dual-Doppler retrieval, which is only applicable for deep convective drafts when three-dimensional scanning C-band or S-band radars are used because of the errors involved in such an analysis. Collis et al. (2013, accepted) show that relative to vertical profiler retrievals of vertical velocity in convective cells that moved over the profilers and through the dual-Doppler lobes, the dual-Doppler analysis used in this chapter has a root mean square error of 1.9 m s^{-1} and a negative bias of 2.2 m s^{-1}. This means that typical oceanic draft vertical velocity magnitudes are similar to dual-Doppler retrieved vertical velocity errors. The three-dimensional updraft definition allows for

selection of updrafts by size, such as deep updrafts that begin in the boundary layer below 1 km and end near the tropopause above 15 km. Only considering these deep updrafts removes most of the three-dimensional dual-Doppler domain including most updrafts, which are usually smaller in size and have lesser peak vertical velocities than the deep updrafts, from consideration of comparison with model output. Most figures that follow in this chapter will only consider this subset of 'deep' three-dimensional updrafts that begin below 1 km and extend to above 15 km. This is justified not only on the grounds of appropriate comparison of observational retrievals and model output, but on the grounds that this subset accounts for anywhere from 75 to 90 percent of the total convective updraft mass flux at mid and upper levels in the dual-Doppler retrieval and CRM simulations for the 1310Z to 1750Z period, as shown in Figure 4.2.

4.3 Deep Updraft Radar Reflectivity, Vertical Velocity, and Size

Direct measurement of deep convective updraft vertical velocity is rare due to obvious safety concerns with aircraft penetrating cores. Although comparisons to previous field studies will be made later in the chapter, no observations near convective cores exist for TWP-ICE. Thus, it is necessary to resort to dual-Doppler retrievals for comparison to simulated drafts.

For both simulated and dual-Doppler retrieved 'deep' three-dimensional updrafts as were defined in Section 4.2, the 50^{th} percentiles of average vertical velocity, maximum vertical velocity, average radar reflectivity, maximum reflectivity, area, and samples as a function of height are compared in Figure 4.3. In this comparison, 1-km horizontal resolution radar reflectivity, which is available for the dual-Doppler lobes close to the

CPOL radar, is used rather than the 2.5-km horizontal resolution radar reflectivity available for the entire CPOL domain. Most simulations produce similar median updraft sizes with the exceptions of DHARMA-2M (x's) and SAM-B (filled circles), which are larger at midlevels. Normalized cumulative distributions of updraft size (not shown) show that the SAM-B updrafts are consistently larger than other CRM simulated updrafts. These two simulations also have the least updraft samples to balance the larger updraft sizes. It is unclear why the updrafts tend to be larger in these two simulations. However, it may be related to the unique prognostic cloud water number concentration schemes used or differences in diffusion. For DHARMA-2M, a slow down in updraft speed around 4 km is causing detrainment that could be increasing the size of updrafts in that simulation. This slow down is discussed later in the chapter. Interestingly, SAM-S (open circles) does not have the large updrafts that SAM-B does with the only difference being the tropospheric thermodynamic nudging, so the model forcing could be interacting with the specific SAM setup to yield larger updrafts.

There is a clear separation of dual-Doppler retrieved vertical velocity represented by the black line and simulated vertical velocity represented by symbols. At the melting level, simulations show maximum vertical velocity values between 10 and 17 m s^{-1}, which is faster than all simulated mass-weighted rain mass mixing ratio fall speeds, meaning rain in these cores is lifted above the melting level if not advected out of the core. Dual-Doppler retrievals, however, show maximum vertical velocity values at the melting level of approximately 8 m s^{-1}. Taking the approximate ~2 m s^{-1} dual-Doppler retrieval negative bias listed in Collis et al. (2013, accepted) into account yields a 10 m s^{-1} maximum vertical velocity value, similar to values in the DHARMA-2M simulation, but

still less than other simulations. As will be discussed in Section 4.4, the smaller peak vertical velocity values in DHARMA-2M than other simulations are due to the unique representation of aerosols in that simulation. Interestingly, the median value of maximum reflectivity at 5 km also matches in DHARMA-2M and observationally retrieved updrafts, but other simulations yield significantly higher maximum reflectivities at this height, which could be due to raindrops that are larger in simulations than in reality or more liquid water content in simulations than in reality. Without observations, it is impossible to know the exact reason for this reflectivity difference, but this issue is explored more in later sections. Maximum vertical velocity differences are larger in the upper troposphere where each simulation's maximum vertical velocity peaks between 21 and 28 m s^{-1} but dual-Doppler retrieved maximum values peak just short of 12 m s^{-1}. Slightly lower horizontal resolution of the dual-Doppler analysis, cutting off of some updrafts at dual-Doppler lobe boundaries, and other assumptions listed in Section 2.5.2 may contribute to a portion of the vertical velocity difference between the retrieval and simulations, but adding the RMSE and bias listed in Collis et al. (2013, accepted) yields only 4 m s^{-1}, so much of these differences are very likely real in the upper troposphere.

The large separation between simulations and observations is also seen in average and maximum radar reflectivity aloft. The median of maximum reflectivity at 10 km is 30 dBZ in observations, but ranges from 37 to 49 dBZ in the simulations. Most simulations also show increasing average reflectivity and constant maximum reflectivity with increasing height below the melting level at ~4.7 km, whereas observations show decreasing average and maximum reflectivity with height. This may be a function of rain that is not efficiently falling out of the simulated deep updrafts, whereas large raindrops

are falling out of observed deep updrafts, which lends credence to low and midlevel updrafts being stronger in simulations than in observations. Despite similar vertical velocity profiles in all simulations, there is considerable spread in radar reflectivity aloft, which is due to different assumptions in the microphysics schemes as discussed in Chapter 3.

Interestingly, the 90th percentile of CRM deep updraft properties in Figure 4.4 yields a much different result than the 50th percentile. Maximum vertical velocity between the surface and 10 km is now similar in dual-Doppler retrievals and simulations with values between 15 and 20 m s^{-1} at the melting level. Above 10 km, however, the dual-Doppler retrieval and simulations still diverge with simulations showing substantially stronger updrafts. While there are still the same differences in average radar reflectivity as seen in the 50th percentile, the observed maximum radar reflectivity profile is now a little closer to the simulated profiles. It is worth noting that the only six observationally derived deep updrafts have values greater than or equal to the 90th percentile, whereas two to three times as many samples exist at percentiles greater than 90 percent in the simulations. Therefore, the median profiles are likely better represented than the 90th percentile. The 90th percentile of maximum reflectivity at 10 km is 37 dBZ in observations and ranges from 40 to 50 dBZ in the simulations. The value not only remains more constant with height below 5 km, but also parallels the UKMO-2 simulation (left pointing triangle) aloft as in Figure 4.4, which uses two-moment graupel with $\mu = 2.5$ instead of 0 as is used in other two-moment schemes. This lowers the graupel radar reflectivity by reducing the number of large graupel particles through narrowing of the size distribution, but the prediction of number concentration is very

important. UKMO-1 (right pointing triangle) with one-moment graupel and $\mu = 2.5$ nearly produces the highest reflectivity aloft. Radar reflectivity aloft for all simulations is still higher than observed and a significant spread exists between 5 and 10 km despite a spread in updraft vertical velocities that would not suggest such large differences in radar reflectivity. Two-moment schemes outperform one-moment schemes in general due their ability to increase number concentration to offset large ice water contents that will be discussed in the next section. MESONH actually produces the lowest reflectivities between 6 and 9 km because of its unique *m-D* relationships for snow and graupel in a one-moment scheme that prevents very high reflectivities from being possible, but the gradient in radar reflectivity with height is completely wrong aloft, something common to one-moment schemes.

Figure 4.5 shows that LAMs also show a significant high bias in reflectivity with all four simulations producing median values of maximum reflectivity over 40 dBZ at a 10 km altitude. The very large reflectivities in WRF-T (squares) between 5 and 8 km are due to the very large graupel particles there, as mentioned in Chapters 2 and 3. All LAMs also produce median values of maximum vertical velocity greater than 10 m s^{-1} at the melting level, but values aloft are less than in the CRMs, peaking between 15 and 20 m s^{-1}. Average vertical velocities are also lower in LAMs than in CRMs, although updraft sizes and number of samples are comparable. The unique simulation is WRF-W (triangles), which has smaller and weaker updrafts than other simulations have, which will be discussed later in the chapter. As is shown in the Figure 3.7 time series, WRF-M2 exhibits a double peak in convective precipitation while the other WRF simulations exhibit a near constant high amount of convective precipitation between 12Z on January

23 and 6Z and January 24 rather than the single peak evident in observations and CRM simulations. Thus, some of the difference in median deep updraft properties may be related to offsets in location and timing of the event relative to observations and the CRM simulations, especially considering that simulated statistics are limited to the CPOL domain and the ECMWF forcing is biased, as will be discussed in Chapter 5.

The 90^{th} percentiles of maximum radar reflectivity in LAMs shown in Figure 4.6 are substantially higher than observed, as was the case for the 50^{th} percentiles. In all but the WRF-W simulation, midlevel maximum vertical velocity in the LAMs exceeds 20 m s^{-1}, higher than they reach in the CRMs. In the upper troposphere, all but the WRF-W simulation (triangles) have peak vertical velocities between 34 and 40 m s^{-1}, which fall within the distribution of CRM values. A possible reason for lower vertical velocities in WRF-W than in other simulations is that it has a much drier upper troposphere, as is shown in Figure 5.28 in Chapter 5. It also has a different condensate profile in updrafts, as will be discussed in the next section. Despite the WRF-W outlier, it is clear that similar biases exist in both CRMs and LAMs, although greater variability is seen in LAMs.

4.4 Deep Updraft Hydrometeor Properties

Examination of hydrometeor mass mixing ratios in Figure 4.7 shows important differences between simulations due to the microphysics scheme used. Cloud water mixing ratios, for example, are strongly dependent on the representation of aerosols. For two-moment representations of cloud water, idealized aerosol number concentration profiles for three different size modes were used that were based on active monsoon

observations from the ACTIVE field campaign (Vaughan et al. 2008; Fridlind et al. 2010), which overlapped TWP-ICE and was also based in Darwin, Australia. The unique scheme in DHARMA-2M (x's) leads to significant differences from the other two-moment cloud water schemes that do not include consumption of aerosols. DHARMA-2M produces the least cloud water with the median of the maximum mixing ratio around 1 g kg^{-1} at midlevels, whereas the other simulations with two-moment schemes have values around 3 g kg^{-1}, the highest of all simulations. There are also important differences between one-moment and two-moment schemes. For average cloud water mixing ratios (not shown), all two-moment schemes have less cloud water than all one-moment schemes except in the upper troposphere. One-moment schemes use a constant cloud water number concentration without consideration of cloud condensation nuclei (CCN). Significant cloud water mixing ratios exist up to the homogeneous freezing level, which is not all that surprising given the high simulated vertical velocity magnitudes, but such high liquid water mixing ratios are rarely if at all observed in tropical oceanic deep convection at temperatures colder than -20°C (Stith et al. 2004; Stith et al. 2006; Heymsfield et al. 2009). This may further indicate that simulated updrafts could be too strong, although the deep convection observed in this case is likely stronger than in these other tropical field campaigns. Without in situ observations, it is difficult to judge the amount of cloud water that is expected at the homogeneous freezing level. Lawson et al. (2010) showed that homogeneous freezing of cloud water was a source for ice particles at 11 km ($T = -47°C$) in an intense convective cell off of the Central American coast during the Tropical Chemistry, Cloud, and Climate Coupling (TC4) field campaign. That cell also contained substantial amounts of 1-mm diameter

graupel, so there are intense cells over the ocean near coastlines that appear to homogeneously freeze cloud water droplets.

Precipitation-sized hydrometeors, including graupel/hail, snow, and rain, are less affected by representation of cloud water than by size distribution assumptions, with an exception being the effect on rain of including a more complex cloud droplet nucleation scheme that accounts for aerosol consumption in DHARMA-2M. Between 3 and 8 km altitudes, DHARMA-2M shown with x's in Figure 4.3 is closer to observationally retrieved vertical velocity values than other simulations. In a low cloud condensation nuclei (CCN) 'clean' environment such as this case, most CCN are consumed and rain quickly forms in convective updrafts. With minimal entrainment, this leads to very high supersaturations with respect to liquid water in the DHARMA-2M simulation, sometimes greater than 30 percent, in the CCN-free and cloud water free updraft core, which limits condensational heating and weakens the maximum updraft vertical velocity (x's) in Figures 4.3 and 4.4. Note, however, that the updraft vertical velocity recovers to match other simulations in the upper troposphere due to a significant amount of water still being available for latent heat release through freezing. This is also the likely reason for the agreement in maximum reflectivity at low and midlevels between DHARMA-2M (x's) and observations in Figure 4.3. The SAM simulations, unique in their use of hail instead of graupel for representation of rimed ice, have the lowest rimed ice mixing ratios and highest snow mixing ratios aloft. This is not all that surprising because hail mass fall speeds are often more than twice those of graupel. The slow mass fall speed of graupel (2–4 m s^{-1}) is important because it means a large amount of graupel gets lofted high into the upper troposphere in deep, strong convective updrafts and advected over large areas,

producing larger than observed regions of radar reflectivity of 40 dBZ or greater identified as convective in the Steiner et al. (1995) algorithm. Interestingly, this leads to median convective rain rates in all but the UKMO-1 and UKMO-2 simulations that are less than those observed despite higher maximum convective rain rates, as shown in Varble et al. (2011). Of the schemes using graupel, the lowest graupel mixing ratios and highest snow mixing ratios are in the UKMO-1 and UKMO-2 simulations that use a gamma size distribution shape parameter of 2.5 rather than 0. Of these two simulations, the two-moment UKMO-2 simulation produces more graupel and less snow than the one-moment UKMO-1, but produces convective radar reflectivity aloft much closer to observations because the size of graupel in UKMO-2 is much smaller due to predicted higher number concentrations.

Median values of maximum rain mixing ratio peak between 5.5 and 10 g kg^{-1} just below the melting level for all simulations, showing that a significant portion of rain is not falling out of deep convective updraft cores before reaching temperatures where raindrops begin freezing. This is consistent with an increase in maximum radar reflectivity with height in modeled deep convective updrafts, as was shown in Figures 4.3 and 4.5. Furthermore, the 90^{th} percentile of maximum mass mixing ratios in Figure 4.8a reaches 9 to 12 g kg^{-1} in all but one simulation at 3 km, indicating little mixing with the environment. Such high water contents in cores stronger than 10 m s^{-1} leads to very large ice mixing ratios aloft, peaking from 9.5 to 12 g kg^{-1} in the median profiles in Figure 4.7 and 11 to 14 g kg^{-1} in the 90^{th} percentile in Figure 4.8a. It is interesting to note that the highest maximum condensate mixing ratios are produced in the sensitivity simulations in which the thermodynamic profile is nudged toward the forcing profile. As will be

discussed later in the chapter, this nudging produces a higher CAPE in the sensitivity simulations, which may be linked to the higher convective condensate values. The 90th percentile of condensate mixing ratios in WRF-W agrees well with those in the CRM simulations, although they drop off faster above 10 km, perhaps due to the smaller and weaker updrafts in WRF-W. WRF-M and WRF-M2 produce even larger 90th percentile peak condensate mixing ratios than those in the CRM simulations of 14-16 g kg^{-1} at 5 km and 16-17 g kg^{-1} at 12 km. WRF-T is the only simulation that doesn't have a relative minimum between 6 and 7 km that is produced by different fall speeds between rain and precipitation sized ice. This is due to the unique graupel formulation in the Thompson scheme, as discussed in the next paragraph.

Shown in Figure 4.9, median values of maximum liquid mass mixing ratio vary from 6 to 9 g kg^{-1} in the LAM simulations and occur just below the melting level, which is similar to the CRM results. Significant amounts of cloud water in all but the WRF-W run exist up to 8-10 km altitudes, also similar to many of the CRM runs. Median values of maximum ice mass maxing ratios peak between 6 to 10 g kg^{-1} aloft, and are lower in the WRF-W and WRF-T runs than in any CRM simulations. For WRF-W, this is consistent with its lower vertical velocities that may be related to a dry bias aloft, as will be discussed later in this chapter. For WRF-T, the Thompson scheme uses a variable size intercept for graupel that produces very large graupel sizes when mass mixing ratios are high to mimic the transition to hail, and a graupel fall speed relationship based on Heymsfield and Kajikawa (1987) that produces higher fall speeds than the relationship used in the Morrison scheme that is based on Ferrier et al. (1995) (see Figure 2.3). This produces large fall speeds for graupel, especially when mass mixing ratios are high,

producing a convergence in condensate mass at 5–6 km that further increases graupel sizes and prevents large graupel amounts from being lofted high into the troposphere.

The aforementioned intense convective cell in Lawson et al. (2010), penetrated at an 11-km altitude and having a peak updraft vertical velocity of 20 m s^{-1}, had a peak IWC of 2.4 g m^{-3}, which is one of the largest published values for tropical oceanic convection. This is but one sample, but considering the lack of higher values in peer-reviewed literature, the similar tropical coastal environment and maximum updraft vertical velocity magnitude as the median simulated values of maximum updraft vertical velocity make it a worthwhile case for comparison. Despite the similar peak updraft vertical velocity, the peak IWC in Lawson et al. (2010), also presumably measured at a finer resolution than the model resolutions, is significantly less than the median value of peak CRM simulated IWC at that altitude, which varies from 3.5–4.3 g m^{-3} in Figure 4.10a. Figure 4.10b shows that median peak IWC in WRF-M (diamonds) and WRF-M2 (dashed line) fall in line with the CRM simulations, whereas WRF-W (triangles) and WRF-T (squares) have lesser peak IWCs aloft, matching the Lawson et al. (2010) value of 2.4 g m^{-3} at 11 km. For WRF-W, this is consistent with lower peak water contents at low and midlevels, which could be related to smaller updraft sizes and easier fall out of rain. For WRF-T, this is consistent with high fall speeds for large graupel that allows most graupel to fall out of the updraft by 11 km, as shown in Figure 4.9. Figure 4.10 also shows that median peak IWCs occur around 8–9 km in altitude in all simulations except for WRF-T, which has peak water contents continuously dropping off from midlevels upward. By 15 km, peak IWCs are half of their values at 8–9 km, so substantial amounts of ice are falling out of the updrafts, but not at a fast enough rate to substantially affect buoyancy reduction

due to water loading because mixing ratios shown in Figures 4.7–4.9 remain high between 8-km and 15-km altitudes. Figure 4.10 also shows that while liquid mixing ratios peak just below the melting level, peak LWCs peak between 3-km and 4-km altitudes showing that some rain is falling out of the updraft cores before reaching the melting level, but not enough to dramatically bring down the amount of rain being lofted.

Interestingly, the 90th percentile of peak water contents shown in Figure 4.11b shows extremely high water contents in the WRF-T simulation at midlevels, which are due to the high graupel fall speeds leading to an accumulation of condensate between 4 and 6 km. The x-axis of Figure 4.11 only goes to 12 g m^{-3}, but the 90th percentile peak value in WRF-T is 17 g m^{-3} with the 99th percentile going to 25 g m^{-3}! This may be the cause of the decrease in 90th percentile maximum vertical velocity between 3 and 8 km in Figure 4.6 that does not appear in other simulations. Note that despite these huge water contents, the peak water contents in the upper troposphere are not significantly higher in WRF-T, likely because these high water contents are not being frozen instantaneously, but are accumulating over time. WRF-W, which had amongst the lowest water contents in the 50th percentile, now falls in line with the CRM simulations that yield anywhere from 4 to 5.5 g m^{-3} at 11 km in the 90th percentile, approximately twice the IWC reported in Lawson et al. (2010). Meanwhile, WRF-M and WRF-M2 have the highest water contents aloft, producing 6 g m^{-3} at 11 km. At low levels, maximum water contents tend to peak at higher altitudes with values of about 7–11 g m^{-3}, except in the case of WRF-T, which is much higher as already discussed.

4.5 Downdrafts and Cold Pools

Convective downdrafts, like updrafts, were identified with a threshold vertical velocity of -1 m s^{-1}, but the dual-Doppler data show strong convective downdrafts at low and midlevels that are untrustworthy based on comparison with previous literature showing in situ (e.g., Lucas et al. 1994) and remotely sensed (e.g., May and Rajopadhyaya 1999; Uma and Rao 2008) vertical velocity in tropical convective downdrafts within moist environments. In fact, simulated downdraft vertical velocities fall in line with tropical oceanic and coastal values in previous literature. Furthermore, the 2.2 m s^{-1} dual-Doppler retrieval bias and 1.9 m s^{-1} RMSE are similar in magnitude to the typical average convective downdraft speed. Thus, analysis is limited to model comparisons. Figure 4.12 shows that downdraft vertical velocity at a 1-km altitude varies much more than updraft vertical velocity, with the strongest downdraft values greater than 5 m s^{-1} in the SAM simulations (circles) and weakest downdraft values in the DHARMA-2M (x's) simulation. This is likely due to a combination of differences in dense ice representation and rain water contents. The SAM simulations use hail, which falls out faster than graupel. This acts to concentrate hydrometeor mass into a smaller area that can increase water loading and lower the height level to which the melting of dense ice extends. Thus, SAM simulations have the strongest convective downdrafts. This is consistent with previous mid-latitude continental studies that found colder cold pools when hail was used rather than graupel (Gilmore et al. 2004; Morrison and Milbrandt 2011; Van Weverberg et al. 2012). UKMO-1 (right pointing triangle) also has relatively strong downdrafts, likely due to greater amounts of large graupel produced in that simulation relative to other CRM simulations using graupel. Higher rain water

content, some of which detrains at midlevels, also increases convective downdraft strength through water loading and not surprisingly, DHARMA-2M has the lowest rain water content and weakest convective downdrafts. These results are consistent with those found in Mrowiec et al. (2012) that compared DHARMA-2M to SAM-B and DHARMA-B. Vertical velocity PDFs at 1 km in WRF-W, WRF-M, and WRF-M2 are very similar with convective drafts that tend to be slightly stronger than in CRM simulations. WRF-T has the strongest downdrafts, consistent with large fast-falling graupel in the Thompson scheme that was discussed in the last section.

Convective downdrafts bring lower moist static energy air from midlevels down into the boundary layer, which forms cold pools that locally limit surface-based instability but force convergence on their spreading boundaries, which can produce new convective updrafts. Low-level horizontal cross-sections in the boundary layer (not shown) support the results of Del Genio et al. (2012) that new updraft formation during this active monsoon period occurs on cold pool outflow boundaries, but above the boundary layer, updrafts are more isolated and driven by deeper layer forcing. As will be shown later in the chapter, most cold pool boundaries that are convergent at a 50-m altitude are already divergent or no longer strongly convergent at a 550-m altitude because most cold pools were shallow. Regions of deeper layer updraft forcing can result from dynamically produced midlevel negative pressure perturbations (e.g., Rotunno and Klemp 1984) and localized regions of deeper cold pools produced by merging cold pools, situations in which the cold pool and vertical wind shear interactions are maximized (e.g., Rotunno et al. 1988), and probably other conditions relating to the time history of convective downdraft strength and location associated with any given convective cell.

Sections 4.6.2 and 4.6.3 discuss the relative importance of simulated cold pool and convective updraft interactions with vertical wind shear in a bit more detail. Any differences that do exist in simulated cold pools do not appear to substantially affect deep convective updraft vertical velocity, which is distributed similarly in all simulations at low levels in Figure 4.11 and in most simulations at midlevels in the statistics shown in Sections 4.3 and 4.4.

4.6 Production Mechanisms for Strong Updrafts

4.6.1 Entrainment

Simulated deep convective updrafts that are much stronger, especially in the upper troposphere, than those in dual-Doppler retrievals coupled with the large simulated water contents aloft beg the question of how such conditions are produced in the simulations. Figure 4.13 shows example vertical cross sections through strong deep convective updrafts in four of the CRM simulations, one for each dynamical core used. Moist static energy (MSE), which is color filled, remains almost constant with height in the updraft cores signified by the thick black vertical velocity contours meaning little entrainment of environmental air is occurring in the core of the updrafts. Moist static energy with units of Kelvin is defined in equation 4.1:

$$MSE = T + \frac{gz}{c_p} + 1 \times 10^6 (2.501 - 0.00237 T_c) \frac{q_v}{c_p}, \tag{4.1}$$

where T is temperature in Kelvin, g is gravity, z is height, c_p is the specific heat capacity of air at constant pressure, T_c is the temperature in Celsius, and q_v is the water vapor

mixing ratio. Shown in Figure 4.14, the 50th to 90th percentiles of maximum MSE in deep convective updraft cores for each of the four dynamical cores decrease by 0 to 3 K from the boundary layer to 5 km whereas the environment drops off by 10 to 13 K. Neglecting the effects of ice, undiluted parcel ascent would be characterized by constant MSE with height, but some studies insist that this is rare in tropical oceanic environments because of parcel mixing with the low and midlevel environmental air where MSE quickly decreases to a minimum (e.g., Zipser 2003; Romps and Kuang 2010).

In TOGA-COARE observations, for example, Wei et al. (1998) concluded that entrainment reduced convective updraft buoyancy by 2 K while water loading reduced it by 0.5 K at 700 mb. This differs from the simulations in which buoyancy reduction by water loading is equal to or greater than that by entrainment. Large eddy simulations (LES) of a TRMM LBA case over the Amazon (Khairoutdinov and Randall 2006) with horizontal grid spacing of 100 m and vertical grid spacing of 50–100 m, show that tropical deep convective updraft MSE in those environments typically drops off substantially in the low and mid troposphere due to mixing with the environment. However, updrafts still reach the tropopause because latent heat release due to freezing increases the moist static energy at upper levels, as discussed in Zipser (2003) and Fierro et al. (2009). While the TRMM LBA LES case does not have deep convection as strong as seen in this TWP-ICE MCS case, the differences in their updraft core MSE and the updraft core MSE in this case are substantial, which deserves further investigation.

The TWP-ICE CRM simulations clearly have some updraft cores that are not mixing much with the environment at low and midlevels, which may be leading to some of the microphysics problems aloft. This is supported by the very large liquid water

contents in strong deep convective cores shown in Figures 4.10 and 4.11, high supersaturations in DHARMA-2M due to consumption of all available CCN, and very large peaks in vertical velocity aloft due to large amounts of freezing condensate. Of course, MSE at midlevels is not only a function of midlevel entrainment, but also of boundary layer mixing that determines the initial thermodynamics of the air being lifted. Petch et al. (2002) recommend horizontal grid spacing of at least a quarter of the depth of the surface to cloud base to properly represent boundary layer mixing. For this case, that would be on the order of 100 m. Insufficient representation of boundary layer mixing could be another issue contributing to improper convective strength, but this is difficult to analyze without observations.

As in the CRMs, the median value of maximum deep convective updraft MSE in LAMs shown in Figure 4.15 only drops off by a few Kelvin between the surface and 5 km, while remaining fairly constant above 5 km, whereas the environment significantly drops off between the surface and 5 km. The 90^{th} percentile even increases by a few Kelvin just above the melting level in all but WRF-W in 4.15a due to the latent heat release from large amounts of freezing. This difference in WRF-W is consistent with its weaker and smaller updrafts with generally lesser rain shown in Figures 4.5, 4.6, and 4.9 through 4.11.

Bryan et al. (2003) and Craig and Dörnbrack (2008) concluded that 1 km was insufficient to resolve buoyancy in convective clouds that they simulated. A recent modeling study of a mid-latitude continental squall line by Bryan and Morrison (2012) also showed large sensitivity to horizontal resolutions between 1 km and 250 m due to greater large eddy entrainment and cloud water evaporation in the higher resolution

simulation, but that was in a different large-scale environment that was notably drier. Unfortunately, no TWP-ICE observations directly related to convective entrainment exist, and thus, this theory of too little dilution remains speculative. Preliminary results from a quarter domain (88 km by 88 km size) DHARMA-2M simulation using ~100 m horizontal resolution and 192 vertical levels shows that increased resolution does cause greater entrainment at low and midlevels, which increases the transition time from shallow to deep convection as found in Khairoutdinov and Randall (2006). Despite this, bubble-like cores of shedding thermals in the high resolution simulation that are not resolved by the ~900-m grid spaced simulations remain nearly undiluted and are collectively able to still transport very high amounts of condensed water aloft while reaching similarly high vertical velocities as in the ~900-m run, albeit on a smaller scale. It appears that these smaller shedding thermals achieve this by detraining at midlevels so that regions of rising motion, ~10 km across and with vertical velocities of 1–5 m s^{-1}, are generated with new updrafts 1–2 km across with vertical velocities of 10–20 m s^{-1} forming and thriving in the broader region of rising motion with higher MSE than the free atmosphere at midlevels. This is consistent with LES findings by Zhao and Austin (2005) and Heus et al. (2009) for deepening shallow cumulus, but of course this case involves deep convection in a much more unstable environment. Even in the so-called "giga-LES" simulation of idealized mean GATE phase III conditions (1300 J kg^{-1} of convective available potential energy (CAPE) and less shear than this case), which had 100-m horizontal grid spacing and 256 vertical levels, the 99th percentile of convective updraft vertical velocities reaches 20–30 m s^{-1} in the upper troposphere (Khairoutdinov et al. 2009), but there are no observations in the upper troposphere to verify whether such

values are realistic in that type of environment. These top updrafts are also associated with less condensate than this TWP-ICE case, but with the maximum updraft speeds, are consistent with the intense cell encountered in TC4 described in Lawson et al. (2010) and detailed in Section 4.4.

4.6.2 Large-scale Environment

Further complicating comparison of this case with other tropical cases is the unique large-scale environment. While the thermodynamic profile derived from observed soundings for this MCS suggests a tropical oceanic environment with very low cloud base of a few hundred meters and high relative humidity throughout the troposphere, there is substantial convective available potential energy (CAPE) and moderate vertical shear present between 0 and 3 km, which is more typical of break period continental squall lines (Keenan and Carbone 1992). Indeed, this MCS does eventually form a potent squall line after a substantial period of widespread isolated convective cells. The 0–3 km and 0–6 km vertical wind shear in the variational analysis sounding during the beginning of this event is moderate (10–15 m s^{-1}) with domain median bulk Richardson (BRN) shear of over 50 m^2 s^{-2} shown in Figures 4.16 and 4.17 and an anticyclonic rotated hodograph (not shown) favorable in the southern hemisphere for supercells based on values shown in Thompson et al. (2003) when given sufficient instability.

Domain median surface-based CAPE values of over 2000 J kg^{-1} occur early in the event in CRM and LAM simulations as shown in Figures 4.16 and 4.17, while maximum grid point values reach 4000 J kg^{-1} in some simulations showing plenty of instability is

present. Dividing these CAPE values by the bulk Richardson shear values yields the commonly used bulk Richardson number, but bulk Richardson numbers suitable for supercellular convection based on Thompson et al. (2003) can be found for low CAPE and low shear situations not conducive to supercell, and therefore, it is better to separately analyze the CAPE and bulk Richardson shear. These instability and vertical shear parameters calculated from the variational analysis sounding also fit in well with typical values found in mid-latitude continental supercell convection (Thompson et al. 2003).

It is unclear, however, how well the variability of these environmental parameters is captured in the simulations, which could be contributing to overly intense convection. The variational analysis used to force the CRMs gives domain mean quantities, when in reality some portion of the domain could have higher vertical shear in magnitude or direction and another portion could have higher CAPE at any given time. This is not to say that the CRM simulations perfectly follow the forcing. Figure 4.16 shows that the forcing sounding has higher median CAPE than baseline simulations early in the event and all simulations late in the event with median BRN shear that exceeds all simulations, although the downward trend in both quantities is visible in the forcing and simulations. Figure 4.16 also shows that the sensitivity simulations have higher CAPE at the beginning of the event, which is due to MSE drift (discussed in Fridlind et al. (2012)) that is higher at low levels than upper levels in the baseline simulations. This higher CAPE is the likely reason for slightly stronger convection in the sensitivity simulations.

LAM simulations, on the other hand, almost perfectly follow the ECMWF time series of surface-based CAPE shown in Figure 4.17. The BRN shear, however, is

substantially higher than in the ECMWF analysis and slightly exceeding that in the CRM simulations, but exhibiting the same downward trend with time. It is worth noting the high sensitivity of these convective environmental parameters to slight changes in wind or MSE. The difference between a BRN shear favorable for supercells (50 m^2 s^{-2}) and one not favorable for supercells (25 m^2 s^{-2}) is 3 m s^{-1} in the difference between the air density weighted mean 0–6 km wind and the air density weighted mean 0–500 m wind. Similarly, a couple Kelvin decrease in MSE through cooling or drying in the boundary layer can significantly reduce surface-based CAPE, again putting convection into a different regime. Over warm sea surfaces, the boundary layer MSE is regulated by the competing effects of cooling and drying by convective downdrafts and warming and moistening by heat fluxes from the ocean to the atmosphere. It is unclear how well these processes are handled in CRMs and LAMs.

4.6.3 Convective Mode

It is clear that the representation of the large-scale environment in the simulations is suitable to spawn left and right moving cells in the DHARMA simulations with left movers displaying supercell characteristics shown in Figure 4.18 and thus being stronger and more long-lived than the right movers. Strong updraft forcing through 2–3 km results from a strong vertical pressure gradient produced by shear induced midlevel negative pressure perturbations of 1–2 hPa or greater, as discussed in Rotunno and Klemp (1984). This forcing is strong enough to accelerate the updraft to 10–15 m s^{-1} despite negative or neutral buoyancy due to large water loading in 4.18a–c. The lift in a negatively buoyant environment likely helps to limit low and midlevel entrainment,

especially in the upshear portion of the updraft, which, as discussed in several studies in the late 1960s and 1970s (Barnes 1969; Wilhelmson 1974; Ramond 1978; Heymsfield et al. 1978), is protected by midlevel positive pressure perturbations caused by the interaction of the easterly flow with the slower moving updraft. As shown in Figure 4.18d and 4.19c, this is the case in the simulations as well. Above the 3-km height level of the peak negative pressure perturbation, water loading slows the updraft in some cases and detrainment occurs. The rain that exits the updraft here is pushed downshear where it fuels a convective downdraft that increases the horizontal gradient in vertical velocity and further increases tilting and stretching of environmental horizontal vorticity. This is already enhanced in left mover updraft developing regions relative to right moving updraft developing regions, again due to dynamic interactions between the preexisting updrafts and the vertical shear. Figure 4.20b shows the extreme vertical shear induced by the left moving cell in the region of updraft formation to the west-southwest of the cell. As discussed in Rotunno and Klemp (1984), nonlinear shear interactions in this region produce the midlevel pressure perturbation that causes the leftward propagation of the cell. Although it is clear from Figure 4.19a–b that low-level convergence is organized by cold pools, they are secondary to the forcing caused by the shear-induced pressure perturbations for the left-moving cells, as mentioned in Rotunno and Klemp (1984). Lower pressure under these perturbations at low levels helps to induce greater inflow as well, shown by the relative wind vectors in 4.19a–b to the south and west of the left-moving cell.

Despite detrainment below the melting level, the updraft often remains strong enough to loft substantial condensate above the melting level, where rain quickly freezes

into graupel or hail, depending on the microphysics scheme used. Freezing of very large condensate contents provides an increase in temperature of ~2–4 K to the updraft through latent heating, which causes the large increase in thermal buoyancy in 4.18a and large peak in updraft speeds in the upper troposphere. The deep convective updraft core speeds in the mid and upper troposphere are easily strong enough to quickly loft graupel and snow into the upper troposphere, which allows advection of moderate to large water contents over large areas. When these large ice water contents melt, it produces high radar reflectivity identified as convective, which appears to be one reason for the high bias in simulated convective area and lower than observed mean convective rain rate in simulations. Interestingly, in these left movers, some of the rain that is detrained before reaching the melting level ends up in regions of new updraft formation, which could be another process by which large rain water contents are produced. All simulations have not been thoroughly checked for left and right movers and analysis is hindered by a lack of four-dimensional pressure fields for most CRM simulations, but strong updrafts that take advantage of the vertical shear and instability are present in all simulations as shown earlier in the deep updraft statistics. Similar strong left moving cells with associated large midlevel negative pressure perturbations, some larger than those in the DHARMA simulations, are produced in the WRF-M simulation (not shown), and therefore this is not a symptom of the model setup.

Figures 4.19 and 4.20 show example horizontal cross-sections that include a strong left-moving cell near $x = 55$ km and $y = 50$ km and a right-moving multicellular region near $x = 70$ km and $y = 105$ km. Updrafts are not highly correlated with regions of positive buoyancy at low and midlevels as shown in Figure 4.19e or surface-based

CAPE in Figure 4.20a because they are controlled by vertical pressure gradient forcing controlled by cold pools and interactions between updrafts and vertical shear. Figure 4.19d-e shows strong negative buoyancy and a positive pressure perturbation gradient at 1 km to the south of the multicellular cluster associated with a relatively deep cold pool. This cold pool is able to force convergence in Figure 4.19a–b over a depth greater than most cold pool edges. Two negative pressure perturbations lobes at 2.5 km are visible on the northwest side of two updraft lobes due to interaction with vertical shear, but these are small relative to the large negative perturbations created by the left-moving cell. Although the left-moving cell has a cold pool associated with it, the shear-induced midlevel pressure perturbation, not the cold pool, creates the peak pressure perturbation gradient force in Figure 4.19d to the south-southwest of the cell, whereas the cold pool is on the north-northwest side the cell. Comparing Figure 4.19c to 4.20b shows that the midlevel pressure perturbations are highly correlated with the BRN shear and this shear is related to the vertical vorticity shown in Figure 4.19f with left movers strongly cyclonically rotating and right movers anticyclonically rotating. This is also shown in the example vertical cross-sections through a left mover in Figure 4.18f and a right mover 4.21f.

Although not evident in Figure 4.21, the right moving updrafts are forced by a combination of dynamically produced pressure perturbations and cold pools. Approximately 3–4 km to the west of this the south-north vertical cross-section in Figure 4.21 is the midlevel negative pressure perturbation peaking at 2.5 km. The positive pressure perturbation at the surface in Figure 4.21d and the strong perturbation pressure gradient acceleration in Figure 4.21e at low levels is due to the cold pool. The primary

difference with left movers is that the nonhydrostatic pressure gradient force associated with the midlevel pressure perturbation is significantly stronger than it is for right movers. As the DHARMA simulations go on, instability and vertical shear decrease as shown in Figure 4.15, and cold pools begin to exert a larger control with cells moving more toward the north in broken lines (not shown). Despite being generally weaker than the left movers, these right movers still lift significant amounts of condensate above the melting level as evidenced by the water loading acceleration in Figure 4.21b with low and midlevel vertical velocities of 5–10 m s^{-1} combined with rain mass-weighted fall speeds of 4–8 m s^{-1}. This condensate freezes and fuels strong upper tropospheric vertical velocities of 30 m s^{-1} and greater in Figure 4.21a–c. Although not shown, right movers are not as undiluted as left movers, but they are still able to maintain small cores of fairly high MSE in many cases. They also likely have more detrainment to stratiform regions relative to left movers due to their more favorable updraft tilt, although this was not explored in depth.

As discussed in Chapter 3 and shown by Varble et al. (2011), microphysics assumptions surely create some convective precipitation structure issues. Differences based on dense ice and snow representation can produce substantially different reflectivity distributions, however the fact that all CRM and LAM configurations overestimate reflectivity and produce updraft statistics that differ from both dual-Doppler retrievals and previously published statistics suggests representation of convective dynamics needs to be further explored as a source for bias. This requires analysis of the representation of the large-scale environment, the subgrid scale turbulence, and the covariance of vertical velocity and condensate. Although entrainment tends to receive

more attention, proper observation and model representation of the size of convective updraft cores and variability of vertical velocity within them may be just as important. Aircraft observations of maritime tropical convection near Darwin during EMEX show half of updraft cores observed were 1 km in width or less at low and midlevels (Lucas et al. 1994). While these are aircraft transects, this indicates that many convective updraft cores may not be adequately resolved with a 1-km horizontal grid spaced model. In fact, as discussed previously, a quarter domain DHARMA-2M simulation with ~100-m horizontal grid spacing shows smaller congestus clouds with 1–2 km wide shedding thermals, although only slight reductions of peak vertical velocity and condensate aloft are found as nearly undiluted bubbles rise through broader ~10 km wide regions of rising motion generated through substantial congestus detrainment.

Without significantly improved convective and stratiform biases in the quarter domain LES simulation, sources other than horizontal resolution are likely involved in producing biases including the imposed large-scale model forcing, although poor representation of turbulence on the scale of meters to tens of meters could be an important source as well. Investigating these sources is beyond the scope of this study, but many small errors due to model forcing and physics approximations could be interacting in nonlinear ways that lead to different convective regimes than were observed. For example, updraft vertical velocity changes of a few meters per second at the melting level can result in significant changes in the amount of rain lofted and frozen.

Despite observed peak radar reflectivity aloft that is in between that observed in typical active and break period convection, convection as strong as that in the simulations does not appear in observational retrievals. Rather small differences in the large-scale

environment, updraft forcing, entrainment, and microphysics could alter the balance between vertical shear and instability leading to weaker convection in reality, but this is speculation and more research on this topic is needed. The possibility that large amounts of water are being lofted and ice multiplication processes such as Hallett-Mossop (Hallet and Mossop 1974) or ice-ice collisions (Yano and Phillips 2011) are limiting ice size in reality can also not be ruled out, although this scenario seems less likely based on the lack of very strong observationally retrieved vertical velocities in the upper troposphere, which would be expected purely from latent heat release in the freezing of such large water contents.

The simulated large-scale environmental variability is not perfect. Improper covariance of low and midlevel instability and vertical shear can affect convective mode, especially if subgrid scale approximations in microphysics and possibly turbulence interact to shift convection into a different regime. If convection enters a strong convective mode such as that of a supercell, the supercell can keep forcing new supercellular updrafts through its interaction with the environment, which leads to strong long-lived storms. Even in nonsupercells, the large buoyancy produced by large amounts of freezing rain produces a hydrostatic drop in pressure that can reinforce convergence into the region where convection is already occurring. Tripoli and Cotton (1980) performed numerical simulations that showed that the low and midlevel updraft is sensitive to the convergence feeding it air. The low pressure caused by the updraft can accelerate low-level outflow to reinforce the updraft if the pressure gradient is strong enough. Furthermore, the more strongly concentrated the low-level convergence is, the greater the fraction of updraft air below 5 km will be that originates in the boundary

layer, a process that could strongly modulate the convective strength and amount of condensate lifted. Some of these processes may be at work in the TWP-ICE CRM and LAM simulations, but further research is needed to look into factors controlling convective strength.

4.7 Discussion

Lang et al. (2007) is one of the few studies that compared tropical simulated deep convective vertical velocities with those in dual-Doppler retrievals. They concluded that CRM simulations using ~1-km horizontal grid spacing produce convective vertical velocity similar to that observed. They included entire dual-Doppler domains in their comparison, which is not advised based on biases and errors of at least a few meters per second in such datasets and the large fraction of convective updraft mass flux contributed by large, strong updrafts. They focused on maximum vertical velocity values, but as shown in this chapter, these values can be similar in distributions of maximum updraft vertical velocity that are very different. Furthermore, they failed to acknowledge that comparable convective vertical velocity does not guarantee accurate convective updraft dynamics and microphysics. For example, if a simulated convective updraft is 1 K warmer than an observed convective updraft in the same environment, this can be offset by about 3.3 g kg^{-1} more hydrometeor loading in the simulated updraft to yield the same buoyancy in both updrafts. This is not to say that modeling studies have not displayed 30 m s^{-1} and greater updraft vertical velocities in tropical maritime environments before. Zeng et al. (2008) showed that three-dimensional simulations of a South China Sea Monsoon Experiment (SCSMEX) case and a Kwajalein Experiment (KWAJEX) case

using 1-km horizontal grid spacing, 41 vertical levels, and a 256 km by 256 km domain produced vertical velocities of 30 m s^{-1} and greater throughout the upper troposphere with associated high cloud water and graupel mass mixing ratios. They also showed that these values were substantially higher in three-dimensional simulations than two-dimensional simulations, but did not investigate the reasons for this or do any comparisons with observational datasets.

Of the in situ tropical oceanic convective vertical velocity and liquid water content in situ measurements in the literature, only a select few (Zipser and Gautier 1978; Jorgensen and LeMone 1989) show vertical velocity values close to those in the simulated deep convective updraft cores for this case, and the few deep convective condensate measurements near the melting level or in mixed phase regions are questionable in sustained regions of high water content due to the instrumentation used. These studies show peak vertical velocity values of 15 m s^{-1} around 6-km altitudes in strongly forced tropical depression and MCS cases with updrafts that are on the order of 10 km wide or greater when spatial resolution is degraded to 1 km. While tropical coastal convection in a monsoon trough environment is often more intense than over the open ocean (Petersen and Rutledge 2001; Xu and Zipser 2012) and this MCS case is comparable to strongly forced tropical depression convection over the ocean in Zipser and Gautier (1978) and Houze et al. (2009), it is still weaker than typical break period continental convection (May and Ballinger 2007; Xu and Zipser 2012). May and Rajopadhyaya (1999) used ground-based vertical profilers at Darwin to examine convective updraft properties in both active and break monsoon periods. Despite including primarily break period convection, they found a 90^{th} percentile maximum

vertical velocity of approximately 8 m s^{-1} at 5 km and 11 m s^{-1} at 10 km, similar to the median dual-Doppler values for this case. The drawback of their comparison is that they also included shallow and decaying updrafts in addition to mature updrafts in their statistics. Purely deep updraft statistics using profilers in a near coastal site in India (Uma and Rao 2008), however, show very similar peak vertical velocity values to those shown in May and Rajopadhyaya (1999). For deep cores greater than 10 km in extent in their study, many of which are sampled in MCSs, peak values of 15 m s^{-1} are retrieved in the upper troposphere with values of around 10 m s^{-1} at 4–5 km altitudes.

Heymsfield et al. (2010) used nadir-viewing airborne Doppler radar to examine intense deep convective updraft vertical velocities in several near coastal environments. Specifically targeting overshooting cloud tops, their mean oceanic maximum vertical velocity profile reaches 10 m s^{-1} at 5 km and 13 m s^{-1} at 10 km, lower than the median values in the simulations, but almost identical to median dual-Doppler values for this case. The peak vertical velocity in the mean profile also occurs at an altitude of 10 km, the same as that in dual-Doppler retrievals. There is no reason to think that there is anything special about 10 km, but it is interesting that observational retrievals show peak vertical velocities well below cloud top while simulated peak vertical velocities tend to be closer to cloud top. The peak oceanic vertical velocity in Heymsfield et al. (2010) at 5 km is 17 m s^{-1} and 25 m s^{-1} at 10 km, which are very close to the 90^{th} percentile of dual-Doppler maximum vertical velocities for this case, which are 15 m s^{-1} at 5 km and 23 m s^{-1} at 10 km. These higher percentiles also agree well with the 20 m s^{-1} peak vertical velocity at 11 km measured in an intense TC4 convective cell reported in Lawson et al. (2010). It should be noted that these are not weak tropical oceanic cells out in the middle

of the Intertropical Convergence Zone, but tropical oceanic cells near coastlines of Central America, the Caribbean, and the Gulf of Mexico, where more intense cells with some lightning are expected. Heymsfield et al. (2010) also show that the mean of the maximum radar reflectivity in these cells at 10 km is 30 dBZ, which agrees perfectly with the dual-Doppler retrievals from TWP-ICE, but is significantly lower than simulated values. Maximum radar reflectivities at 10 km approach 40 dBZ, again consistent with observations in this case. Heymsfield et al. (2010) attributes acceleration between cloud base and $T = 0°C$ in these intense oceanic updrafts near coasts to unloading of large raindrops, which increases updraft buoyancy despite appreciable entrainment. If this is true, then this is far different than the simulated intense updrafts, which do not unload much rainwater but maintain high vertical velocities by not entraining much environmental air. It is difficult to know how intense tropical oceanic updrafts are behaving in nature without more co-located, coincident, and redundant in situ and remote sensing observations of vertical velocity and condensate, something that should be a goal in future field campaigns.

The evidence presented here shows that simulated convective updrafts for a TWP-ICE MCS are too strong in all CRM and LAM setups. This is especially true in the upper troposphere, which suggests that too much freezing of rain is occurring based on the large rain water contents being lofted. Preliminary results indicate that nearly undiluted and large updrafts do not appear to be due to unresolved large eddies. They do appear related to a different convective mode than occurred in observations, which could be a result of nonlinear interactions with some possible feedbacks between several imperfect approximations in the models.

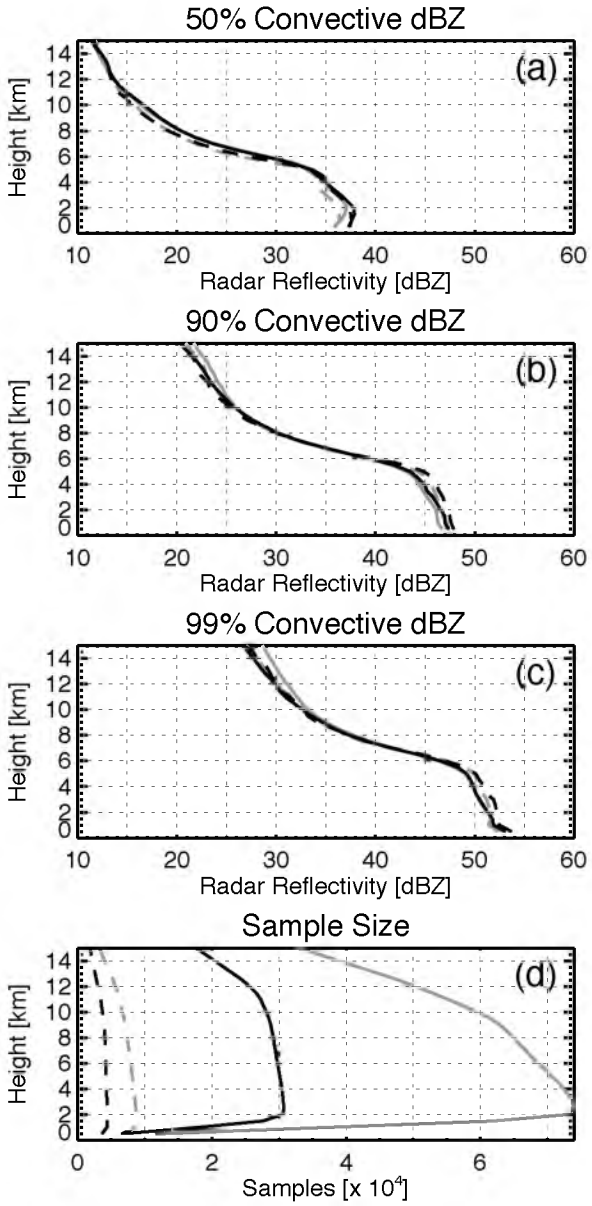

Figure 4.1. The (a) 50th, (b) 90th, and (c) 99th percentiles of convective radar reflectivity with (d) sample size for the dual-Doppler lobes (dashed lines) and pentagonal model forcing domain (solid lines). Gray lines represent the entire MCS event while black lines represent the 1310Z through 1750Z period on January 23rd for which dual-Doppler retrievals are available.

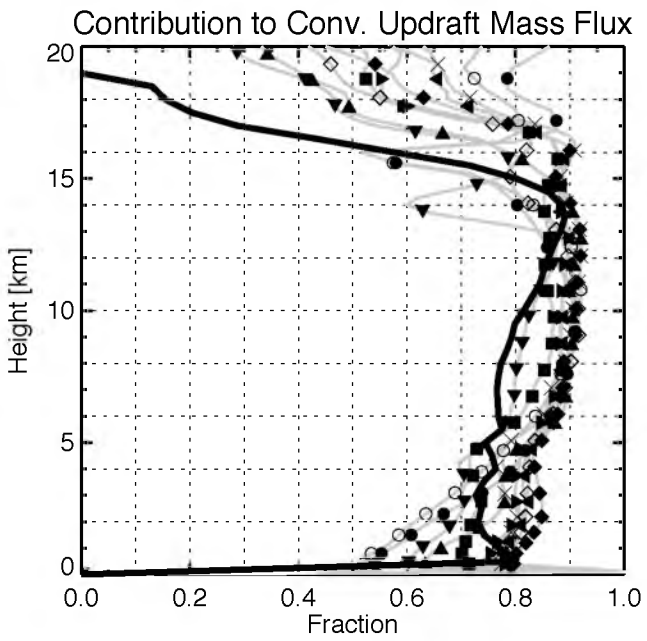

Figure 4.2. The percentage contribution of three-dimensionally defined updrafts beginning below 1 km and ending above 15 km to the total convective updraft mass flux between 1310Z and 1750Z on January 23rd for all CRM simulations (gray lines and symbols defined in Table 2.1) and the dual-Doppler retrieval (solid black line).

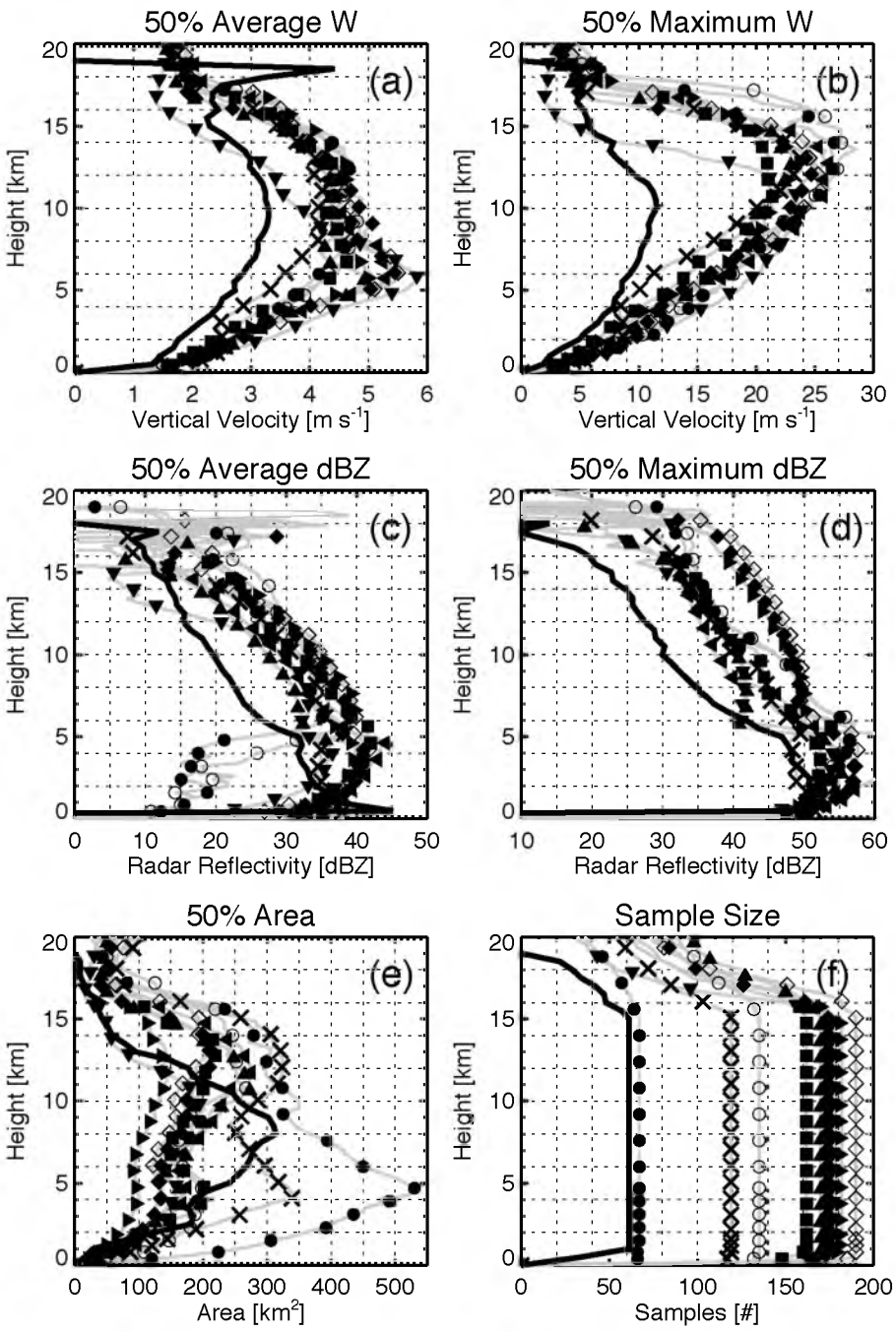

Figure 4.3. The median profiles of several variables are shown for three-dimensionally defined convective updrafts beginning below 1 km and ending above 15 km in both CRMs (symbols defined in Table 2.1) and dual-Doppler retrievals (solid black line) for the period of 1310Z to 1750Z on January 23rd. Average vertical velocity is shown in (a), maximum vertical velocity in (b), average radar reflectivity in (c), maximum radar reflectivity in (d), area in (e), and sample size in (f).

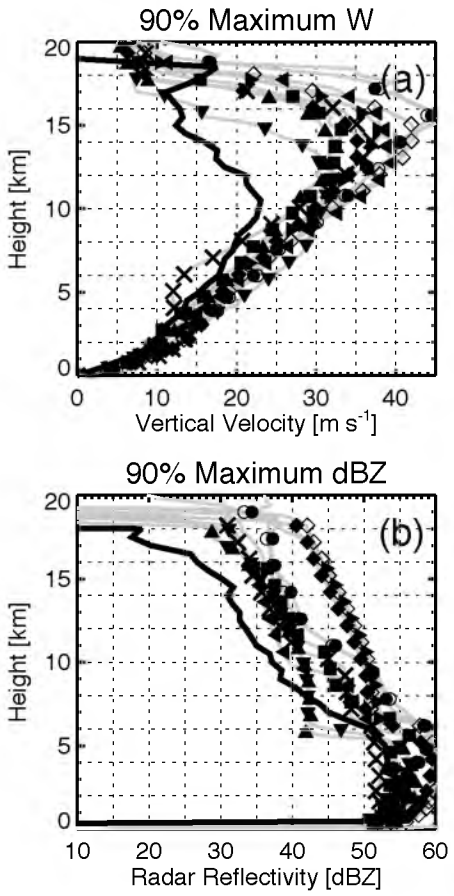

Figure 4.4. The 90th percentile profiles of (a) maximum vertical velocity and (b) maximum radar reflectivity are shown for three-dimensionally defined convective updrafts beginning below 1 km and ending above 15 km in both CRMs (symbols defined in Table 2.1) and dual-Doppler retrievals (solid black line) for the period of 1310Z to 1750Z on January 23rd.

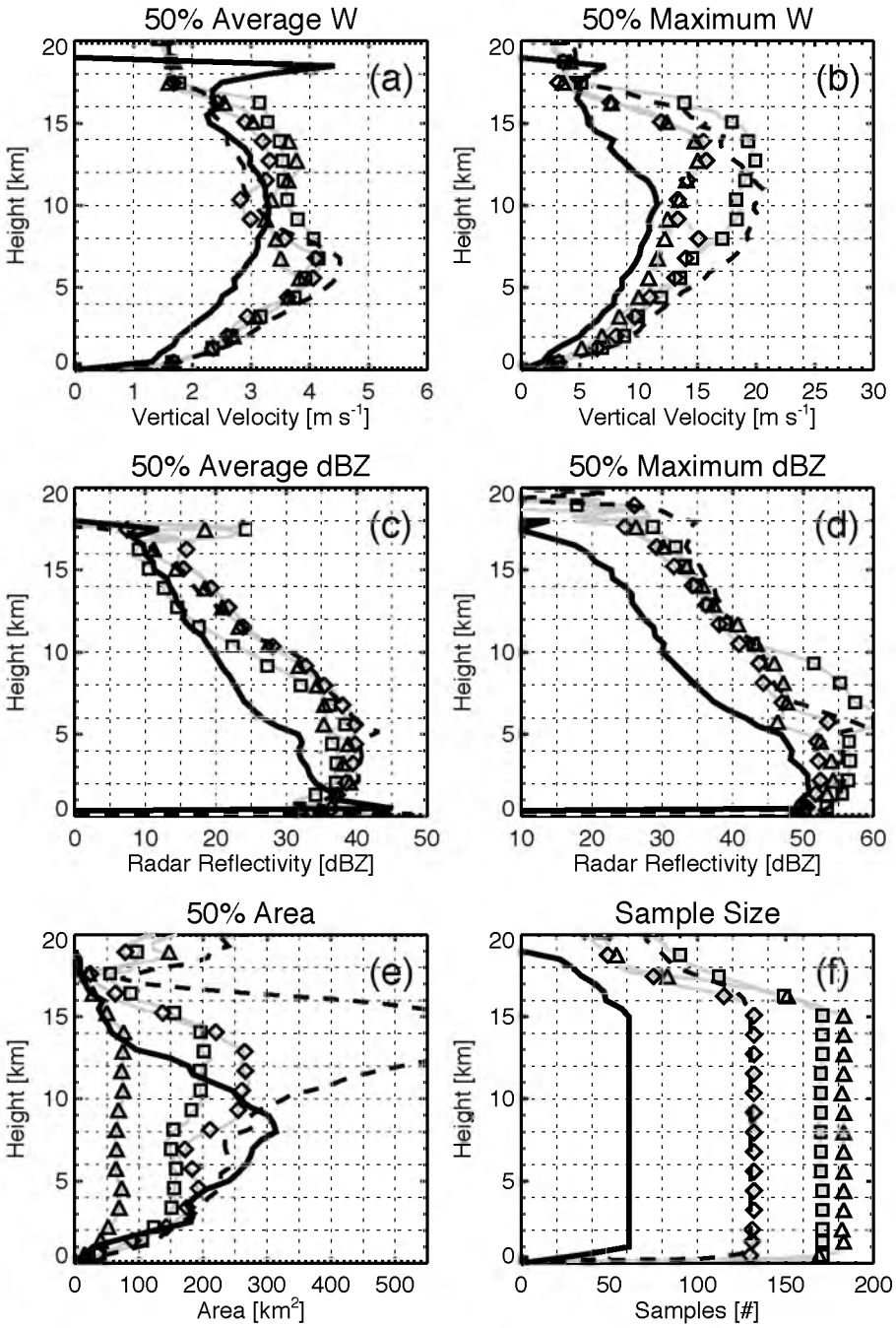

Figure 4.5. The median profiles of several variables are shown for three-dimensionally defined convective updrafts beginning below 1 km and ending above 15 km in both LAMs (symbols defined in Table 2.3) and dual-Doppler retrievals (solid black line) for the period of 1310Z to 1750Z on January 23rd. Average vertical velocity is shown in (a), maximum vertical velocity in (b), average radar reflectivity in (c), maximum radar reflectivity in (d), area in (e), and sample size in (f). Only LAM updrafts located in the CPOL domain are included.

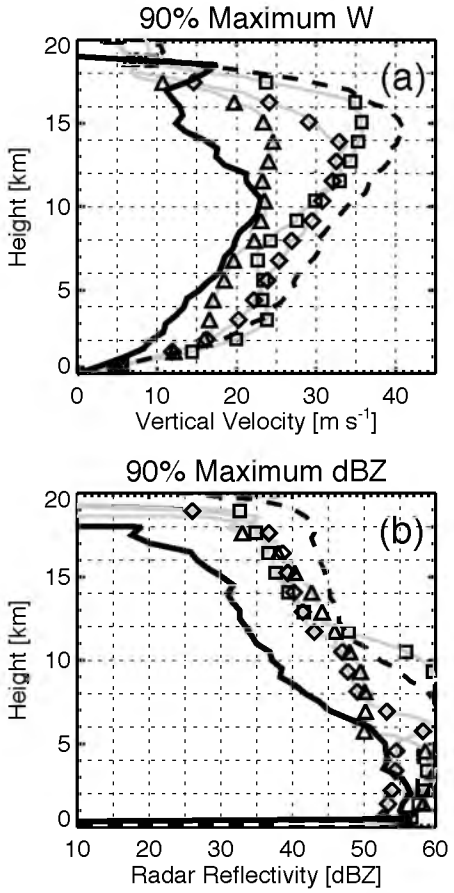

Figure 4.6. The 90th percentile profiles of (a) maximum vertical velocity and (b) maximum radar reflectivity are shown for three-dimensionally defined convective updrafts beginning below 1 km and ending above 15 km in both LAMs (symbols defined in Table 2.3) and dual-Doppler retrievals (solid black line) for the period of 1310Z to 1750Z on January 23rd. Only LAM updrafts located in the CPOL domain are included.

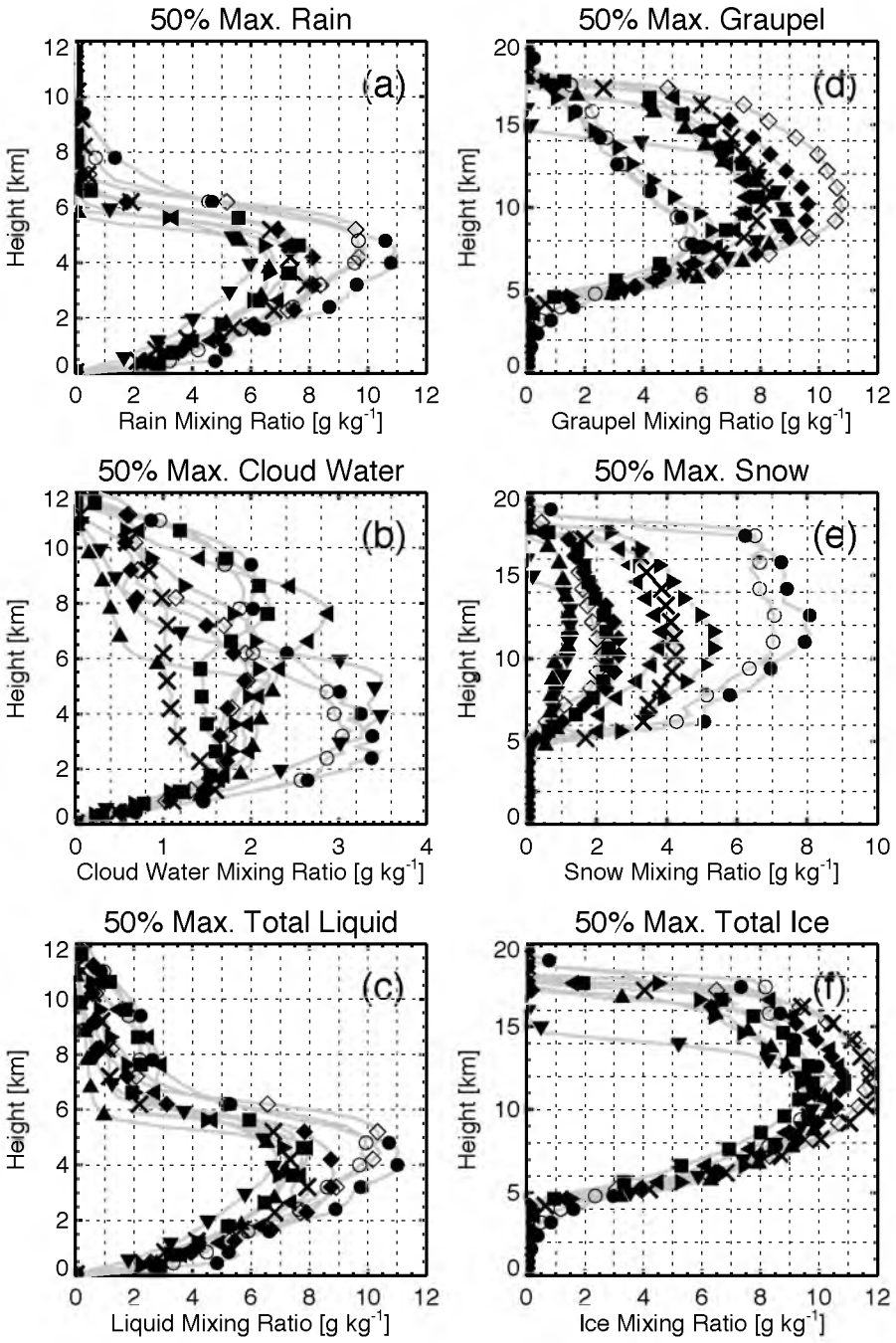

Figure 4.7. The median profiles of CRM simulated maximum (a) rain, (b) cloud water, (c) total liquid, (d) graupel, (e) snow, and (f) total ice mixing ratios in three-dimensionally defined deep convective updrafts that being below 1 km and end above 15 km for the period of 1310Z to 1750Z on January 23rd. Symbols are defined in Table 2.1.

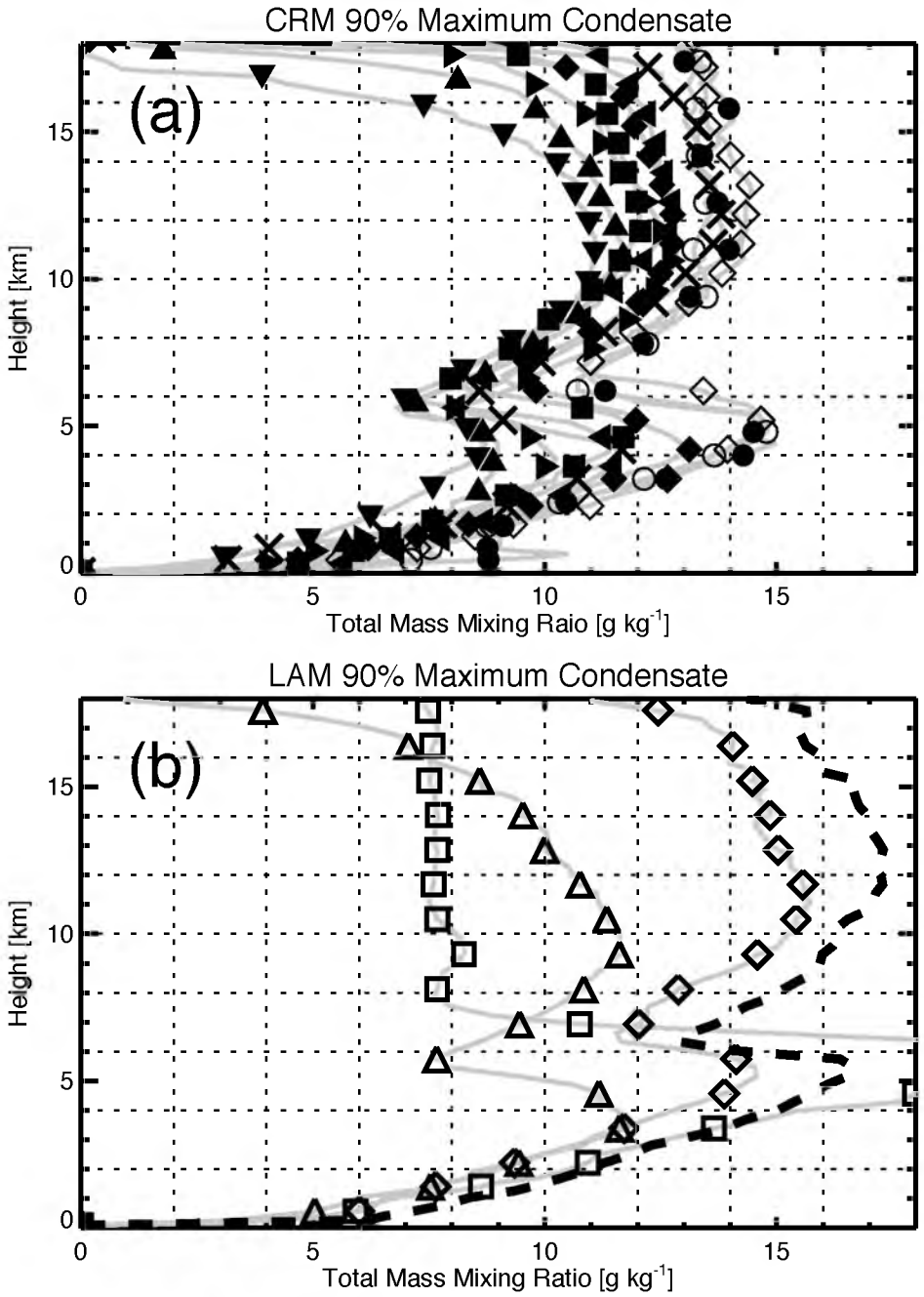

Figure 4.8. The 90th percentile profiles of maximum total hydrometeor mixing ratios in three-dimensionally defined deep convective updrafts that begin below 1 km and end above 15 km for the period of 1310Z to 1750Z on January 23rd within (a) CRM simulations (symbols defined in Table 2.1) and (b) LAM simulations (symbols defined in Table 2.3). Only LAM updrafts located in the CPOL domain are included.

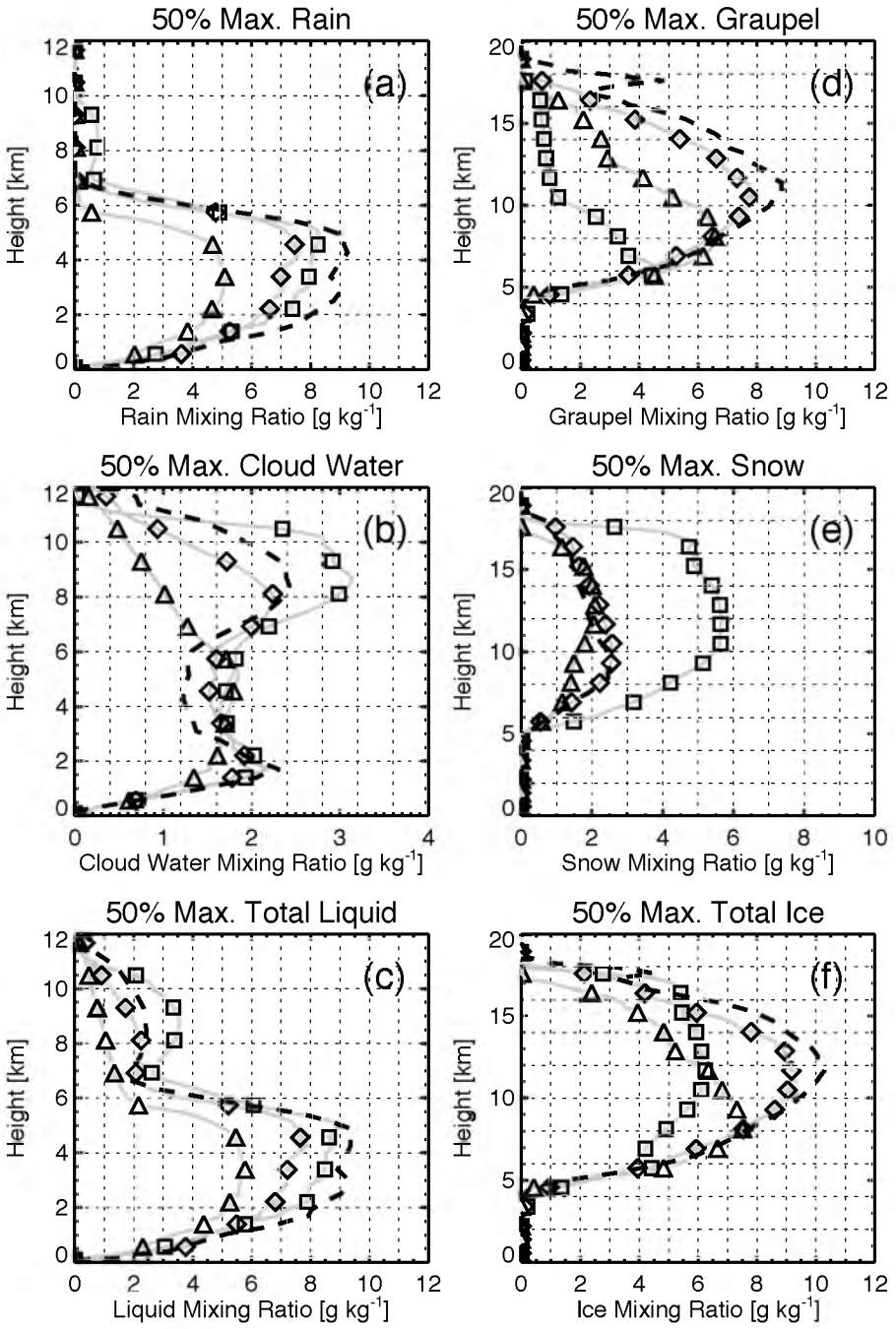

Figure 4.9. The median profiles of LAM simulated maximum (a) rain, (b) cloud water, (c) graupel, (d) snow, (e) total liquid, and (f) total ice mixing ratios in three-dimensionally defined deep convective updrafts that begin below 1 km and end above 15 km. Only LAM updrafts located in the CPOL domain are included. Symbols are defined in Table 2.3.

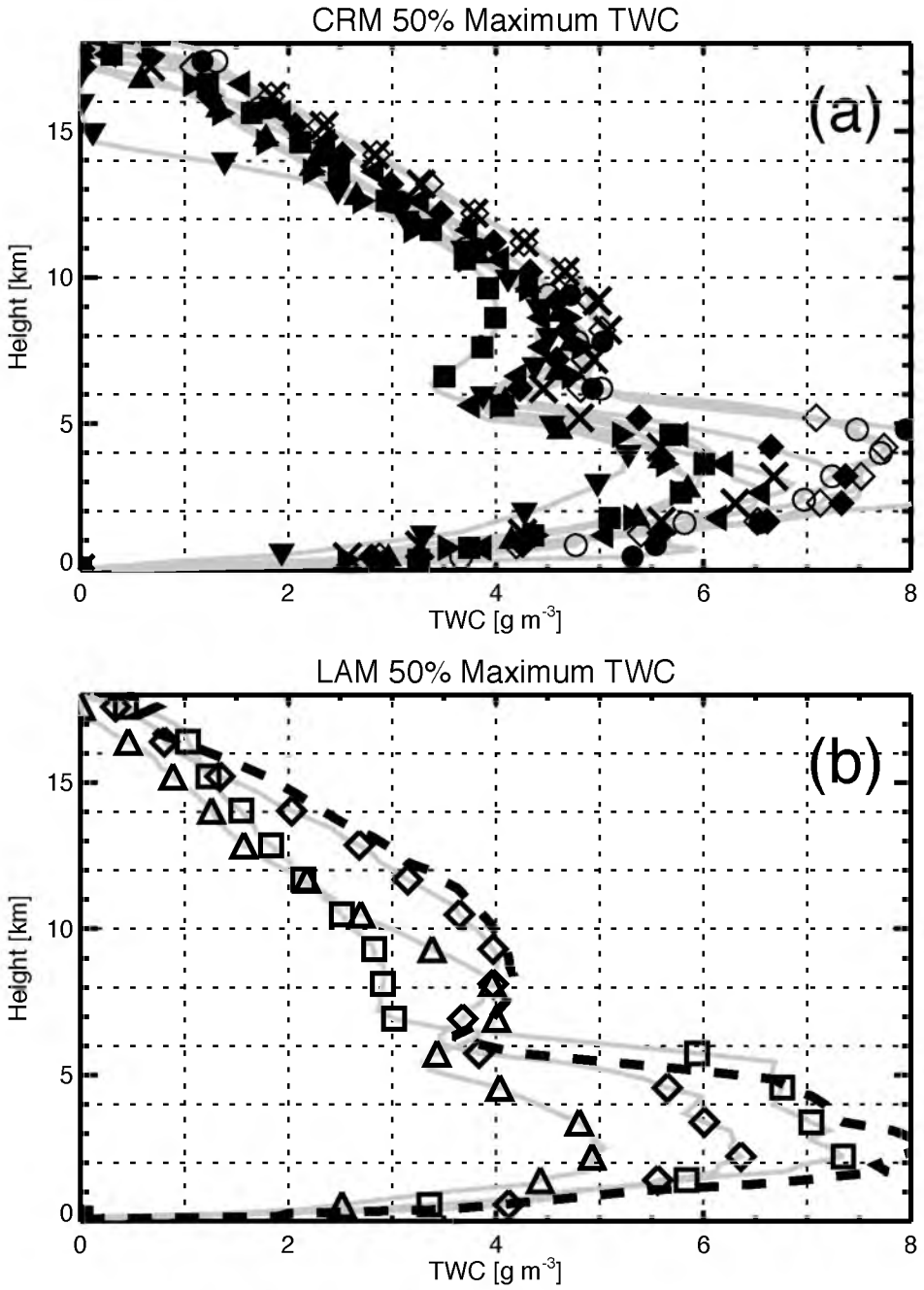

Figure 4.10. The median profiles of maximum total hydrometeor water contents in three-dimensionally defined deep convective updrafts beginning below 1 km and ending above 15 km for the 1310Z to 1750Z period on January 23rd within (a) CRM simulations (symbols defined in Table 2.1) and (b) LAM simulations (symbols defined in Table 2.3). Only LAM updrafts located in the CPOL domain are included.

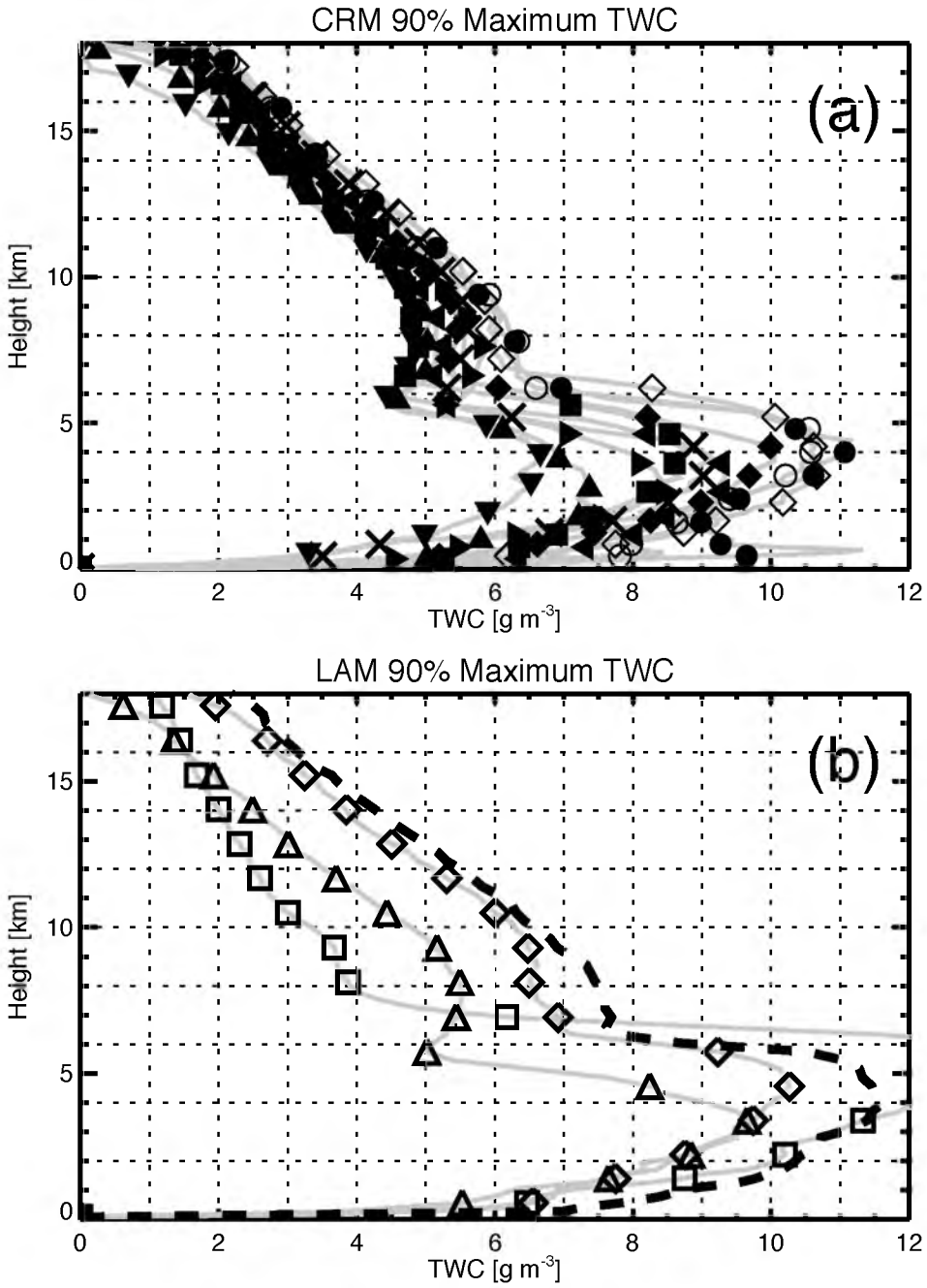

Figure 4.11. The 90th percentile profiles of maximum total hydrometeor water contents in three-dimensionally defined deep convective updrafts beginning below 1 km and ending above 15 km for the 1310Z to 1750Z period on January 23rd within (a) CRM simulations (symbols defined in Table 2.1) and (b) LAM simulations (symbols defined in Table 2.3). Only LAM updrafts located in the CPOL domain are included.

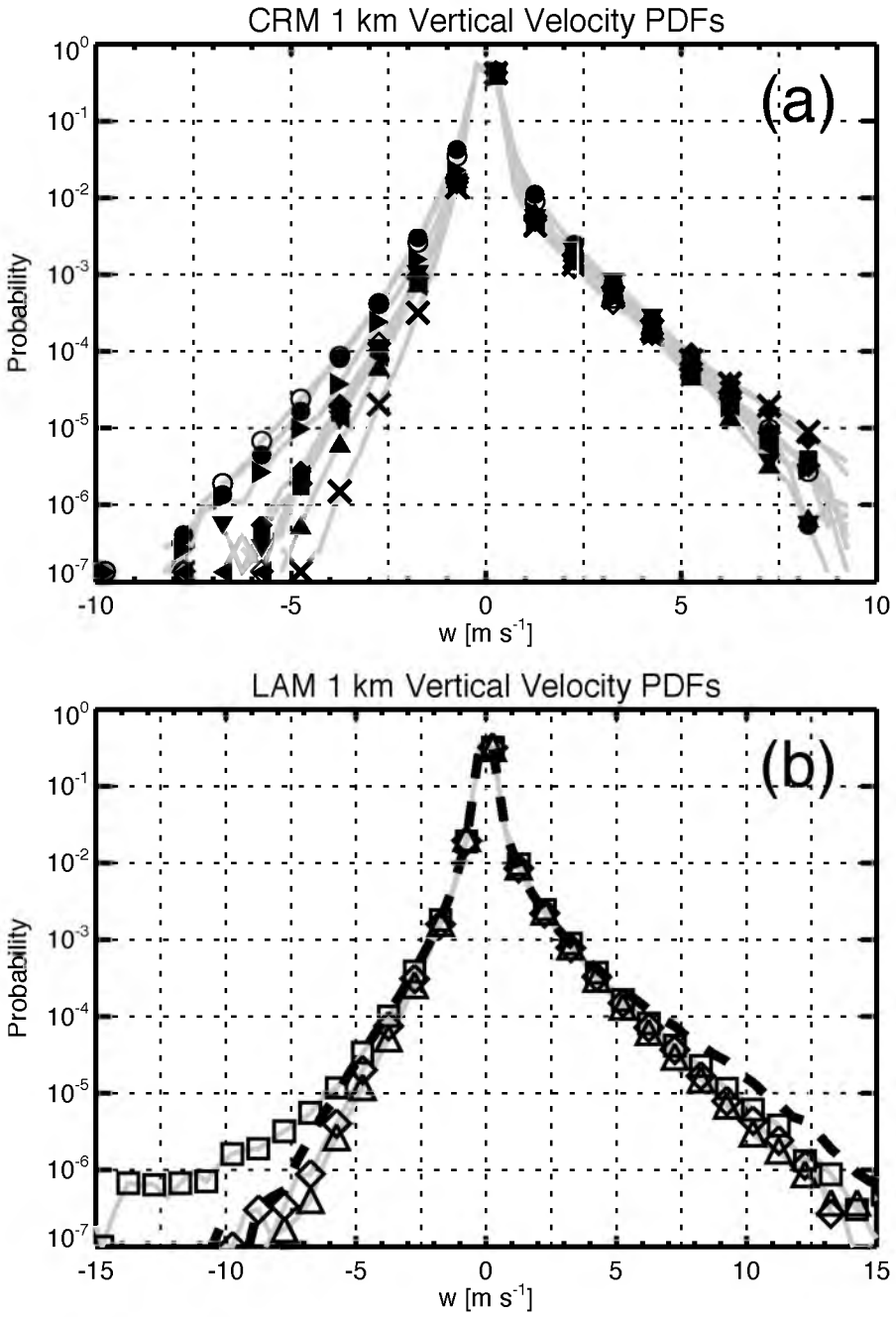

Figure 4.12. The probability distribution of vertical velocity at a 1-km altitude for (a) all CRM simulations (symbols defined in Table 2.1) and (b) all LAM simulations (symbols defined in Table 2.3). LAM statistics are limited to the CPOL domain. Note the x-axes are different for the two panels.

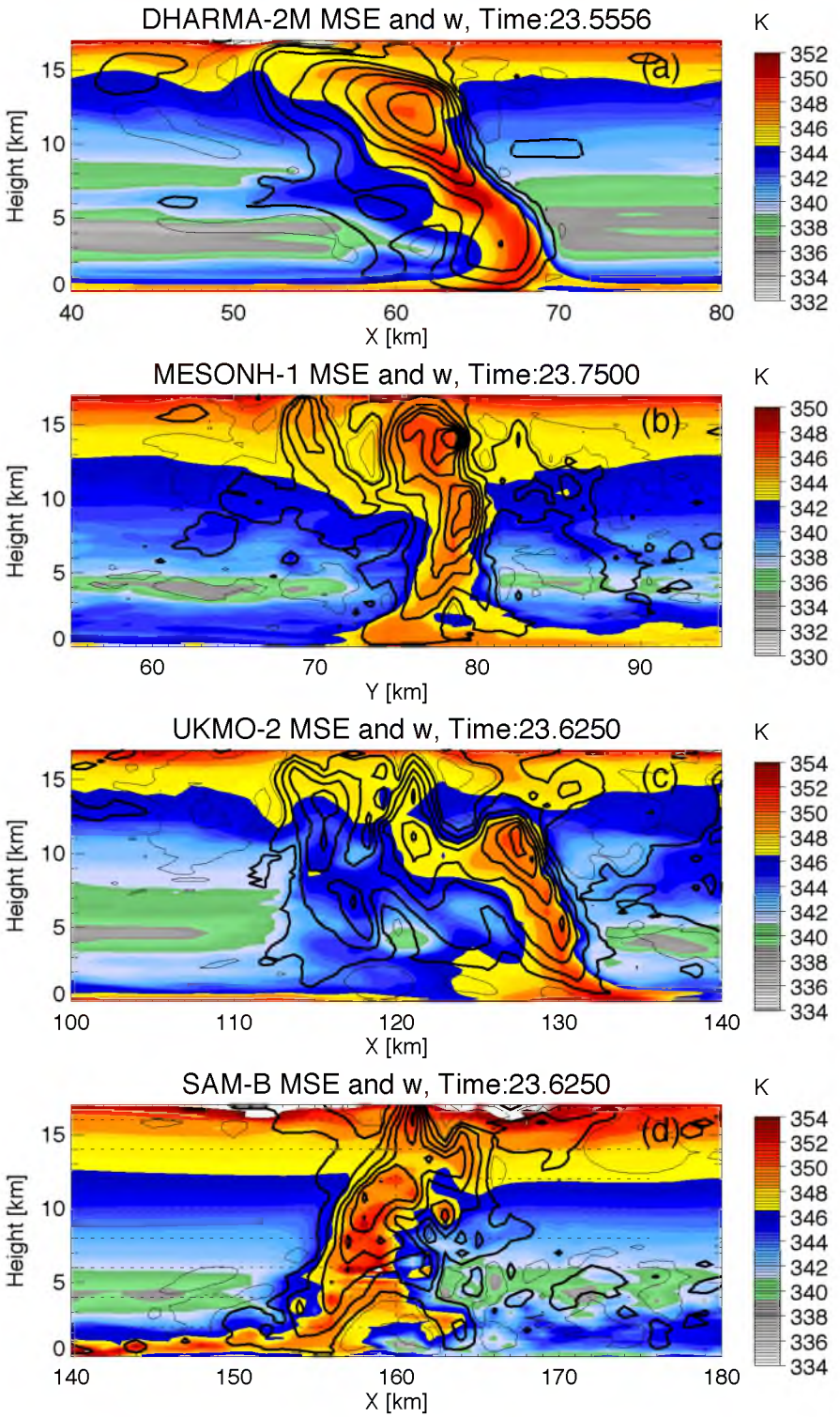

Figure 4.13. Example vertical cross-sections through strong deep convective updrafts are shown for each of the CRM dynamical cores: (a) DHARMA, (b) MESONH, (c) UKMO, and (d) SAM. Moist static energy is color filled. Upward vertical velocity is contoured in thick black at 1, 5, 10, 15, 20, 25, and 30 m s^{-1}, while downward vertical velocity is contoured in thin black at -1 and -5 m s^{-1}.

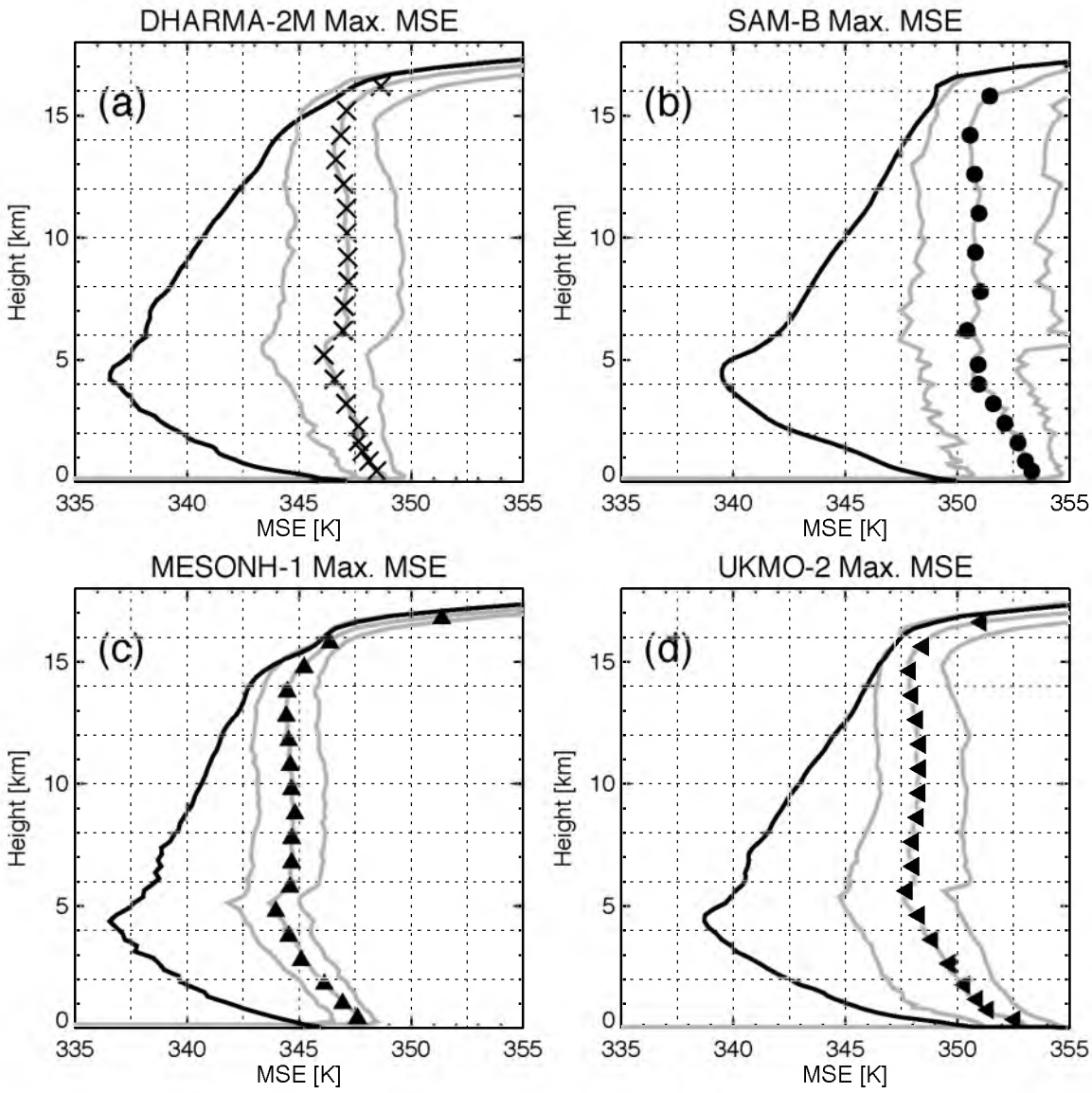

Figure 4.14. Profiles of moist static energy for four simulations: (a) DHARMA-2M, (b) SAM-B, (c) MESONH-1, and (d) UKMO-2. The domain-mean (environmental) profiles are shown in black. The median profiles of maximum moist static energy in three-dimensionally defined deep convective updrafts beginning below 1 km and ending above 15 km for the 1310Z to 1750Z period on January 23rd are shown with symbols. The 10^{th} and 90^{th} percentiles are shown with gray lines.

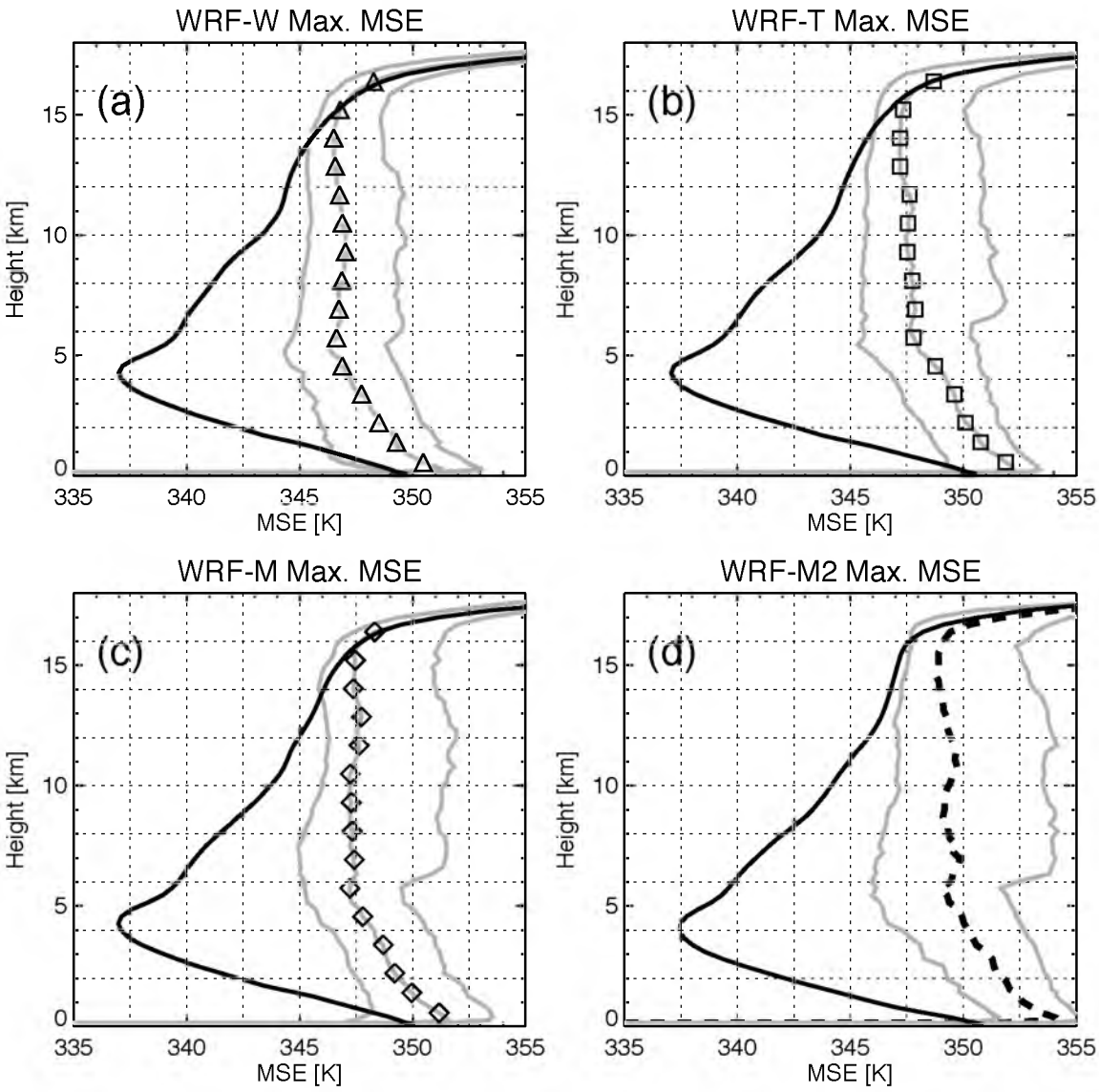

Figure 4.15. Profiles of moist static energy for (a) WRF-W, (b) WRF-T, (c) WRF-M, and (d) WRF-M2. The domain-mean (environmental) profiles are shown in black. The median profiles of maximum moist static energy in three-dimensionally defined deep convective updrafts beginning below 1 km and ending above 15 km for the 1310Z to 1750Z period on January 23rd are shown with symbols. The 10^{th} and 90^{th} percentiles are shown with gray lines. Only LAM updrafts in the CPOL domain are included.

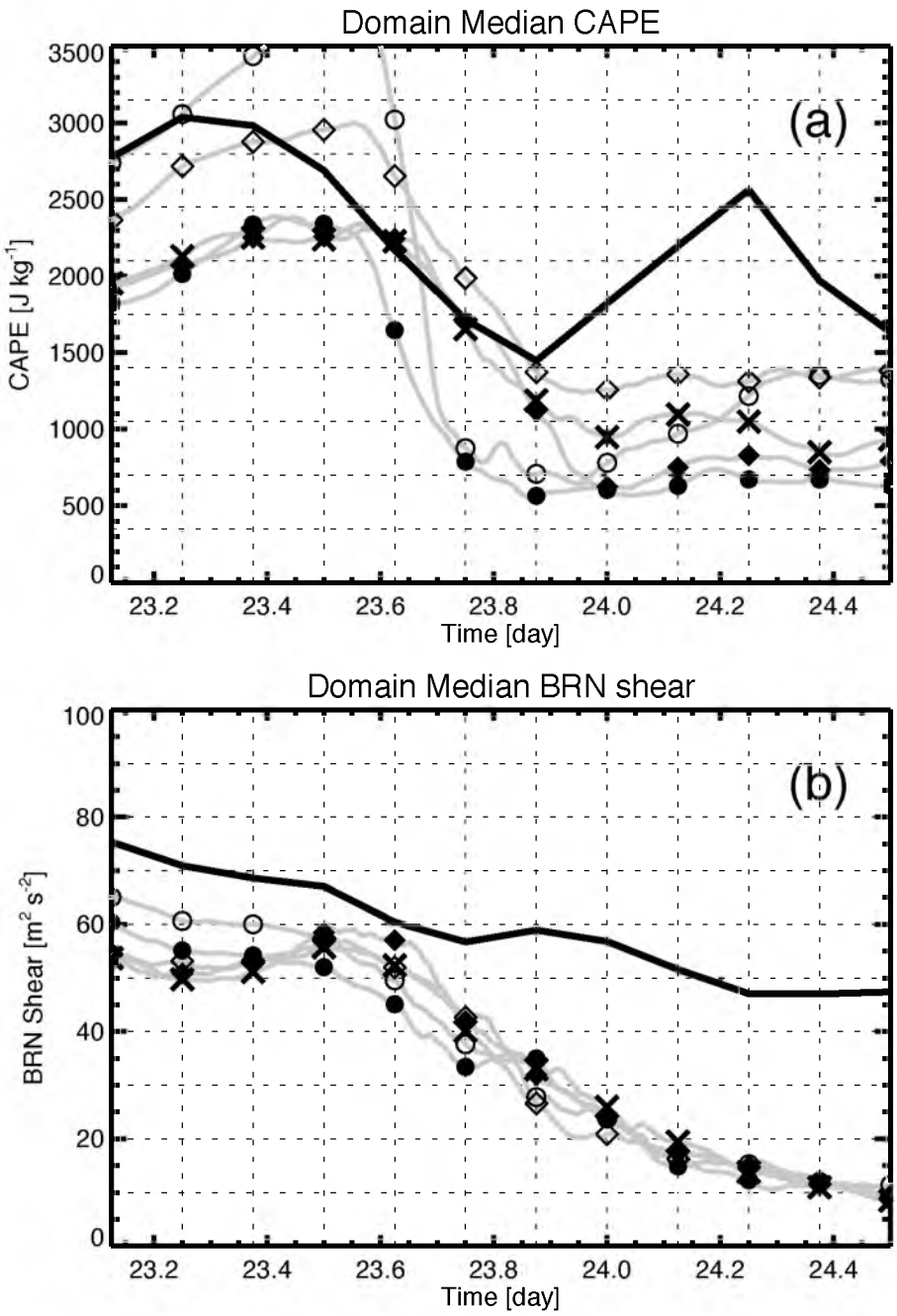

Figure 4.16. A time series of the MCS event from 3Z on January 23rd to 12Z on January 24th showing domain-median CRM (a) surface-based CAPE and (b) bulk Richardson vertical wind shear. Symbols are defined in Table 2.1. The variational analysis used to force the CRMs is shown in solid black at three-hour resolution. Only DHARMA and SAM simulations are shown because pressure profiles were not provided for the UKMO simulations and outputted horizontal wind fields in the MESONH simulations are of questionable accuracy.

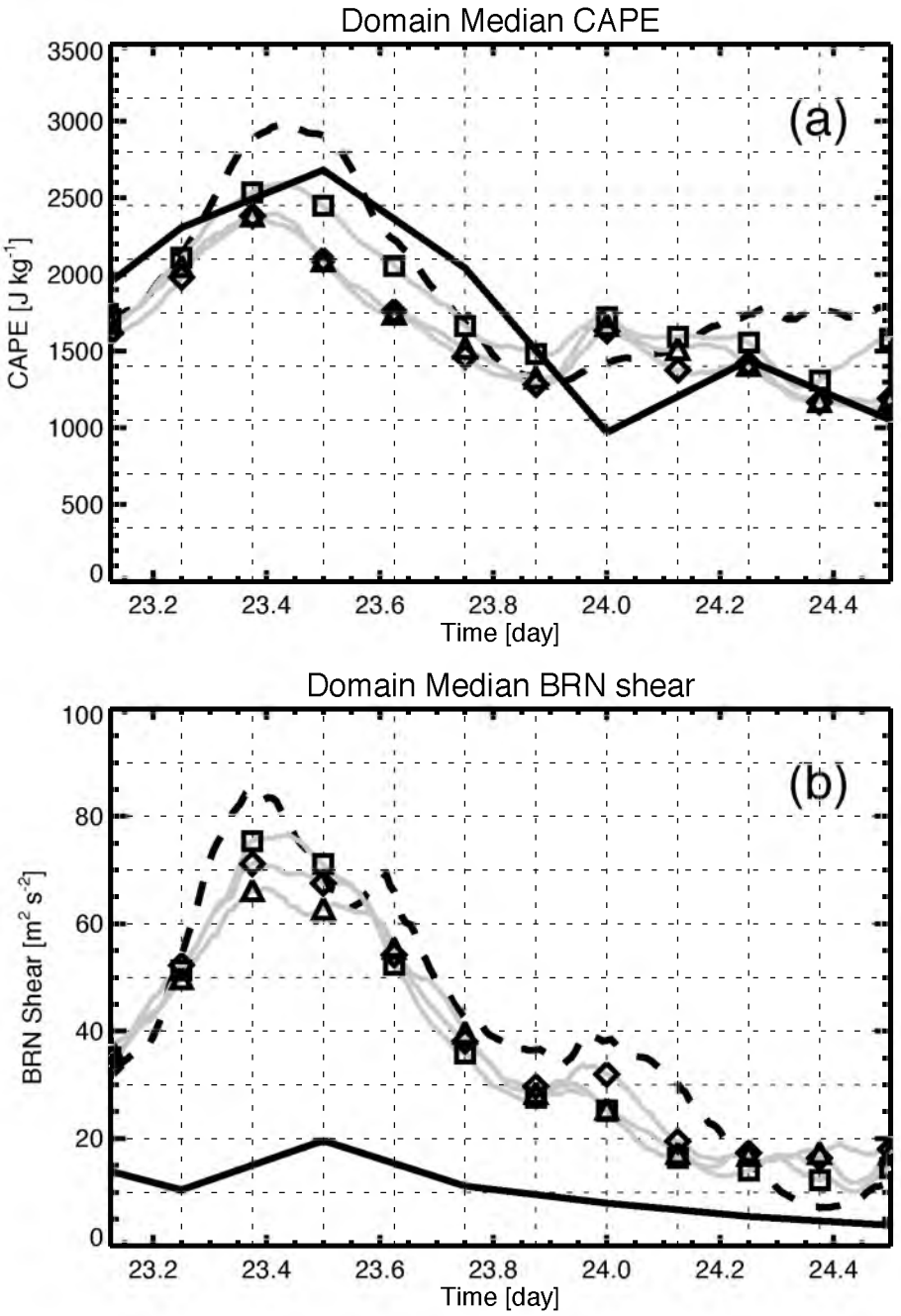

Figure 4.17. A time series of the MCS event from 3Z on January 23rd to 12Z on January 24th showing domain-median LAM (a) surface-based CAPE and (b) bulk Richardson vertical wind shear within the CPOL domain. The three-hourly ECMWF analysis in the CPOL domain is shown in solid black.

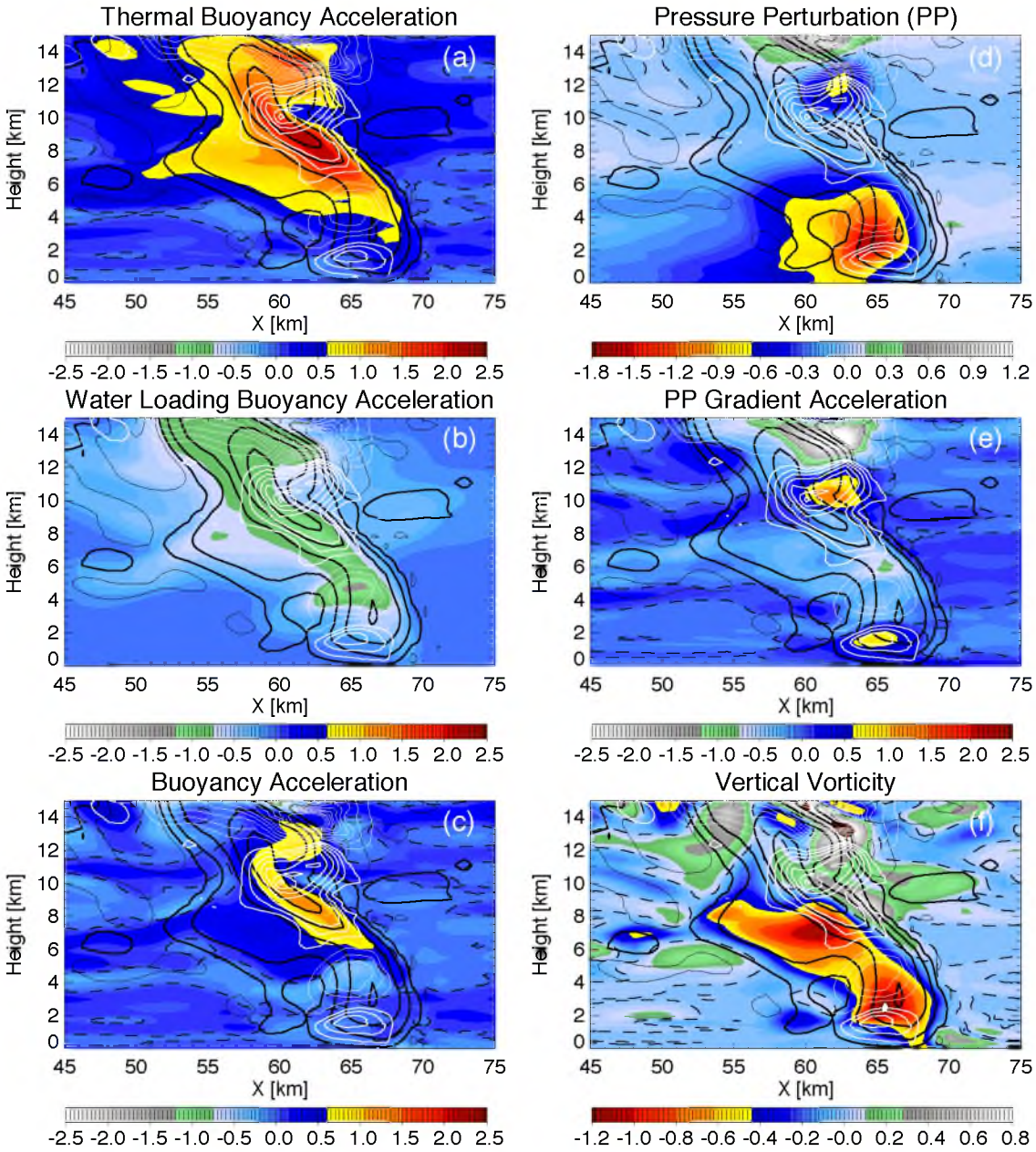

Figure 4.18. Example vertical cross-sections through a strong long-lived "left-moving" deep convective updraft in the DHARMA-2M simulation at 1320Z showing (a) thermal buoyancy acceleration [1×10^{-1} m s^{-2}], (b) water loading buoyancy acceleration [1×10^{-1} m s^{-2}], (c) total buoyancy acceleration [1×10^{-1} m s^{-2}], (d) pressure perturbation [hPa], (e) vertical pressure perturbation gradient acceleration [1×10^{-1} m s^{-2}], and (f) vertical vorticity [1×10^{-2} s^{-1}]. Zero lines are shown in dashed black, vertical velocity (1, 5, 10, 15, 20, 25, and 30 m s^{-1}) is contoured in solid black, and Dw/Dt (every 0.02 m s^{-2}) is contoured in white. Cell motion is primarily from right to left (westward).

Figure 4.19. Example horizontal cross-sections at 1350Z in the DHARMA-2M simulation showing color filled (a) 50-m divergence [1×10^{-4} s^{-1}], (b) 550-m divergence [1×10^{-4} s^{-1}], (c) 2.5-km pressure perturbations [Pa], (d) 1 km vertical pressure perturbation gradient acceleration [1×10^{-2} m s^{-2}], (e) 1-km total buoyancy acceleration [1×10^{-2} m s^{-2}], and (f) 2.5-km vertical vorticity [1×10^{-4} s^{-1}] over a 90 km by 90 km section of the model domain with zero lines shown in dashed black. 2.5-km altitude vertical velocity is shown with black contours (-5, -1, 1, 5, 10, and 15 m s^{-1}). Relative wind vectors at the same altitude as the color filled variables are shown in white.

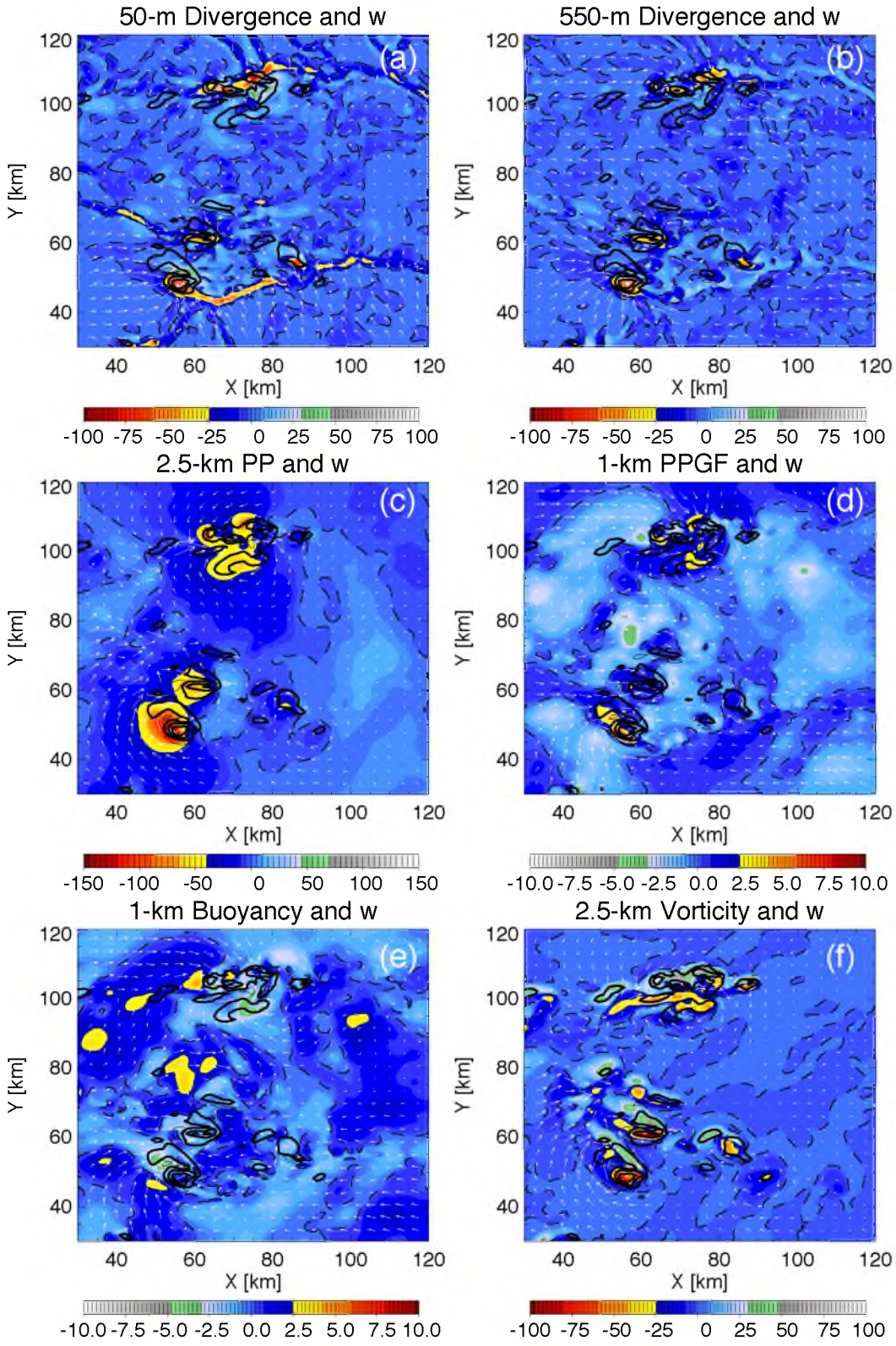
50-m Divergence and w
(a)
550-m Divergence and w
(b)
2.5-km PP and w
(c)
1-km PPGF and w
(d)
1-km Buoyancy and w
(e)
2.5-km Vorticity and w
(f)
Y [km]
X [km]
120
100
80
60
40
-100 -75 -50 -25 0 25 50 75 100
-150 -100 -50 0 50 100 150
-10.0 -7.5 -5.0 -2.5 0.0 2.5 5.0 7.5 10.0

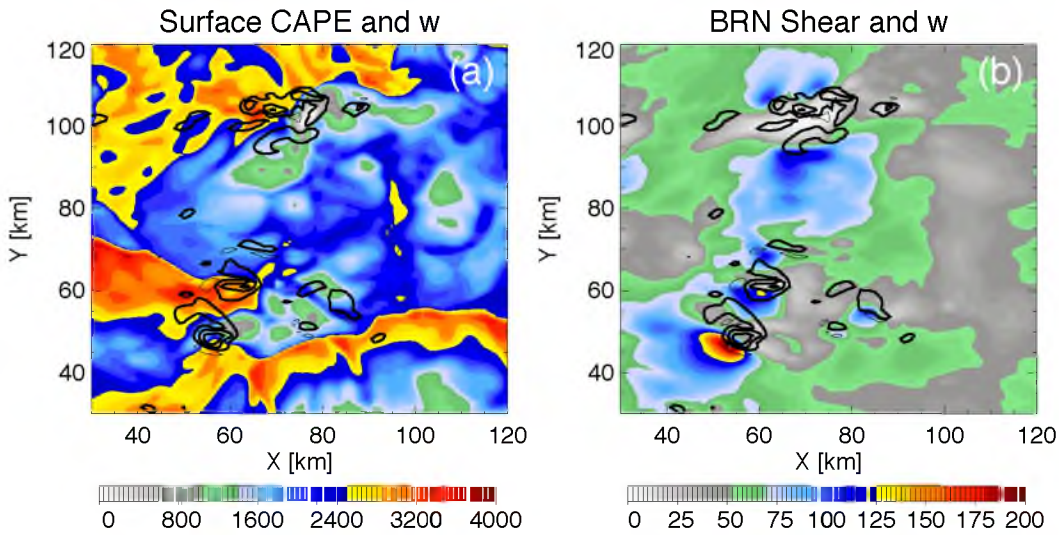

Figure 4.20. Example horizontal cross-sections at 1350Z in the DHARMA-2M simulations showing color filled (a) surface-based CAPE [J kg^{-1}], and (b) bulk Richardson shear [m^2 s^{-2}] over a 90 km by 90 km section of the model domain. 2.5-km altitude vertical velocity is shown with black contours (-5, -1, 1, 5, 10, and 15 m s^{-1}).

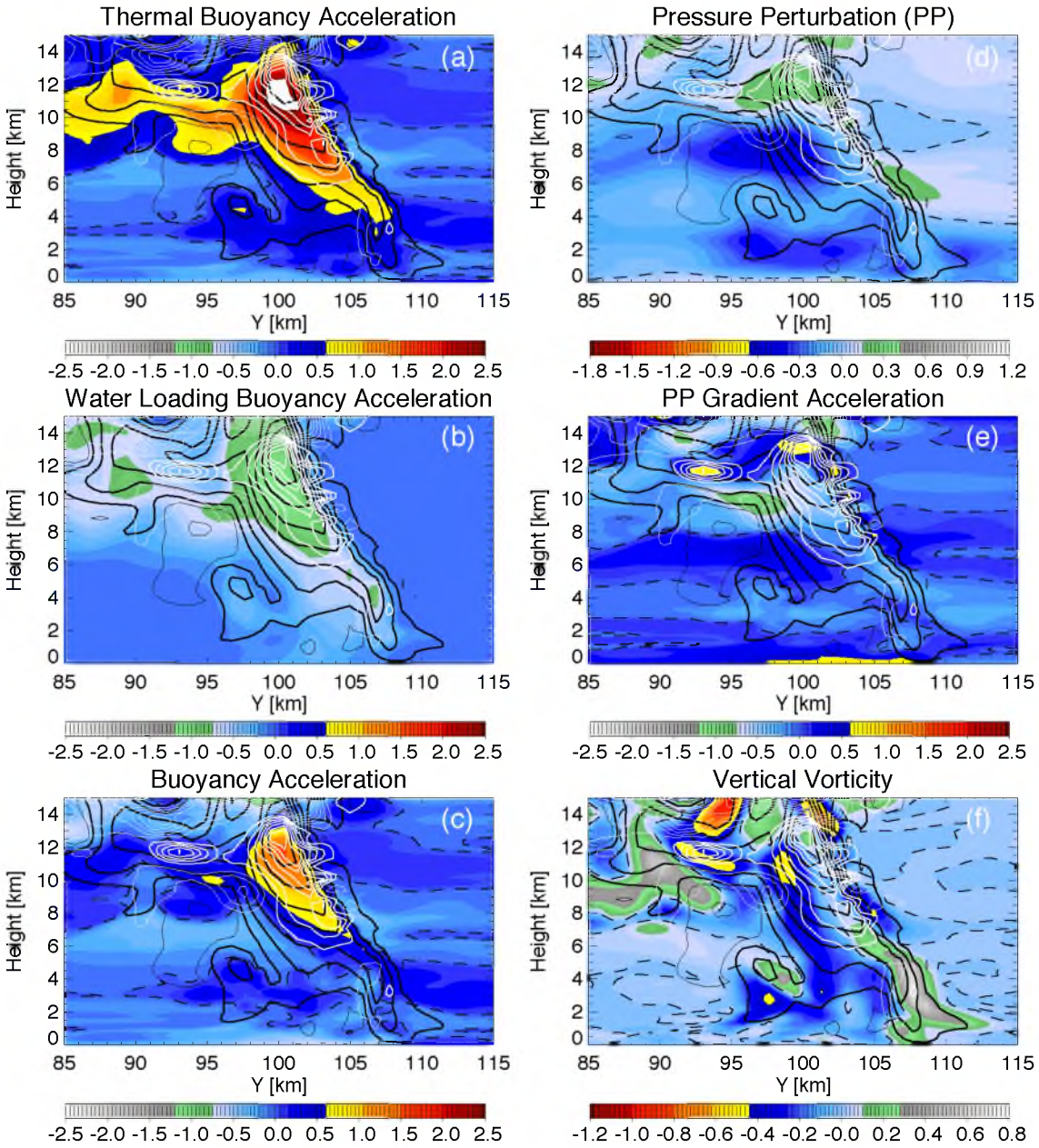

Figure 4.21. Example vertical cross-sections through a strong "right-moving" deep convective updraft in the DHARMA-2M simulation at 1350Z showing (a) thermal buoyancy acceleration [1×10^{-1} m s^{-2}], (b) water loading buoyancy acceleration [1×10^{-1} m s^{-2}], (c) total buoyancy acceleration [1×10^{-1} m s^{-2}], (d) pressure perturbation [hPa], (e) vertical pressure perturbation gradient acceleration [1×10^{-1} m s^{-2}], and (f) vertical vorticity [1×10^{-2} s^{-1}]. Zero lines are shown in dashed black, vertical velocity (1, 5, 10, 15, 20, 25, and 30 m s^{-1}) is contoured in solid black, and Dw/Dt (every 0.02 m s^{-2}) is contoured in white. Cell motion is primarily from left to right and into the cross-sections (northwestward).

CHAPTER 5

RAIN MICROPHYSICS

5.1 Overview

Chapter 4 showed that deep convective updrafts appear to be too strong in both CRM and LAM simulations, which would be expected to impact stratiform regions in different ways than the convection did in reality. Stratiform rain biases in simulations of MCSs using one-moment schemes have been shown in previous studies (e.g., Morrison et al. 2009; Luo et al. 2010; Bryan and Morrison 2012). They show that excessive evaporation often leads to a low bias in simulated stratiform rain rates for one-moment rain schemes, while two-moment schemes perform much better due to their ability to predict number concentration, which eliminates excessive small raindrops. These studies generally stop short of extensively comparing two-moment simulations of stratiform rain properties to those observed to see if two-moment schemes have biases as well. As was shown in Chapter 3, both one-moment and two-moment schemes show low biases in stratiform rain rate for TWP-ICE CRM and LAM simulations. No TWP-ICE in situ ice observations exist in well-developed stratiform regions, but several observationally retrieved rain microphysics datasets exist, including those from a disdrometer, multiple vertical profilers, and CPOL, that are used in this chapter to explain this discrepancy with previous studies and characterize simulated rain microphysics errors. Hypotheses are

then generated that connect these errors to stratiform ice and convective regions. All figures and statistics discussed in this chapter use simulation output and observational retrievals from the MCS event alone.

5.2 Sampling

Vertical profiler retrievals are a major part of this chapter, but comparing them to simulations is difficult. A vertical profiler only observes precipitation that passes over the profiler's location, whereas a three-dimensional model domain has more than 30,000 surface grid points. This introduces a large difference in the total number of samples in addition to differences in sample volume (i.e., the profiler does not observe a ~1-km^2 footprint at any given time but rather a smaller footprint over a short time period). Furthermore, not all samples are independent as successive profiles or point measurements in a large stratiform region will be highly correlated with one another. To circumvent this issue, mean profiles of variables are obtained at all grid points in each model by only including samples where simulated radar reflectivity is greater than or equal to 5 dBZ for the dual-profiler retrieval profile depth between 1.5 and 4 km. Furthermore, only "deep" stratiform profiles are considered. For Doppler velocity profiles, a radar reflectivity of at least 5 dBZ is required at approximately a 4.5-km altitude for the profile to be included in statistics. Profiles in this distribution that do not contain at least 40 sample times are discarded to avoid contamination from outliers. This is much more important in the LAM simulations than the CRM simulations because a significant number of LAM profiles have low sample sizes. The number 40 was chosen because it leads to median simulation sample sizes that are similar in magnitude to the

observationally derived sample size. For the LAM simulations, an additional restriction that discards all profiles outside of the CPOL domain is enforced. From each final simulation distribution, the 1st, 10th, 50th, 90th, and 99th percentile profiles are obtained and the underlying profiles determine the model spread. A single temporal mean profile obtained from the observational retrievals is then compared to these percentiles and the spread for a given model. Differences due to sample volume in observational retrievals and simulations are assumed to be minimal in stratiform regions, which by definition vary slowly in space and time. As was discussed in Chapter 2, the dual-profiler retrieval resolution varies with height but is slightly higher than model output. Six-panel figures comparing the dual-profiler retrievals to CRM output will be shown throughout this chapter. DHARMA-S, UKMO-2, MESONH-2, and SAM-S were left out of these figures because they are very similar to DHARMA-B, UKMO-1, MESONH-1, and SAM-B, respectively.

Having only samples in time and not in space, the dual-profiler retrieval is not representative of stratiform rain properties in the entire domain for this one event. This is clearly shown in Figure 5.1. This does not mean that it shouldn't be used, but that it should be put into proper context. The CPOL retrievals at a 2.5-km altitude show higher occurrences of radar reflectivity over 30 dBZ and rain rates over 2 mm hr^{-1}, even if CPOL retrieval uncertainty is taken into account. The dual-profiler retrievals also show larger D_0 values and smaller N_w values at most percentiles. These differences could be due to sampling differences and retrieval errors. Figure 5.2 shows the CPOL retrievals for the grid point closest to the profilers' location. The two retrievals agree much better in this comparison, which indicates that much of the difference in Figure 5.1 is due to

differences in samples. The differences that remain in Figure 5.2 are likely due to differences in sampling volume and retrieval technique, especially the larger dual-profiler samples of D_0 greater than 1.6 mm and $\log(N_w)$ greater than 3.5. Physically, these results make sense. The most well-developed and long-lived stratiform region was centered to the north of Darwin during the MCS event. Having many samples outside or on the edge of this stratiform region should yield fewer samples of high radar reflectivity and rain rate. Although not as obvious, they also yield fewer samples of low D_0 and high N_w, which may be due to less depletion of small raindrops through evaporation and raindrop breakup that may be occurring in strong stratiform rain.

5.3 Stratiform Radar Reflectivity and Rain Rate

As shown in Chapter 3, stratiform rainfall is underestimated in CRM and LAM simulations and the distribution of 2.5-km stratiform radar reflectivity substantially differs from observations. Figure 5.1 shows that dual-profiler retrieved radar reflectivity and rain rate distributions are missing higher values that appear in the CPOL retrieval. Since the dual-profiler retrievals that are heavily used in this chapter are not entirely representative, it is worth comparing the radar reflectivity and rain rate profiles derived from the profilers to the CRM and LAM simulations.

Figure 5.3 shows that the median of most CRM simulated mean radar reflectivity profiles is less than that in profiler observations. The lone exception is UKMO-2M, which has a median profile that almost matches the observationally retrieved profile. The dual-profiler retrieved mean profile, however, does fit within the distributions of all but the DHARMA-B simulation. Interestingly, the observed profile remains nearly constant

with height whereas simulations with one-moment rain schemes that assume $\mu = 0$ (DHARMA-B and MESONH-1) decrease toward the surface. Two-moment rain schemes in DHARMA-2M, UKMO-2M, and SAM-B, on the other hand, produce increasing values toward the surface. UKMO-2 using a one-moment scheme with $\mu = 2.5$ is the only simulation with a near constant radar reflectivity profile. LAM simulations in Figure 5.4 have higher radar reflectivities consistent with the results in Chapter 3, and therefore the observed profile fits well within the distribution of mean profiles in all of the simulations. Consistent with the CRM simulations, two-moment schemes in WRF-M and WRF-M2 show radar reflectivity slightly increasing toward the surface, while one-moment WRF-W shows radar reflectivity remaining approximately constant or slightly decreasing.

Figures 5.5 and 5.6 show distributions of CRM and LAM simulated stratiform rain rate profiles, respectively, with the dual-profiler retrieved mean profile in solid black. The dual-profiler retrieved profile fits within the distribution of possible profiles for every simulation, and some simulations such as UKMO-1 and WRF-W produce higher mean rain rates in a majority of profiles. This may appear to contradict the results in Chapter 3, but one must consider the profiler samples in the context of the CPOL samples. The profiler was in a location that missed a long period of well-developed stratiform rain that covered the CPOL domain to the north of the profiler location. As shown in Figure 5.2, dual-profiler retrievals of radar reflectivity, rain rate, D_0 and $\log(N_w)$ agree much better with CPOL retrievals over the profiler location than with CPOL retrievals for the entire domain that show many more samples of high stratiform rain rates. The mean 2.5-km altitude CPOL stratiform rain rate for the MCS event is 1.85 mm

hr^{-1} with an uncertainty range from 1.11 to 3.14 mm hr^{-1}. This means that the mean 2.5-km altitude dual-profiler retrieval is approximately the same as the lower uncertainty bound of the mean CPOL stratiform rain rate over the whole pentagonal forcing domain, and this is supported by Figures 5.1 and 5.2. This also means that only WRF-W produces mean stratiform rain rates close to mean CPOL derived stratiform rain rates at 2.5 km.

5.4 Stratiform Doppler Velocity

In stratiform regions, the vertical velocity is small (i.e., $|w| < 1$ m/s) and hence, S-band Rayleigh Doppler velocity is primarily a function of precipitation-sized particle fall speed. Simulated Doppler velocity is calculated from model output in an idealized manner similar to radar reflectivity so that a comparison can be made with observations, as is described in Section 2.3. While the one-moment schemes underestimate Doppler velocity in Figure 5.7, the two simulations (UKMO-1 and UKMO-2) that assume $\mu = 2.5$ are 1 m s^{-1} closer to observations than the simulations using $\mu = 0$, indicating a μ value greater than 0 may better approximate the stratiform rain size distribution. Simulations using various versions of the Morrison two-moment microphysics scheme predict Doppler velocity well at some height levels, but this is somewhat unexpected because all simulations underestimate radar reflectivity. Furthermore, the Doppler velocity profile shape is best approximated by one-moment schemes despite the lower than observed values. Observed Doppler velocity decreases linearly from 7.5 m s^{-1} at 4 km to 6.5 m s^{-1} at the surface due to increasing atmospheric density. In two-moment schemes, the Doppler velocity either remains constant or increases toward the surface indicating that

the rain size distribution is shifting too much toward larger raindrops, which is characteristic of excessive size sorting.

As shown in Figure 5.8, the dependence of LAM rain Doppler velocities on the prediction of rain number concentration is similar to that in the CRM simulations. The only one-moment scheme, WSM6, under-predicts the Doppler velocity by 1 to 1.5 m s^{-1}, although it does produce higher Doppler velocities than DHARMA-B and MESONH-1, the two CRM simulations with one-moment rain and $\mu = 0$. This is consistent with higher reflectivities and rain rates in WRF-W than in DHARMA-B and MESONH-1. WRF-W is also the only LAM simulation to reproduce the Doppler velocity vertical profile slope that shows the effect of air density dominating over any changes to raindrop size. WRF-T produces values similar to observed at all altitudes, but has the problem of incorrect slope that all two-moment rain schemes have, which is likely related to size sorting problems. WRF-M and WRF-M2 have this same issue but only from the melting level down to the 2.5-km height level before Doppler velocities begin decreasing toward the surface. This is likely a result of overly high Doppler velocities reaching limiting values in these simulations and air density effects taking over once those values are reached.

5.5 Stratiform Liquid Water Content

Figure 5.9 shows that simulations using one-moment schemes have profiles close to the retrieved mean LWC profile, which varies from 0.06 to 0.09 g m^{-3}, while those using two-moment schemes are furthest from observed values varying from 0.03 to 0.05 g m^{-3} between 1.5 and 3 km. Combined with the comparisons in Section 5.7, this

suggests that low rain rates are manifested in fall speeds for one-moment schemes with $\mu = 0$ (DHARMA-B, MESONH-1) and LWC for two-moment schemes (DHARMA-2M, UKMO-2M, SAM-B), whereas LWC in one-moment schemes with $\mu = 0$ are closer to observed and fall speeds in two-moment schemes are closer to observed. As might be expected, one-moment schemes with $\mu = 2.5$ such as UKMO-1 fall in between. Considering that reflectivity and rain rates are lower in CRM simulations than observations and lower observed reflectivities and rain rates are correlated with higher observationally retrieved D_0 and lower N_w, lower LWC should be expected in simulations while Doppler velocity remains fairly unchanged if they are to be consistent with observational retrievals.

Stratiform rain water content at the surface is compared to those retrieved by the Joss-Waldvogel disdrometer, but this disdrometer (described in Section 2.4.3) does not report raindrops smaller than 0.308 mm or larger than 5.258 mm. Therefore, simulated rain water content that is compared with the disdrometer is calculated for that limited range of sizes using incomplete gamma functions. Figure 5.10 shows that disdrometer observed liquid water contents have a median value of 0.07 g m^{-3} at the surface for raindrops larger than 0.308 mm, whereas median simulated values vary between 0.015 and 0.05 g m^{-3}. Radar reflectivity calculated from the disdrometer observations is within 1–2 dBZ of both the approximately co-located and coincident CPOL distribution at an altitude of 0.5 km and the 0.5-km altitude S-band profiler distribution. When the coincident requirement is dropped, then reflectivity distributions are very similar to those in Figure 5.2, so the disdrometer observations fit with the profiler and CPOL observations. This also means that the disdrometer sample is biased toward lower

stratiform reflectivities and rain rates at higher percentile values of these variables, as were the CPOL and S-band distributions at the location of the disdrometer in Figure 5.1. If the disdrometer location were more representative of all stratiform regions within the pentagonal domain in Figure 2.1, one could imagine that the disdrometer LWC distribution would have more samples at values greater than 0.1–0.2 g m^{-3}. That stated, lower percentiles are probably fairly representative assuming LWC varies as reflectivity and rain rate vary because lower percentiles of reflectivity and rain rate are similar for the disdrometer location and the entire pentagonal domain, as shown in Figure 5.1.

DHARMA-B, MESONH-1, and SAM-B have the highest median LWC of about 0.04–0.05 g m^{-3}. DHARMA-B and MESONH-1 are the simulations with the lowest mass-weighted rain fall speeds and this is reflected in the Doppler velocity in Figure 5.7, and therefore LWC would have to be higher than observed if it were to balance the fall speeds and reproduce observed rain rates. The disdrometer normalized CDF fits within the spread of 100 randomly selected simulated normalized CDFs for those simulations in Figure 5.10. The simulations (DHARMA-2M and UKMO-2M) with more realistic Doppler velocities of 6–7 m s^{-1} at the surface have much lower median LWC between 0.015 and 0.02 g m^{-3}, which cannot be accounted for by sampling and supports results drawn from the dual-profiler retrieval. The disdrometer normalized CDF does not fit within the spread of 100 randomly selected simulated normalized CDFs for these simulations in Figure 5.10.

The LAM LWC profiles in Figure 5.11 tell a slightly different story. Most WRF-W mean profiles have higher LWC than the mean observationally retrieved profile, while the median of WRF-T and WRF-M mean profiles are similar to the mean observationally

retrieved profile. In the case of WRF-W, the median LWC values are slightly greater than 0.1 g m^{-3}, significantly higher than the other simulations, despite being the only simulation to use a one-moment rain scheme (WSM6). The observationally derived profile would fall between the 1st and 10th WRF-W percentile profiles. Even with slightly lower than observed Doppler velocities, higher LWC values than observationally retrieved give WRF-W rain rates higher than those in the dual-profiler retrievals and similar to CPOL retrievals. Unfortunately, WRF-W, WRF-T, and WRF-M greatly under-predict stratiform area, as shown in Chapter 3. For the only simulation that produces stratiform area close to observed (WRF-M2), stratiform LWC is clearly lower than observed and falls in line with two-moment rain schemes used in the CRM simulations with LWC decreasing toward the surface. Comparisons to disdrometer observations in Figure 5.12 confirm the profiler comparison. WRF-W produces the highest LWCs followed by WRF-M, then WRF-T, and finally WRF-M2, which generally produces much lower LWC. The observationally derived profile, however, fits within the spread of 100 randomly selected normalized CDFs containing 40 or more samples for all simulations. However, some variables such as raindrop size, discussed next, and previously discussed Doppler velocity show greater disagreement between simulations and observationally derived values.

5.6 Stratiform Raindrop Size

Figure 5.13 shows simulated and CPOL observationally retrieved histograms of 2.5-km altitude stratiform median volume diameter (D_0) and the logarithm base-10 of the normalized size intercept ($\log(N_w)$). These variables are defined in Section 2.4.2. For

this figure and similar figures to follow, simulated values are calculated at the native simulation grid spacing, whereas CPOL retrievals are on a 2.5-km spaced horizontal grid. Simulated values were not calculated for 2.5-km grid spacing because it would require numerical solutions for size distributions that are no longer gamma distributions at that grid spacing. This difference in grid spacing should create minimal differences.

One-moment rain schemes with $\mu = 0$ (diamonds; up and down pointing triangles) in CRM simulations perform the worst with typical D_0 values around 0.6 mm that are significantly less than typical observed values of 1.2 mm. Typical N_w values for these schemes are 8×10^3 or 1×10^4 mm^{-1} m^{-3} ($\log(N_w)$ = 3.9 or 4) when most observationally retrieved $\log(N_w)$ values fall between 2.5 and 4 with a peak around 3.3. UKMO-1 and UKMO-2 (left and right pointing triangles), which use $\mu = 2.5$, produce greater D_0 values by about 0.2 mm over the one-moment schemes that use $\mu = 0$. UKMO-1 and UKMO-2 also do better predicting N_w with most values falling between 3 and 3.7. Two-moment rain schemes (circles, square, and x's) in CRM simulations are able to produce larger drops like those observed with distributions that are slightly too broad. Two-moment schemes represent the spread of observed N_w values better than UKMO-1 and UKMO-2, although their distributions are shifted to slightly lower values than observed. These two-moment issues may be due to a combination of excessive size sorting (Wacker and Seifert 2001; Morrison et al. 2009) and a fixed μ value of 0.

Vertical profiles of mass-weighted mean diameter (D_m), defined in Section 2.4.4 and shown in Figure 5.14 also look very different in one-moment and two-moment schemes and yield insight into the evolution of stratiform raindrops as they fall toward the surface. Recall that for a gamma distribution, $D_m = \frac{4+\mu}{3.67+\mu} D_0$. For one-moment

schemes with $\mu = 0$ in CRM simulations, D_m remains fairly constant at 0.8 mm, far lower than the observationally retrieved 1.4 mm. This can lead to excessive mass-relative evaporation in drier subcloud environments as discussed in Morrison et al. (2009). For the humid TWP-ICE active monsoon, this is not as important, but the mass-weighted fall speed is reduced by having too many small droplets, which produces the lower than observed rain rates despite LWC that is closer to observationally retrieved values. Increasing μ to 2.5 in UKMO-1 and UKMO-2 increases D_m to about 1 mm, closer to the observed value. If the dual-profiler retrieval were more representative of the entire CPOL domain, the one-moment schemes would be even closer to observations because observed D_m would be smaller based on Figures 5.1 and 5.2.

Although not shown, dual-profiler retrieved μ values in stratiform regions yield median values of 2 to 3 and mean values of 4 to 5 with only slight changes with height between 1.5 and 4 km altitudes. This indicates that a microphysics scheme with either a variable μ parameter or one greater than 0 such as the UKMO value of 2.5 will likely better represent stratiform rain because it is better able to represent the dispersion (narrowness) of the stratiform rain size distribution. Two-moment schemes also have LWCs that compare well with observations at 4 km, but have N_w values (not shown) that are too high and D_m values in Figure 5.14b, d, and f that are too low. Moving down from 4 km to 1.5 km, D_m increases by 0.2–0.3 mm to match observational retrievals in agreement with the comparison with CPOL retrievals at 2.5 km in Figure 5.13, while N_w (not shown) and LWC in Figure 5.9 decrease to less than those in observational retrievals. The D_m and N_w changes with height are likely more a function of size sorting than evaporation based on the humid subcloud environment and minimal change in one-

moment schemes with $\mu = 0$. The accumulation of reflectivity, rain rate, Doppler velocity, LWC, and raindrop size comparisons suggests that stratiform rain rates are too low at 2.5 km because they are too low at 4 km. This implies that there is likely not enough ice water content in CRM simulations just above the melting level, as is discussed further in Section 5.9.

Figure 5.15 shows LAM and CPOL observationally retrieved stratiform rain D_0 and $\log(N_w)$ distributions at a 2.5-km altitude. The difference between the one-moment WSM6 microphysics scheme in WRF-W (triangles), which strongly peaks at 0.6 mm, and the two-moment Morrison scheme in WRF-M (diamonds) and WRF-M2 (dashed line), which broadly peak around 1.3 mm, is similar to the difference between the one-moment and two-moment schemes in the CRM simulations. WRF-T (squares) is unique in that it uses a two-moment rain formulation but has few samples of D_0 greater than the observationally retrieved peak of 1.2 mm, whereas WRF-M and WRF-M2 have many samples greater than 1.5 mm. The reasons for this difference in two-moment schemes are still unclear and need to be further investigated, but may be related to an initially higher rain number concentration in WRF-T just below the melting level due to its unique snow scheme that was discussed in Chapters 3 and 4. Smaller D_0 in WRF-T is associated with N_w values in Figure 5.15b that almost match those retrieved with CPOL, whereas N_w values in WRF-M and WRF-M2 are generally lower than the CPOL retrieved values, which is consistent with the large D_0 values and the CRM statistics from runs using the Morrison two-moment scheme. As in the CRM simulations, a one-moment rain scheme such as WSM-6 in WRF-W that assumes a constant size intercept performs poorly with respect to stratiform raindrop size.

A comparison of the spread of time-mean profiles of D_m in the LAM simulations and the time-mean dual-profiler retrieved profile between 1.5- and 4-km altitudes are shown in Figure 5.16. Consistent with the CRM results, WRF-W with one-moment rain shows very little spread and little change in D_m with height as is produced in the observational retrieval, but with an offset of 0.5 mm to lower values. The rest of the WRF simulations employ two-moment schemes that show D_m increasing from 4 km down to 1.5 km, also consistent with CRM results and the conclusion that excessive size sorting is occurring. D_m values reach larger sizes in the WRF-M2 simulation because it does not have the same artificial limit on the slope parameter (λ) that WRF-M has, but instead uses a raindrop breakup parameterization described in Morrison et al. (2012). As was hypothesized from the comparisons in Figure 5.15, 4 km WRF-T D_m values are less than those in WRF-M and WRF-M2, a major reason for the difference at 2.5 km.

5.7 Convective Raindrop Size

The size of raindrops in convective updrafts is important because raindrop fall speeds determine whether the rain will be lofted and frozen or whether it will fall out of the updraft. Furthermore, as shown in Morrison et al. (2012), the size of rain in convective downdrafts affects the evaporative cooling rate, which impacts the strength of the downdraft and cold pool. Dual-profiler DSD retrievals do not give a large enough sample size to be used in convective regions, but the CPOL retrievals at a 2.5-km altitude yield sample sizes large enough to be compared with simulated convective rain DSD properties. Figure 5.17 shows histograms of CRM simulated versus CPOL retrieved convective D_0 and $\log(N_w)$ values for the entire MCS event. There is a stark contrast

between one-moment and two-moment microphysics schemes as was the case for the stratiform statistics. However, the one-moment schemes (diamonds; up and down triangles) with $\mu = 0$ perform well in approximating the observed D_0 distribution in convective regions, whereas they performed poorly in stratiform regions. It is not all that surprising that one-moment rain schemes do well in convective regions because most of them fix N_w close to 8×10^3 or 1×10^4 mm^{-1} m^{-3} ($\log(N_w)$ = 3.9 or 4) and $\mu = 0$, which guarantees a preponderance of small raindrops (see solid black line in Figure 1.1) as might be expected on average in high rain rates due to raindrop breakup (Srivastava 1971; McTaggart-Cowan and List 1975; Tokay and Short 1996). Despite being slightly worse in replicating CPOL derived N_w, UKMO-1 and UKMO-2 using a one-moment scheme with $\mu = 2.5$ best approximates the CPOL derived D_0 distribution. The observational retrieval actually shows a majority of N_w values greater than 1×10^4 mm^{-1} m^{-3}, whereas two-moment schemes predict most N_w values an order of magnitude less than that. Two-moment schemes produce a D_0 distribution that is too broad with too many samples below 0.8 mm and above 1.8 mm values. The two-moment D_0 values between 0.2 and 0.8 mm occur in convective updrafts where large amounts of cloud water are converting to raindrops. The sharp D_0 peak between 1.8 and 1.9 mm in some two-moment simulations is due to the use of limits on λ, which prevents excessively large raindrops in the absence of a raindrop breakup scheme. Recent versions of the Morrison scheme, such as the one used in DHARMA-2M and WRF-M2, have been updated to include a raindrop breakup formulation (Morrison et al. 2012) in which D_0 is relaxed to an equilibrium value of 2.2 mm. This does not have nearly as significant an effect on distributions of D_0 and N_w as do differences in the number of prognostic

moments or the value of μ. The primary difference between the newer version of the Morrison scheme and older versions is that the extreme peak between 1.8 and 1.9 mm due to artificial limits on λ in the absence of a raindrop breakup parameterization is removed.

Figure 5.18 shows LAM simulated and CPOL retrieved D_0 and $\log(N_w)$ distributions for convective regions at a 2.5-km altitude. As in CRM simulations, the LAM simulations that use two-moment rain schemes have convective D_0 distributions that are too broad. Whereas the small D_0 values are primarily associated with conversion of large cloud water contents to rain, the large D_0 values may be due to excessive size sorting (see Wacker and Seifert (2001) and Morrison et al. (2009)) and insufficient balancing of raindrop formation, collision-coalescence, and breakup processes. It is also not possible to rule out effects from melting ice on initial raindrop size and influences of CCN on cloud water amount and droplet size, which can affect rain formation and collision-coalescence. WRF-T (squares) produces many more small raindrops than WRF-M (diamonds) and WRF-M2 (dashed line) as occurred in stratiform regions, while the λ limits in WRF-M and WRF-T produce sharp peaks in the D_0 distribution. Whereas the CRM simulations that used one-moment schemes closely resembled the CPOL derived D_0 distribution that peaks around 1.4 mm, the distribution in WRF-W (triangles) peaks at a lower value of 1 mm even though CPOL derived convective N_w values tend to be higher than the constant value of 8×10^3 mm^{-1} m^{-3} ($\log(N_w) = 3.9$) in WRF-W. Convective N_w distributions in two-moment schemes have too many low values, consistent with the large D_0 values. The sensitivity of convective D_0 and N_w values to different convective raindrop breakup parameterizations needs to be further tested in

tropical environments to rule out other factors and isolate the role of excessive size sorting.

5.8 Correlating Radar Reflectivity, Rain Rate, and Raindrop Sizes

Comparing distributions of individual variables is informative, but investigating their variability versus one another yields additional information. Figures 5.19 and 5.20 show that both CPOL retrieved and simulated convective radar reflectivity increases as D_0 increases. Two-moment schemes shaded in 5.19b–d and 5.20 typically produce larger values of D_0 for a given radar reflectivity between 30 and 50 dBZ. One-moment schemes with $\mu = 0$ (dashed) produce the best fit, but are also slightly offset to higher D_0 for a given radar reflectivity, which is consistent with CPOL retrievals producing N_0 values larger than what is assumed in the constant size intercept one-moment schemes. When μ is increased to 2.5 in a one-moment scheme (shaded in 5.19a), simulated values move farther away from CPOL retrieved values. For the two-moment schemes, it is unclear whether this discrepancy with observational retrievals is primarily due to representation of raindrop formation and breakup or excessive size sorting, but judging from results in the previous sections, a good deal of it is probably due to excessive size sorting.

Figures 5.21 and 5.22 show that for a given convective rain rate, D_0 is generally larger in two-moment schemes as well. Observational retrievals show D_0 asymptote to between 1.5 and 2 mm at high rain rates, but simulations with two-moment schemes asymptote to higher values at lower rain rates relative to CPOL retrievals. As was the case for radar reflectivity, one-moment schemes with $\mu = 0$ (dashed) perform best, but also produce values of D_0 that are too large at high rain rates, again likely owing to higher

size intercepts in observational retrievals produced by raindrop breakup that constant size intercept one-moment schemes cannot replicate.

The relationship between stratiform radar reflectivity and D_0 is represented better by some two-moment schemes than was convective radar reflectivity and D_0, as shown in Figures 5.23b–d and 5.24. The primary issue in most two-moment schemes is the overproduction of low stratiform radar reflectivities. For the two-moment schemes that do produce high stratiform reflectivities in 5.23b and 5.24b, D_0 is larger in simulations than observational retrievals, likely due to excessive size sorting. As opposed to convective regions, one-moment schemes with $\mu = 0$ (dashed) generally yield the worst fit to observational retrievals in stratiform regions with smaller radar reflectivities for a given D_0 value than observationally retrieved. Increasing μ to 2.5 in a one-moment scheme in Figure 5.23a shows much better agreement with CPOL retrievals, indicating as previous results and other studies have, that μ is generally greater than 0 in stratiform regions due to a lack of very small raindrops and less dispersion. As was mentioned in Section 5.6, dual-profiler retrievals produce median values of μ between 2 or 3 at all height levels between 1.5 and 4 km with mean values between 4 and 5.

Two-dimensional histograms of stratiform rain rate versus D_0 in Figures 5.25 and 5.26 reinforce conclusions drawn from Figures 5.23 and 5.24. For a given rain rate, D_0 is too small in one-moment schemes with $\mu = 0$, but increasing the value of μ to 2.5 produces better results. The two-moment schemes that reproduce the radar reflectivity versus D_0 relationship but had too many low radar reflectivities also reproduce the rain rate versus D_0 relationship but with too many low rain rates, an exception being the Thompson scheme in the WRF-T simulation. As mentioned in previous sections, this

may be related to the unique snow formulation used in the Thompson scheme. For the two-moment schemes that produce higher reflectivities, D_0 is too large for a given rain rate, likely due in part to excessive size sorting. Incorrect initial size of raindrops produced by melting snow could also be an issue for WRF-M and WRF-M2. As shown in Figure 5.15, these simulations have larger raindrops at 4 km than other simulations using two-moment schemes.

Although not shown, two-dimensional histograms of radar reflectivity and rain rate versus $\log(N_w)$ produce the same conclusions as those drawn above. Two-moment schemes can also replicate the shift from smaller D_0 and N_w in stratiform regions to larger D_0 and N_w in convective regions, although the values are different in observational retrievals and simulations. This distinct shift that clearly separated convective and stratiform regions was shown in Bringi et al. (2009).

5.9 Link to Ice Water Content Aloft

Figure 5.27 shows that stratiform rain rates at a 4-km altitude are well correlated to stratiform ice water content (IWC) at a 5.5-km altitude for all simulations. The slope of their relationship varies based on the microphysics scheme used but increasing 5.5-km IWC increases 4-km rain rate in all cases. DHARMA-B is an outlier from other simulated relationships because it uses the Grabowski (1999) microphysics scheme that uniquely combines cloud ice and snow and places a substantial portion of the IWC into the cloud ice mode yielding much slower fall speeds for a given IWC than are produced by other simulations. One-moment schemes produce higher 4-km rain rates for a given 5.5-km IWC than two-moment schemes, which is likely related to the size sorting issues

in the two-moment schemes. With all CRM simulations and WRF-M2 under-predicting stratiform rain rate just below the melting level, it is clear that increasing IWC just above the melting level will yield greater rain rates. Further evidence for this assertion is shown by the WRF-W, WRF-T, and WRF-M simulations (5.27g-i), which give stratiform rain rates closest to observed and also have the highest stratiform IWCs at 5.5 km.

It is interesting to note that the SAM simulations, which use hail rather than graupel and are more stable in the upper troposphere than other simulations, as shown in the environmental MSE profiles in Figure 4.14, produce more stratiform IWC than other CRM simulations using two-moment schemes. Faster fallout of hail than graupel allows a greater amount of snow to form as shown in Figure 4.7, and the greater stability aloft relative to other simulations may allow for more convective detrainment of condensate and buoyancy into stratiform regions at midlevels, but this is purely speculation. To have insufficient IWC at the melting level in stratiform regions does suggest that convective detrainment and representation of the large-scale environment including model forcing methodology are possible sources for the low bias in stratiform rain rate. Del Genio et al. (2012) found that free tropospheric relative humidity had a significant impact on the growth and maintenance of stratiform regions, while several others (Tao et al. 1995; Ferrier et al. 1996; Morrison et al. 2009; Luo et al. 2010) have pointed out that strong convection that primarily detrains in the upper troposphere does not transfer condensate, buoyancy, and momentum to stratiform regions at midlevels as effectively as weaker convection that detrains at lower levels. Unfortunately, diagnosing this detrainment in three-dimensional simulations is much more difficult than the primarily studied idealized two-dimensional squall line simulations.

To examine possible effects of environmental humidity and vertical velocity on stratiform IWC, mean profiles of these variables are separated into convective, stratiform, and nonclassified regions and plotted in Figures 5.28 and 5.29. Figure 5.28 confirms the assertion in Del Genio et al. (2012) that the ECMWF analysis has a dry bias. Relative to the variational analysis at 18Z on 1/23 shown in black in 5.28a–c, the ECMWF analysis in the CPOL domain at 18Z on 1/23 shown in black in 5.28d–f is drier throughout the troposphere. This dry bias is clearly present in nonclassified regions of all LAM simulations in 5.28f. WRF-M2 (dashed line), which produced much more stratiform area than the other WRF simulations but with lesser mean rain rates, differs from the other WRF simulations in that it is significantly more humid in the upper troposphere above 10 km. It's also slightly more humid in convective and stratiform regions between 10-km and 15-km altitudes. This may lessen sublimation rates of detrained ice in the upper troposphere and produce some growth of ice above 12 km where conditions are slightly supersaturated with respect to ice on average. As was mentioned in Chapter 4, WRF-W (triangles) has a significant dry bias above 8 km, which could be leading to smaller and weaker convective updrafts. The causes for this are unknown, but could be related to interactions of the WSM6 scheme with other parameterizations in the outer domains. CRM simulations produce relative humidity (*RH-RHi*) profiles that are close to those in the variational analysis, but tend to be slightly drier at low levels. It is unclear how this relates to convective properties, but *RHi* values aloft are similar between CRM simulations and the variational analysis.

Despite similarities in *RHi* aloft, CRM simulations show a wide range of mean stratiform vertical velocity profiles in Figure 5.29b. With the exception of DHARMA-B,

simulated mean stratiform vertical velocity profiles switch from negative to positive between 6 and 9 km. LAM simulated vertical velocities also switch over from negative to positive vertical velocity at 7 km, nearly 2 km above the melting level. No immediately clear correlations exist between convective updraft properties and stratiform vertical velocity profiles. CRM mean vertical velocity profiles in nonclassified regions show a lot of variability with magnitudes similar to those in stratiform regions. Generally positive vertical velocity in the upper troposphere may be related to deposition in anvils with *RHi* greater than 100 percent and significant amounts of cloud ice (not shown) at those levels. LAMs exhibit much lower vertical velocities in nonclassified regions. Higher vertical velocities in both nonclassified and stratiform regions in WRF-M and WRF-M2 that used the Morrison microphysics scheme may be related to more cloud ice and greater *RHi* in those simulations. Differences in CRM and LAM simulated mean convective vertical velocity profiles are partially due to differences in convective area, i.e., simulations with more convective area have lesser mean vertical velocity, but all profiles have a similar shape. Unfortunately, there are no clear connections between humidity, vertical velocity, and stratiform IWC just above the melting level. If anything, humidity and vertical velocity in nonconvective regions appear more related to stratiform area than to stratiform precipitation intensity.

This does not mean that convective properties are not having an impact on stratiform properties common to all CRM and LAM simulations. An immediately obvious problem using the CRMs to simulate the MCS case is that the domain size with assumed periodic lateral boundary conditions is unable to resolve the mesoscale circulations associated with the observed squall line and stratiform region. This inhibits a

mesoscale potential vorticity anomaly and strong mesoscale updraft from forming, which likely reduces stratiform rainfall by effectively reducing *RHi* and increasing cloud base. As shown in Figures 5.28b and 5.28e, many simulations produce mean stratiform *RHi* profiles above the melting level that are subsaturated. This leads to mean sublimation of stratiform ice before it ever reaches the melting level and mean downward motion beginning at 7–8 km in Figures 5.29b and 5.29e rather than at the melting level or below the melting level, where cloud base would be expected to be found in a more well-developed stratiform region, as shown in Chen and Frank (1993) and discussed more broadly in Houze (2004). Because the CRMs are forced to reproduce overall rainfall, too little stratiform rainfall requires too much convective rainfall. Over-predicted stratiform area and under-predicted rain rates, however, are found throughout the simulated six-day active monsoon period as are convective biases, so unresolved mesoscale circulations are only one piece of the puzzle for the MCS event.

There is also the impact of convective updraft tilting on detrainment. The simulated left moving supercellular convection tends to be downshear tilted, which limits detrainment to stratiform regions relative to upshear tilted updrafts as one would have expected during the squall phase that occurred in observations. This is related to the propagation speed of the convective cells. Supercell propagation is controlled by the midlevel negative pressure perturbations and is slower than the advecting winds at midlevels. Despite reverse environmental vertical shear above 5 km, this slow movement creates downshear updraft tilting. The observed system clearly developed into a fast moving squall line with a trailing stratiform region indicating upshear updraft tilting, which reduces precipitation efficiency relative to downshear tilting as discussed in Ferrier

et al. (1996), while maximizing detrainment to stratiform regions. Therefore, convective mode may not only play a role in convective updraft properties as discussed in Chapter 4, but also play a role in detrainment to stratiform regions. This deserved further attention in future research.

Lastly, there is the issue of large IWCs in convective updrafts being advected over large regions and inflating the size of convective areas using the Steiner et al. (1995) convective-stratiform separation algorithm. This is especially noticeable in WRF simulations that produce areas of slower moving convection near the center of the mesoscale cyclonic rotation that develops, which leads to an accumulation of large amounts of ice in that region. This ice melts and often produces radar reflectivity echoes of over 40 dBZ at 2.5 km, which is immediately classified as convective. In reality, the dynamics in such regions are likely closer to stratiform than convective, and not including them in stratiform statistics may lower mean stratiform rain rates. This effect appears to be secondary to other effects however, and correcting for it would not completely make up for the large differences in observed and simulated stratiform rainfall.

5.10 Discussion

Stratiform rain is not only dependent on the rain microphysics, but also the amount of ice aloft, which is a function of convective detrainment. Therefore, there is no perfect fix for the distribution of stratiform rain without getting convective regions and large-scale forcing correct. Observational retrievals of rain DSDs do in fact show that there is not enough stratiform ice melting into rain in simulations, without distinguishing

features between one-moment and two-moment microphysics schemes. This finding is somewhat different from results shown for simulations of mid-latitude continental squall lines (e.g., Morrison et al. 2009; Bryan and Morrison, 2012) in which two-moment rain schemes outperformed one-moment schemes because of excessive evaporation in the one-moment schemes. Subcloud relative humidity is much higher in this case, which limits excessive evaporation in one-moment schemes. This takes the focus off of one-moment schemes and shifts it on to both one-moment and two-moment schemes. Fall speeds are reasonable in some two-moment simulations and over-predicted in others, but LWC is too low, whereas LWC is reasonable in several one-moment schemes that set $\mu = 0$, but fall speeds are too low. One-moment schemes with $\mu = 2.5$ produce LWC that is slightly too low and fall speeds that are slightly too low, a result that falls in between the one-moment and two-moment scheme results with $\mu = 0$. WRF simulations that produce the highest stratiform rain rates that are closest to observed also have the highest stratiform IWC. Therefore, it appears that low biased stratiform rain rates are due to low biased stratiform IWC. Consistency in CPOL and dual-profiler retrievals gives confidence in this conclusion. As is discussed in Luo et al. (2010), the issue with stratiform IWC may be related to simulated convective updrafts being too strong, which produces too much convective detrainment at high levels above 10 km rather than between 5 and 10 km. Morrison et al. (2009) also showed greater detrainment of buoyancy and condensate from convective regions to stratiform regions in weaker convection. Stronger convective modes in simulations could be playing a role in amplifying convective precipitation efficiency and increasing the contribution of convective updrafts to the overall upward mass flux aloft at the expense of stratiform

development. Additionally, the CRM simulations are not able to resolve mesoscale circulations on the scale of their domain size, while stratiform area in LAM simulations is limited by low biases in relative humidity in the ECMWF analysis. Lastly, the Steiner algorithm is defining some unrealistically large convective regions in some simulations because of the large IWCs produced in convective updrafts being lofted high and being advected over large regions. If this were not occurring, presumably more area would be identified as stratiform and perhaps improve some of the simulated stratiform statistics.

Despite the need for improvements in convective dynamics and microphysics, there are still potential improvements based on observational retrievals of stratiform rain that can be implemented and tested in cloud-resolving simulations. Among these are a three-moment bulk scheme allowing variable μ, a two-moment bulk scheme with variable diagnostic μ, and a two-moment bulk scheme with μ greater than 0. UKMO simulations using $\mu = 2.5$ generally produce the best agreement with stratiform observational retrievals. One-moment simulations using $\mu = 0$ produce too many small raindrops and two-moment simulations using $\mu = 0$ produce excessive size sorting. Both can be at least partially solved by increasing μ. Several observational studies (Waldvogel 1974; Tokay and Short 1996; Bringi et al. 2003, 2009) also show typical μ values can be substantially greater than 0, especially in stratiform regions. This has impacts on fall speed, processes such as evaporation, and reflectivity used to define convective and stratiform regions. The problem with a three-moment bulk rain scheme is that it increases computing time with the addition of a prognostic variable. There are several diagnostic μ-λ relationships based on observations that exist in the literature that would minimally increase computing time (e.g., Zhang et al. 2003; Milbrandt and Yau 2005;

Cao et al. 2008; Seifert 2008), but these need to be tested more extensively in addition to $\mu = 2.5$ two-moment bulk schemes in simulations of a variety of convective systems.

Raindrop size is also problematic in convective regions. Morrison et al. (2012) showed strong dependence of mid-latitude squall line simulations on the parameterization of raindrop breakup due to its influence on rain evaporation in convective downdrafts, which then affect downdraft and cold pool intensity. Comparisons of simulated and observationally retrieved convective D_0 and N_w distributions at a 2.5-km altitude show that simulations employing two-moment rain schemes tend to have too many large raindrops. Almost certainly, some of this is due to excessive size sorting, but it is unclear whether this is the dominant cause or whether microphysical processes such as raindrop formation and breakup are greater causes. Of course, at this altitude, D_0 and N_w distributions are going to be sensitive to the location of cloud water conversion to rainwater and the relation of rain mass and number concentration fall speeds to vertical velocity. Furthermore, in the rain forming environment of a convective draft, many situations often do not yield equilibrium between collision-coalescence and raindrop breakup (McFarquhar et al. 2010). Morrison et al. (2012) show that altering the raindrop breakup parameterization in a two-moment simulation of a mid-latitude continental squall line significantly alters the evolution of the squall line. The parameterization in the current Morrison microphysics scheme in the WRF-ARW model relaxes D_0 to an equilibrium 2.2 mm, which is greater than any values in the CPOL retrieval. These points suggest that the parameterization of raindrop breakup should be tested further in different large-scale environments and model setups to test whether 2.2 mm is a

reasonable value and if so, the reasons that observational retrievals and/or simulations produce values far different than this equilibrium value.

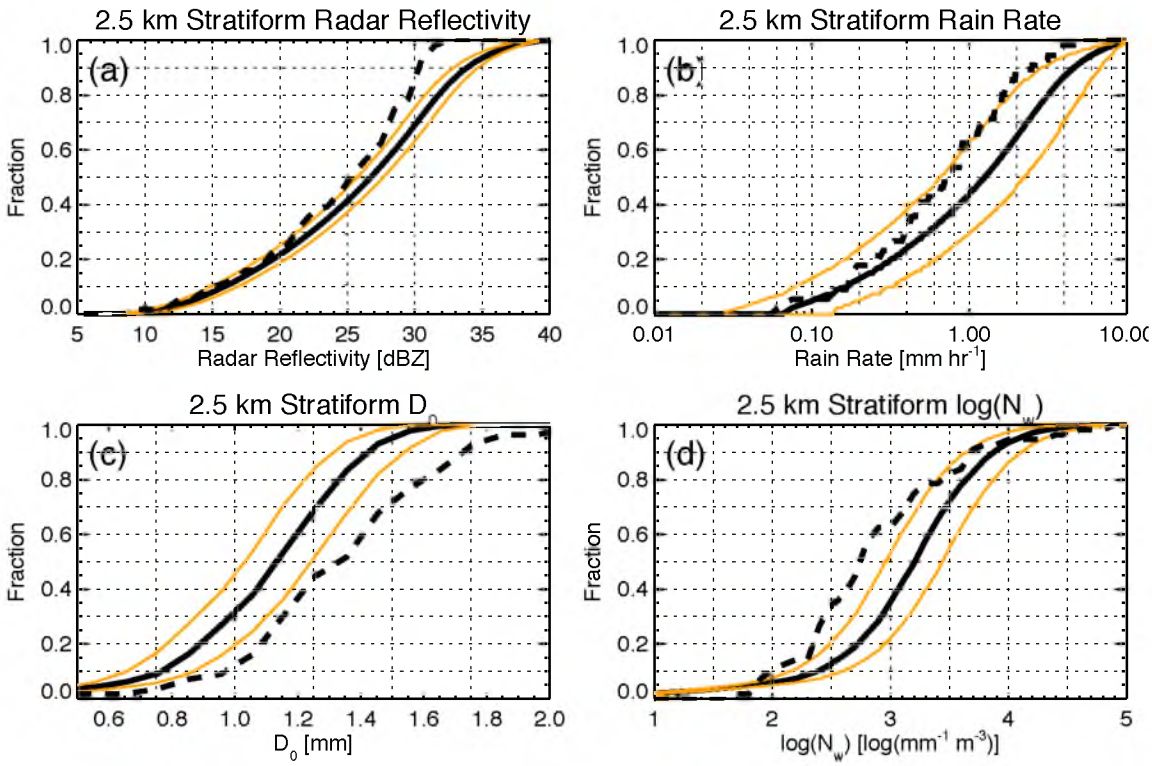

Figure 5.1. Normalized cumulative distributions of stratiform (a) radar reflectivity, (b) rain rate, (c) median volume diameter (D_0), and (d) normalized size intercept ($\log(N_w)$) for CPOL retrievals (solid black) and dual-profiler retrievals (dashed black) at an altitude of 2.5 km. Orange lines indicate uncertainty in CPOL retrievals. Dual-profiler retrievals were sampled every 10 minutes but CDFs are similar when all one-minute stratiform samples are included.

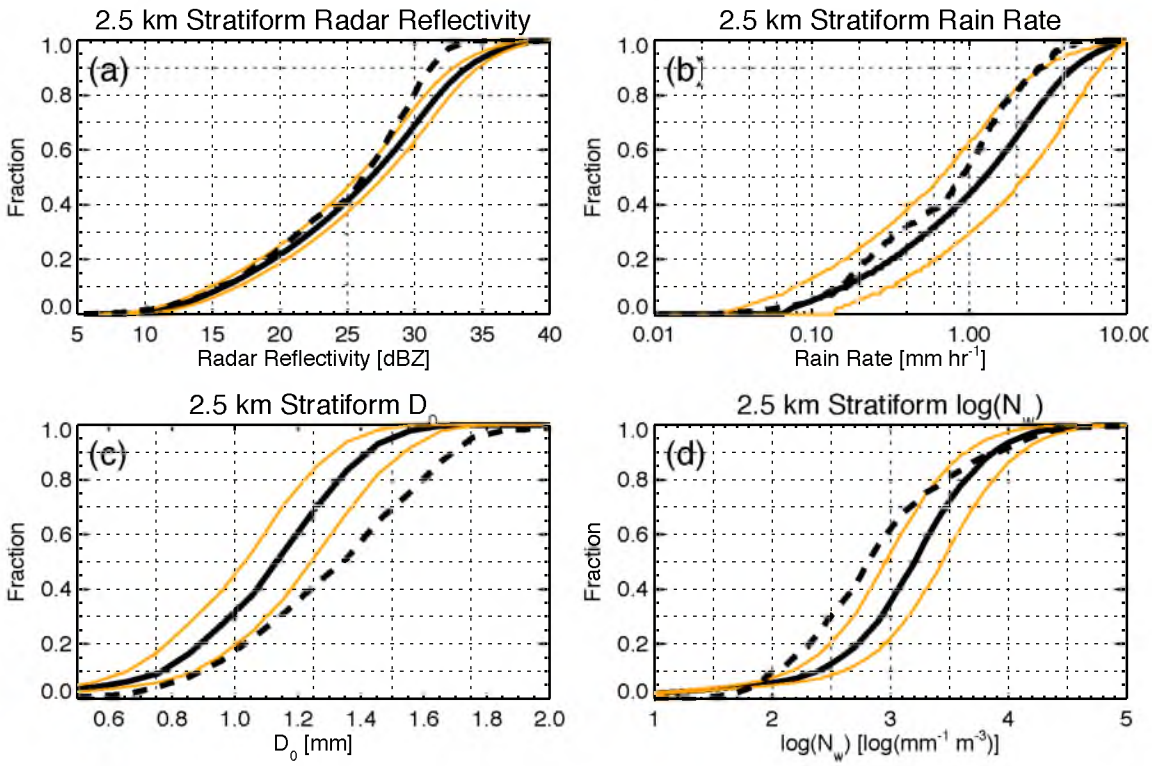

Figure 5.2. Normalized cumulative distributions of stratiform (a) radar reflectivity, (b) rain rate, (c) median volume diameter (D_0), and (d) normalized size intercept ($\log(N_w)$) for CPOL retrievals (solid black) at the grid point closest to the profiler location and dual-profiler retrievals (dashed black) at an altitude of 2.5 km. Orange lines indicate uncertainty in CPOL retrievals. Dual-profiler retrievals were sampled every 10 minutes but CDFs are similar when all one-minute stratiform samples are included.

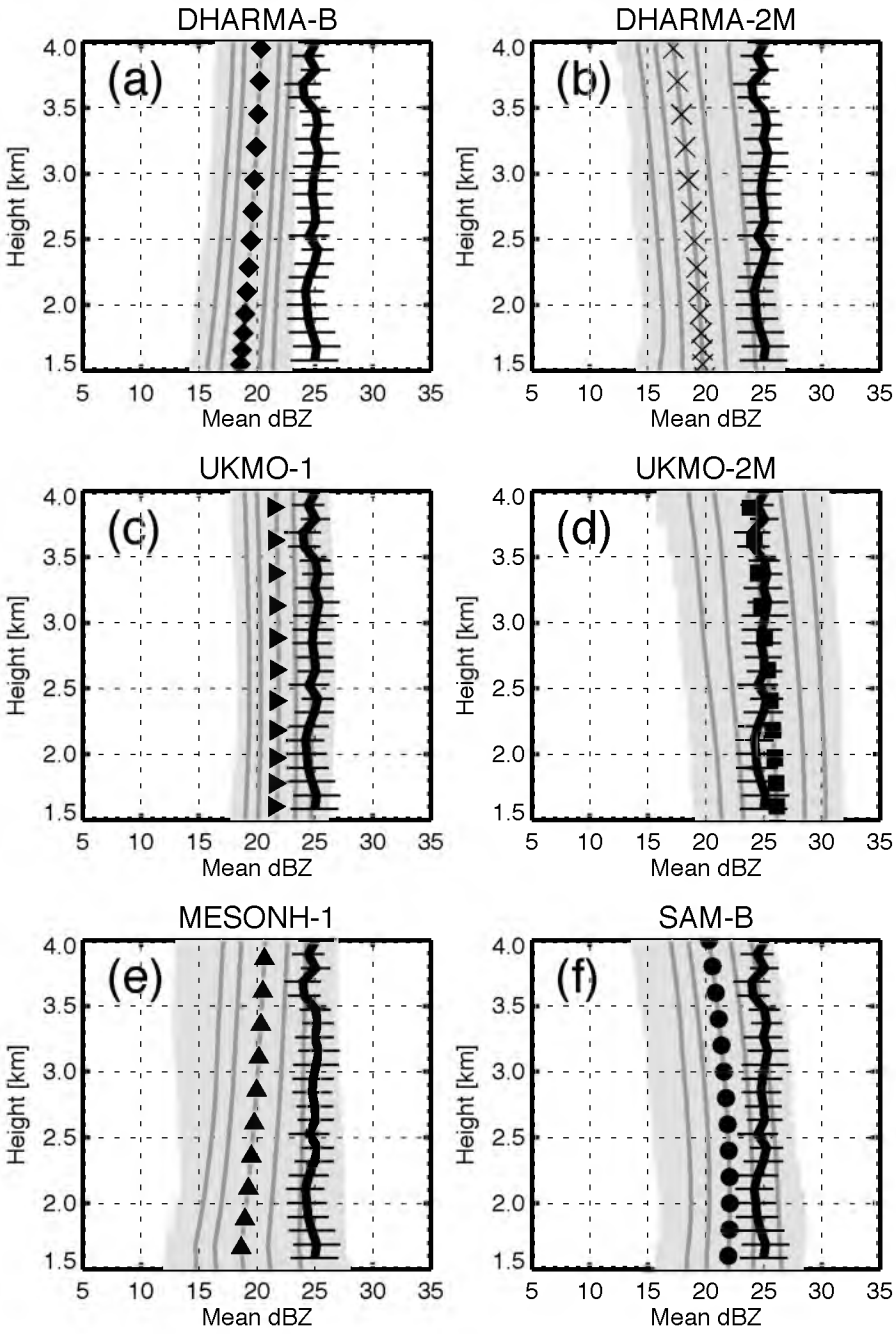

Figure 5.3. Temporal mean deep stratiform radar reflectivity profiles for (a) DHARMA-B, (b) DHARMA-2M, (c) UKMO-1, (d) UKMO-2M, (e) MESONH-1, and (f) SAM-B. The solid black line represents the temporal mean profile derived from dual-profiler retrievals with the standard error represented by horizontal bars. Simulations have a population of mean profiles, one at each horizontal grid point in the model, and are thus represented by a distribution. Mean profiles are discarded from the distribution if they do not have at least 40 samples. The median of this distribution is represented with symbols. The 1st, 10th, 90th, and 99th percentiles are shown in dark gray with the filled area encompassing all valid profiles.

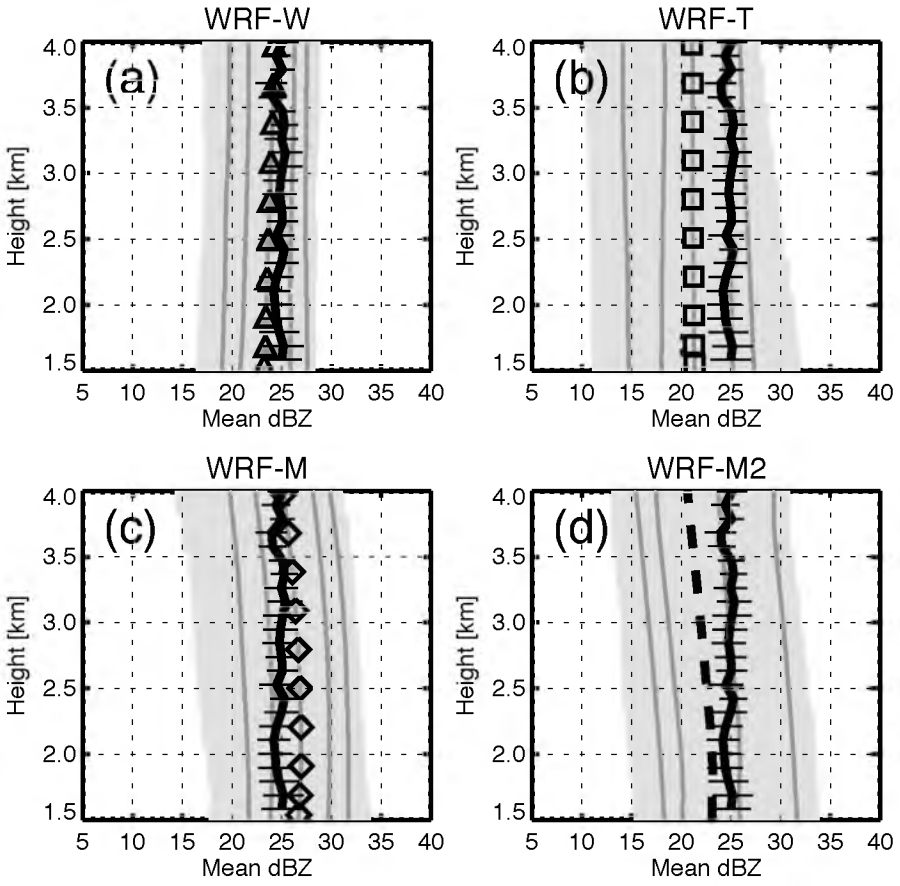

Figure 5.4. Temporal mean deep stratiform rain radar reflectivity profiles for (a) WRF-W, (b) WRF-T, (c) WRF-M, and (d) WRF-M2. The solid black line represents the temporal mean profile derived from dual-profiler retrievals with the standard error represented by horizontal bars. Simulations have a population of mean profiles, one at each horizontal grid point in the model, and are thus represented by a distribution. Mean profiles are discarded from the distribution if they do not have at least 40 samples. The median of this distribution is represented with symbols. The 1st, 10th, 90th, and 99th percentiles are shown in dark gray with the filled area encompassing all valid profiles.

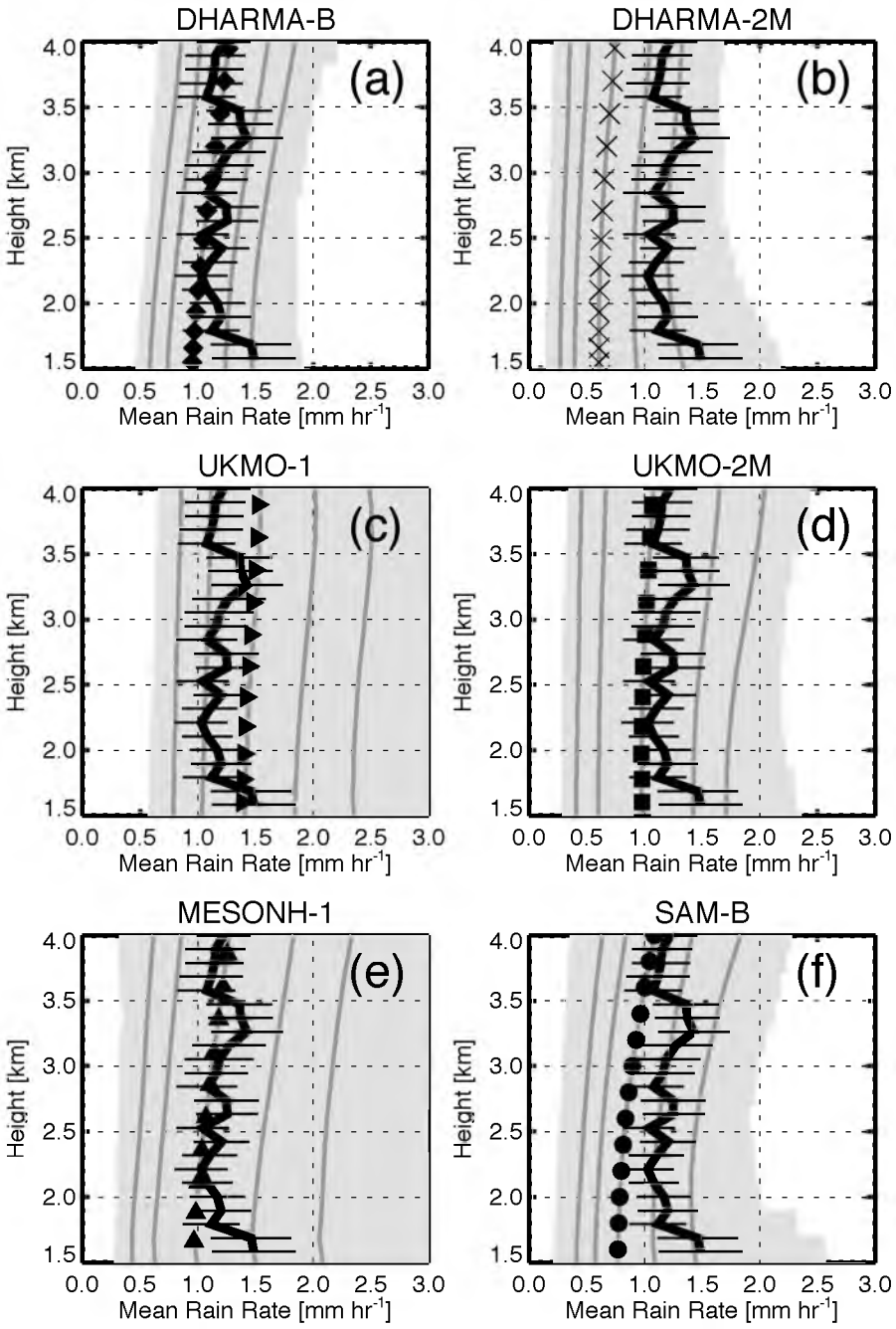

Figure 5.5. Temporal mean deep stratiform rain rate profiles for (a) DHARMA-B, (b) DHARMA-2M, (c) UKMO-1, (d) UKMO-2M, (e) MESONH-1, and (f) SAM-B. The solid black line represents the temporal mean profile derived from dual-profiler retrievals with the standard error represented by horizontal bars. Simulations have a population of mean profiles, one at each horizontal grid point in the model, and are thus represented by a distribution. Mean profiles are discarded from the distribution if they do not have at least 40 samples. The median of this distribution is represented with symbols. The 1st, 10th, 90th, and 99th percentiles are shown in dark gray with the filled area encompassing all valid profiles.

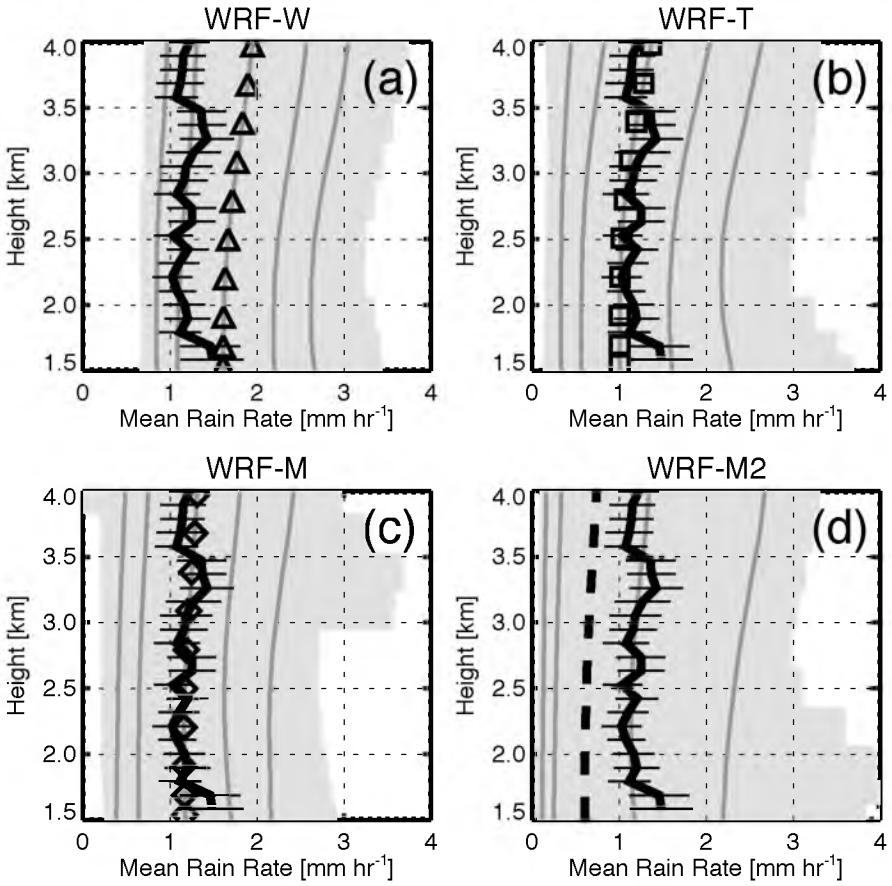

Figure 5.6. Temporal mean deep stratiform rain rate profiles for (a) WRF-W, (b) WRF-T, (c) WRF-M, and (d) WRF-M2. The solid black line represents the temporal mean profile derived from dual-profiler retrievals with the standard error represented by horizontal bars. Simulations have a population of mean profiles, one at each horizontal grid point in the model, and are thus represented by a distribution. Mean profiles are discarded from the distribution if they do not have at least 40 samples. The median of this distribution is represented with symbols. The 1st, 10th, 90th, and 99th percentiles are shown in dark gray with the filled area encompassing all valid profiles.

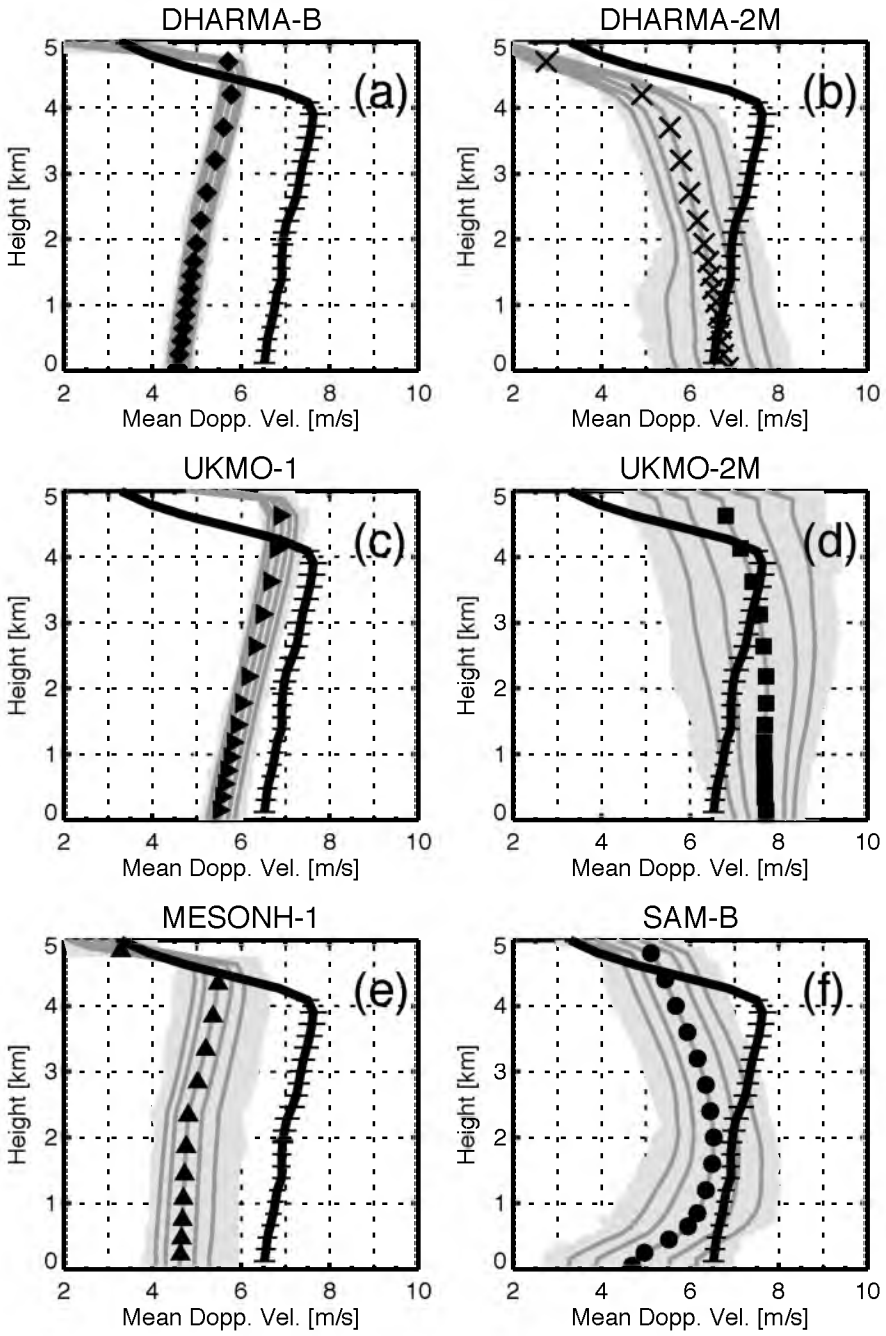

Figure 5.7. Temporal mean deep stratiform Doppler velocity profiles for (a) DHARMA-B, (b) DHARMA-2M, (c) UKMO-1, (d) UKMO-2M, (e) MESONH-1, and (f) SAM-B. The solid black line represents the temporal mean profile derived from dual-profiler retrievals with the standard error represented by horizontal bars. Simulations have a population of mean profiles, one at each horizontal grid point in the model, and are thus represented by a distribution. Mean profiles are discarded from the distribution if they do not have at least 40 samples. The median of this distribution is represented with symbols. The 1st, 10th, 90th, and 99th percentiles are shown in dark gray with the filled area encompassing all valid profiles.

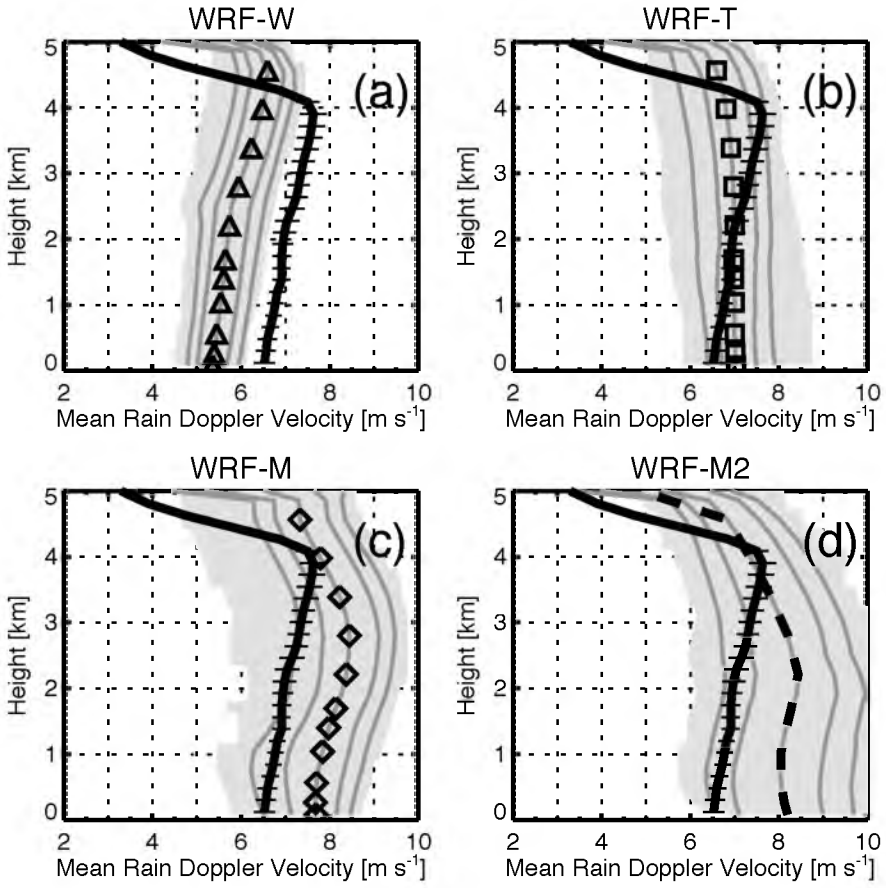

Figure 5.8. Temporal mean deep stratiform rain Doppler velocity profiles for (a) WRF-W, (b) WRF-T, (c) WRF-M, and (d) WRF-M2. The solid black line represents the temporal mean profile derived from dual-profiler retrievals with the standard error represented by horizontal bars. Simulations have a population of mean profiles, one at each horizontal grid point in the model, and are thus represented by a distribution. Mean profiles are discarded from the distribution if they do not have at least 40 samples. The median of this distribution is represented with symbols. The 1st, 10th, 90th, and 99th percentiles are shown in dark gray with the filled area encompassing all valid profiles.

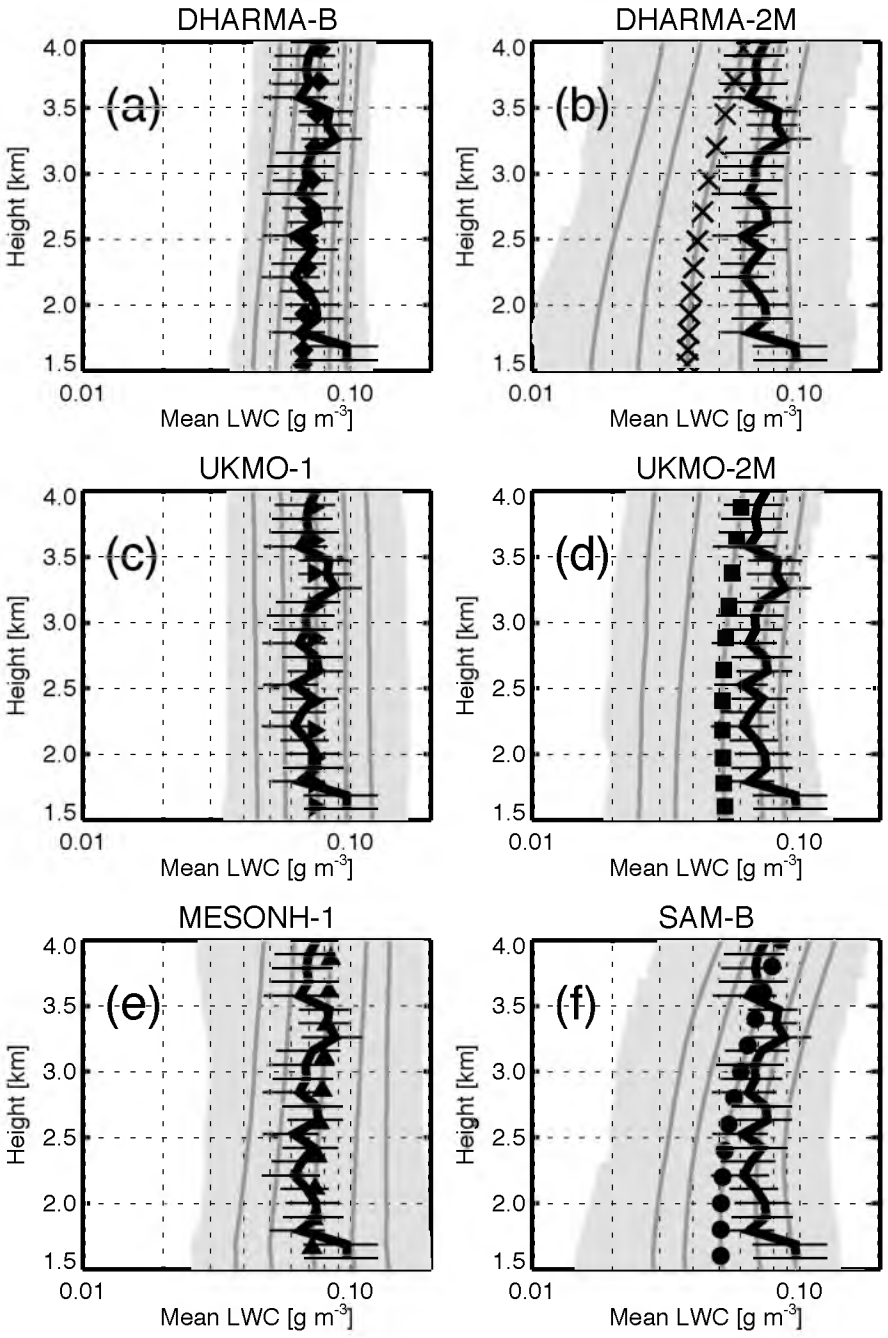

Figure 5.9. Temporal mean stratiform rain water content profiles for (a) DHARMA-B, (b) DHARMA-2M, (c) UKMO-1, (d) UKMO-2M, (e) MESONH-1, and (f) SAM-B. The solid black line represents the temporal mean profile derived from dual-profiler retrievals with the standard error represented by horizontal bars. Simulations have a population of mean profiles, one at each horizontal grid point in the model, and are thus represented by a distribution. Mean profiles are discarded from the distribution if they do not have at least 40 samples. The median of this distribution is represented with symbols. The 1st, 10th, 90th, and 99th percentiles are shown in dark gray with the filled area encompassing all valid profiles.

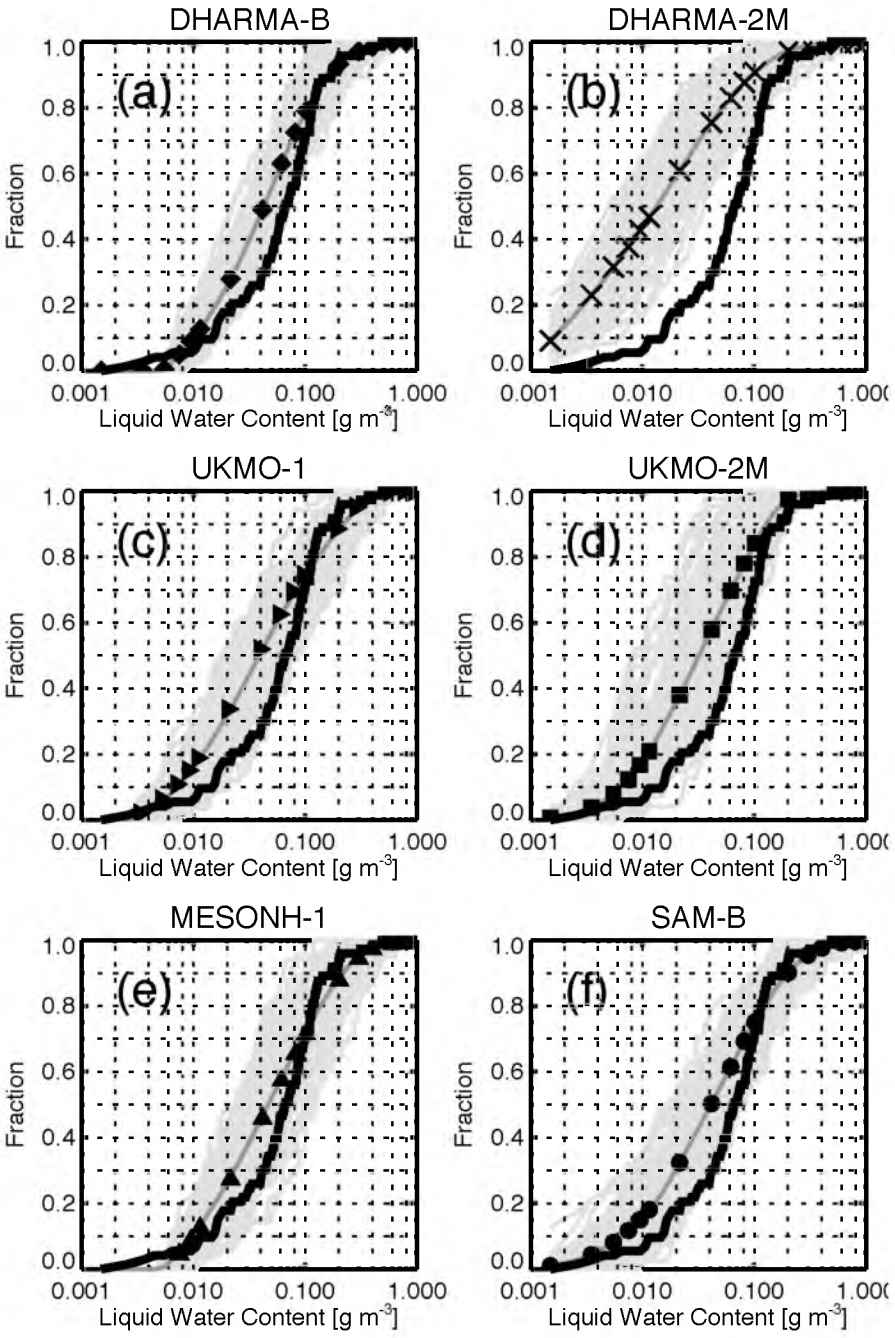

Figure 5.10. Normalized cumulative distributions of stratiform liquid water content for raindrops between 0.308 mm and 5.258 mm. Dark gray lines and symbols represent six different CRM simulations: (a) DHARMA-B, (b) DHARMA-2M, (c) UKMO-1, (d) UKMO-2M, (e) MESONH-1, and (f) SAM-B. The solid black line represents disdrometer observations, and the light gray lines represent 100 randomly selected distributions with at least 40 samples for each simulation shown.

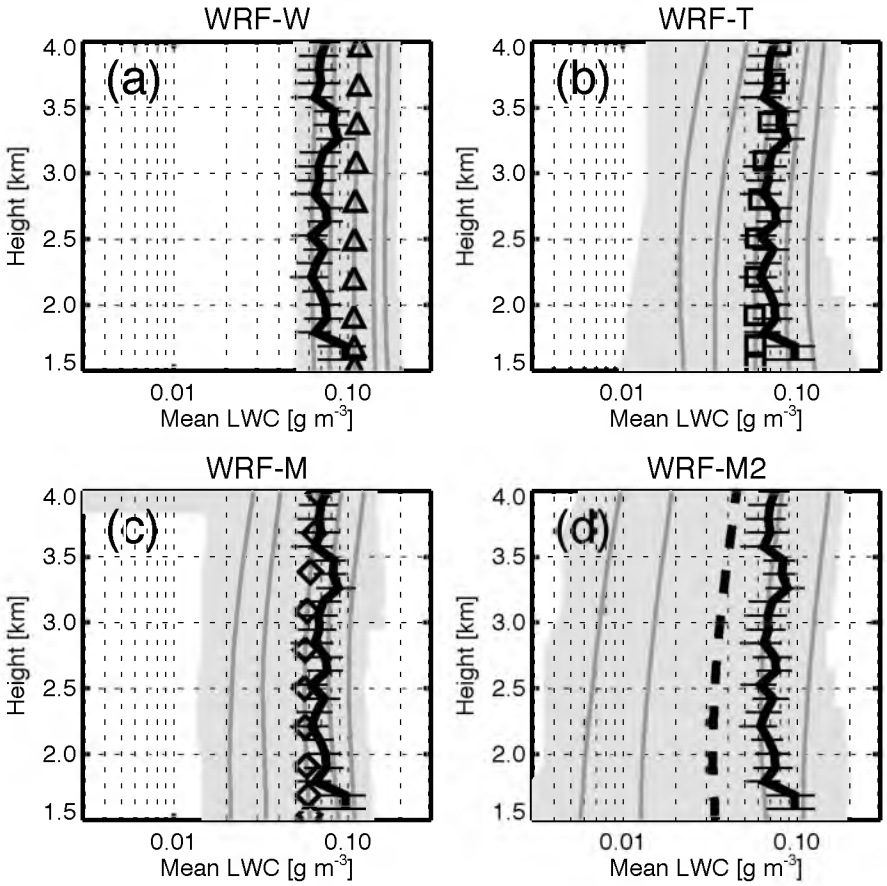

Figure 5.11. Temporal mean stratiform rain water content profiles for (a) WRF-W, (b) WRF-T, (c) WRF-M, and (d) WRF-M2. The solid black line represents the temporal mean profile derived from dual-profiler retrievals with the standard error represented by horizontal bars. Simulations have a population of mean profiles, one at each horizontal grid point in the model, and are thus represented by a distribution. Mean profiles are discarded from the distribution if they do not have at least 40 samples. The median of this distribution is represented with symbols. The 1st, 10th, 90th, and 99th percentiles are shown in dark gray with the filled area encompassing all valid profiles.

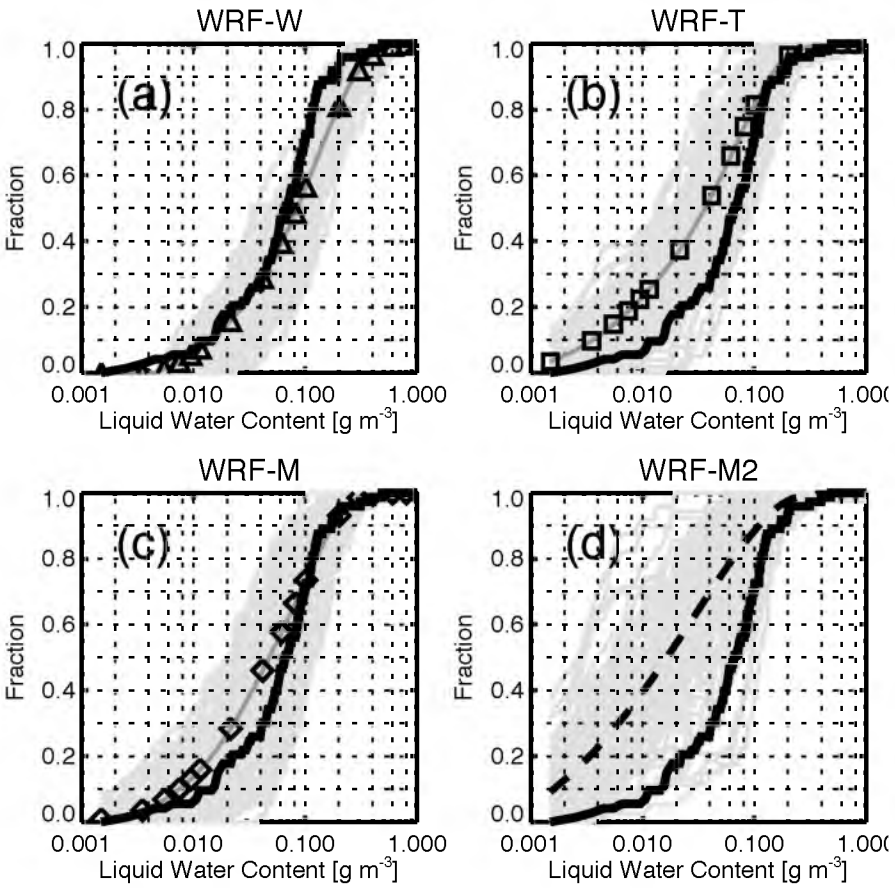

Figure 5.12. Normalized cumulative distributions of stratiform liquid water content for raindrops between 0.308 mm and 5.258 mm. Dark gray lines and symbols represent four different LAM simulations: (a) WRF-W, (b) WRF-T, (c) WRF-M, and (d) WRF-M2. The solid black line represents disdrometer observations, and the light gray lines represent 100 randomly selected distributions with at least 40 samples for each simulation shown.

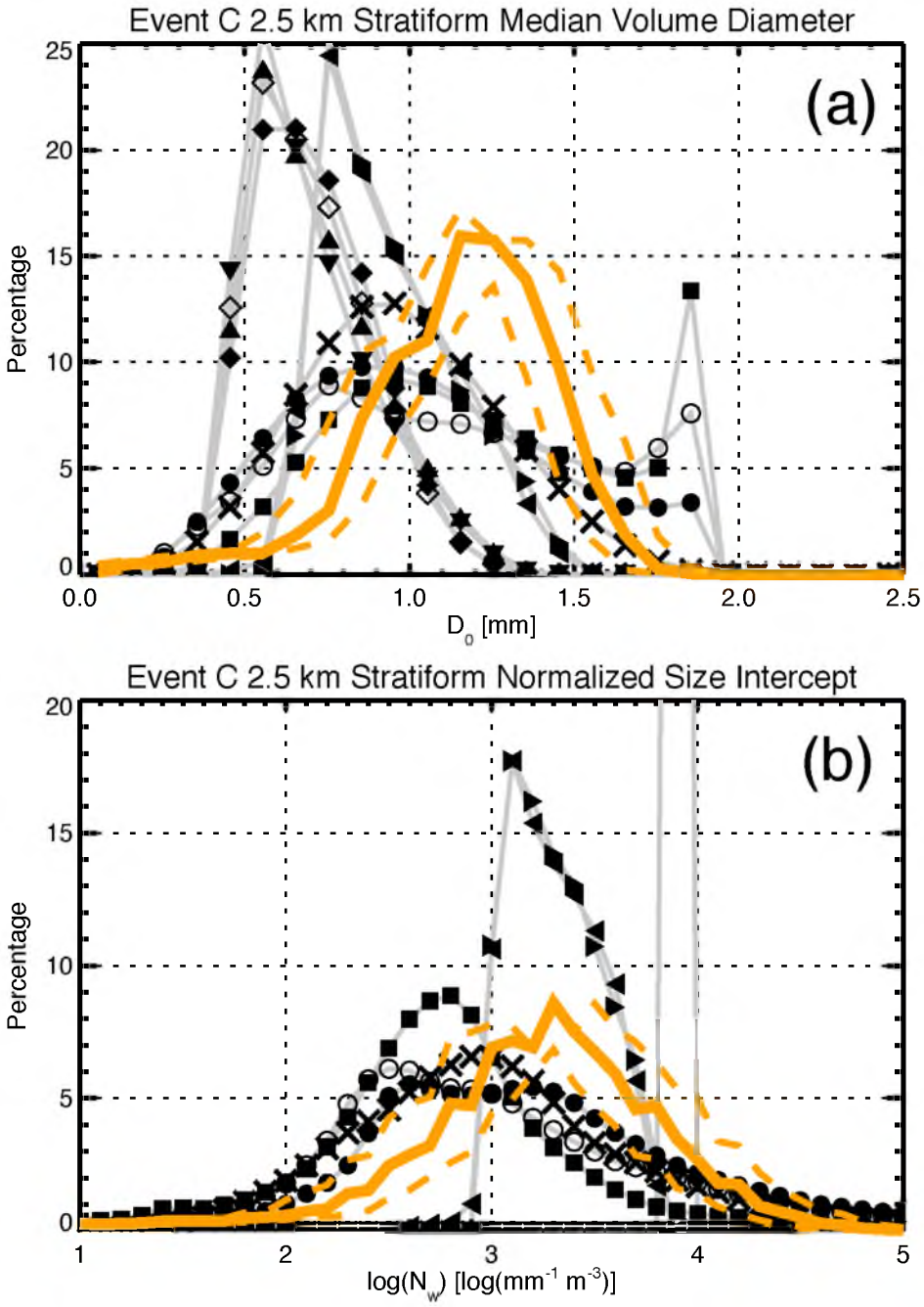

Figure 5.13. Histograms of stratiform rain (a) median volume diameter (D_0) and (b) normalized size intercept ($\log(N_w)$) at a 2.5-km altitude for each CRM simulation (symbols defined in Table 2.1) and the CPOL retrieval (thick orange line). Observational uncertainty (see May et al. (2011)) is shown with dashed orange lines.

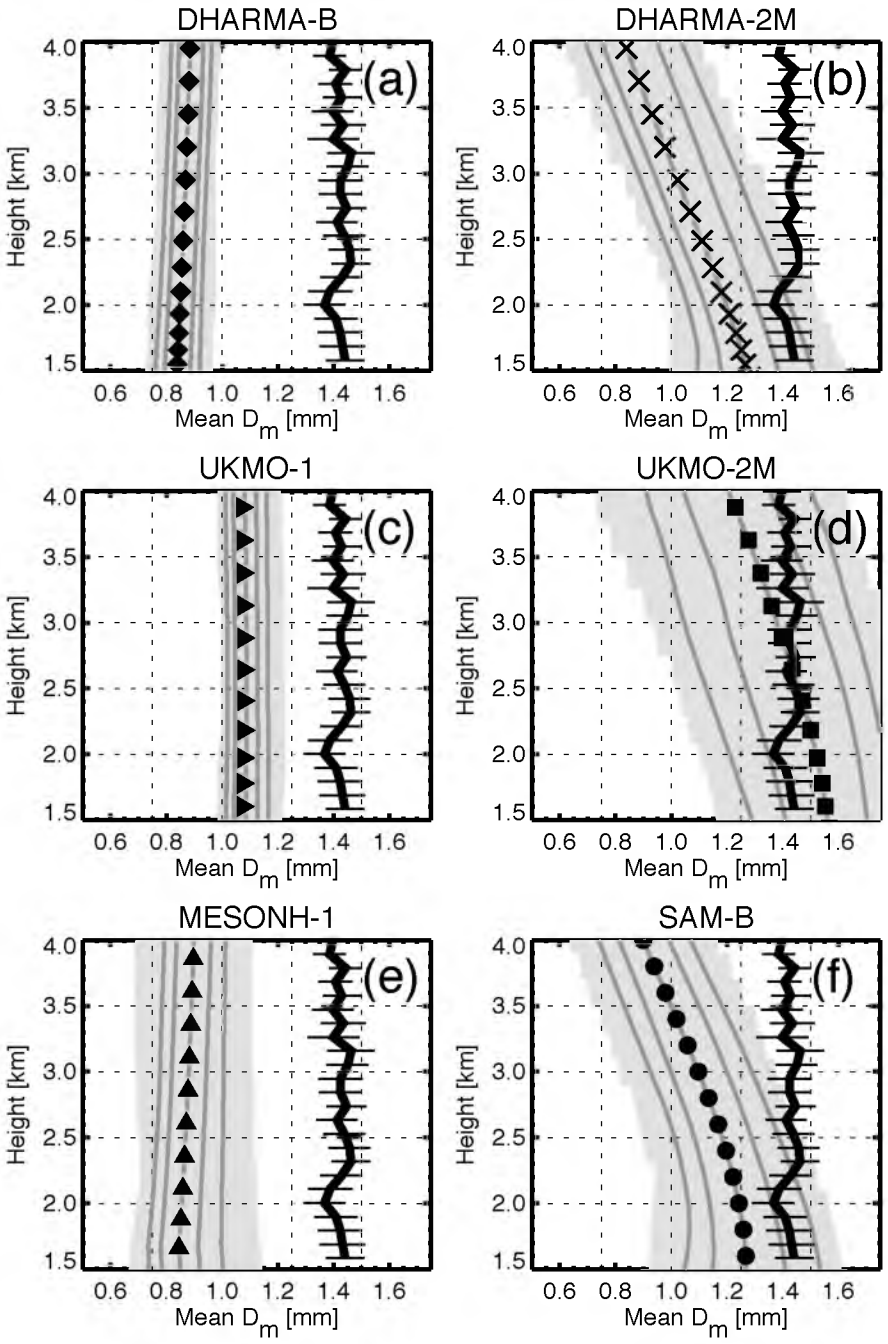

Figure 5.14. Temporal mean stratiform rain mass-weighted mean diameter (D_m) profiles for (a) DHARMA-B, (b) DHARMA-2M, (c) UKMO-1, (d) UKMO-2M, (e) MESONH-1, and (f) SAM-B. The solid black line represents the temporal mean profile derived from dual-profiler retrievals with the standard error represented by horizontal bars. Simulations have a population of mean profiles, one at each horizontal grid point in the model, and are thus represented by a distribution. Mean profiles are discarded from the distribution if they do not have at least 40 samples. The median of this distribution is represented with symbols. The 1st, 10th, 90th, and 99th percentiles are shown in dark gray with the filled area encompassing all valid profiles.

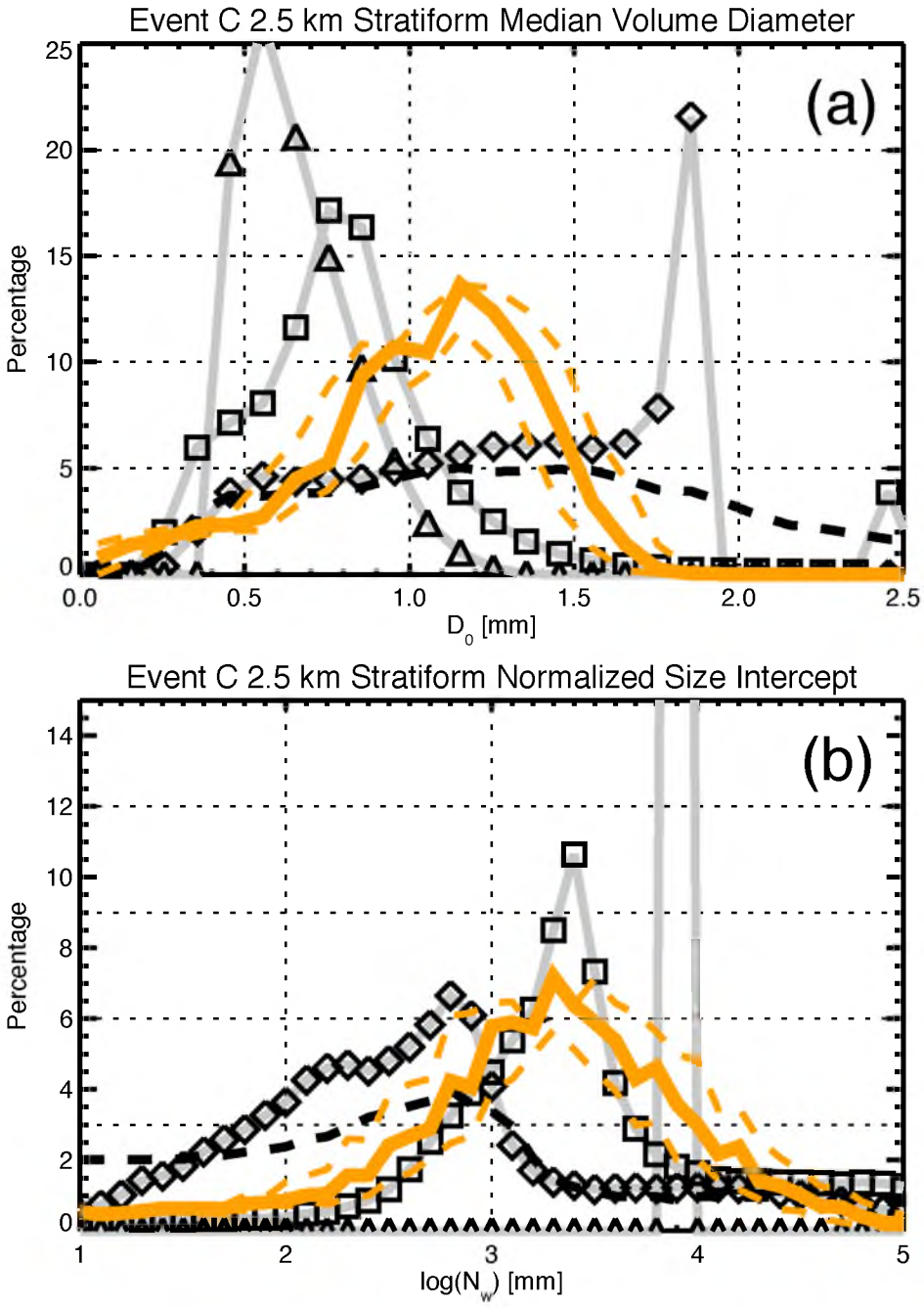

Figure 5.15. Histograms of (a) stratiform rain median volume diameter (D_0) and (b) normalized size intercept ($\log(N_w)$) at a 2.5-km altitude for each LAM simulation (symbols defined in Table 2.3) and the CPOL retrieval (thick orange line). Observational uncertainty (see May et al. (2011)) is shown with dashed orange lines. LAM output is limited to the CPOL domain.

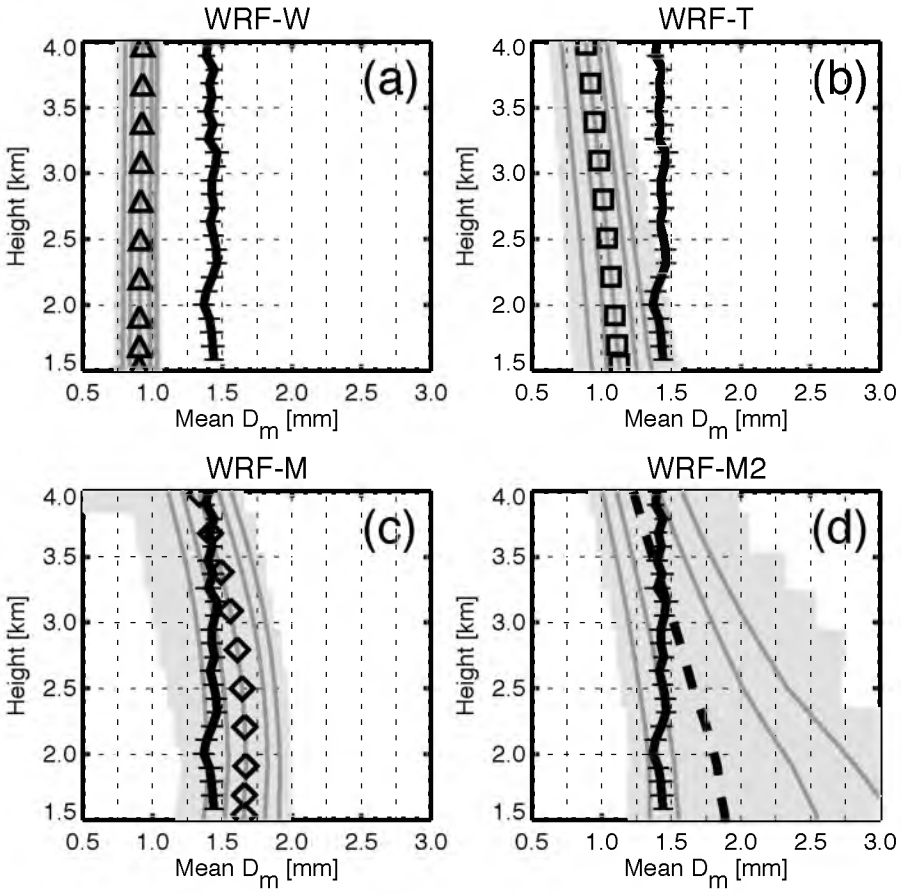

Figure 5.16. Temporal mean stratiform rain mass-weighted mean diameter (D_m) profiles for (a) WRF-W, (b) WRF-T, (c) WRF-M, and (d) WRF-M2. The solid black line represents the temporal mean profile derived from dual-profiler retrievals with the standard error represented by horizontal bars. Simulations have a population of mean profiles, one at each horizontal grid point in the model, and are thus represented by a distribution. Mean profiles are discarded from the distribution if they do not have at least 40 samples. The median of this distribution is represented with symbols. The 1st, 10th, 90th, and 99th percentiles are shown in dark gray with the filled area encompassing all valid profiles.

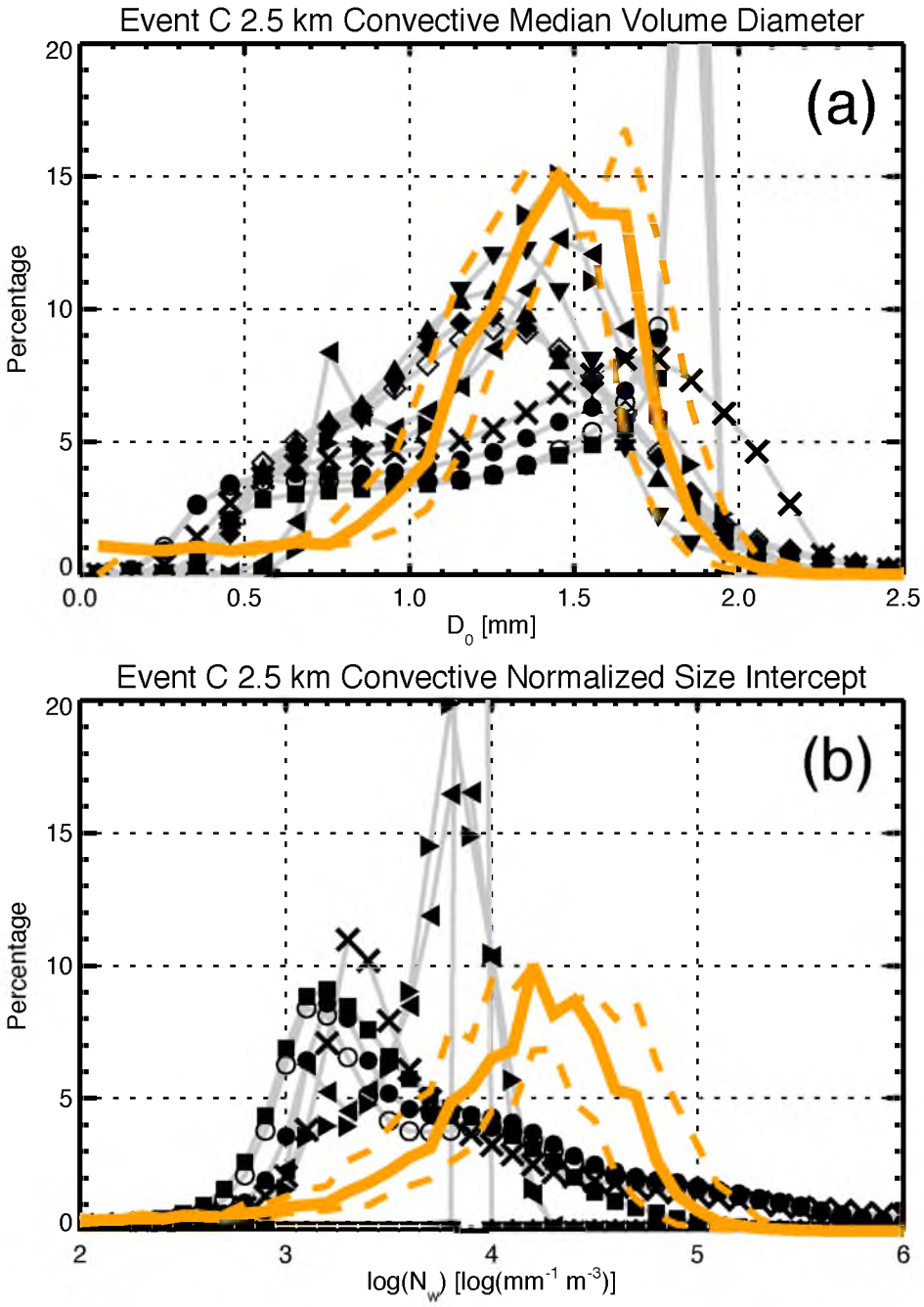

Figure 5.17. Histograms of convective rain (a) median volume diameter (D_0) and (b) normalized size intercept ($\log(N_w)$) at a 2.5-km altitude for each CRM simulation (symbols defined in Table 2.1) and the CPOL retrieval (thick orange line). Observational uncertainty (see May et al. (2011)) is shown with dashed orange lines.

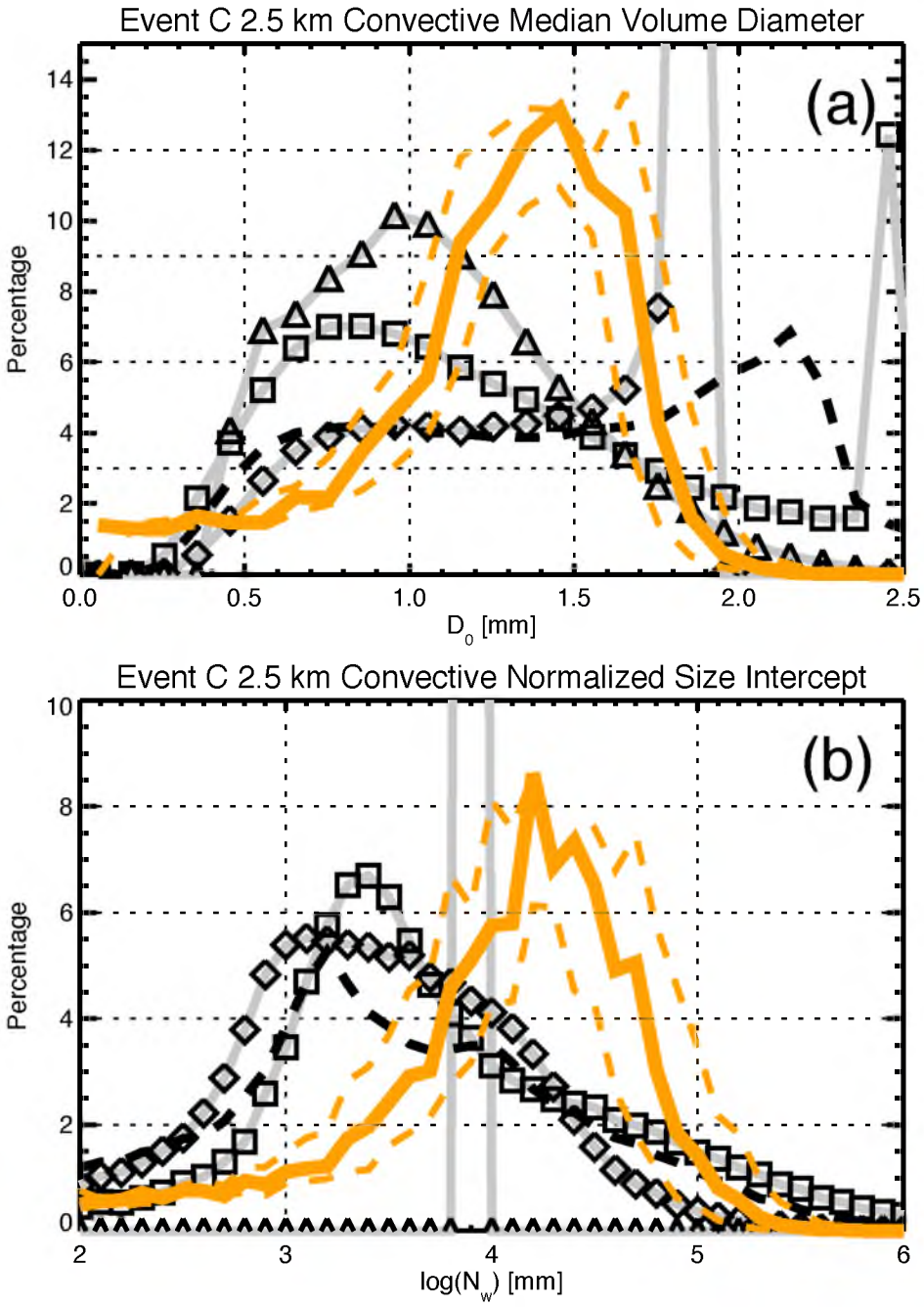

Figure 5.18. Histograms of (a) convective rain median volume diameter (D_0) and (b) normalized size intercept ($\log(N_w)$) at a 2.5-km altitude for each LAM simulation (symbols defined in Table 2.3) and the CPOL retrieval (thick orange line). Observational uncertainty (see May et al. (2011)) is shown with dashed orange lines. LAM output is limited to the CPOL domain.

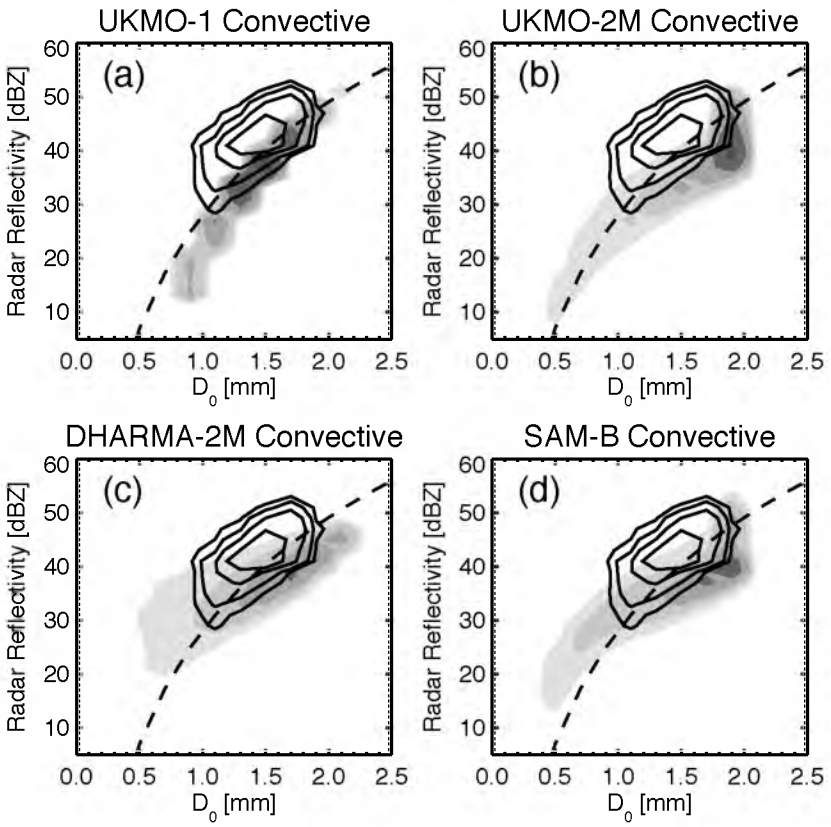

Figure 5.19. Two-dimensional histograms of convective radar reflectivity versus median volume diameter at a 2.5-km altitude are gray filled for (a) UKMO-1, (b) UKMO-2M, (c) DHARMA-2M, and (d) SAM-B. The dashed line represents one-moment rain schemes in DHARMA-B and MESONH-1. CPOL retrievals are contoured in black. Contour intervals are 0.5, 1, 2, 4, and 8%.

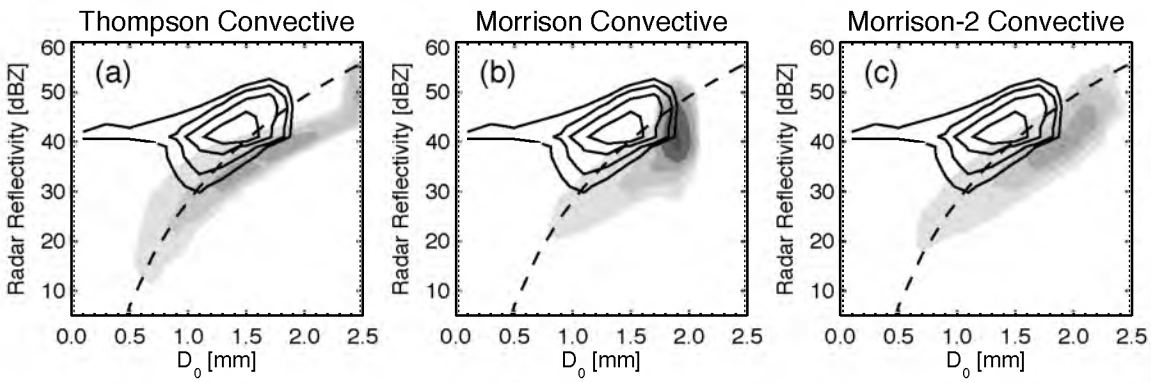

Figure 5.20. Two-dimensional histograms of convective radar reflectivity versus median volume diameter at a 2.5-km altitude are gray filled for (a) WRF-T, (b) WRF-M, and (c) WRF-M2. The dashed line represents the one-moment rain scheme in WRF-W. CPOL retrievals are contoured in black. Contour intervals are 0.5, 1, 2, 4, and 8%.

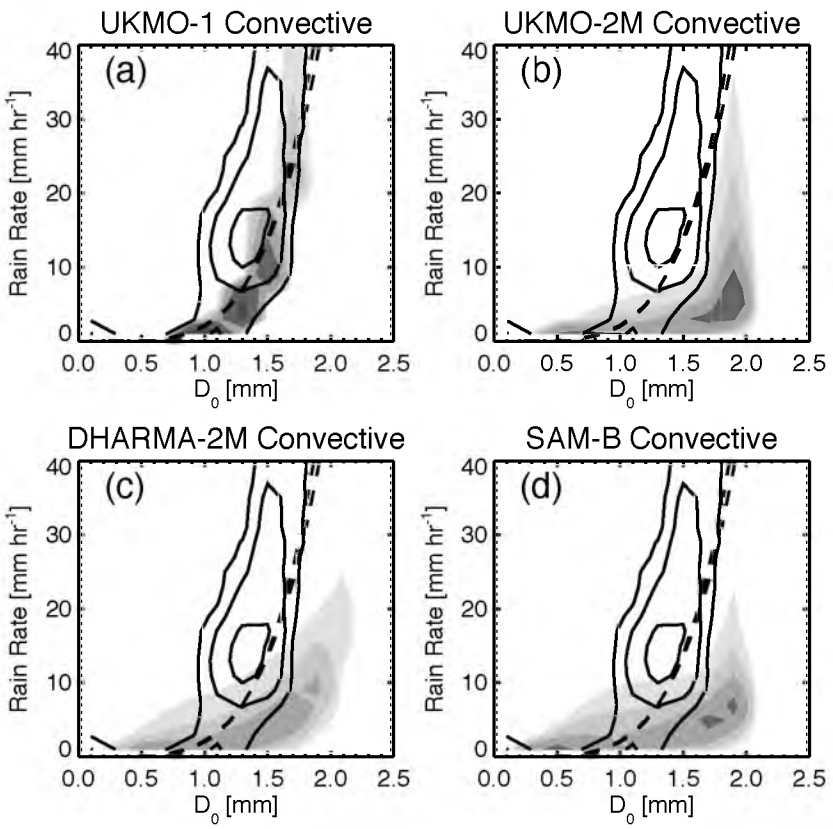

Figure 5.21. Two-dimensional histograms of convective rain rate versus median volume diameter at a 2.5-km altitude are gray filled for (a) UKMO-1, (b) UKMO-2M, (c) DHARMA-2M, and (d) SAM-B. The dashed line represents one-moment rain schemes in DHARMA-B and MESONH-1. CPOL retrievals are contoured in black. Contour intervals are 0.5, 1, 2, 4, and 8%.

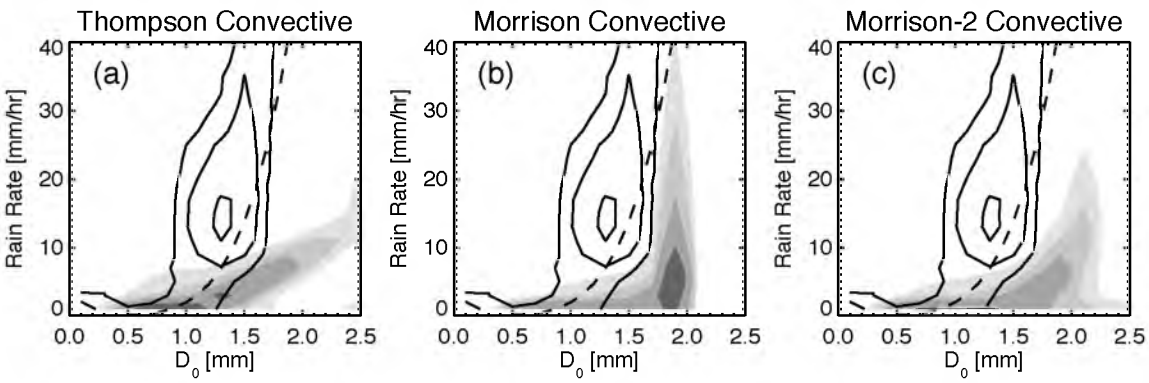

Figure 5.22. Two-dimensional histograms of convective rain rate versus median volume diameter at a 2.5-km altitude are gray filled for (a) WRF-T, (b) WRF-M, and (c) WRF-M2. The dashed line represents the one-moment rain scheme in WRF-W. CPOL retrievals are contoured in black. Contour intervals are 0.5, 1, 2, 4, and 8%.

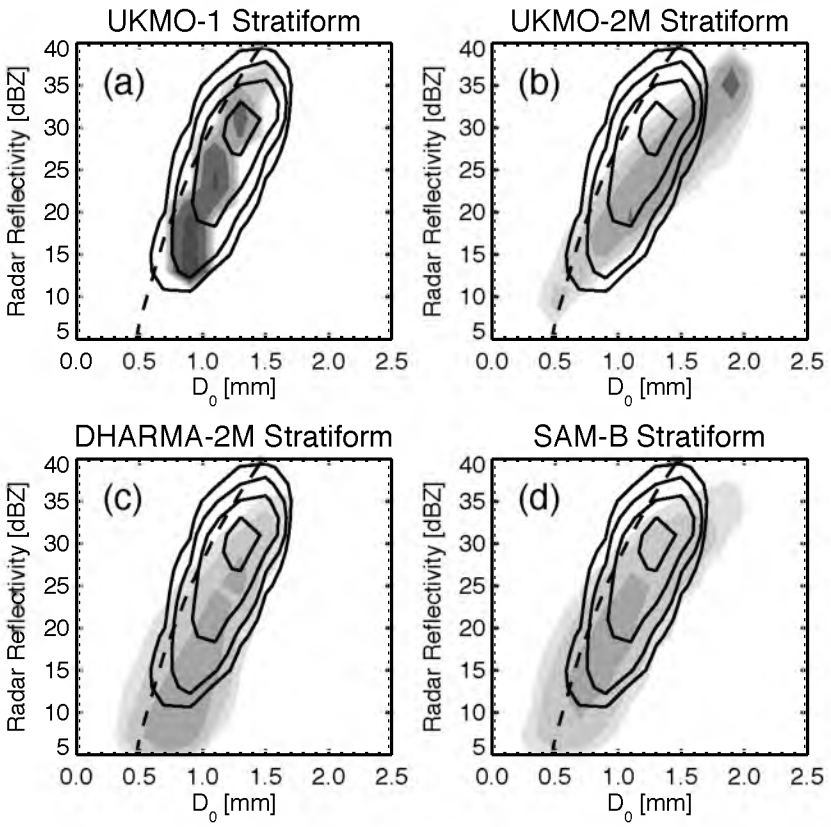

Figure 5.23. Two-dimensional histograms of stratiform radar reflectivity versus median volume diameter at a 2.5-km altitude are gray filled for (a) UKMO-1, (b) UKMO-2M, (c) DHARMA-2M, and (d) SAM-B. The dashed line represents one-moment rain schemes in DHARMA-B and MESONH-1. CPOL retrievals are contoured in black. Contour intervals are 0.5, 1, 2, 4, and 8%.

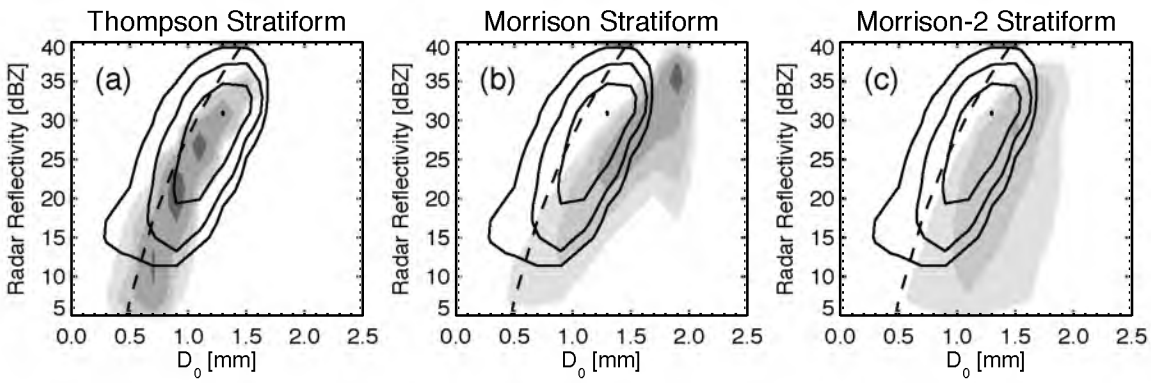

Figure 5.24. Two-dimensional histograms of stratiform radar reflectivity versus median volume diameter at a 2.5-km altitude are gray filled for (a) WRF-T, (b) WRF-M, and (c) WRF-M2. The dashed line represents the one-moment rain scheme in WRF-W. CPOL retrievals are contoured in black. Contour intervals are 0.5, 1, 2, 4, and 8%.

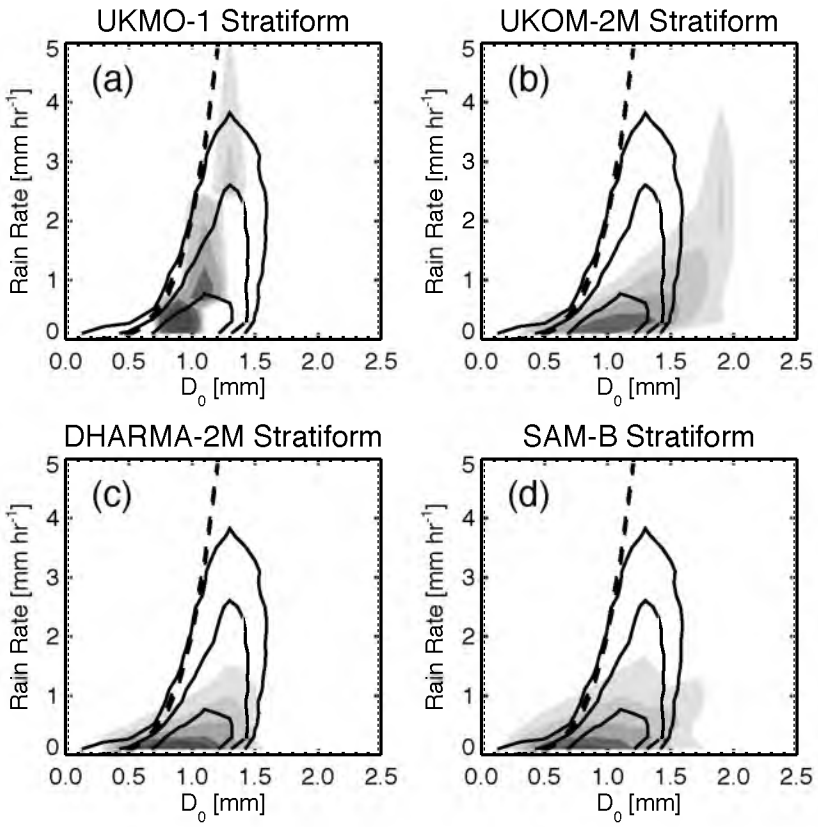

Figure 5.25. Two-dimensional histograms of stratiform rain rate versus median volume diameter at a 2.5-km altitude are gray filled for (a) UKMO-1, (b) UKMO-2M, (c) DHARMA-2M, and (d) SAM-B. The dashed line represents one-moment rain schemes in DHARMA-B and MESONH-1. CPOL retrievals are contoured in black. Contour intervals are 0.5, 1, 2, 4, and 8%.

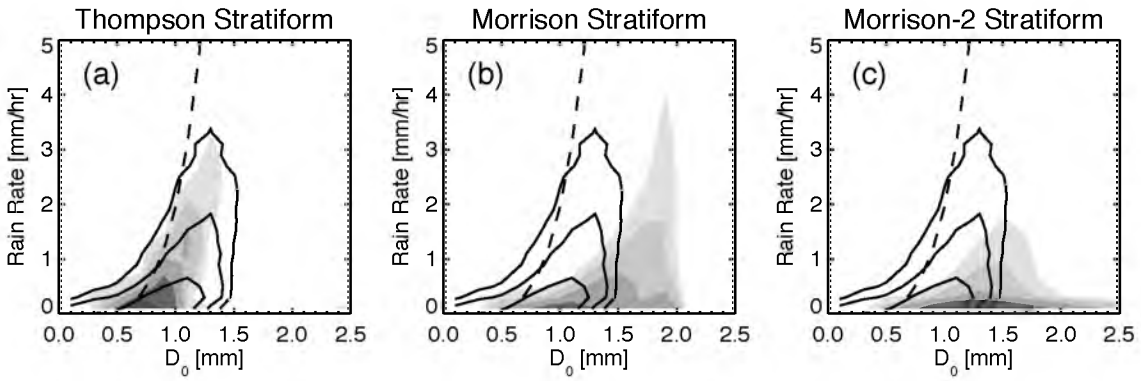

Figure 5.26. Two-dimensional histograms of stratiform rain rate versus median volume diameter at a 2.5-km altitude are gray filled for (a) WRF-T, (b) WRF-M, and (c) WRF-M2. The dashed line represents the one-moment rain scheme in WRF-W. CPOL retrievals are contoured in black. Contour intervals are 0.5, 1, 2, 4, and 8%.

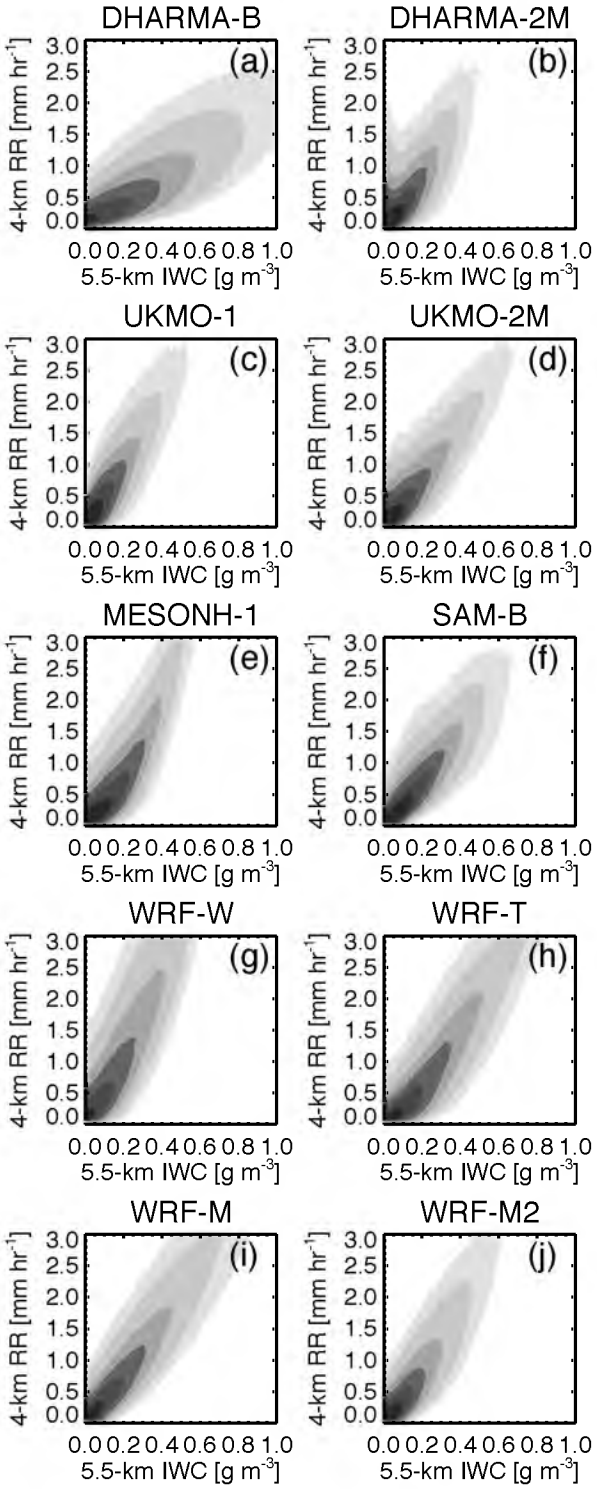

Figure 5.27. Two-dimensional histograms of 4-km simulated stratiform rain rate and 5.5-km simulated stratiform IWC for (a) DHARMA-B, (b) DHARMA-2M, (c) UKMO-2, (d) UKMO-2M, (e) MESONH-1, (f) SAM, (g) WRF-W, (h) WRF-T, (i) WRF-M, and (j) WRF-M2. Contour intervals are 0.01, 0.02, 0.05, 0.1, 0.2, and 0.5%.

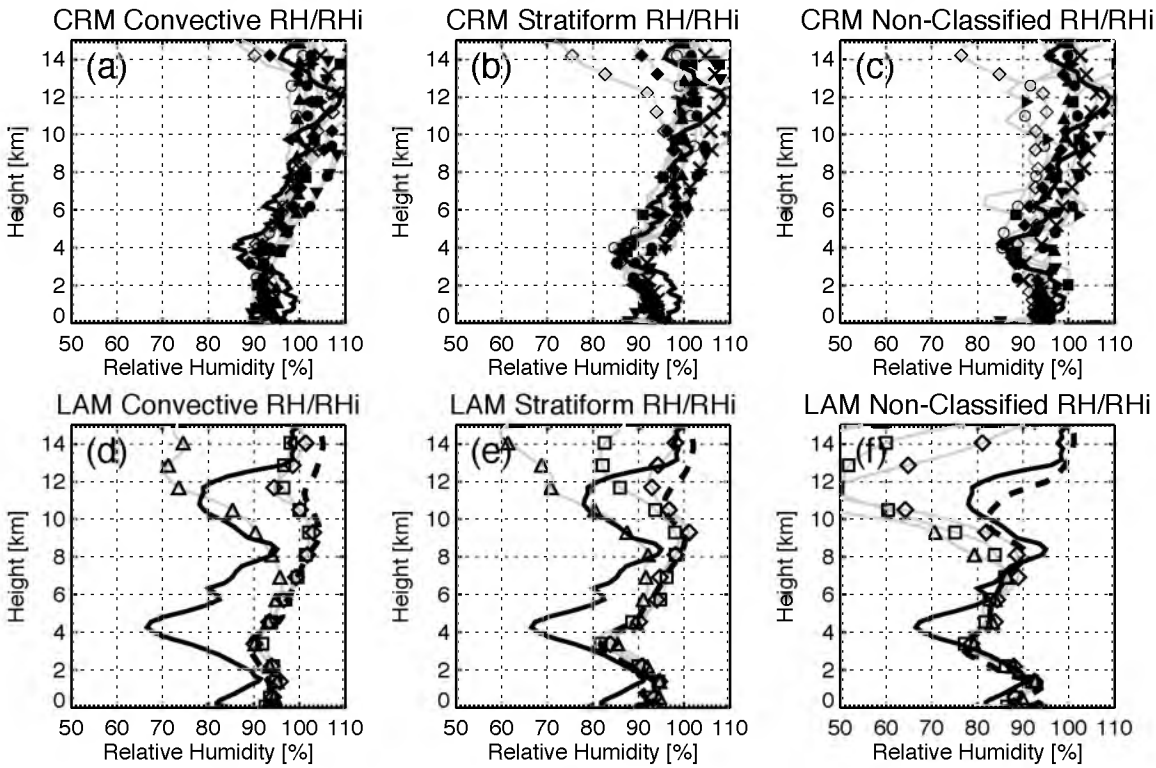

Figure 5.28. Mean convective, stratiform, and nonclassified *RH-RHi* profiles in the (a–c) CRM simulations (symbols defined in Table 2.1) and variational analysis (solid black) at 18Z on 1/23 and (d–f) LAM simulations (symbols defined in Table 2.3) and the ECMWF analysis (solid black) within the CPOL domain at 18Z on 1/23. The variational analysis and ECMWF profiles are domain means (not separated in convective, stratiform, and nonclassified regions). *RH* is shown for temperatures warmer than 0°C and *RHi* is shown for temperature colder than 0°C.

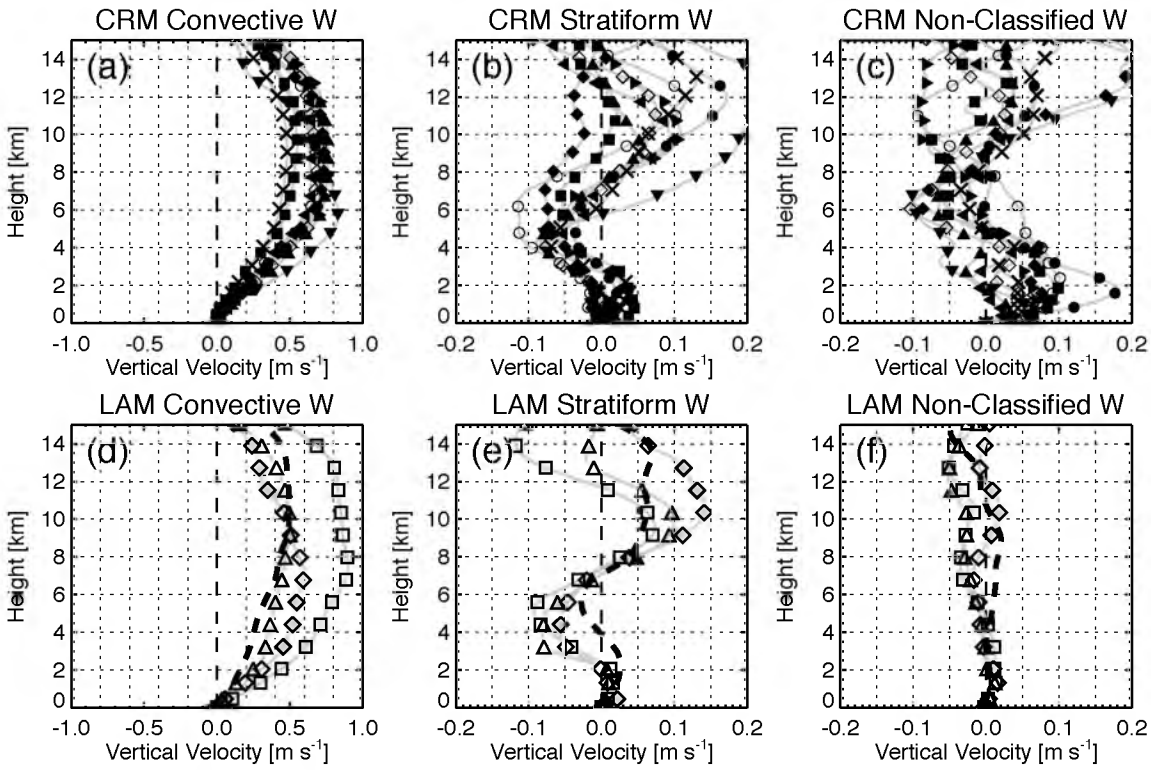

Figure 5.29. Mean convective, stratiform, and nonclassified vertical velocity profiles in the (a–c) CRM simulations (symbols defined in Table 2.1) at 18Z on 1/23 and (d–f) LAM simulations (symbols defined in Table 2.3) within the CPOL domain at 18Z on 1/23. The variational analysis vertical velocity was interpolated to model height levels and included in the CRM profiles. Note the x-axes for convective and stratiform regions differ.

CHAPTER 6

CONCLUSIONS

6.1 Summary

Specific TWP-ICE CRM and LAM simulation biases found in this research and published in Varble et al. (2011), namely a high bias in convective area and radar reflectivity aloft as well as a low bias in stratiform rainfall, are not entirely surprising. Such results had been found in previous literature discussed in Section 1.2.4, especially for simulations using one-moment bulk microphysics schemes. Differences between simulations are more correlated with hydrometeor size distribution assumptions than differences in hydrometeor water contents. Unlike in past studies, two-moment schemes did not outperform one-moment schemes for this study despite the clear advantage of two-moment schemes in representing sedimentation of different sized hydrometeors and effects of phase changes on hydrometeor size distributions. One likely reason for the difference from past studies is that the humid maritime environment of this case differs from most mid-latitude continental cases, which limits major issues in one-moment schemes, such as excessive evaporation. Another issue in increasingly complex microphysics schemes is the lack of high quality observations to constrain the schemes. While more complex schemes should be more realistic in theory, they also have more

freedom to be wrong, which is one of the reasons that arbitrary thresholds are often put in place, which can be seen in statistics such as those in Chapter 5.

Results from detailed comparison with observational retrievals show, however, that causes for simulation biases are likely much more complicated than simply improving ice microphysics schemes as has been commonly emphasized in some previous literature; rather, they depend on achieving the correct interplay between model forcing, resolution, and physics complexity to yield proper interactions between dynamics and microphysics that produce appropriate convective modes. Mode not only encompasses instantaneous structural properties, but also involves convective life cycle. Both are important in determining system precipitation coverage and the proportioning of convective to stratiform precipitation, which in the case of mesoscale systems alters the large-scale environment.

This conclusion is based upon comparison of many different CRM and LAM simulations with observational retrievals of convective vertical velocity and raindrop size distributions. Without significant sample sizes of in situ convective region properties, it is difficult to prove that simulated convective updrafts are stronger than observed, but a significant amount of indirect evidence has been shown to support this conclusion including comparisons with a dual-Doppler retrieval and comparison of convective vertical velocity and condensate values with relevant published literature. This does not appear to be due to unresolved eddies based on results of a 100-m horizontal grid spaced and 192 vertical level quarter domain DHARMA-2M simulation. Therefore, it appears to be linked to some mixture of model forcing biases and interactions between dynamics and microphysics that are able to shift convective feedbacks and mode from those that

occurred in reality. Interactions between convective dynamics and microphysics are sensitive to the microphysics and subgrid scale turbulence parameterizations, both of which could be factors in the difference between simulations and observations.

Both the intensity of simulated convection and the inability of the CRM setup to resolve mesoscale circulations are likely linked to the under-prediction of ice water content just above the melting level in simulations with appropriately large areas of stratiform precipitation, which reduces simulated stratiform rain rates. This occurs because moistening of mid and upper levels by means of mesoscale ascent and convective detrainment are not adequate and lead to ice sublimation and mesoscale descent in many stratiform regions above the melting level. For the LAM simulations that do have some higher stratiform rain rates, stratiform ice water content is higher but stratiform area is far too low. This is partially due to dry biases in the ECMWF forcing, but also due to the convection, which dominates vertical mass flux in the upper troposphere, detrains near the tropopause, and does not efficiently transfer condensate and buoyancy to stratiform regions. These convective issues are present in CRM simulations as well, but the dry bias is not present in those simulations. Instead, the domain size with periodic lateral boundary conditions prevents mesoscale circulations from forming that are necessary for producing a large and well-developed stratiform region.

A unique aspect of this research was the comparison of CRMs and LAMs, which has not been thoroughly done to date, at least for the topics considered in this research. While some differences were apparent, such as the location and timing of convection and the amount of stratiform area, these differences make sense in the context of the different

model forcings and boundary conditions. Many other model biases relative to observations that relate to microphysics and convective dynamics were present in both model setups, an important finding because such biases could have possibly been attributed to idealized model forcing without such a comparison.

Despite the differences in CRM and LAM forcing biases, lack of mesoscale circulations due to limited CRM domain sizes and dry biases in LAM simulations, and the apparent differences in convective strength, these simulations do show that there are specific microphysics assumptions that could be improved without much of an increase in computing time. These microphysics scheme alterations are not simply changes to tunable parameters to achieve agreement in one variable, but changes that should produce improvement and be more physically realistic. As pointed out in de Rooy et al. (2012), implementation of potential improvements in GCM convective parameterizations often lead to worse simulations because the parameterizations have become so full of unphysical tunable parameters that are set to compensate for errors. The same can be said of some model physics variables such as hydrometeor conversion thresholds and collection efficiencies used in cloud-resolving simulations. The following are changes in hydrometeor properties based on intercomparison of many simulations with observations guided by past observational results that could improve bulk microphysics schemes with some that have been preliminarily tested, as will be discussed in Section 6.4:

1. Inclusion of a fast falling dense precipitating ice species (i.e., hail), or a variable dense precipitating ice density such as that in Milbrandt and Morrison (2013) with a fall speed relationship that covers a larger range of fall speeds than is currently done in most schemes. This would better represent the faster fall speeds of frozen

raindrops, which are very common, and alter the amount of dense ice in the upper troposphere. Setting the graupel μ parameter to greater than 0 may prevent excessively large graupel from occurring and improve radar reflectivity comparisons, but it is unclear whether this is more realistic.

2. A rain μ parameter greater than 0, such as 2.5 used in the UKMO model, or a diagnostic μ-λ relationship based on observations such as that in Cao et al. (2008). This may improve excessive size sorting issues in two-moment rain schemes and produce more realistic fall speeds. It would also likely affect evaporation rates, but the impacts of such effects are unknown at this time.
3. Inclusion of a more aggressive raindrop breakup parameterization to prevent very large diameters from occurring in convective rain. Such parameterizations have major impacts on mesoscale convective systems in mid-latitude continental situations (e.g., Morrison et al. (2012)) through alteration of evaporation rates, but have not been thoroughly tested in the deep tropics.
4. Implementation of a nonspherical snow mass-diameter relationship that allows density to decrease with size, as used in the MESONH or Thompson schemes, where mass is proportional to $D^{1.9}$ and D^2, respectively. Such relationships are based on observations in Locatelli and Hobbs (1974) and Field et al. (2005). It is important that this is used in schemes that diagnostically vary the size intercept or predict number concentration to avoid low biased radar reflectivities in regions of snow aggregation.

6.2 Caveats

This research is not free from caveats. It is limited in that it focuses primarily on one event that isn't even an ideal case for CRM simulations, but it was the only case that could be compared with LAM simulations, which was valuable in finding common errors to the two approaches. Other cases need to be modeled in the future to test the universality of conclusions drawn by this research and past studies. This research is also limited by the definitions used for convective and stratiform regions as well as convective drafts. Although the convective and stratiform separation technique is one of the most commonly used ones that was based on Darwin radar data, it may not be as appropriate for simulations as it is for observations because some simulations, such as the WRF-M simulation, produce large regions with reflectivity greater than 40 dBZ that are automatically classified as convective using the Steiner et al. (1995) separation algorithm but are clearly not convective based on the vertical velocity field. These regions are a result of very large IWCs accumulating in certain regions and high biases in reflectivity when assuming $\mu = 0$ due to excessive size sorting and a greater number of large raindrops relative to narrower distributions with μ greater than 0 that are expected in stratiform regions based on the results in Chapter 5 and previous observational studies. Lastly, this research is limited by uncertainties in observational retrievals, especially when very few in situ measurements were obtained. Retrieval uncertainties were mentioned throughout previous chapters, but these are estimations and not perfect. Furthermore, as was shown in Chapter 5, there are representativeness errors due to sample sizes, sampling volumes, and dependency of measurements in space and time. These were not handled in depth in this research because of the focus on large differences

between observationally derived and simulated properties. Although the recommendations for microphysics scheme alterations are partially based on these large differences, only preliminary results have been obtained from simulations using the scheme alterations. These altered schemes need to be tested more intensively for this case and other cases with different convective morphologies and large-scale environmental conditions to show whether they work universally or whether they are suited for only specific conditions.

6.3 Implications

The first implication of this research is that properly modeling the relationship between convective system properties and the large-scale environment is significantly more complex than closing the knowledge gap in mixed phase and ice microphysics. While it is obvious that atmospheric dynamics impacts cloud microphysics through saturation and cloud microphysics impacts atmospheric dynamics through latent and radiative heating, these two topics have often been treated separately in studies evaluating mesoscale model simulations. Often, this is because trustworthy co-located and coincident observations relevant to dynamics and microphysics within the context of scanning remote sensing that could help constrain these interactions simply do not exist in sufficient sample sizes, especially in climatically important locations such as the deep tropics. This convective dynamics and microphysics problem will be difficult to solve until large numbers of aircraft penetrations of deep convection in multiple life cycle stages are performed at temperatures between 10°C and -40°C because remote sensing retrievals of microphysics properties such as LWC and IWC are not trustworthy in

heavily precipitating conditions. The distributions of basic variables such as vertical velocity and total condensate are not well understood, much less microphysics processes in the mixed phase region. Penetrating aircraft exist, but there needs to be a push in the atmospheric sciences community to penetrate weak to moderate tropical convection that contains vertical velocities of similar magnitude to hydrometeor fall speeds. These, after all, are the types of convective systems that are so hard to simulate with cloud-resolving models and the types of systems relevant to large-scale tropical circulations.

With the research results shown in this dissertation comes a word of caution to those that tune microphysics schemes to match specific moments of hydrometeor size distributions such as Rayleigh reflectivity. While this as an appealing approach to improving simulations because of its relative ease, it is dangerous in that it can cover up the true causes of model biases. Such methods curtail progress in improving predictability of weather and climate because many of these models are currently used to improve GCM parameterizations and satellite retrievals. With quickly increasing horizontal resolution in GCMs, microphysics schemes now used in CRMs, LAMs, and LES simulations will be used in GCMs in the not too distant future, so now is the time to improve them.

6.4 Future Work

Out of intercomparing numerous CRM and LAM simulations of TWP-ICE active monsoon convective systems with observations, several aspects of bulk microphysics schemes arose as possibly contributing to model biases. Some differences in large-scale convective and stratiform areas between CRMs and LAMs appear related to differences

in large-scale forcing and initial conditions. Many other biases within convective and stratiform regions relating to rain rate, radar reflectivity, convective vertical velocity, and rain DSDs appear related to bulk microphysics assumptions and to the resolved interactions between dynamics and microphysics.

Code has already been written by Hugh Morrison at the National Center for Atmospheric Research to test out the suggested bulk microphysics scheme alterations outlined in Section 6.1. This code has been implemented and tested in the Morrison 2-moment bulk microphysics scheme in WRF version 3.3.1. Fine-tuning and analysis of these new simulations is still being performed at the current time. Preliminary results are as follows:

1. Altering the snow *m-D* relationship from $m = \frac{\pi}{6}\rho_s D^3$, where m is mass, D is diameter, and ρ_s is bulk snow density, to $m = 0.01855D^{1.9}$ taken from Locatelli and Hobbs (1974), used in Brown and Francis (1995) and the MESONH scheme, and similar to the *m-D* relationship used in Field et al. (2005) and the Thompson scheme, lowers the excessively high snow radar reflectivities aloft in convective and stratiform regions as was expected.
2. A diagnostic rain gamma shape parameter (μ) that varies as a function of the gamma slope parameter (λ) using the relationship in Cao et al. (2008) increases stratiform area and decreases convective area because it reduces some radar reflectivities that were greater than 40 dBZ to less than 40 dBZ. It also improves excessive size sorting of raindrops, but does not completely solve that issue. It also may be shifting DSDs too much toward smaller sizes, especially in convective regions, but this needs to be studied more. Finally, because the

distribution of raindrop sizes changes, it has a non-negligible effect on evaporation and freezing rates. These changes are still being studied.

3. The latest Morrison scheme in WRF has a new raindrop breakup parameterization based on the one that gave the best results out of a number of them tested for an idealized mid-latitude continental squall line in Morrison et al. (2012). WRF-M2 had this parameterization and it produced very little difference in convective DSDs. More aggressive drop breakup formulations will be tested in future work to see if better agreement can be found between simulated and observationally retrieved DSDs. If better agreement is found, the effects of such changes in the raindrop breakup parameterization will be studied. Changes had a substantial effect on convective downdrafts and cold pool strength in mid-latitude environments, but this effect may be lessened in more humid tropical situations.
4. For two simulations that are exactly the same except for the precipitating dense ice representation in the Morrison scheme, hail does indeed reduce reflectivity in the upper troposphere relative to graupel because it falls out faster. Recall that hail in this context refers to precipitating ice with the same density as pure ice rather than precipitating ice with a density of 400 kg m^{-3}. More importantly, though, it has a fall speed relationship of $v = 114.5D^{0.5}$ rather than $v = 19.3D^{0.37}$ in the Morrison scheme. Where hail does exist, reflectivity is often higher, and more snow is produced in the updrafts when hail is used. Because hail takes longer to melt and it falls out over a smaller region than graupel, it tends to increase the strength of convective downdrafts, which probably has a non-negligible effect on cold pool strength, but these possible effects have yet to be studied.

5. Analysis nudging has a significant impact on mesoscale precipitation structure. Winds, temperature, and water vapor can all be nudged in any domain and at any chosen altitudes in the WRF simulations with a nudging strength that can be set to any value. Without any nudging, two-way nested WRF simulations of this MCS case are likely too random because of the large domains involved and accumulating errors related to numerical approximations, which makes it difficult to attribute differences between simulations to changes in the microphysics. A two-way nested WRF run using the same setup as WRF-M was performed without nudging in D2–D4, for example, and the simulation produced results that were more different from WRF-M than WRF-W or WRF-T were. With too much nudging, however, biases in the analysis used to force the simulations are too dominant. More research is needed to test the sensitivity of simulations to this nudging to find optimum methods for applying it. Assimilation of surface and sounding meteorological observations may also reduce errors due to the analysis biases, which are known to be quite significant at times in data sparse regions such as the oceanic tropics. For a smaller non-MCS case, a CRM setup with periodic boundary conditions would be a better option because many of the errors associated with the LAM setup would be avoided. For an MCS case that is not a fairly meridionally symmetric squall line, however, a CRM with a horizontal domain size of a few hundred kilometers by a few hundred kilometers is generally to small to allow mesoscale circulations necessary to simulating the evolution of the stratiform region to develop.

Sensitivity to horizontal resolution is also being studied with a quarter domain (88 km by 88 km) DHARMA-2M simulation with ~100-m horizontal grid spacing and 192 vertical levels. This simulation was performed by Ann Fridlind at NASA Goddard Institute for Space Studies. Preliminary results show that grid spacing of ~100 m is insufficient to significantly reduce high vertical velocities and condensate amounts aloft, although they are reduced some in the upper troposphere when the grid spacing is degraded to ~900 m. The higher resolution does appear to affect the transition time from congestus to deep convection, as was found in Khairoutdinov and Randall (2006), but detrainment by more numerous smaller congestus clouds at midlevels leads to broad regions of rising motion in which new shedding thermals thrive. This is different from convective updrafts in the ~900 m horizontal grid spaced and 96 vertical level DHARMA-2M simulations in which updrafts are more or less continuous throughout the troposphere because large eddies are not resolved. Future work will involve greater investigation into the high resolution DHARMA-2M run and the suite of WRF simulations testing microphysics alterations of the Morrison two-moment bulk scheme.

Interactions between dynamics and microphysics that were singled out as being especially important will be tested in new model simulations. For example, the impact of latent heat release from the freezing of rain on the upper tropospheric vertical velocities can be studied by running simulations that do not include this latent heat release, and altering the fall speed relationship can test the impact of rain fallout. Sensitivity to representation of the large-scale environment should also be tested by altering analysis nudging techniques and assimilating soundings into LAM simulations to better represent zonal variability in instability and shear. Even with all of these test possibilities, the large

number of nonlinear processes interacting in systems full of buffers and feedbacks makes it difficult to single out specific processes as especially important to larger scale precipitation structures. An important tool for attacking this problem in future research will be the use of Lagrangian methods to track parcel properties as they move through convective updrafts in a variety of model complexities.

Although not in my immediate upcoming plans, future research should focus on quantifying errors due to model forcing methodology and work to test sensitivity to subgrid scale turbulence parameterizations by using higher order turbulence closures, none of which were used in the simulations for this case. As was mentioned in Section 2.1.1, multiday CRM simulations are subject to imbalances between surface fluxes and radiative flux divergence that cause model MSE drift. It is unclear how such imbalances affect cloud and precipitation properties. It is clear, however, that many errors are common to all CRM and LAM simulations. Among these errors was convection that was too strong, which in DHARMA-2M is only slightly weakened by resolution of large eddies. It is possible that grid spacing down to 10 m may be necessary to resolve important turbulent structures that can impact convective feedbacks and modes through interactions with dynamics and microphysics, but before doing that, it would be worthwhile to test different turbulence parameterizations against each other in various model setups to see if noticeable differences emerge.

While TWP-ICE was focused on the relationship between convective properties and the large-scale environment, observations and retrievals relevant to characterizing convective drafts were limited. The recent 2011 Mid-latitude Continental Convective Clouds Experiment (MC3E) centered on the ARM Southern Great Plains site in north-

central Oklahoma also shares the focus of relating convective properties to the large-scale environment. Far more observational datasets are available from MC3E to make more progress toward evaluating and identifying areas for improvement in cloud-resolving and limited area model simulations of deep convective systems. This is a good opportunity to test the conclusions drawn in this dissertation with different convective environments by comparing MC3E simulations and observational retrievals against those from TWP-ICE.

REFERENCES

Ackerman, A., O. Toon, D. Stevens, A. Heymsfield, V. Ramanathan, and E. Welton, 2000: Reduction of tropical cloudiness by soot. *Science,* **288**, 1042-1047.

Barnes, S. L., 1969: Some aspects of a severe, right-moving thunderstorm, deduced from mesonetwork rawinsonde observations. *J. Atmos. Sci.,* **27**, 634-648.

Bechtold, P., J.-L. Redelsperger, I. Beau, M. Blackburn, S. Brinkop, J.-Y. Grandper, A. Grant, D. Gregory, F. Guichard, C. How, and E. Ioannidou, 2000: A GCSS model intercomparison for a tropical squall line observed during TOGA-COARE. II: Intercomparison of single-column models and a cloud-resolving model. *Quart. J. Royal Meteor. Soc.,* **126**, 865-888.

Belamari, S., 2005: Report on uncertainty estimates of an optimal bulk formulation for surface turbulent fluxes, *Marine EnviRonment and Security for the European Area – Integrated Project (MERSEA IP), Deliverable D.4.1.2,* Plouzané, France.

Blossey, P. N., C. S. Bretherton, J. Cetrone, and M. Kharoutdinov, 2007: Cloud-resolving model simulations of KWAJEX: Model sensitivities and comparisons with satellite radar observations. *J. Atmos. Sci.,* **64**, 1488-1508.

Bohren, C. F. and L. J. Battan, 1980: Radar backscattering by inhomogeneous precipitation particles. *J. Atmos. Sci.,* **37**, 1821-1827.

Bougeault, P., P. Mascart, and J.-P. Chaboureau, 2009: The Meso-NH Atmospheric Simulation System: Scientific Documentation, Version 4.8, *Meteo-France/CNRS.*

Bringi, V. N., C. R. Williams, M. Thurai, and P. T. May, 2009: Using dual-polarized radar and dual-frequency profiler for DSD characterization: A case study from Darwin, Australia. *J. Atmos. Oceanic Tech.,* **26**, 2107-2122.

Brown, P. R. A. and P. N. Franci, 1995: Improved measurements of the ice water content in cirrus using a total-water probe. *J. Atmos. Oceanic Technol.,* **12**, 410-414.

Bryan, G. H., J. C. Wyngaard, and J. M. Fritsch, 2003: Resolution requirements for the simulation of deep moist convection. *Mon. Wea. Rev.,* **131**, 2394-2416.

Bryan, G. H., J. C. Knievel, and M. D. Parker, 2006: A multimodel assessment of RKW Theory's relevance to squall-line characteristics. *Mon. Wea. Rev.*, **134**, 2772-2792.

Bryan, G. H., and H. Morrison, 2012: Sensitivity of a simulated squall line to horizontal resolution and parameterization of microphysics. *Mon. Wea. Rev.,* **140**, 202-225.

Cao, Q., G. Zhang, E. Brandes, T. Shuur, A. Ryzhkov, and K. Ikeda, 2008: Analysis of video disdrometer and polarimetric radar data to characterize rain microphysics in Oklahoma. *J. Appl. Meteor. Clim.,* **47**, 2238-2255.

Chen, S. S. and W. M. Frank, 1993: A numerical study of the genesis of extratropical convective mesovortices. Part I: Evolution and dynamics. *J. Atmos. Sci.,* **50**, 2401-2426.

Colella, P. and P. Woodward, 1984: The piecewise parabolic method (PPM) for gas-dynamical simulations. *J. Comput. Phys.,* **54**, 174-201.

Collins, W. D., J. Wang, J. T. Kiehl, G. J. Zhang, D. I. Cooper, and W. E. Eichinger, 1997: Comparison of tropical ocean-atmosphere fluxes with the NCAR Community Climate Model CCM3. *J. Climate,* **10**, 3047-3058.

Collis, S., A. Protat, P. T. May, and C. Williams, 2013: Statistics of storm updraft velocities from TWP-ICE including verification with profiling measurements. *J. Applied Meteor. and Clim.,* **70**, accepted.

Cotton, W. R., G. J. Tripoli, R. M. Rauber, and E. A. Mulvihill, 1986: Numerical simulation of the effects of varying ice crystal nucleation rates and aggregation processes on orographic snowfall. *J. Clim. Appl. Meteor.*, **25**, 1658-1680.

Cox, G. P., 1988: Modelling precipitation in frontal rainbands. *Quart. J. Roy. Meteor. Soc.,* **114**, 115-127.

Craig, G. C., and A. Dörnbrack, 2008: Entrainment in cumulus clouds: What resolution is cloud-resolving? *J. Atmos. Sci.,* **65**, 3978-3988.

Cuxart, J., P. Bougeault, and J.-L. Redelsperger, 2000: A turbulence scheme allowing for mesoscale and large-eddy simulations. *Quart. J. Roy. Meteor. Soc.,* **126**, 1-30.

de Rooy, W. C., P. Bechtold, K. Frohlich, C. Hohenegger, H. Jonker, D. Mironov, A. P. Siebesma, J. Teixeira, and J.-I. Yano, 2013: Entrainment and detrainment in cumulus convection: an overview. *Quart. J. Royal Meteor. Soc.,* **139**, 1-19.

Deardorff, J. W., 1970: A numerical study of three-dimensional turbulent channel flow at large Reynolds number. *J. Fluid Mech.,* **41**, 453-480.

Debye, P., 1929: *Polar Molecules*. The Chemical Catalog Company, New York.

Del Genio, A. D., and W. Kovari, 2002: Climatic properties of tropical precipitating convection under varying environmental conditions. *J. Climate*, **15**, 2597-2615.

Del Genio, A. D. and J. Wu, 2010: The role of entrainment in the diurnal cycle of continental convection. *J. Climate,* **23**, 2722-2738.

Del Genio, A. D., J. Wu, and Y. Chen, 2012: Characteristics of mesoscale organization in WRF simulations of convection during TWP-ICE. *J. Climate,* **25**, 5666-5688, doi:10.1175/JCLI-D-11-00422.1.

Donner, L. J., 1993: A cumulus parameterization including mass fluxes, vertical momentum dynamics, and mesoscale effects. *J. Atmos. Sci.,* **50**, 889-906.

Donner, L. J., C. J. Seman, R. S. Hemler, and S. Fan, 2001: A cumulus parameterization including mass fluxes, vertical momentum dynamics, and mesoscale effects: Thermodynamic and hydrological aspects in a general circulation model. *J. Climate,* **14**, 3444-3463.

Dudhia, J., 1989: Numerical study of convection observed during the Winter Monsoon Experiment using a mesoscale two-dimensional model. *J. Atmos. Sci.*, **46**, 3077-3107.

Edwards, J. M. and A. Slingo, 1996: Studies with a flexible new radiation code. Part I: Choosing a configuration for a large-scale model. *Quart. J. Roy. Meteor. Soc.,* **122**, 689-719.

Feingold, G., R. L. Walko, B. Stevens, and W. R. Cotton, 1998: Simulations of marine stratocumulus using a new microphysical parameterization scheme. *Atmos. Res.,* **47-48**, 505-528.

Ferrier, B. S., 1994: A double-moment multiple-phase four-class bulk ice scheme. Part I: Description. *J. Atmos. Sci.*, **51**, 249-280.

Ferrier, B. S., W.-K. Tao, and J. Simpson, 1995: A double-moment multiple-phase four-class bulk ice scheme. Part II: Simulations of convective storms in different large-scale environments and comparison with other bulk parameterizations. *J. Atmos. Sci.,* **52**, 1001-1033.

Ferrier, B. S., J. Simpson, and W.-K. Tao, 1996: Factors responsible for precipitation efficiency in midlatitude and tropical squall simulations. *Mon. Wea. Rev.,* **124**, 2100-2125.

Field, P. R., R. J. Hogan, P. R. A. Brown, A. J. Illingsworth, T. W. Choularton, and R. J. Cotton, 2005: Parameterization of ice-particle size distributions for mid-latitude stratiform cloud. *Quart. J. Roy. Meteor. Soc.*, **131**, 1997-2017.

Fierro, A. O., J. Simpson, M. A. LeMone, J. M. Straka, and B. F. Smull, 2009: On how hot towers fuel the Hadley cell: An observational and modeling study of line-organized convection in the equatorial trough from TOGA COARE. *J. Atmos. Sci.*, **66**, 2730-2746.

Fowler, L. D., D. A. Randall, and S. A. Rutledge, 1996: Liquid and ice cloud microphysics in the CSU general circulation model. Part I: Model description and simulated microphysical processes. *J. Climate*, **9**, 489-529.

Fridlind, A., A. Ackerman, J. Petch, P. Field, A. Hill, G. McFarquhar, S. Xie, and M. Zhang, 2010: ARM/GCSS/SPARC TWP-ICE CRM Intercomparison Study. NASA Tech. Memo. NASA TM-2010-215858, 24 pp.

Fridlind, A. M., and Coauthors, 2012: A comparison of TWP-ICE observational data with cloud-resolving model results. *J. Geophys. Res.*, **117**(D05204), doi:10.1029/2011JD016595.

Ghan, S. J., L. R. Leung, and Q. Hu, 1997: Application of cloud microphysics to NCAR community climate model. *J. Geophys. Res.*, **102**(D14), doi:10.1029/97JD00703.

Ghan, S. J., and Coauthors, 2000: An intercomparison of single column model simulations of summertime midlatitude continental convection. *J. Geophys. Res.*, **105**(D2), doi: 10.1029/1999JD90071.

Gilmore, M. S., J. M. Straka, and E. N. Rasmussen, 2004: Precipitation uncertainty due to variations in precipitation particle parameters within a simple microphysics scheme. *Mon. Wea. Rev.*, **132**, 2610-2627.

Grabowski, W. W., 1999: A parameterization of cloud microphysics for long-term cloud-resolving modeling of tropical convection. *Atmos. Res.*, **52**, 17-41.

Grabowski, W. W., 2001: Coupling cloud processes with the large-scale dynamics using the cloud-resolving convection parameterization (CRCP). *J. Atmos. Sci.*, **58**, 978-997.

Grabowski, W. W., P. Bechtold, A. Cheng, R. Forbes, C. Halliwell, M. Khairoutdinov, S. Lang, T. Nasuno, J. Petch, W.-K. Tao, R. Wong, X. Wu, and K.-M. Xu, 2006: Daytime convective development over land: A model intercomparison based on LBA observations. *Quart. J. Royal Meteor. Soc.*, **132**, 317-344.

Gray, M. E. B., J. Petch, S. H. Derbyshire, A. R. Brown, A. P. Lock, H. A. Swann, and P. R. A. Brown, 2001: Version 2.3 of the Met Office Large Eddy Model: Part II. Scientific documentation. Met O (APR) Turbulence and Diffusion Note No. 276.

Hallett, J. and S. C. Mossop, 1974: Production of secondary ice particles during the riming process. *Nature,* **249**, 26-28.

Hamilton, K., R. A. Vincent, and P. May, 2004: Darwin Area Wave Experiment (DAWEX) field campaign to study gravity wave generation and propagation. *J. Geophys. Res.*, **109**(D20), doi:10.1029/2003JD004393.

Hartmann, D. L., H. H. Hendon, and R. A. Houze, Jr., 1984: Some implications of the mesoscale circulations in tropical cloud clusters for large-scale dynamics and climate. *J. Atmos. Sci.*, **41**, 113-121.

Heus, T., H. J. J. Jonker, H. E. A. van den Akker, E. J. Griffith, M. Koutek, and F. H. Post, 2009: A statistical approach to the life cycle analysis of cumulus clouds selected in

a virtual reality environment. *J. Geophys. Res.*, **114**(D06208), doi:10.1029/2008JD010917.

Heymsfield, A. J., P.N. Johnson, and J. E. Dye, 1978: Observations of moist adiabatic ascent in northeast Colorado cumulus congestus clouds. *J. Atmos. Sci.*, **35**, 1689-1703.

Heymsfield, A. J. and M. Kajikawa, 1987: An improved approach to calculating terminal velocities of plate-like crystals and graupel. *J. Atmos. Sci.*, **44**, 1088-1099.

Heymsfield, A. J., A. Bansemer, G. Heymsfield, A. O. Fierro, 2009: Microphysics of maritime tropical convective updrafts at temperatures from -20° to -60°. *J. Atmos. Sci.*, **66**, 3530–3562.

Heymsfield, G. M., L. Tian, A. J. Heymsfield, L. Li, S. Guimond, 2010: Characteristics of deep tropical and subtropical convection from nadir-viewing high-altitude airborne Doppler radar. *J. Atmos. Sci.*, **67**, 285–308.

Hong, S.-Y., and J.-O. J. Lim, 2006: The WRF single-moment 6-class microphysics scheme (WSM6). *J. Korean Meteor. Soc.*, **42**, 129-151.

Hong, S.-Y., Y. Noh, and J. Dudhia, 2006: A new vertical diffusion package with an explicit treatment of entrainment processes. *Mon. Wea. Rev.*, **134**, 2318-2341.

Houze, R. A., Jr., P. V. Hobbs, P. H. Herzegh, and D. B. Parsons, 1979: Size distributions of precipitation particles in frontal clouds. *J. Atmos. Sci.*, **36**, 156-162.

Houze, R. A., Jr., 1982: Cloud clusters and large-scale vertical motions in the tropics. *J. Meteor. Soc. Japan*, **60**, 396-410.

Houze, R. A., Jr., 1989: Observed structure of mesoscale convective systems and implications for large-scale heating. *Quart. J. Roy. Meteor. Soc.*, **115**, 425-461.

Houze, R. A., Jr., 1997: Stratiform precipitation in regions of convection: A meteorological paradox? *Bull. Am. Meteor. Soc.*, **78**, 2179-2196.

Houze, R. A., Jr., 2004: Mesoscale convective systems. *Rev. Geophys.*, **42**, RG4003.

Houze, R. A., Jr., W-C. Lee, and M. M. Bell, 2009: Convective contribution to the genesis of Hurricane Ophelia. *Mon. Wea. Rev.*, **137**, 2778-2800.

Ikawa, M., and K. Saito, 1991: Description of a nonhydrostatic model developed at the Forecast Research Department of the MRI. Tech. Res. MRI No. 28, Meteorological Research Institute, Japan, 238 pp.

Johnson, R. H., 1984: Partitioning tropical heat and moisture budgets into cumulus and mesoscale components: Implications for cumulus parameterization. *Mon. Wea. Rev.*, **112**, 1590-1601.

Jorgensen, D. P. and M. A. LeMone, 1989: Vertical velocity characteristics of oceanic convection. *J. Atmos. Sci.,* **46**, 621-640.

Kain, J. S., 2004: The Kain-Fritsch convective parameterization: An update. *J. Appl. Meteor.,* **43**, 170-181.

Keenan, T. D. and R. E. Carbone, 1992: A preliminary morphology of precipitation systems in tropical northern Australia. *Quart. J. Royal Meteor. Soc.,* **118**, 283-326.

Keenan, T. D., K. Glasson, F. Cummings, T. S. Bird, J. Keeler, and J. Lutz, 1998: The BMRC/NCAR C-band polarimetric (C-POL) radar system. *J. Atmos. Oceanic Tech.,* **15**, 871-886.

Keenan, T., and Coauthors, 2000: The Maritime Continent Thunderstorm Experiment (MCTEX): Overview and some results. *Bull. Amer. Meteor. Soc.,* **81**, 2433-2455.

Kessler, E., 1969: On the distribution and continuity of water substance in atmospheric circulations. *Meteor. Monogr.,* **10**, 1-84.

Khairoutdinov, M. F., and D. A. Randall, 2001: A cloud resolving model as a parameterization in the NCAR Community Climate System Model: Preliminary results. *Geophys. Res. Lett.*, **28**, 3617-3620.

Khairoutdinov, M., and D. Randall, 2003: Cloud resolving modeling of the ARM summer 1997 IOP: Model formulation, results, uncertainties, and sensitivities. *J. Atmos. Sci.,* **60**, 607-625.

Khairoutdinov, M. F., and D. A. Randall, 2006: High-resolution simulation of shallow-to-deep convection transition over land. *J. Atmos. Sci.,* **63**, 3421-3436.

Khairoutdinov, M. F., S. K. Krueger, C.-H. Moeng, P. A. Bogenschutz, and D. A. Randall, 2009: Large-eddy simulation of maritime deep tropical convection. *J. Adv. Model. Earth Syst.,* **1**(4), 13 pp., doi:10.3894/JAMES.2009.1.15.

Kiehl, J. T., J. J. Hack, G. B. Bonan, B. A. Boville, D. L. Williamson, and P. J. Rasch, 1998: The National Center for Atmospheric Research Community Climate Model: CCM3. *J. Climate,* **11**, 1131-1149.

Kim, D., and Coauthors, 2009: Application of MJO simulation diagnostics to climate models. *J. Climate,* **22**, 6413-6436.

Kingsmill, D. E., S. E. Yuter, A. J. Heymsfield, P. V. Hobbs, A. V. Korolev, J. L. Stith, A. Bansemer, J. A. Haggerty, and A. L. Rangno, 2004: TRMM common microphysics products: A tool for evaluating spaceborne precipitation retrieval algorithms. *J. Appl. Meteor.*, **43**, 1598-1618.

Kuang, Z. and C. S. Bretherton, 2006: A mass-flux scheme view of a high-resolution simulation of a transition from shallow to deep cumulus convection. *J. Atmos. Sci.*, **63**, 1895-1909.

Kummerow, C., and Coauthors, 2001: The evolution of the Goddard Profiling Algorithm (GPROF) for rainfall estimation from passive microwave sensors. *J. Appl. Meteor.*, **40**, 1801-1820.

Lafore, J. P., J. Stein, N. Asencio, P. Bougeault, V. Ducrocq, J. Duron, C. Fischer, P. Héreil, P. Mascart, V. Masson, J. P. Pinty, J. L. Redelsperger, E. Richard, and J. Vilà-Guerau de Arellano, 1998: The Meso-NH atmospheric simulation system. Part I: Adiabatic formulation and control simulations. *Annales Geophysicae,* **16**, 90-109.

Lang, S., W.-K. Tao, J. Simpson, R. Cifelli, S. Rutledge, W. Olson, and J. Halverson, 2007: Improving simulations of convective systems from TRMM LBA: Easterly and westerly regimes. *J. Atmos. Sci.*, **64**, 1141-1164.

Lang, S. E., W.-K. Tao, X. Zeng, and Y. Li, 2011: Reducing the biases in simulated radar reflectivities from a bulk microphysics scheme: Tropical convective systems. *J. Atmos. Sci.*, **68**, 2306-2320.

Lawson, R. P., E. Jensen, D. L. Mitchell, B. Baker, Q. Mo, and B. Pilson, 2010: Microphysical and radiative properties of tropical clouds investigated in TC4 and NAMMA. *J. Geophys. Res.*, **115**(D00J08), doi:10.1029/2009JD013017.

LeMone, M. A. and E. J. Zipser, 1980: Cumulonimbus vertical velocity events in GATE. Part I: Diameter, intensity, and mass flux. *J. Atmos. Sci.*, **37**, 2444-2457.

Leonard, B. P., M. K. MacVean, and A. P. Lock, 1993: Positivity-preserving numerical schemes for multidimensional advection. NASA Technical Memorandum 106055 (ICOMP-93905), NASA, Greenbelt, MD.

Li, Y., E. J. Zipser, S. K. Krueger, and M. A. Zulauf, 2008: Cloud-resolving modeling of deep convection during KWAJEX: Part I: Comparison to TRMM satellite and ground-based observations. *Mon. Wea. Rev.*, **136**, 2699-2712.

Li, X., W.-K. Tao, A. P. Khain, J. Simpson, and D. E. Johnson, 2009: Sensitivity of a cloud-resolving model to bulk and explicit bin microphysical schemes. Part II: Cloud microphysics and storm dynamics interactions. *J. Atmos. Sci.*, **66**, 22-40.

Lilly, D. K., 1967: The representation of small-scale turbulence in numerical simulation experiments. *Proceedings of IBM Scientific Symposium on Environmental Sciences, IBM Form No. 320-1951*, 195-210.

Lin, J.-L., and Coauthors, 2006: Tropical intraseasonal variability in 14 IPCC AR4 climate models. Part I: Convective signals. *J. Climate,* **19**, 2665-2690.

Lin, Y.-L., R. D. Farley, and H. D. Orville, 1983: Bulk parameterization of the snow field in a cloud model. *J. Climate Appl. Meteor.*, **22**, 1065-1092.

Lin, Y. and B. A. Colle, 2011: A new bulk microphysical scheme that includes riming intensity and temperature-dependent characteristics. *Mon. Wea. Rev.*, **139**, 1013-1035.

Lin, Y., and Coauthors, 2012: TWP-ICE global atmospheric model intercomparison: Convection responsiveness and resolution impact. *J. Geophys. Res.*, **117**(D09111), doi:10.1029/2011JD017018.

Locatelli, J. D. and P. V. Hobbs, 1974: Fall speeds and masses of solid precipitation particles. *J. Geophys. Res.*, **79**(15), doi:10.1029/JC079i015p02185.

Lohmann, U., and E. Roeckner, 1996: Design and performance of a new cloud microphysics scheme developed for the ECHAM general circulation model. *Climate Dynamics*, **12**, 557-572.

Lucas, C., E. J. Zipser, M. A. Lemone, 1994: Vertical velocity in oceanic convection off tropical Australia. *J. Atmos. Sci.*, **51**, 3183–3193.

Luo, Y., Y. Wang, H. Wang, Y. Zheng, and H. Morrison, 2010: Modeling convective-stratiform precipitation processes on a Mei-Yu front with the Weather Research and Forecasting model: Comparison with observations and sensitivity to cloud microphysics parameterizations. *J. Geophys. Res.*, **115**(D18117), doi:10.1029/2010JD013873.

Mapes, B. E. and R. A. Houze, Jr., 1995: Diabatic divergence profiles in western Pacific mesoscale convective systems. *J. Atmos. Sci.*, **52**, 1807-1828.

Mapes, B. E., S. Tulich, J. Lin, and P. Zuidema, 2006: The mesoscale convection life cycle: Building block or prototype for large-scale tropical waves? *Dyn. Atmos. Oceans*, **42**, 3-29.

Mapes, B. E. and R. Neale, 2011: Parameterizing convective organization to escape the entrainment dilemma. *J. Adv. Model. Earth Syst.*, **3**(2), 20 pp., doi:10.1029/2011MS000042.

Marshall, J. S. and W. Mc K. Palmer, 1948: The distribution of raindrops with size. *J. Meteor.*, **5**, 165–166.

Matsui, T., X. Zeng, W-K. Tao, H. Masunaga, W. S. Olson, and S. Lang, 2009: Evaluation of long-term cloud-resolving model simulations using satellite radiance observations and multifrequency satellite simulators. *J. Atmos. Oceanic Tech.*, **26**, 1261-1274.

May, P. T. and D. K. Rajopadhyaya, 1999: Vertical velocity characteristics of deep convection over Darwin, Australia. *Mon. Wea. Rev.*, **127**, 1056–1071.

May, P. T. and A. Ballinger, 2007: The statistical characteristics of convective cells in a monsoon regime (Darwin, Northern Australia). *Mon. Wea. Rev.,* **135**, 82–92.

May, P. T., J. H. Mather, G. Vaughan, K. N. Bower, C. Jakob, G. M. McFarquhar, and G. G Mace, 2008: The Tropical Warm Pool International Cloud Experiment. *Bull. Amer. Meteor. Soc.*, **89**, 629-645.

May, P. T., V. N. Bringi, and M. Thurai, 2011: Do we observe aerosol impacts on DSDs in strongly forces tropical thunderstorms? *J. Atmos. Sci.,* **68**, 1902-1910.

McCumber, M., W.-K. Tao, J. Simpson, R. Penc, and S. T. Soong, 1991: Comparison of ice-phase microphysical parameterization schemes using numerical simulations of tropical convection. *J. Appl. Meteor.,* **30**, 985-1004.

McFarquhar, G. M. and A. J. Heymsfield, 1997: Parameterization of tropical cirrus ice crystal size distributions and implications for radiative transfer: Results from CEPEX. *J. Atmos. Sci.,* **54**, 2187-2200.

McFarquhar, G. M., H. Zhang, G. Heymsfield, J. B. Halverson, R. Hood, J. Dudhia, F. Marks, 2006: Factors affecting the evolution of Hurricane Erin (2001) and the distributions of hydrometeors: Role of microphysical processes. *J. Atmos. Sci.,* **63**, 127-150.

McFarquhar, G. M., 2010: Raindrop size distribution and evolution. *Rainfall: State of the Science, Geophys. Monogr. Series 191*, 49-60, doi:10.1029/2010GM000971.

McTaggart-Cowan, J. D. and R. List, 1975: Collision and breakup of water drops at terminal velocity. *J. Atmos. Sci.,* **32**, 1401-1411.

Milbrandt, J. A. and M. K. Yau, 2005: A multimoment bulk microphysics parameterization. Part 1: Analysis of the role of the spectral shape parameter. *J. Atmos. Sci.,* **62**, 3051-3064.

Milbrandt, J. A. and M. K. Yau, 2005: A multimoment bulk microphysics parameterization. Part II: A proposed three-moment closure and scheme description. *J. Atmos. Sci.,* **62**, 3065-3081.

Milbrandt, J. A. and H. Morrison, 2013: Prediction of graupel density in a bulk microphysics scheme. *J. Atmos. Sci.,* **70**, 410-429.

Mlawer, E. J., S. J. Taubman, P. D. Brown, M. J. Iacono, and S. A. Clough, 1997: Radiative transfer for inhomogeneous atmospheres: RRTM, a validated correlated-k model for the longwave. *J. Geophys. Res.,* **102**(D14), doi:10.1029/97JD00237.

Moncrieff, M. W., D. E. Waliser, M. J. Miller, M. A. Shapiro, G. R. Asrar, and J. Caughey, 2012: Multiscale convective organization and the YOTC virtual global field campaign. *Bull. Amer. Meteor. Soc.,* **93**, 1171-1187, doi:10.1175/BAMS-D-11-00233.1.

Monin, A. S. and A. M. Obukhov, 1954: Basic laws of turbulent mixing in the surface layer of the atmosphere. *Tr. Geofiz. Inst. Akad. Nauk SSSR,* **24**, 163-187.

Morrison, H. and W. W. Grabowski, 2008: A novel approach for representing ice microphysics in models: Description and tests using a kinematic framework. *J. Atmos. Sci.,* **65**, 1528-1548.

Morrison, H., G. Thompson, and V. Tatarskii, 2009: Impact of cloud microphysics on the development of trailing stratiform precipitation in a simulated squall line: Comparison of one- and two-moment schemes. *Mon. Wea. Rev,* **137**, 991-1007.

Morrison, H. and J. Milbrandt, 2011: Comparison of two-moment bulk microphysics schemes in idealized supercell thunderstorm simulations. *Mon. Wea. Rev.,* **139**, 1103-1130.

Morrison, H., S. A. Tessendorf, K. Ikeda, and G. Thompson, 2012: Sensitivity of a simulated mid-latitude squall line to parameterization of raindrop breakup. *Mon. Wea. Rev.*, **140**, 2437-2460.

Mrowiec, A. A., C. Rio, A. M. Fridlind, A. S. Ackerman, A. D. Del Genio, O. M. Pauluis, A. C. Varble, and J. Fan, 2012: Analysis of cloud-resolving simulations of a tropical mesoscale convective system observed during TWP-ICE: Vertical fluxes and draft properties in convective and stratiform regions. *J. Geophys. Res.,* **117**(D19), doi:10.1029/2012JD017759.

Neale, R., and J. Slingo, 2003: The maritime continent and its role in the global climate: A GCM study. *J. Climate*, **16**, 834-848.

Petch, J. C. and M. E. B. Gray, 2001: Sensitivity studies using a cloud-resolving model simulation of the tropical west Pacific. *Quart. J. Royal Meteor. Soc.,* **127**, 2287-2306.

Petch, J. C., A. R. Brown, and M. E. B. Gray, 2002: The impact of horizontal resolution on the simulations of convective development over land. *Quart. J. Roy. Meteor. Soc.,* **128**, 2031-2044.

Petersen, W. A. and S. A. Rutledge, 2001: Regional variability in tropical convection: Observations from TRMM. *J. Climate,* **14**, 3566–3586.

Piascek, S. A. and G. P. Williams, 1970: Conservation properties of convection difference schemes. *J. Comput. Phys.,* **6**, 392-405.

Pinty, J.-P., 2002: A quasi 2-moment microphysical scheme for mixed-phase clouds at mesoscale with sensitivity to aerosols (CCN and IN), *11th Conference on Cloud Physics*, Amer. Meteor. Soc.

Ramond, D., 1978: Pressure perturbations in deep convection: An experimental study. *J. Atmos. Sci.,* **35**, 1704-1711.

Randall, D., M. Khairoutdinov, A. Arakawa, and W. Grabowski, 2003: Breaking the cloud parameterization deadlock. *Bull. Amer. Meteor. Soc.*, **84**, 1547-1564.

Randall, D. A., and Coauthors, 2007: Climate models and their evaluation. *Climate Change 2007: The Physical Science Basis, Contribution of Working Group I to the Fourth Assessment Report of the Intergovernmental Panel on Climate Change*. S. Soloman et al., Ed., Cambridge Univ. Press, Cambridge, U. K., 589-662.

Redelsperger, J.-L., P. R. A. Brown, F. Guichard, C. How, M. Kawasima, S. Lang, T. Montmerle, K. Nakamura, K. Saito, C. Seman, W. K. Tao, and L. J. Donner, 2000: A GCSS model intercomparison for a tropical squall line observed during TOGA-COARE. Part I: CRM results. *Quart. J. Royal Meteor. Soc.,* **126**, 823-863.

Reisner, J., R. M. Rasmussen, and R. T. Bruintjes, 1998: Explicit forecasting of supercooled liquid water in winter storms using the MM5 mesoscale model. *Quart. J. Roy. Meteor. Soc.*, **124**, 1071-1107.

Riehl, H., and J. S. Malkus, 1958: On the heat balance in the equatorial trough zone. *Geophysica,* **6**, 503-538.

Romps, D. M. and Z. Kuang, 2010: Do undiluted convective plumes exist in the upper tropical troposphere? *J. Atmos. Sci.,* **67**, 468–484.

Rotstayn, L. D., 1997: A physically based scheme for the treatment of stratiform clouds and precipitation in large-scale models. I: Description and evaluation of the microphysical processes. *Quart. J. Roy. Meteor. Soc.*, **123**, 1227-1282.

Rotunno, R. and J. Klemp, 1984: On the rotation and propagation of supercell thunderstorms. *J. Atmos. Sci.,* **42**, 271-292.

Rotunno, R., J. B. Klemp, and M. L. Weisman, 1988: A theory for strong, long-lived squall lines. *J. Atmos. Sci.,* **45**, 463-485.

Rutledge, S. A., and P. V. Hobbs, 1984: The mesoscale and microscale structure and organization of clouds and precipitation in midlatitude cyclones. XII: A diagnostic modeling study of precipitation development in narrow cold-frontal rainbands. *J. Atmos. Sci.*, **41**, 2949-2972.

Rutledge, S. A., E. R. Williams, and T. D. Keenan, 1992: The Down Under Doppler and Electricity Experiment (DUNDEE): Overview and preliminary results. *Bull. Amer. Meteor. Soc.,* **73**, 3-16.

Ryzhkov, A. V., T. J. Schuur, D. W. Burgess, P. L. Heinselman, S. E. Giangrande, and D. S. Zrnic, 2005: The joint polarization experiment: Polarimetric rainfall measurements and hydrometeor classification. *Bull. Amer. Meteor. Soc.,* **89**, 809-824.

Schumacher, C. and R. A. Houze, Jr., 2003: Stratiform rain in the tropics as seen by the TRMM precipitation radar. *J. Climate,* **16**, 1739-1756.

Schumacher, C., R. A. Houze, Jr., and I. Kraucunas, 2004: The tropical dynamical response to latent heating estimates derived from the TRMM precipitation radar. *J. Atmos. Sci.*, **61**, 1341-1358.

Seifert, A., 2008: On the parameterization of evaporation of raindrops as simulated by a one- dimensional rainshaft model. *J. Atmos. Sci.*, **65**, 3608-3619.

Shige, S., Y. N. Takayabu, S. Kida, W.-K. Tao, X. Zeng, C. Yokoyama, T. L'Ecuyer, 2009: Spectral Retrieval of Latent Heating Profiles from TRMM PR Data. Part IV: Comparisons of Lookup Tables from Two- and Three-Dimensional Cloud-Resolving Model Simulations. *J. Climate*, **22**, 5577–5594.

Shutts, G. J. and M. E. B. Gray, 1994: A numerical modeling study of the geostrophic adjustment process following deep convection. *Quart. J. Royal Meteor. Soc.*, **120**, 1145-1178.

Skamarock, W. C., J. B. Klemp, J. Dudhia, D. O. Gill, D. M. Barker, M. G. Duda, X.-Y. Huang, W. Wang, and J. G. Powers, 2008: A description of the Advanced Research WRF version 3. NCAR Technical Note, NCAR/TN-475+STR.

Smith, P. L., 1984: Equivalent radar reflectivity factors for snow and ice particles. *J. Climate Appl. Meteor.*, **23**, 1258-1260.

Smolarkiewicz, P. K. and W. W. Grabowski (1990), The multidimensional positive definite advection transport algorithm – Nonoscillatory option. *J. Comput. Phys.*, **86**, 355-375.

Srivastava, R. C., 1971: Size distribution of raindrops generated by their breakup and coalescence. *J. Atmos. Sci.*, **28**, 410-415.

Steiner, M., R. Houze, and S. E. Yuter, 1995: Climatological characterization of three-dimensional storm structure from operational radar and rain gauge data. *J. Appl. Meteor.*, **34**, 1978-2007.

Stephens, G., 2005: Cloud feedbacks in the climate system: A critical review. *J. Climate*, **18**, 237-273.

Stevens, B., 2005: Atmospheric moist convection. *Annu. Rev. Earth Planet. Sci.*, **33**, 605-643.

Stevens, D. E. and C. S. Bretherton, 1996: A forward-in-time advection scheme and adaptive multilevel flow solver for nearly incompressible atmospheric flow. *J. Comput. Phys.*, **129**, 284-295.

Stevens, D. E., A. S. Ackerman, and C. S. Bretherton, 2002: Effects of domain size and numerical resolution on the simulation of shallow cumulus convection. *J. Atmos. Sci.*, **59**, 3285-3301.

Stith, J. L., J. E. Dye, A. Bansemer, A. J. Heymsfield, C. A. Grainger, W. A. Petersen, and R. Cifelli, 2002: Microphysical observations of tropical clouds. *J. Appl. Meteor.,* **41**, 97-117.

Stith, J. L., J. A. Haggerty, A. Heymsfield, C. A. Grainger, 2004: microphysical characteristics of tropical updrafts in clean conditions. *J. Appl. Meteor.,* **43**, 779–794.

Stith, J. L., J. Haggarty, C. Grainger, and A. Detwiler, 2006: A comparison of the microphysical and kinematic characteristics of mid-latitude and tropical convective updrafts and downdrafts. *Atmos. Res.,* **82**, 350-366.

Tao, W-K., J. R. Scala, B. Ferrier, and J. Simpson, 1995: The effect of melting processes on the development of a tropical and midlatitude squall line. *J. Atmos. Sci.*, **52**, 1934-1948.

Straka, J. M. and E. R. Mansell, 2005: A bulk microphysics parameterization with multiple ice precipitation categories. *J. Appl. Meteor.*, **44**, 445-466.

Tao, W.-K., J. R. Scala, B. Ferrier, and J. Simpson, 1995: The effect of melting processes on the development of a tropical and mid-latitude squall line. *J. Atmos. Sci.,* **52**, 1934-1948.

Tao, W.-K., and M. W. Moncrieff, 2009: Multiscale cloud system modeling. *Rev. Geophys.*, **47**, RG4002.

Thompson, G., R. M. Rasmussen, and K. Manning, 2004: Explicit forecasts of winter precipitation using an improved bulk microphysics scheme. Part I: Description and sensitivity analysis. *Mon. Wea. Rev.,* **132**, 519–542.

Thompson, G., P. R. Field, R. M. Rasmussen, and W. D. Hall, 2008: Explicit forecasts of winter precipitation using an improved bulk microphysics scheme. Part II: Implementation of a new snow parameterization. *Mon. Wea. Rev.,* **136**, 5095-5115.

Thompson, R. L., R. Edwards, J. A. Hart, K. L. Elmore, and P. Markowski, 2003: Close proximity soundings within supercell environments obtained from the Rapid Update Cycle. *Wea. Forecasting,* **18**, 1243-1261.

Tiedtke, M., 1993: Representation of clouds in large-scale models. *Mon. Wea. Rev.*, **121**, 3040-3061.

Tokay, A., and D. A. Short, 1996: Evidence from tropical raindrop spectra of the origin of rain from stratiform versus convective clouds. *J. Appl. Meteor.*, **35**, 355-371.

Tokay, A., A. Kruger, and W. F. Krajewski, 2001: Comparison of drop size distribution measurements by impact and optical disdrometers. *J. Appl. Meteor., 40*, 2083-2097.

Toon, O. B., C. P. McKay, T. P. Ackerman, and K. Santhanam, 1989: Rapid calculation of radiative heating rates and photodissociation rates in inhomogeneous multiple scattering atmospheres. *J. Geophys. Res.,* **94**(D13), doi:10.1029/JD094iD13p16287.

Tripoli, G. J. and W. R. Cotton, 1980: A numerical investigation of several factors contributing to the observed variable intensity of deep convection over South Florida. *J. Appl. Meteor.,* **19**, 1037-1063.

Uma, K. N. and T. Narayana Rao, 2008: Characteristics of vertical velocity cores in different convective systems observed over Gadanki, India. *Mon. Wea. Rev.,* **137**, 954-975.

Van Weverberg, K., A. M. Vogelmann, H. Morrison, and J. A. Milbrandt, 2012: Sensitivity of idealized squall line simulations to the level of complexity used in two-moment bulk microphysics schemes. *Mon. Wea. Rev.,* **140**, 1883-1907.

Van Weverberg, K., A. M. Vogelmann, W. Lin, E. P. Luke, A. Cialella, P. Minnis, M. Khaiyer, E. R. Boer, and M. P. Jensen, 2013: The role of microphysics parameterization in the simulation of mesoscale convective system clouds and precipitation in the Tropical Western Pacific. *J. Atmos. Sci.*, **70**, 1104-1128.

Varble, A., A. M. Fridlind, E. J. Zipser, A. S. Ackerman, J.-P. Chaboureau, J. Fan, A. Hill, S. A. McFarlane, J.-P. Pinty, and B. Shipway, 2011: Evaluation of cloud-resolving model intercomparison simulations using TWP-ICE observations: Precipitation and cloud structure. *J. Geophys. Res.,* **116**(D12206), doi:10.1029/2010JD015180.

Vaughan, G., K. Bower, C. Schiller, A. R. MacKenzie, T. Peter, H. Schlager, N. R. P. Harris, P. T. May, 2008: SCOUT-O3/ACTIVE: High-altitude aircraft measurements around deep tropical convection. *Bull. Amer. Meteor. Soc.,* **89**, 647–662.

Wacker, U. and A. Seifert, 2001: Evolution of rain water profiles resulting from pure sedimentation: Spectral vs. parameterized description. *Atmos. Res.,* **58**, 19-39.

Waldvogel, A., 1974: The N_0 jump of raindrop spectra. *J. Atmos. Sci.,* **31**, 1067-1078.

Webster, P. J. and R. A. Houze, Jr., 1991: The Equatorial Mesoscale Experiment (EMEX): An overview. *Bull. Amer. Meteor. Soc.,* **72**, 1481-1505.

Wei, D., A. M. Blyth, and D. J. Raymond, 1998: Buoyancy of convective clouds in TOGA COARE. *J. Atmos. Sci.,* **49**, 1386-1395.

Weill, A., L. Eymard, G. Caniaux, D. Hauser, S. Planton, H. Dupuis, A. Brut, C. Guerin, P. Nacass, A. Butet, S. Cloché, R. Pedreros, D. Bourras, H. Giordani, G. Lachaud, and G. Bouhours, 2003: Toward better determination of turbulent air-sea fluxes from several experiments. *J. Climate,* **16**, 600-618.

Weisman, M. L. and J. B. Klemp, 1984: The structure and classification of numerically simulated convective storms in directionally varying wind shears. *Mon. Wea. Rev.*, **112**, 2479-2498.

Weisman, M. L. and R. Rotunno, 2004: "A theory for strong long-lived squall lines" revisited. *J. Atmos. Sci.*, **61**, 361-382.

Wilhelmson, R., 1974: The life cycle of a thunderstorm in three dimensions. *J. Atmos. Sci.*, **31**, 1629-1651.

Williams, C. R., and K. S. Gage, 2009: Raindrop size distribution variability estimated using ensemble statistics. *Ann. Geophys.*, **27**, 555-567.

Wilson, D. R., and S. P. Ballard, 1999: A microphysically based precipitation scheme for the UK Meteorological Office Unified Model. *Quart. J. Roy. Meteor. Soc.*, **125**, 1607-1636.

Wu, X., W. Grabowski, and M. Moncrieff, 1998: Long-term behavior of cloud systems in TOGA COARE and their interactions with radiative and surface processes. Part I: Two-dimensional modeling study. *J. Atmos. Sci.*, **55**, 2693-2714.

Wu, X., and M. W. Moncrieff, 2001: Sensitivity of single-column model solutions to convective parameterizations and initial conditions. *J. Climate*, **14**, 2563-2582.

Xie, S., and Coauthors, 2002: Intercomparison and evaluation of cumulus parameterizations under summertime midlatitude continental conditions. *Quart. J. Royal Meteor. Soc.*, **128**, 1095-1135.

Xie, S., T. Hume, C. Jakob, S. Klein, R. McCoy, and M. Zhang, 2010: Observed large-scale structures and diabatic heating and drying profiles during TWP-ICE. *J. Climate,* **23**, 57-79.

Xu, K.-M., and Coauthors, 2002: An intercomparison of cloud-resolving models with the Atmospheric Radiation Measurement summer 1997 Intensive Observation Period data. *Quart. J. Royal Meteor. Soc.,* **128**, 593-624.

Xu, W. and E. J. Zipser, 2012: Properties of deep convection in tropical continental, monsoon, and oceanic rainfall regimes. *Geophys. Res. Lett.,* **39**(L07802), doi:10.1029/2012GL051242.

Yano, J.-I. and V. T. J. Phillips, 2011: Ice-ice collisions: An ice multiplication process in atmospheric clouds. *J. Atmos. Sci.,* **68**, 322-333.

Zeng, X., W.-K. Tao, S. Lang, A. Y. Hou, M. Zhang, and J. Simpson, 2008: On the sensitivity of atmospheric ensembles to cloud microphysics in long-term cloud-resolving model simulations. *J. Meteor. Soc. Japan,* **86A**, 45-65.

Zhang, G., J. Vivekanandan, E. A. Brandes, R. Meneghini, and T. Kozu, 2003: The

shape-slope relation in observed gamma raindrop size distributions: Statistical error or useful information? *J. Atmos. Oceanic Tech.*, **20**, 1106-1119.

Zhao, M., and P. H. Austin, 2005: Life cycle of numerically simulated shallow cumulus clouds. Part I: Transport. *J. Atmos. Sci.*, **62**, 1269-1290.

Zhou, Y. P., W.-K. Tao, A. Y. Hou, W. S. Olson, C.-L. Shie, K.-M. Lau, M.-D. Chou, X. Lin, and M. Grecu, 2007: Use of high-resolution satellite observations to evaluate cloud and precipitation statistics from cloud-resolving model simulations. Part I: South China Sea Monsoon Experiment, *J. Atmos. Sci*., **64**, 4309–4329.

Zhu, P., J. Dudhia, P. R. Field, A. Fridlind, A. Varble, E. Zipser, J. Petch, M. Chen, and Z. Zhu, 2012: A limited area model (LAM) intercomparison study of a TWP-ICE active monsoon mesoscale convective event. *J. Geophys. Res.*, **117**(D11208), doi:10.1029/2011JD016447.

Zipser, E. J. and C. Gautier, 1978: Mesoscale events within a GATE tropical depression. *Mon. Wea. Rev.*, **106**, 789-805.

Zipser, E. J. and K. R. Lutz, 1994: The vertical profile of radar reflectivity of convective cells: A strong indicator of storm intensity and lightning probability? *Mon. Wea. Rev.*, **122**, 1751-1759.

Zipser, E. J., 2003: Some views on "hot towers" after 50 years of tropical field programs and two years of TRMM data. *Meteor. Monogr.*, **29**, 49-58.